

2018

Antibacterial Properties of TiO₂ Nanotubes coated with nano-ZnO and nano-Ag

Gunpath, Urvashi Fowdar

<http://hdl.handle.net/10026.1/11155>

<http://dx.doi.org/10.24382/1008>

University of Plymouth

All content in PEARL is protected by copyright law. Author manuscripts are made available in accordance with publisher policies. Please cite only the published version using the details provided on the item record or document. In the absence of an open licence (e.g. Creative Commons), permissions for further reuse of content should be sought from the publisher or author.



**Antibacterial Properties of TiO₂ Nanotubes coated
with nano-ZnO and nano-Ag**

by

URVASHI FOWDAR GUNPUTH

B.Sc., M.Sc. PhD.

A thesis submitted to Plymouth University in partial fulfilment for the degree
of

DOCTOR OF PHILOSOPHY

School of Marine Science and Engineering

Faculty of Science and Engineering

September 2017

~ i ~

Copyright Statement

This copy of the thesis has been supplied on condition that anyone who consults it is understood to recognise that its copyright rests with its author and that no quotation from the thesis and no information derived from it may be published without the author's prior consent.

Acknowledgments

First and foremost I would like to thank god, my spiritual master and my parents who helped me step in the research world which was a field of uncertainty for them. Then I would like to acknowledge the ongoing support of my husband who never let me give up and pushed me forwards during my weak times. He helped me boost my morale and aim higher always.

This project would not even be there if not for the funding provided by the Faculty of Science and Engineering of Plymouth University which I gratefully acknowledge. My supervisory team was the best support that I could have which I did not have to ask for and I would get it. I thank Huirong Le for believing in me and helping me at all times. I thank Richard Handy for the push towards the best and the ongoing support. I thank Chris Tredwin who monitored our progress and improved my self-confidence. Also I would like to include Alex Besinis in this part as he mentored me as a supervisor when required.

A special recognition goes to Terry Richards, the head of the technical team in the mechanical engineering lab. He has always been there from beginning till the end not only as a technician but also as a very good friend. Among the technical team, special thanks go to Zoltan (M. Eng.), Glenn, Roy, Peter (SEM), Andy from chemistry and Andy from Biology, Lynne, Will and Michelle (Biology) without whom, this project would have been impossible to implement.

Last but not least I would like to thank Kitti, my best friend at Plymouth University with whom I worked side by side and who not only helped me academically but helped my personal life during my time in Plymouth.

AUTHOR'S DECLARATION

At no time during the registration for the degree of **Doctor of Philosophy** has the author been registered for any other University award without prior agreement of the Graduate Sub-Committee.

Work submitted for this research degree at the Plymouth University has not formed part of any other degree either at Plymouth University or at another establishment.

This study was financed with the aid of a studentship from **Plymouth University**.

A programme of advanced study was undertaken, which included **Modules for Animal Testing** on Rodents and Rabbits by the Home Office with the aim of obtaining a personal licence for animal testing.

Relevant scientific seminars and conferences were regularly attended at which work was often presented and several papers prepared for publication.

Publications (or presentation of other forms of creative and performing work):

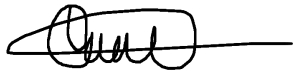
- U Danookdharree, H. R. Le, C. Tredwin. The effect of initial etching sites on the morphology of anodised TiO₂ nanotubes on Ti-6Al-4V alloy. *Journal of Electrochemical Society*, 162 (2015) E213-222, 2015.
DOI:10.1149/2.0011511jes.
- U Gunpath and H. R. Le. (2017) Anodised TiO₂ nanotubes as a scaffold for antibacterial silver nanoparticles on titanium implant. Manuscript being corrected after reviewers comments (For publication in *Materials Science & Engineering C*)
- U Gunpath and H Le. (2017) Composite coatings for implants and tissue engineering. *Biomedical composites*. 2nd Edition. Ed. L Ambrosio.
ISBN: 9780081007594

- Drafts of 1 papers are with the supervisor at the moment with the aim of publishing in the Biomaterials and nanomaterials related journals.
- 3 more papers being written with the aim of getting published in the biomaterials and nanomaterials journals.

Presentation and Conferences Attended:

- U Danookdharree, H. Le, R Handy, C. Tredwin. Antibacterial Properties and Molecular Biocompatibility of TiO₂-ZnO Nanocomposite Coatings for Dental Implants. BSODR Annual meeting, 6-8 September 2017
- U Danookdharree, H. Le, R Handy, C. Tredwin. Synthesis of a long term antibacterial coating involving strongly adhered ZnO nanoparticles to titania nanotubes for hip implant material. Institution of Mechanical engineers (IMEche): Hip Surgery: A Joint Engineering and Surgical Challenge, 3-4 November 2015
- U Danookdharree, H. Le, R Handy, C. Tredwin. Antibacterial coating made of strongly adhered nanosilver to titania nanotubes for dental implants. International Association for Dental Research Annual Meeting, 14-16 Sep 2015.
- U Danookdharree, H. R. Le, Antimicrobial silver nanoparticles on titanium dioxide nanotubes grown on Ti-6Al-4V medical grade alloy. The 2nd Symposium on Diagnostics and the Developing World, Brunel University, London, 23 March 2015
- U. Danookdharree, H. R. Le, R. Handy, C. Tredwin. Tailoring the Interfacial Adhesion of Anodised TiO₂ Nanotubes on Ti-6Al-4V Alloy for Medical Implants. 26th Annual Conference of the European Society for Biomaterials (ESB), 31st August – 3rd September 2014, Liverpool, UK.

Word count of main body of thesis: 43 995

Signed: 

Date: 19/03/2018

~ v ~

Abstract

Introduction

TiO₂ nanotubes grown on titanium alloy are known to increase the biocompatibility of the alloy when used in dental/orthopaedic implants.

Furthermore, their nanotubular structures can act as antibacterial agent carrier and as a scaffold for tissue engineering with the aim of adding antibacterial properties to the implant. This study aims at fabricating an antibacterial and biocompatible nanocomposite coating on Ti-6Al-4V involving nano-ZnO and nano-Ag.

Materials and Methods

Initially, TiO₂ nanotubes were self-assembled on the polished surface of medical grade Ti-6Al-4V alloy discs using anodisation. First silver nanoparticles were chemically reduced from silver ammonia using delta-δ-gluconolactone for different duration on the nanotubes to form TiO₂-Ag composite coating. Nano HA was added to the latter coating with the aim of reducing toxicity from silver, hence forming TiO₂-Ag-HA coating. Secondly, nano-ZnO was thermo-chemically grown on the TiO₂ nanotubes using zinc nitrate and hexamethylenetetramine. They were then annealed at 350-550 °C hence forming TiO₂-ZnO. HA was grown on the latter coating by a biomimetic method whereby the coated discs were placed in a concentrated simulated body fluid at 37 °C forming TiO₂-ZnO-HA.

The stability of the 4 coatings, TiO₂-Ag, TiO₂-Ag-HA, TiO₂-ZnO and TiO₂-ZnO-HA were assessed using the dialysis method (n=3 each) and then exposed to *S.aureus* for 24 hours in BHI broth. Their antibacterial properties were assessed using different assays and microscopic imaging with respect to different controls

(n=6 each for assays and n=3 for imaging). Their biocompatibility properties were assessed in the presence of primary human osteoblast cells in DMEM media with the help of biochemical assays, molecular gene expression and microscopic imaging (n=3).

Results

Both silver and zinc coated nanotubes showed significant level of antibacterial properties with silver coating being more bactericidal than the coating containing zinc. Nonetheless, the zinc oxide coatings were more biocompatible than the silver coating.

Conclusion and future works

Nano silver and zinc oxide containing composite coatings were successfully synthesised and tested in the presence of bacteria and human cells. The final conclusion was that nano-silver was still toxic and nano-ZnO coatings were more biocompatible.

Table of Contents

ABSTRACT	6
TABLE OF CONTENTS	8
LIST OF FIGURES	15
LIST OF TABLES	24
CHAPTER 1	1
GENERAL INTRODUCTION	1
1. 1 INTRODUCTION	2
1.2 NANOTECHNOLOGY IN MEDICINE	2
1.3 ORTHOPAEDIC AND DENTISTRY IMPLANTS	5
1.3.1 <i>Metallic bone implants</i>	6
1.3.2 <i>Metal Toxicology</i>	8
1.3.3 <i>Infection of implants</i>	9
1.4 TiO ₂ NANOTUBES.....	10
1.4.1 <i>Self-assembly of TiO₂ nanotubes on titanium based material</i>	15
1.4.2 <i>Scaffold for bone tissue engineering</i>	20
1.4.3 <i>Toxicological aspect</i>	22
1.4.4 <i>Antibacterial properties</i>	23
1.4.5 <i>Drug delivery system</i>	23
1.5 NANO-SILVER	25
1.5.1 <i>Chemical reduction of silver ions to silver nanoparticles</i>	28
1.6 NANO-ZINC OXIDE.....	30
1.7 NANO-HYDROXYAPATITE	32
1.8 HYPOTHESES	34
1.9 AIM AND OBJECTIVES	35
CHAPTER 2	37
OPTIMISATION OF THE ANODISATION PROCESS FOR THE SELF-ASSEMBLY OF TiO₂ NANOTUBES ON THE SURFACE OF Ti-6Al-4V DISCS	37

2.1 INTRODUCTION	38
2.2 MATERIALS AND METHODS	39
2.2.1 <i>Ti-6Al-4V disc pre-anodisation preparation</i>	39
2.2.2 <i>Anodisation of Ti-6Al-4V discs</i>	40
2.2.3 <i>SEM imaging and measurements the of TiO₂ nanotubes</i>	41
2.2.4 <i>Interfacial adhesion test</i>	42
2.2.5 <i>Growth of TiO₂ nanotubes at different time interval</i>	44
2.2.6 <i>Statistical analysis</i>	44
2.3 RESULTS	45
2.3.1 <i>Effect of pH on anodisation current, nanotubes morphology and adhesive strength of nanotubes to Ti-6Al-4V alloy</i>	45
2.3.2 <i>Effect of initial sweep rate on anodisation current, nanotubes morphology and adhesive strength of nanotubes to Ti-6Al-4V alloy</i>	52
2.3.3 <i>Different stages of self-assembly of TiO₂ nanotubes</i>	60
2.4 DISCUSSION.....	63
2.4.1 <i>Current density variation during anodisation</i>	63
2.4.2 <i>Effect of pH</i>	66
2.4.3 <i>Effects of sweep rate</i>	68
2.4.4 <i>Stages of nanotube formation</i>	69
2.4.5 <i>Theory of initial etching sites</i>	70
2.5 CONCLUSION	73
CHAPTER 3	74
PILOT STUDY- AMORPHOUS TiO₂ NANOTUBES AS A SCAFFOLD FOR SILVER NANOPARTICLES ON TITANIUM ALLOY	74
3.1 INTRODUCTION	75
3.2 MATERIALS AND METHODS	75
3.2.1 <i>Growth of silver nanoparticles</i>	76
3.2.2 <i>Morphological observations on TiO₂ nanotubes coated with Ag-NPs</i>	77
3.2.3 <i>Measurement of silver ion release after 24 hours</i>	78
3.2.4 <i>Statistical Analysis</i>	80

3.3 RESULTS	80
3.3.1 Silver nanoparticles synthesis using Method 1	80
3.3.2 Silver nanoparticles synthesis using Method 2	83
3.3.3 Total dissolved silver in SBF	85
3.4 DISCUSSION.....	88
3.4.1 Synthesis of micro-clusters (cluster as a whole within the micrometre scale) of Ag-NPs on amorphous TiO ₂ nanotubes.....	88
3.4.2 Synthesis of nano-clusters (cluster as a whole within the nanometre scale) of Ag-NPs on amorphous TiO ₂ nanotubes.....	90
3.4.3 Comparison of clustering of nanoparticles on amorphous TiO ₂ nanotubes.....	91
3.5 CONCLUSIONS	94
CHAPTER 4	95
GENERAL MATERIALS AND METHODS	95
4.1 GENERAL MATERIALS AND METHODS	96
4.2 SYNTHESIS OF AG-NP AND NANO-ZNO LOADED TiO ₂ NANOTUBES.....	97
4.2.1 Post anodisation annealing	97
4.2.2 ADDITION OF SILVER NANOPARTICLES AND NANO ZINC OXIDE	98
4.3 DIALYSIS EXPERIMENT AND THE RELEASE OF DISSOLVED METAL.....	99
4.4 ANTIBACTERIAL TEST	100
4.4.1 Plate preparation and exposure to <i>S. aureus</i>	102
4.4.2 Cell viability.....	104
4.4.3 Lactate production	104
4.5 BIOCOMPATIBILITY TEST	107
4.5.1 Osteoblast cell culture	107
4.5.2 Plate preparation for osteoblast cells exposure to samples.....	108
4.5.3.1 Homogenate and media collection	109
4.5.3.2 Protein assay on homogenate	110
4.5.3.3 Lactate dehydrogenase assay on homogenate and media	111
4.5.3.4 Alkaline phosphatase assay on cell homogenate and media	112
4.5.3.5 Glutathione assay on cell homogenate.....	113
4.5.4 Relative gene expression using comparative Ct method.....	115

4.5.4.1 RNA extraction using RNeasy Kit.....	115
4.5.4.2 Block preparation using QuantiNova SYBR Green RT Kit.....	116
4.5.4.3 Comparative Ct for quantitative PCR.....	118
4.6 CHANGE IN IONIC CONCENTRATION OF MEDIA AFTER.....	119
4.7 IMAGING COATED SAMPLES USING SEM	120
4.8 STATISTICAL ANALYSIS	121
CHAPTER 5	123
TiO₂ NANOTUBES EMBEDDED WITH SILVER NANOPARTICLES ON Ti-6Al-4V	
ALLOY AND THEIR RESPECTIVE ANTIBACTERIAL PROPERTIES AND	
BIOCOMPATIBILITY	123
5.1 INTRODUCTION.....	124
5.2 MATERIALS AND METHODS	125
5.2.1 Silver nanoparticles composite coating synthesis.....	125
5.2.2 Addition of hydroxyapatite	126
5.2.3 Antibacterial test of the silver composite coating	127
5.2.4 Biocompatibility test of the AgNp composite coating	127
5.3 RESULTS	128
5.3.1 Imaging and analysis of Ag-Np containing nanocomposite coating.....	128
5.3.1.1 Imaging of coating after addition of nano HA.....	133
5.3.2 Dialysis Experiment.....	135
5.3.3 Antibacterial Properties of nanocomposite coating.....	138
5.3.3.1 Cell viability of S. aureus	138
5.3.3.2 Lactate production of exposed S.aureus	139
5.3.3.3 Silver ions release in broth from coating.....	142
5.3.3.4 Bacterial Adhesion of bacteria - Microscopic imaging	144
5.3.4 Biocompatibility of nanocomposite coating	146
5.3.4.1 Protein Assay	147
5.3.4.2 Alkaline phosphatase	148
5.3.4.3 Lactate dehydrogenase assay.....	150
5.3.4.4 Glutathione Assay	152
5.3.4.5 Trace Element Analysis.....	153

5.3.4.5 Microscopic imaging of adhered cells.....	155
5.3.4.6 Electrolytes measurement.....	157
5.3.5 PCR data of markers in exposed osteoblast cells.....	160
5.4 DISCUSSION.....	164
5.4.1 Antibacterial properties.....	164
5.4.2 Biocompatibility.....	166
5.4.3 PCR data for markers in osteoblast cells.....	168
5.5 CONCLUSION.....	169
CHAPTER 6.....	170
TiO₂ NANOTUBES EMBEDDED WITH ZINC OXIDE NANOSTRUCTURES ON Ti-6Al-4V ALLOY AND THEIR RESPECTIVE ANTIBACTERIAL PROPERTIES AND BIOCOMPATIBILITY.....	170
6.1 INTRODUCTION.....	171
6.2 MATERIALS AND METHODS.....	172
6.2.1 ZnO composite coatings synthesis.....	172
6.2.2. Addition of hydroxyapatite on TiO ₂ -ZnO.....	173
6.2.2 Antibacterial test of the nano ZnO composite coating.....	174
6.2.3 Biocompatibility test of the nano ZnO composite coating.....	175
6.3 RESULTS.....	175
6.3.1 Microscopic imaging and surface analysis.....	175
6.3.2 Dialysis Experiment.....	190
6.3.3 Antibacterial Properties of nanocomposite coating.....	194
6.3.3.1 Viability of S. aureus.....	194
6.3.3.2 Lactate production of exposed S. aureus.....	196
6.3.3.3 Zinc ions release into the culture media from the coatings.....	198
6.3.3.4 Bacterial Adhesion – Microscopic imaging.....	200
6.3.4 Biocompatibility of the nanocomposite coatings.....	202
6.3.4.1 Protein concentration of cell homogenates.....	203
6.3.4.2 Alkaline phosphatase assay.....	204
6.3.4.3 Lactate dehydrogenase assay.....	206
6.3.4.4 Trace element analysis.....	208

6.3.4.5 Glutathione Assay	210
6.3.4.6 Electrolyte concentration	211
6.3.4.7 Microscopic imaging of adhered cells.....	215
6.3.5 PCR data for markers in exposed osteoblast cells	217
6.4 DISCUSSION.....	221
6.4.1 Antibacterial properties.....	222
6.4.2 Biocompatibility of the composite coatings with osteoblasts.....	224
6.5 CONCLUSION	228
CHAPTER 7	229
GENERAL DISCUSSION	229
7.1 NANOCOMPOSITE COATING FOR IMPLANTS.....	232
7.1.2 Comparison of nano-ZnO to Ag-Np composite coatings	235
7.2 CLINICAL PERSPECTIVE.....	237
7.3 LIMITATIONS.....	239
7.4 FUTURE WORKS	241
APPENDIX	242
APPENDIX A.....	243
APPENDIX B.....	244
REFERENCES	245
PUBLICATION	267
PUBLICATION 1	268
PUBLICATION 2	278
6.1 INTRODUCTION	282
6.2 TYPES OF COMPOSITE COATINGS	283
6.2.1 ANTI-WEAR COATINGS	284
6.2.2 BIOCOMPATIBLE COATINGS	286
6.2.3 ANTI-BACTERIAL COATINGS.....	288
6.3 SYNTHESIS OF COMPOSITE COATINGS.....	290

6.3.1 CHEMICAL DEPOSITION	291
6.3.2 ELECTROPHORETIC DEPOSITION	294
6.3.3 ELECTROCHEMICAL DEPOSITION (ANODISING, ELECTROPLATING)	295
6.3.4 BIOMIMETIC DEPOSITION	296
6.3.5 OTHER DEPOSITION METHODS	298
6.4 SMART COMPOSITE COATINGS	300
6.5 SUMMARY	301
ACKNOWLEDGMENTS	301
REFERENCES	301

List of figures

Figure 1.1: Anodisation process figuring the anode which is the sample to be coated being in an electrolyte containing ions which causes the redox reactions to take place. The pH and temperature of the electrolytes are measured using the pH meter. A voltage is applied to the anode and cathode (copper used in this study) using a power supply which provides the resulting anodising current. All the data are recorded in a computer so as to be able to compute all of them together. 11

Figure 1.2: The reduction process of silver ammonia complex to silver nanoparticles in the presence of glucose starting with (A) the complex binding with the glucose molecule, (B) the formation of silver nanoparticles, ammonia and a radical ending with (C) a lactone molecule, ammonia and the nanoparticles..... 29

Note. From ‘Time dependence of nucleation and growth of silver nanoparticles’(Hussain *et al.* 2011). 29

Figure 2.1: Electrochemical cell setup for anodisation 41

Figure 2. 2 : The effect of the change in pH on the (A) anodising current density with time in the first 1 second and (B) voltage in the first 1 second. 46

Figure 2.3: The effect of the change in pH on the (a) anodising current density with time during the first 50 s, (B) voltage during the first 50 s and (C)) anodising current density with time between 1000 s and 3600 s of the anodisation process 47

Figure 2.4: The effect of the change in pH on the (A) nanotubes pore diameter and wall thickness and (B) porosity of the nanotubes coating and the current density at the end of the anodisation. The alphabets present the significance in difference between the differently treated samples at 95 % confidence interval (Transformed One-way ANOVA, n = 3) 49

Figure 2.5: The effect of the change in pH on the pull off load per unit (for adhesion test) whereby the alphabets present the significance in difference between the differently treated samples at 95 % confidence interval (Kruskal-Wallis, n = 3)..... 50

Figure 2.6: SEM images of the TiO₂ nanotubes formed after anodisation performed with the pH of the electrolyte solution at (A) 3, (B) 4 and (C) 5 (×50 000) and (D) at pH 6 (×10 000) magnification. (E) EDS analysis of the microparticles on (D)..... 51

Figure 2.7: The effect of the change in initial sweep rate on the (A) anodising current density with time in the first 1 second and (B) voltage in the first 1 second of the anodisation process.	53
Figure 2.8: The effect of the change in initial sweep rate on the (A) anodising current density with time in the first 100 second, (B) with voltage in the first 100 second and (C) with time between 1000 s and 3600 s of the anodisation process.....	54
Figure 2.9: The effect of the change in initial sweep rate on the (A) nanotubes pore diameter and wall thickness and (B) porosity of the nanotubes coating and the current density at the end of the anodisation whereby the alphabets present the significance in difference between the differently treated samples at 95 % confidence interval (Transformed One-way ANOVA, n=3).....	56
Figure 2.10: The effect of the change in initial sweep rate on the pull off load per unit are for adhesion test whereby the alphabets present the significance in difference between the differently treated samples at 95 % confidence interval (Transformed One-way ANOVA, n=3).	57
Figure 2.11: SEM images of the TiO₂ nanotubes formed after anodisation with an initial sweep rate of (A) 0.2, (B) 0.5 (C) 0.8, (D) 1.0 and (E) 1.5 V/s. Images are at x50 000 magnification.	59
Figure 2.12: SEM images of the surface of polished and cleaned Ti-6Al-4V discs at (A) 5 (Inside figure is of the same surface at a lower magnification concentration on just the alpha alloy), (B) 10, (C) 15, (D) 20, (E) 25, (F) 30 and (G) 60 minutes of anodisation at 20 V (0.5 V/s) in an electrolyte of pH 4 at x 50 000 magnification.	61
Figure 2.13: The EDS analysis of the α- and β- part of the coated discs surface after 60 minutes of anodisation from Figure 2.12 G.	62
Figure 2.14: (A, B and C) Current density variation with respect to time during anodisation zoomed in for various time intervals. (D) Anodisation current density variation with time highlighting the part when there is no change in current density. (E) An illustration of the presence of the electrical double layer for the IPE effect..	64
Figure 2.15: Vertical and horizontal cross sections of TiO₂ nanotubes models growing (A) in an electrolyte of low and high pH and (B) at an initial low and high sweep rates. The first part in both A and B highlights the changes happening on single	

nanotubes whereas the second part shows the distribution, size and quantity of the nanotubes grown in the various conditions..... 72

Figure 3.1. SEM images of silver nanoparticles forming micro-clusters on TiO₂ nanotubes (A) aTiO₂-Ag0.005, (B) aTiO₂-Ag0.01 and (C) aTiO₂-Ag0.015 being viewed at a low magnification of ×1000. Panel D-F shows the respective coatings at a higher magnification of ×25 000. Panel (G-I) shows the respective EDS analysis of the silver nanoparticles. 82

Figure 3.2: SEM images of nanoclusters of silver nanoparticles. The exposure time to silver ammonia was (A) 1 minutes, (B) 5 minutes and (C) 10 minutes and exposure to δ-gluconolactone was maintained at 5 minutes. (D), (E) and (F) shows a higher magnification SEM images of aTiO₂-Ag1G5, aTiO₂-Ag5G5 and aTiO₂-Ag10G5 respectively. (G-I) EDS analysis of the silver nanoparticles coated aTiO₂..... 84

Figure 3.3: Concentration of total silver dissolved in acidified SBF measured by ICP-OES after 24 hour exposure of the aTiO₂ discs from (A) method 1 and (B) Method 2 of silver nanoparticles synthesis. The different letters indicate the statistically significant differences in between samples at a confidence interval of 95 % (One-way ANOVA, n=3) 86

Figure 4.1 (A) Plate setup for the coated samples with the respective controls for biochemical assays and imaging (24-well plate) (B) Summary of biochemical assays performed for the antibacterial tests. The figure illustrates one well from the plate in (A) with the titanium alloy disc at the bottom covered with the BHI broth containing the *S. aureus*. Briefly after the overnight exposure, the exposed broth is centrifuged after which the supernatant is used for the lactate production assay and the pellets for Live/Dead assay. The bacteria which were attached to the disc were removed and allowed to grow in BHI broth for 5 hours. Then the resulting broth was centrifuged and the supernatant is used for the lactate production assay and the pellets for Live/Dead assay. All the supernatant and pellets were used for ICP as well..... 101

Figure 4.2: Example calibration curve for the (A) Live/Dead® Backlight™ Kit following the protocol from Invitrogen and (B) Lactate production assay with respect to the standards used in the respective protocols..... 106

Figure 4.3: Plate preparation for samples exposure to primary osteoblast cells grown in DMEM media in triplicates exposed on different plates	108
Figure 4.4: Different 24-well plates' setup for biocompatibility tests with each plate at a different passage number per replicate. Plate 1-3 was the first replicate with the 4 th passage number being used for the biochemical assays, PCR and SEM analysis.	108
Figure 4.5: Example calibration data for protein assay on (A) day 4 and (B) day 10 with respect to the standards provided with the kit.	111
Figure 4.6: Absorbance readings for standards used in the calibration of the glutathione assay read at a wavelength of 412 nm. The concentration of glutathione standards used were (A) 0 mg/mL ($R^2=0.8999$), (B) 10 mg/mL ($R^2= 0.9978$), (C) 20 mg/mL ($R^2= 0.9652$), (D) 30 mg/mL ($R^2=0.9994$), (E) 40 mg/mL ($R^2 = 0.9993$) and (F) 50 mg/mL ($R^2= 0.9991$) and the data was made to fit a sigmoidal shape of 3 parameters using SigmaPlot with the R^2 value representing the line fit.	114
Figure 4.7 : Calibration data for GSH assay at 0-50 mg/mL GSH standards with absorbance read at 412 nm over 15 min ($R^2 = 0.9998$ for polynomial linear fit).	115
Figure 4.8: A sample 384-well block preparation for PCR with the 3 replicates per samples included. One more similar plates was prepared and used as a technical replicate for the experiment.	117
Figure 5.1: SEM images of Ti-6Al-4V discs coated with TiO ₂ -Ag3 at (A) ×10 000 and (B) ×30000 magnification. The spherical white structures in 5.1 B are considered to be the silver nanoparticles, the EDS analysis of which is shown in (C).....	129
Figure 5.2: SEM images of Ti-6Al-4V discs coated with TiO ₂ -Ag7 at (A) ×5 000 and (B) ×30000 magnification. The spherical white structures in 5.2 B are considered to be the silver nanoparticles, the EDS analysis of which is shown in (C).....	130
Figure 5.3: SEM images of Ti-6Al-4V discs coated with TiO ₂ -Ag10 at (A) ×5 000 and (B) ×30000 magnification. The spherical white structures in 5.3 B are considered to be the silver nanoparticles, the EDS analysis of which is shown in (C).....	131
Figure 5.4: SEM images of (A) TiO ₂ -Ag7 (×5000) and (B) TiO ₂ -Ag7-HA (×200) at low magnifications and their magnified versions in (C, ×30 000) and (D, ×1000) respectively (n=3). (E) and (F) represents the EDS analysis of TiO ₂ -Ag7 and TiO ₂ -Ag7-HA respectively.	134

Figure 5.5: Concentration of (A) silver ions in the acidified SBF from the dialysis beakers (external media) as measured by the ICP-MS instrument, (B) calcium ions and (C) phosphorus ions in the acidified SBF from the dialysis beakers as measured by the ICP-OES instrument.	136
Figure 5.6 : Concentration of (A) silver ions in the acidified SBF from the beaker and the dialysis bag after 24 hours of dialysis (Mean \pm S.E.M, Kruskal-Wallis, n=3) and (B) calcium and phosphorus ions in the acidified content of the beaker (external media) and the dialysis bag after 24 hours of dialysis (Kruskal-Wallis, n=3). The alphabets show the significance in differences in the concentration of the ions between the differently coated samples and their respective locations at 95.0 % confidence level.	137
Figure 5.7 Percentage of live to dead <i>S. aureus</i> cells in (A) exposed media and (B) incubated detached cells presented as Mean \pm S.E.M (Kruskal-Wallis, n=6). The different alphabets represent the statistically significant differences between the different samples at a confidence interval of 95 %.....	139
Figure 5.8 Amount of Lactate produced by <i>S. aureus</i> in (A) exposed media and (B) incubated adhered cells. Data are presented as mean \pm S.E.M (Kruskal-Wallis, n=6). The different alphabets represent the statistically significant differences between the different samples at a confidence interval of 95 %	141
Figure 5.9: Concentration of (A) silver, (B) Calcium and (C) Potassium ions present in exposed media after 24 hours exposure of samples to <i>S. aureus</i> in BHI broth. The data are presented as Mean \pm S.E.M with the different alphabets representing the statistically significant differences between the different samples at a confidence interval of 95 %, (n=6).	143
Figure 5.10: SEM images (JEOL 7001) at a magnification of $\times 1000$ of <i>S. Aureus</i> grown (A) in just media as a control and (B) on uncoated TiO ₂	144
Figure 5.11: SEM images (JEOL 7001) at a magnification of $\times 1000$ of <i>S. Aureus</i> grown (A) in aqueous Silver Nitrate and (B) in the presence of Silver nanoparticles	145
Figure 5.12: SEM images (JEOL 7001) at a magnification of $\times 1000$ of <i>S. Aureus</i> grown (A) on TNT-nAg and (B) on TNT-nAg/Ha.	146

Figure 5.13: Concentration of protein in cell homogenates from attached osteoblast cells on TiO₂-Ag7 and TiO₂-Ag7-HA disks and the controls at day 4 and 10 of exposure. The data are presented as Mean ± S.E.M with the alphabets represent the significance in difference among the various parameters involved at a confidence interval of 95 % (Kruskal-Wallis, n=3). 147

Figure 5.14: ALP activity of osteoblast cells in (A) homogenate and (B) exposed media. The values are represented as Mean ± S.E.M. The different alphabets represent the statistically significant differences between the different samples on different days at a confidence interval of 95 % (Kruskal-Wallis, n=3). 149

Figure 5.15: LDH activity of osteoblast cells in (A) homogenate and (B) exposed media. The values are represented as Mean ± S.E.M. The different alphabets represent the statistically significant differences between the different samples on different days at a confidence interval of 95 % (Kruskal-Wallis, n=3). 151

Figure 5.16: Glutathione concentration in homogenate of cells exposed to samples and controls on day 4 and day 10. The data are presented as Mean ± S.E.M. The different alphabets represent the statistically significant differences between the different samples on different days at a confidence interval of 95 % (Kruskal-Wallis, n=3). 152

Figure 5.17: ICP readings for silver in the (A) Homogenate and (B) exposed media of the osteoblast cells grown on the samples and controls. The data are presented as Mean ± S.E.M..... 154

Figure 5.18 : SEM images of (A) and (B) TiO₂, (C) and (D) TiO₂-Ag7 and (E) and (F) TiO₂-Ag7-HA viewed at low (×100) and high magnifications (×1500) respectively. 156

Figure 5.19: Change in gene expression of FAK in osteoblast cells grown on TiO₂-Ag7 and TiO₂-Ag7-HA on day 4 and 10 of exposure, with respect to the cells grown on TiO₂ after normalisation with respect to β-actin (Mean ± S.E.M, Kruskal- Wallis, p=0.05, n=3). The different alphabets represent the statistically significant differences between the different samples on different days at a confidence interval of 95 %. 160

Figure 5.20: Change in gene expression of (A) RunX-2, (B) ALP, (C) OC and (D) CA1 in osteoblast cells grown on TiO₂-Ag7 and TiO₂-Ag7-HA on day 4 and 10 of exposure, with respect to the cells grown on TiO₂ after normalisation with respect to β-actin

(Mean ± S.E.M, Kruskal-Wallis, p=0.05, n=3). The different alphabets represent the statistically significant differences between the different samples on different days at a confidence interval of 95 %.....	161
Figure 5.21: Change in gene expression of (A) COX 2, (B) IL 6 and (C) TNFα in osteoblast cells grown on TiO$_2$-Ag7 and TiO$_2$-Ag7-HA on day 4 and 10 of exposure, with respect to the cells grown on TiO$_2$ after normalisation with respect to β-actin (Mean ± S.E.M, Kruskal- Wallis, p=0.05, n=3). The different alphabets represent the statistically significant differences between the different samples on different days at a confidence interval of 95 %.....	162
Figure 5.22: Change in gene expression of SOD in osteoblast cells grown on TiO$_2$-Ag7 and TiO$_2$-Ag7-HA on day 4 and 10 of exposure, with respect to the cells grown on TiO$_2$ after normalisation with respect to β-actin (Mean ± S.E.M, Kruskal- Wallis, p=0.05, n=3). The different alphabets represent the statistically significant differences between the different samples on different days at a confidence interval of 95 %.....	163
Figure 6.1: SEM images of Ti alloy with (A) the self assembled titania nanotubes (TiO$_2$) at (A) \times5000 and (B) \times50000 magnification with the (C) the EDS analysis of part of 6.1 B. (D) TiO$_2$ with HA on the surface with (E) the EDS analysis of the HA particle shown.....	177
Figure 6.2: SEM images of Ti alloy with (A) ZnO grown on the TiO$_2$ without any heat treatment at (A) \times10000 and (B) \times30000 magnification with the (C) the EDS analysis of part of 6.2 B. (D) TiO$_2$-ZnO with HA on the surface with (E) the EDS analysis of the HA particle shown.....	179
Figure 6.3: SEM images of Ti alloy with (A) ZnO grown on the TiO$_2$ after 350 $^{\circ}$C heating viewed at (A) \times5000 and (B) \times30000 magnification with (C) the EDS analysis of part of 6.3 B. (D) TiO$_2$-ZnO/350 with HA on the surface with (E) the EDS analysis of the HA particle shown.....	181
Figure 6.4: SEM images of Ti alloy with (A) ZnO grown on the TiO$_2$ after 450 $^{\circ}$C heating viewed at (A) \times5000 and (B) \times30000 magnification with (C) the EDS analysis of part of 6.4 B. (D) TiO$_2$-ZnO/450 with HA on the surface with (E) the EDS analysis of the HA particle shown.....	183

Figure 6.5: SEM images of Ti alloy with (A) ZnO grown on the TiO₂ after 550 °C heating viewed at (A) ×5000 and (B) ×30000 magnification with (C) the EDS analysis of part of 6.5 B. (D) TiO₂-ZnO/550 with HA on the surface with (E) the EDS analysis of the HA particle shown. 185

Figure 6.6: (A) EDS reading for Zinc from the coatings and (B) Roughness of the resulting coating. 187

Figure 6.7: ICP readings of the 3SBF after 24 hours exposure for (A) zinc and (B) calcium and phosphorus 189

Figure 6.8: Concentration of (A) zinc ions in the acidified SBF from the dialysis beakers as measured by the ICP-MS instrument, (B) calcium ions and (C) phosphorus ions in the acidified SBF from the dialysis beakers as measured by the ICP-OES instrument. 192

Figure 6.9: Concentration of (A) zinc ions in the acidified SBF from the beaker and the dialysis bag after 24 hours (Mean ± S.E.M, Transformed One-way ANOVA, n=3) and (E) calcium and phosphorus ions in the acidified content of the beaker and the dialysis bag after 24 hours (Kruskal-Wallis, n=3). The different alphabets show the significant differences in between the different samples on different days at 95.0 % confidence level..... 193

Figure 6.10 : Percentage of live to dead cells in (A) the incubated bacteria and (B) exposed media read from the calibration curve for the BacLight Live/Dead Assay (Mean ± S.E.M, Kruskal-Wallis, n=6). The different alphabets represent the statistically significant differences between the different samples at a confidence interval of 95 %. 195

Figure 6.11: Concentration of lactate in (A) the incubated adhered bacteria and (B) exposed media after calibration (Mean ± S.E.M, Kruskal-Wallis, n=6). The different alphabets represent the statistically significant differences between the different samples at a confidence interval of 95 %. 197

Figure 6.12 Concentration of (A) zinc ions, (B) calcium ions and (C) phosphorus ions in the acidified exposed media after overnight growth of *S.aureus* on the samples and controls read from ICP-OES (Mean ± S.E.M, Kruskal-Wallis, n=6). The different

alphabets represent the statistically significant differences between the different samples at a confidence interval of 95 %.	199
Figure 6.13: SEM images of attached <i>S.aureus</i> after overnight culture on (A) 24 well plate plastic surface [Control] (B) Ti alloy with TiO ₂ nanotubes on the surface [TiO ₂].	200
Figure 6.14: SEM images of attached <i>S.aureus</i> after overnight culture on (A) 24 well plate plastic with zinc chloride on the latter as a negative control for zinc ions [ZnCl ₂] (B) 24 well plate plastic with zinc oxide nanoparticles on the latter as a negative control for nano zinc [nZnO].	201
Figure 6.16: Concentration of protein in cell homogenate from attached osteoblast cells on TiO ₂ -ZnO/350 and TiO ₂ -ZnO-HA/350 and the controls at day 4 and 10 of exposure (Mean ± S.E.M, n=3). The different alphabets represent the statistically significant differences between the different samples on different days at a confidence interval of 95 %.	204
Figure 6.17: ALP activity of (A) osteoblast cells' homogenate grown on the coatings and controls on day 4 and 10 (B) the media in which they grew on day 1, 4, 7 and 10 (Mean ± S.E.M, Kruskal-Wallis, n=3). The different alphabets represent the statistically significant differences between the different samples on different days at a confidence interval of 95 %.	205
Figure 6.18 : LDH activity of osteoblast cells in the homogenate on day 4 and 10. (D in the media on day 1, 4, 7 and 10 (Mean ± S.E.M, Kruskal-Wallis, n=3). The different alphabets represent the statistically significant differences between the different samples between different days at a confidence interval of 95 %.	207
Figure 6.19: Trace element analysis for zinc read by ICP-OES of (A) homogenate of osteoblast cells on day 4 and 10. (B) media in which osteoblast cells were grown on day 1, 4, 7 and 10 (Mean ± S.E.M, Kruskal-Wallis, n=3). The different alphabets represent the statistically significant differences between the different samples between different days at a confidence interval of 95 %.	209
Figure 6.20: Glutathione assay results of homogenates of osteoblast cells on day 4 and day 10. All data are presented as mean ± S.E.M (Kruskal-Wallis, n=3). The different alphabets represent the statistically significant differences between the different samples between different days at a confidence interval of 95 %.	210

Figure 6.22: Change in gene expression of FAK in osteoblast cells grown on TiO₂-ZnO/350 and TiO₂-ZnO-HA/350 on day 4 and 10 of exposure, with respect to the cells grown on TiO₂ after normalisation with respect to β -actin. The different alphabets represent the statistically significant differences between the different samples between different days at a confidence interval of 95 %. 217

Figure 6.23: Change in gene expression of (A) RunX-2, (B) ALP, (C) OC and (D) CA1, in osteoblast cells grown on TiO₂-ZnO/350 and TiO₂-ZnO-HA/350 on day 4 and 10 of exposure, with respect to the cells grown on TiO₂ after normalisation with respect to β -actin. The different alphabets represent the statistically significant differences between the different samples between different days at a confidence interval of 95 %. 218

Figure 6.24: Change in gene expression of (A) COX 2, (B) IL 6 and (C) TNFa, in osteoblast cells grown on TiO₂-ZnO/350 and TiO₂-ZnO-HA/350 on day 4 and 10 of exposure, with respect to the cells grown on TiO₂ after normalisation with respect to β -actin. The different alphabets represent the statistically significant differences between the different samples between different days at a confidence interval of 95 %. 219

Figure 6.25: Change in gene expression of SOD in osteoblast cells grown on TiO₂-ZnO/350 and TiO₂-ZnO-HA/350 on day 4 and 10 of exposure, with respect to the cells grown on TiO₂ after normalisation with respect to β -actin. The different alphabets represent the statistically significant differences between the different samples between different days at a confidence interval of 95 %. 220

List of Tables

Table 1.1: The various combinations of conditions used in the presence of aqueous electrolytes for anodisation and the resulting diameter and thickness of nanotubes formed 13

Table 1.2: Classification of bacterial agents that can be used on the surface of implants 24

Table 1.3: Method of silver nanoparticles synthesis on TiO₂ nanotubes and the bacteria against which their antibacterial properties were tested.	26
Table 4.1: Primers used for PCR in this study	118
Table 5.1: Diameter of silver nanoparticles grown on TiO₂ shown as mean ± S.E.M, n=3 with the alphabets indicating the statistical difference between the samples using One-way ANOVA at a confidence interval of 95 %	132
Table 5.2: Electrolytes' ions concentration in homogenate.	157
Table 5.3: Electrolytes' ions concentration in media	159
.	211
Table 6.2: The concentration of electrolytes ions in the acidified media on day 1, 4, 7 and 10 as measured by ICP-OES presented as mean ± SEM. The alphabets show the significance in differences among the different treatments involved and the different days at a 95 % confidence interval. The different ions were not compared between each other.	214

Chapter 1

General Introduction

1. 1 Introduction

Bacterial infection of bone implants is a major cause of implant failure in the field of orthopaedics and dentistry. In orthopaedics, the majority of bone implants are for knee and hip joint replacements whereby infection of the latter can be life-threatening which in turn requires invasive revision surgery as treatment (Raphel *et al.*, 2016). In dentistry such infections, such as peri-implantitis, cause inflammatory responses around the implant which lead to loss of surrounding bone tissue resulting in the need for costly revision surgeries and sometimes reconstructions of bone defects by bone grafts (Lu *et al.*, 2016). Peri-implantitis starts with the formation of biofilm at the implant surface with the host immune system struggling to combat the infection (Roos-Jansåker, Almhöjd & Jansson, 2017). One of the main solutions to such infection is targeted antibacterial agent delivery from the surface of the implants themselves (Gulati *et al.*, 2012a). The latter prevents and/or reduces biofilm formation from the start. In this context, nanotechnology provides the required platform for such reactions to happen.

1.2 Nanotechnology in medicine

Nanoparticles are particles with at least one primary geometric dimension of less than 100 nm (Nemmar *et al.*, 2013; Rogers *et al.*, 2008). Aggregates of dimensions bigger than 100 nm, formed by nanoparticles, are also considered to be nano (Handy, Owen & Valsami-Jones, 2008). Nanotechnology involves the application of engineered nanomaterials that exploit the novel chemical and

physical properties that become evident at the nanoscale compared to micron scale materials (Nemmar *et al.*, 2013; Tran, Nguyen & Le, 2013)

Nanotechnology has been applied in various fields such as medicine, cosmetics, renewable energies, environmental remediation and biomedical devices (Tran, Nguyen & Le, 2013). The use of nanotechnology in the field of medicine within the diagnostic and therapeutic areas is known as nanomedicine (dos Santos *et al.*, 2014; Mazaheri *et al.*, 2015). Nanomedicine is considered to be an important part of nanotechnology because the biological molecules in the human body function at a nano-level, hence combatting issues at a nano-level is believed to bring the best result (Mazaheri *et al.*, 2015). In the field of orthopaedics and dentistry, nanomedicine is employed because the bone surface has a nanostructure and mimicking the latter surface would help osseointegration of implants (Bjursten *et al.*, 2010; Brammer *et al.*, 2009). With respect to this aspect nano materials are used to coat the surface of medical implants.

A nanocomposite is a two-phase material with one of the phases containing particles with at least one dimension less than 100 nm (Kim *et al.*, 2017; Zhu *et al.*, 2017). Nanocomposite made as coatings on medical devices are used with the aim of enhancing the properties of the device by enhancing the coating properties at the nano scale, depending on the materials involved in the composite (Kim *et al.*, 2017). The synthesis of nanocomposites involves the growth of nanoparticles onto a matrix material (Sivasakthi *et al.*, 2017). In orthopaedic implants several types of nanocomposite coatings are employed with the aim of strengthening, increasing the bioactivity, enhancing lubricating properties of, and providing anti-microbial properties to the implants (Bandyopadhyay *et al.*, 2016; Huang *et al.*, 2014; Kim *et al.*, 2017). The goal is

to allow the implants to be accepted by the body and prevent rejection. An example of such coating is self-assembled TiO₂ nanotubes on titanium acting as a targeted drug delivery system at a nano-level on implants (Losic *et al.*, 2015). A targeted drug delivery system is a technique of drug delivery directly to the required specific tissues without being toxic to the healthy parts (Paul *et al.*, 2017; Sheikhpour, Barani & Kasaeian, 2017). Since the biochemical reactions in the human body take place at a nano-level, nanoparticles are considered to be a significant aspect of the targeted drug delivery system.

TiO₂ nanotubes on bone implants, grown under specific conditions with specific morphologies, have been shown to enhance biocompatibility of the implant (Hao *et al.*, 2013). Having a biocompatible carrier for the drug to be delivered is a main reason to choose TiO₂ as a drug carrier on implants.

Infection of implants is a common cause of malfunction of orthopaedic implants resulting in failure of the latter hence the need for antibacterial targeted drug delivery (Connaughton *et al.*, 2014; Gallo, Holinka & Moucha, 2014). Antibiotics such as gentamicin and cefuroxime have been previously delivered by the nanotubes on implants (Beyth *et al.*, 2015; Chennell *et al.*, 2013). However infections related to implants are normally caused by multiple bacteria which can develop resistance during the treatment period (Getzlaf *et al.*, 2016). This is where transition metal nanoparticles fill in the gap in combatting implants related infection (Manke, Wang & Rojanasakul, 2013; Reidy *et al.*, 2013). The nanoparticles are believed to provide the necessary bactericidal properties by other mechanisms such as direct metal ion toxicity, oxidative stress in some cases and interference in the glial cell line derived neurotrophic factor (GDNF) pathway which results in decreased adhesion of cells to material (Manke, Wang

& Rojanasakul, 2013; Reidy *et al.*, 2013). Among all the nanoparticles, silver nanoparticles are mostly used because of their exceptional chemical and physical properties as compared to their macro-self and because they are easy to manufacture and have been shown to be biocidal (dos Santos *et al.*, 2014). They are considered to be more efficient of an antibacterial agent compared to silver in any other different phase (Prabhu. & Poulouse, 2012).

1.3 Orthopaedic and dentistry implants

The bones in the human body consist of 10 – 20 % collagen, 60 – 70 % bone mineral, and 9 – 20 % water, by weight and they have a modulus of 10-30 GPa (Bauer *et al.*, 2013; Wu *et al.*, 2014). Hence an ideal implant is expected have the same chemical content and mechanical properties and not be toxic. Several types of materials have been considered and used as bone implants materials throughout history. Biomaterials such as metals, ceramics and polymers have been used on their own, and as part of composite materials (Liu, Tian & Jiang, 2013). In order to allow a successful integration of the implant material in the body it has to be or modified to be biocompatible, osteoinductive, porous and have the necessary mechanical properties, microarchitecture and surface properties that are as close as possible to natural bone (Liu, Tian & Jiang, 2013).

Hydroxyapatite (HA) is a bioceramic material with a chemical composition of $\text{Ca}_5(\text{PO}_4)_3\text{OH}$ and a calcium to phosphate ratio of 1.67 with similar chemical properties as bone; but lower mechanical properties especially for load bearing conditions (Arifin *et al.*, 2014; Wagoner Johnson & Herschler, 2011). HA can hence not be used on its own as a bone implant material. Reinforcement of HA

with various biomaterials such as gelatin, collagen, chitosan, carbon nanotubes and many more have been tried with improvement of the mechanical properties and addition of other properties such as antibacterial and enhanced biocompatibility (Venkatesan *et al.*, 2011; Venugopal *et al.*, 2010; Yanovska *et al.*, 2011). However they cannot be always used in load bearing situations as the mechanical strength still does not reach the required values (Venkatesan *et al.*, 2011). Metallic bone implants are chosen in such conditions because of their high mechanical strength (Razavi *et al.*, 2014). However there are issues with their modulus (a measure of stiffness), osseointegration and biocompatibility when metals are used (Chen & Thouas, 2015). Titanium metal and alloys have lower modulus than the metals used in implants and hence are considered the best biomaterial for bone implants (Bauer *et al.*, 2013).

1.3.1 Metallic bone implants

The various metals used for bone/dental implants are cobalt based alloys, stainless steel and titanium and its alloys (Chen & Thouas, 2015). Amongst these metals or alloys, titanium alloys are considered the best in orthopaedics and dentistry. This is because titanium alloy has a modulus of 60 – 110 GPa which is closer to the modulus of bone which is 10 – 30 GPa and lower than the modulus of the other metals/alloys (Arifin *et al.*, 2014; Bauer *et al.*, 2013). Large gaps in modulus between implants and bones lead to stress shielding, causing a decrease in the density of the bone which in turn mostly results in loosening of implants, the opportunity for infection and hence rejection (Geetha *et al.*, 2009). As such, titanium is chosen over the other options because of its high mechanical strength and low modulus.

Corrosion of metallic implants is another cause of loosening and rejection of implants. The inert oxide layer present on the surface of titanium alloy is one feature which prevents leaching of metal ions from the surface of the alloy, hence preventing corrosion (Al-Mobarak N. A., Al-Swayih A. A. & A., 2011). However, the naturally formed oxide layer on titanium metal is more stable than titanium alloy because of the presence of other metal components in the alloy (Liu, Chu & Ding, 2004; Oshida *et al.*, 2010). Nonetheless the oxide layer can be manipulated in the presence of specific external factors so that corrosion can be prevented (Sul, 2003). Such alteration of the surface morphology and chemistry not only prevents corrosion but they also help in the functionalisation of the surface with the aim of helping osseointegration (Brammer *et al.*, 2009). TiO₂ nanotube is the preferred choice of surface modification of the oxide layer on titanium alloy because of its good mechanical strength, excellent resistance to corrosion, and osseointegration capacity without any cytotoxic effects (Gulati *et al.*, 2012b; Mizukoshi, Ohtsu & Masahashi, 2013). There are various methods of synthesising the nanotubes such as sol–gel method, thermal chemical vapour deposition, thermal spraying, sputtering and anodisation which have been practiced for years (Durual *et al.*, 2013; Hao *et al.*, 2013). Among the above examples, anodisation is mostly used because of its simplicity and reliability (Galstyan *et al.*, 2013). The roughness, chemistry and morphology of the nanotubes on the surface of titanium alloy are favourable for osteoblast cells to grow better than on the alloy on its own as shown by many researches (Lan *et al.*, 2013; Peng *et al.*, 2013). Hence they can successfully act as a scaffold for tissue engineering in the field of orthopaedics and dentistry.

1.3.2 Metal Toxicology

Debris from the implants can be a risk of loosening, toxicity and rejection of the latter owing to the inflammatory process involved in the human body (Dalal *et al.*, 2012). Metallic ions released in the body can cause inflammation, oxidative stress, DNA damage, and be toxic (Ortiz *et al.*, 2016). Methods that prevent corrosion of metal surfaces in the body therefore will help to reduce toxicity. However, not all approaches to reducing corrosion result in biocompatibility. For example, chromium based alloy forms a chromium phosphate salt ($\text{Cr}(\text{PO}_4)_4\text{H}_2\text{O}$) which is in turn toxic to osteoblast cells and stainless steel releases chromium, nickel, zinc and cobalt ions which increases the risk of toxicity (Dalal *et al.*, 2012; Ortiz *et al.*, 2016). The toxicity of any metallic material should be tested in different conditions in the presence of different cell lines to overview the hazard. It is also imperative to do cytotoxicity tests on any new metallic materials before using them in-vivo (Park *et al.*, 2013). In the case of bone implants, testing the material in the presence of bone cells would give a better indication of the potential for biocompatibility.

Surface modification of the implant has been shown to enhance osseointegration and increase biocompatibility of the material (Zhao *et al.*, 2013). Nonetheless it is still important to test the toxicity of the material in the presence of the targeted cells once a surface modification has been performed. Titanium based material with self-assembled titania nanotubes on the surface have been demonstrated to enhance the adhesion and proliferation of osteoblast cells (SaOS2 cells) on the nanotubes as compared to titanium without the nanotubes (Wang & Poh, 2013). Despite the fact that the presence of the nanotubes increases biocompatibility of the titanium based material the

addition of hydroxyapatite to the nanotubes further improves the biocompatibility of the implant material (Portan *et al.*, 2012).

1.3.3 Infection of implants

The most common cause of malfunction and failure of bone implants have been associated with infection leading to osteomyelitis and removal of the implants in some cases (Min *et al.*, 2016). Such infections have been mostly associated with gram-positive bacteria mainly *Staphylococcus aureus* but the lower proportion of infection caused by gram-negative bacteria are considered to be very serious as well (Rodríguez-Cano *et al.*, 2014). Dental implant related infections have also been associated with *S. aureus* and in both dental and bone implants involving titanium metal, the latter micro-organisms have been shown to have an affinity for titanium and they have the ability of residing the infectious site for long term (Persson & Renvert, 2014).

Such infections in both bone and dental implants have been associated to the formation of the infectious agents living in a polymer matrix known as biofilm which makes the micro-organisms resistant to the body's immune system (Besinis, De Peralta & Handy, 2014; Min *et al.*, 2016). The formation of biofilm has also been related to the resistance to antibiotics (Dapunt *et al.*, 2014) . Upon placement of implants in the human body, there is a competition between host cells and infectious cells for attachment and for the micro-organisms to attach they need help from the host such as adhesins, such as fibronectin, fibrinogen, fibrin, collagen, laminin, vitronectin, thrombospondin, bone sialoprotein, elastin, and the matrix-binding protein (Widmer, 2001). As such, the presence of antibacterial coating on the surface of implants has the ability of

preventing initial bacterial adhesion and allowing osseointegration to take place better.

1.4 TiO₂ Nanotubes

Growing titanium dioxide (TiO₂) nanotubes on the surface of Ti and Ti alloy is a means of providing the required roughness with a high surface to volume ratio and high reactivities for cells to attach (Mor *et al.*, 2006). TiO₂ nanotubes can be formed on titanium alloy by several methods. The methods used can be divided into template-dependent and template-free methods. Examples of the template dependent method are the atomic layer deposition (ALD) and sol-gel deposition whereby a template, such as aluminium oxide, is required. The latter techniques involve several pre and post synthesis steps while being limited to specific substrates (Galstyan *et al.*, 2013). For example, the processes get divided into two stages and are not straightforward while at the end, the nanotubes have to be separated from the template that aided the nanotubes synthesis. One example of the template free methods is hydrothermal synthesis during which disorganised results are obtained such as nanoflowers (Mali *et al.*, 2012). Another example is electrochemical anodisation which is considered to be the most efficient method for the fabrication of self-organised TiO₂ nanotubes. It involves a simple procedure which is easy to adopt while being inexpensive (Ali *et al.*, 2011; Dikova *et al.*, 2014). This fabrication process is chosen over all the synthesis methods available as it allows the formation of uniform nanotubes arrays and a controllable pore size (Patete *et al.*, 2011; Sreekantan, Saharudin & Wei, 2011).

Anodisation is an electrochemical process whereby TiO₂ nanotubes can be self-assembled on the surface of titanium/titanium alloy. The latter metallic material is made at the anode. Figure 1.1 summarises the anodisation and the influencing parameters.

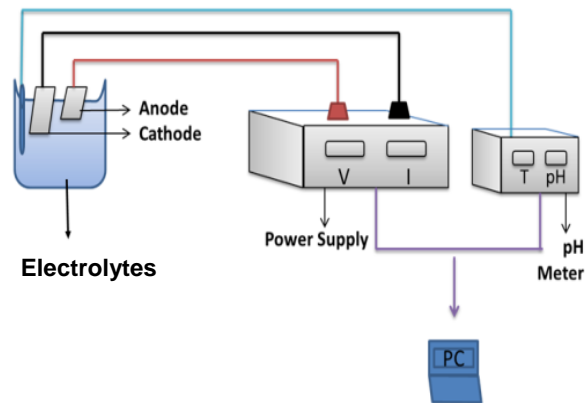


Figure 1.1: Anodisation process figuring the anode which is the sample to be coated being in an electrolyte containing ions which causes the redox reactions to take place. The pH and temperature of the electrolytes are measured using the pH meter. A voltage is applied to the anode and cathode (copper used in this study) using a power supply which provides the resulting anodising current. All the data are recorded in a computer so as to be able to compute all of them together.

The anode is the positively charged electrode while the cathode is the negatively charged electrode and in the electrochemical process, current flows between the electrodes causing redox reactions to take place (Lewandowski & Świdarska-Mocek, 2009). The content of the electrolytes determines what type of reactions take place. The most important part of the electrolytes is the fluoride ions which cause the oxide dissolution. Among the other ions present in an aqueous electrolyte, phosphate ions are considered to be best because of the attachment of phosphate ions to the nanotubes which enhances osseointegration as compared to other anions (Kim *et al.*, 2008a; Lee *et al.*, 2009).

Both the chemical and the electrical aspect are significant in the process and do affect the resulting nanotubes (Lockman *et al.*, 2010; Poznyak *et al.*, 2012; So, Lee & Schmuki, 2012). The electrolyte used in the electrochemical process mainly determines the outcome and various electrolytes have been studied. They can be classified into organic and inorganic electrolytes. The organic electrolytes include ethylene glycol, glycerol, and acetic acid (Pozio *et al.*, 2014; Prosini, Cento & Pozio, 2013; Wang *et al.*, 2011) The inorganic electrolytes are mainly sulphate and phosphate ions-containing electrolytes (Ghicov *et al.*, 2005; Hao *et al.*, 2013; Perez-Jorge *et al.*, 2012). Among the two, inorganic or aqueous electrolytes have been shown to allow the manipulation of the morphology of the nanotubes while generating rough exterior walls as compared to non-aqueous ones. Such a property has been associated with stronger adhesion forces between the nanotubes (Kowalski, Kim & Schmuki, 2013; Macak *et al.*, 2007; Xin *et al.*, 2010). With respect to inorganic electrolytes, Table 1.1 shows the conditions used for anodisation using various electrolytes. When using sulphate containing electrolytes, no sulphur elements have been found on the nanotubes formed, while phosphorus in the phosphate state have been found to attach to the surface of nanotubes (Kim *et al.*, 2008b; Krasicka-Cydzik *et al.*, 2010). Phosphate ions have also been shown to enhance the proliferation of osteoblasts cell which would result in better osseointegration of an implant while being able to buffer the pH of the electrolytes; thus accounting for the choice of phosphate containing electrolytes over sulphate containing electrolytes (Kim *et al.*, 2008b; Lee *et al.*, 2009).

Table 1.1: The various combinations of conditions used in the presence of aqueous electrolytes for anodisation and the resulting diameter and thickness of nanotubes formed

Electrolytes	Voltage / V	Time / Hrs	Temp / °C	Diameter / nm	Thickness / μm	Ref
1M H ₂ SO ₄ + 0.15 wt% HF	20	60	20	100	0.3	Perez-Jorge <i>et al</i> , 2012
1M H ₂ SO ₄ + 0.15 wt% HF	20	0.07	20	20	0.1	Matykina <i>et al</i> , 2011
		1		100	0.18	
0.3 M H ₃ PO ₄ + 0.14 M NH ₄ F	20	2		90	0.4	Luo <i>et al</i> 2008
	30			110		
	40			180		
1M (NH ₄)H ₂ PO ₄ + 0.5 wt% HF	15	1.5	RT	80	0.26	Li <i>et al</i> , 2008
1M (NH ₄) ₂ SO ₄ + 0.5 wt% NH ₄ F	20	1.1	RT	100	0.6	Macak <i>et al</i> , 2005
1 M H ₂ SO ₄ + 0.08 M HF	20	0.5	RT	80	0.25	Mohan <i>et al</i> , 2015
0.2 M H ₃ PO ₄ + 0.4 M NH ₄ F	20	4		67	1	Sarraf <i>et al</i> , 2015

Most of the electrolyte recipes contain fluoride (Table 1.1). The effect of the fluoride ions in the formation of the nanotubes has been shown by different authors such as Perez-Jorge *et al.* (2012), Kim *et al.* (2008), and Ghicov *et al.* (2005) whereby the changes in current distribution have been compared in the presence and absence of fluoride ions (Ghicov *et al.*, 2005; Kim *et al.*, 2008b; Perez-Jorge *et al.*, 2012). When fluoride ions are present, there is an initial decay of current followed by a rise whereas in the absence of the ions, the current stays constant after the initial decay and this leads to a uniform oxide layer being formed with no porosity obtained. This effect has been demonstrated by other authors (Bauer *et al.*, 2013; Ghicov *et al.*, 2005; Lee *et al.*, 2009; Macak *et al.*, 2007). These studies also demonstrated the theoretical chemistry behind the role played by fluoride ions. The reactions of concern happen at the anode which is the titanium based material which starts with the formation of an initial barrier oxide layer forming on the surface of the anode. In the absence of fluoride ions, the non-porous oxide layer will continue to grow. However in the presence of fluoride ions, the barrier layer is etched into porous structures. The continuous etching and oxide layer formation (redox reaction) leads to the formation of the uniformly arranged nanotubes. Since there is the involvement of hydrogen ions in the redox reaction, the pH will affect the resulting nanotubes. Cai *et al.* (2005) reported the increase in height of nanotubes with increase in pH. For the growth duration of 20 hours, at 10V, the thickness of the nanotubes increased from 0.32 μm to 1.40 μm when the pH was changed from 1.3 to 5 (Cai *et al.*, 2005). Paulose *et al.* (2006) worked with sulphate ions similarly for 30 minutes and observed the same pattern with nanotubes length being

0.35 μm at pH 1.1 and 2 μm at pH 5 (Paulose *et al.*, 2006). Even when phosphate ions were used by Matykina *et al.* (2011), the same pattern was observed with a height of 0.32 μm at pH 4.2 and 1.75 μm at pH 4.6 (Matykina *et al.*, 2011). The above studies also reported no change in nanotubes diameter when pH was changed. Increase in thickness has been observed when the temperature of electrolyte solution and duration of anodisation are increased too (Balakrishnan & Narayanan, 2013; Hao *et al.*, 2013; Peremarch *et al.*, 2010).

In addition to the chemical changes, alteration in the applied voltage and duration of the anodisation process affect the resulting morphology of TiO_2 nanotubes. The duration of the process has been shown to cause an increase in the thickness of the nanotubes (Balakrishnan & Narayanan, 2013; Hao *et al.*, 2013; Peremarch *et al.*, 2010). Similar observations have been observed when the applied voltage is increased (Bauer, Kleber & Schmuki, 2006). Bauer *et al.* (2006) demonstrated a change of diameter from 15 to 120 nm and length from 20 nm to 1 μm with respect to voltage varying from 1 to 25V. The latter study also highlighted a limit in the increase in the diameter of the nanotubes to 120 nm with respect to change in voltage (Bauer, Kleber & Schmuki, 2006; Taveira *et al.*, 2005).

1.4.1 Self-assembly of TiO_2 nanotubes on titanium based material

The self-assembly of the nanotubes, being dependent on the electrolytes content, happen through various stages which are explained in this section (Chen *et al.*, 2013a; Kowalski, Kim & Schmuki, 2013):

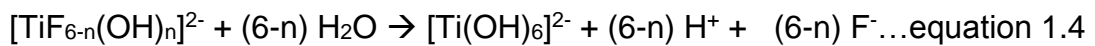
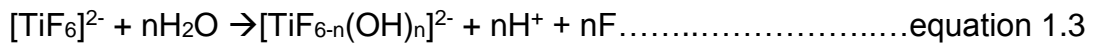
First there is the formation of the uniform oxide layer in the presence of oxide ions as per equation 1.1.



In the presence of fluoride ions, etching of the oxide layer occurs which results in the formation the soluble $[\text{TiF}_6]^{2-}$ complex as follows (equation 1.2):



The latter complex reacts with the water and hydrogen ions in the electrolytes to finally form the nanotubes as detailed in equations 1.3-1.5.



Briefly, there is a competition between the etching and oxidation process. If more fluoride ions are present the etching process will be dominating the reaction. In such electrochemical reactions, there is a point where there is a balance between etching and oxidation and this is known as the equilibrium point (Kowalski, Kim & Schmuki, 2013). Being an electrochemical reaction, this equilibrium along with the whole anodisation process is dependent on the voltage applied and resultant current density. As such the chemical reactions can be associated to the current density involved.

The initial barrier layer formation has been associated with the following equations (Kowalski, Kim & Schmuki, 2013):

$$i = \alpha \exp(\beta E) \dots \text{equation 1.6}$$

$$i = \alpha \exp (\beta U/d) \dots \dots \dots \text{equation 1.7}$$

The etching process is a temperature dependent reaction (Arrhenius type relationship) and followed Fick's Law of diffusion which was characterised by the equation 1.8 (Miller, Vandome & McBrewster, 2009; Portan *et al.*, 2012).

$$i = \alpha \exp \left(\frac{-\Delta G}{RT} \right) \dots \dots \dots \text{equation 1.8}$$

whereby α is a constant, R is the gas constant, T is the temperature and ΔG is the Gibbs energy change.

At chemical equilibrium reaction 1.9 happens as follows (Burrows *et al.*, 2013),

$$\Delta G = \Delta G^{\circ} + RT \ln Q \dots \dots \dots \text{equation 1.9}$$

Whereby G° is the maximum amount of energy change happening and Q is the reaction quotient dependent on the reactants in the reaction and can be expressed as per equation 1.10:

$$Q = \frac{[\text{TiF}_6^{2-}]}{[\text{H}^+]^4 [\text{F}^-]^6} \dots \dots \dots \text{equation 1.10}$$

Thus at equilibrium reactions 1.11 and 1.12 happen (Kowalski, Kim & Schmuki, 2013),

$$i = \frac{\alpha}{Q} \exp \left(\frac{-\Delta G^{\circ}}{RT} \right) \dots \dots \dots \text{equation 1.11}$$

$$i = \alpha \frac{[\text{H}^+]^4 [\text{F}^-]^6}{[\text{TiF}_6^{2-}]} \exp \left(\frac{-\Delta G^{\circ}}{RT} \right) \dots \dots \dots \text{equation 1.12}$$

Since the energy change to the electric field is determined by equation 1.13:

$$G^{\circ} = -nFE^{\circ} \dots \dots \dots \text{equation 1.13}$$

the current density can be related to the concentrations of different ions as per equation 1.14:

$$i = \alpha \frac{[H^+]^4 [F^-]^6}{[TiF_6^{2-}]} \exp\left(\frac{nFE^\circ}{RT}\right) \dots \dots \dots \text{equation 1.14}$$

These equations concentrates on the beginning of the anodisation process whereby both etching and oxidation are taking place.

A step by step analysis of the nanotube formation in hydrofluoric acid at 25 V has been performed where the different stages of nanotube formation was visualised using high resolution microscopy (Dikova *et al.*, 2014). The nanotubes were concluded to grow in differently on pure titanium as compared to Ti-6Al-4V alloy. On pure titanium, nano rods were initially formed followed by the nanotubes whereas on Ti-6Al-4V, nano-nuclei of oxide originated the nanotubes formation. Macak *et al.* (2007) used ammonium sulphate in the presence of fluoride ions at 20 V in order to fabricate nanotubes with an average diameter of 100 nm. The latter study investigated the growth of TiO₂ nanotubes using various models for diffusion controlled growth, for evaluating current efficiency and for length expansion of the nanotubes. The study also analysed the etching versus oxidation processes with the conclusion that the walls of the nanotubes are thicker at the bottom and thinner at the top. Nonetheless no study has actually analysed the step by step growth of the nanotubes from barrier layer formation till nanotubes formation with the help of high resolution microscopy.

Nanotubes forming on titanium metals are more uniform as compared to the nanotubes formed on titanium alloy such as Ti-6Al-4V. TiO₂ nanotubes formed on the surface of Ti-6Al-4V alloy are divided into two phases one being the alpha (α) alloy and the second one being the beta (β) alloy and the nanotubes form successfully on the α -alloy whereas, on the β -alloy the nanotubes do not form properly and hence resulting in dips on the surface (Bortolan *et al.*, 2016; Krasicka-Cydzik *et al.*, 2010). The reason the latter observations was assigned to the fact that the β -phase has a β -stabilizer, vanadium element which dissolves more than the titanium and aluminium oxide (Bortolan *et al.*, 2016).

The as-formed nanotubes are known to be in the amorphous phase (Sun *et al.*, 2015). Due to the high thermal stability of the nanotubes, heating the latter to about 300 -500 °C allows the nanotubes to crystallise and change to anatase phase (Chaves *et al.*, 2016). Between 550 and 700 °C, the crystalline structure stays in a dual phase known as anatase and rutile. And further increase in temperature causes the uniform nanotubes layer to get re-ordered and enter a complete rutile phase (Khudhair *et al.*, 2016). Since the aim of using nanotubes on the surface of titanium alloy is to provide a uniform nano-porous coating, the rutile phase is not considered for synthesis on implants. The anatase phase is considered to allow better attachment and proliferation of osteoblast cells on the latter hence making it a good scaffold for bone tissue engineering (Brammer *et al.*, 2009).

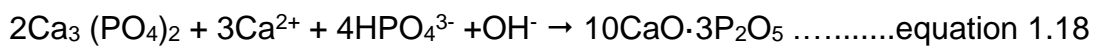
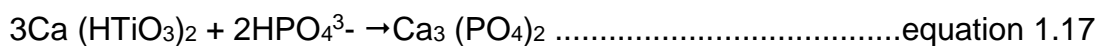
1.4.2 Scaffold for bone tissue engineering

Tissue engineering is the use of material engineering to induce tissue growth (Balint, Cassidy & Cartmell, 2014; Hasan *et al.*, 2014). As such bone tissue engineering involves better osseointegration and effective bone tissue growth. Scaffolds in bone tissue engineering are biocompatible templates which act as a platform for better osteoblast cells adhesion and bone tissue formation (Bose, Roy & Bandyopadhyay, 2012). In orthopaedics, the implants' surface or coatings act as scaffolds for bone tissue engineering. Formulating the right scaffold on the implant surface is significant in obtaining a longer lasting implant. A scaffold is expected to have the necessary chemical and physical properties with respect to the environment where bone is supposed to grow (Tonelli *et al.*, 2012). In the field of orthopaedics, the desirable scaffold would consist of similar chemical and physical properties as bone.

TiO₂ nanotubes grown on titanium based materials have uniformly distributed nanostructure, similar to the bone surface and hence can be a good scaffold for osteoblast tissue engineering. TiO₂ nanotubes have been shown to enhance osteoblast cells growth on the surface due to the nanostructure of the surface (Peng *et al.*, 2013; Wang & Poh, 2013). The anatase form of the nanotubes is preferred as a scaffold for bone tissue engineering.

The more bioactive the scaffold is, the better is the osteoblast cell adhesion and proliferation. The bioactivity provides the necessary proteins and or chemical component on the surface of the scaffold that cells are positively attracted to the latter and gets attached. The surface also allows the cells to

further grow and survive on the surface which enhances osseointegration. HA is regarded as a biocompatible material. Several methods have been employed in order to grow HA on the surface of TiO₂ nanotubes such as sol-gel technique, plasma-spraying, biomimetic deposition, electrodeposition, and laser ablation (Gopi *et al.*, 2011; Huang *et al.*, 2013). Liu *et al.*, (2017) put emphasis on the alkali treatment of TiO₂ before HA could grow on the latter surface (Liu *et al.*, 2017). Several other studies have also treated the nanotubes with sodium hydroxide before allowing HA to be successfully grown on the nanotubes; which in turn increased osteoblast cells attachment and proliferation (Benea *et al.*, 2014; Brammer *et al.*, 2009). Kokubo (1997) shed light on the biomimetic method of growing HA on the surface of the nanotubes by allowing the HA to form at 36.5 °C for 10 days in the presence of a simulated body fluid at pH 7.4 and ion concentrations (Na⁺ 142.0, K⁺ 5.0, Mg²⁺ 1.5, Ca²⁺ 2.5, HCO₃⁻ 4.2, Cl⁻ 147.8, HPO₄³⁻ 1.0, SO₄²⁻ 0.5 mM) which are nearly equal to those of human blood plasma (Kokubo, 1997). In the latter study, the author emphasised on the alkali treatment which works according to the following equations:



The sodium hydroxide reacts with the nanotubes forming sodium titanate (NaHTiO₃) as per equation 1.1 (Kokubo, 1997). NaHTiO₃ then reacts with

calcium ions in the SBF which in turn reacts with phosphorus ions forming calcium phosphate (equation 1.2 and 1.3). If the calcium phosphate is left in the presence of the simulated body fluid with continuous replenishment while maintaining the required pH and temperature hydroxyapatite forms as per equation 4, with the Ca/P ratio being 1.67 (Arafat *et al.*, 2011; Wu *et al.*, 2014). TiO₂ nanotubes thus act better as scaffold for bone tissue to grow when they are made bioactive with the help of post fabrication heat and alkali treatment.

1.4.3 Toxicological aspect

Free TiO₂ nanoparticles have shown some toxicity to cultured cells, but the effects are also dependent on the size and crystal structure of the particles (Iavicoli, Leso & Bergamaschi, 2012; Oberdorster, Ferin & Lehnert, 1994) Mohamed *et al* (2016) investigated the toxicity of the nanotubes with respect to cytotoxicity, genotoxicity, cytoskeletal organisation and mitochondrial health (Mohamed *et al.*, 2017). The latter study observed no deleterious effect on the mitochondria and a non-significant decrease in the cytoskeletal integrity. However the study showed some DNA damage and that the cells were under some oxidative stress. Most studies have shown that TiO₂ nanotubes grown on titanium based biomaterial are biocompatible and enhance the growth of cells on the surface as compared to titanium material without the nanotubes (Brammer *et al.*, 2011; Feng *et al.*, 2003; Indira, Mudali & Rajendran, 2014). Since the biocompatibility aspect generally outweighs the concerns of toxicity, the nanotubes are proposed for use on implants.

1.4.4 Antibacterial properties

TiO₂ nanotubes have been investigated as a bactericidal agent. The nanotubes have been demonstrated to exhibit photochemical disinfection against *E. cloacae SM1*, *E. carotovora*, *S. iniae*, *E. tarda* and *E. coli* in fish farm sterilisation and pesticides successfully (Bekbölet & Araz, 1996; Cheng *et al.*, 2008; Yao *et al.*, 2007). The bactericidal properties have been attributed to the photocatalytic properties of TiO₂ nanotubes. And hence, when grown on implants to be inserted in the human body where there is no UV light, their bactericidal properties diminish or even disappear (Yang *et al.*, 2016). Using the nanotubes matrix as a carrier for antibacterial agents is one solution which can enhance the antibacterial properties of the nanotubes in the human body (Roguska *et al.*, 2016). This is where TiO₂ nanotubes act as a localised drug delivery system.

1.4.5 Drug delivery system

The administration of drugs such as anti-inflammatory and anti-bacterial drugs are not always effective. Some of the reasons for such observation have been assigned to poor distribution, organ toxicity, clinical side effects in the patients and a lack of selectivity (Jia & Kerr, 2013; Losic *et al.*, 2015). Increasing the concentration of drug administered may increase efficacy, but this will also worsen the negative aspects of the drugs. A localised drug delivery system is one solution to this dilemma, whereby the required drug can be delivered in the required amount directly to the site in need hence reducing the risk of toxicity and side effects (Jia & Kerr, 2013). In the case of orthopaedic implants, the antibacterial and/or inflammatory drugs can be

delivered directly by making the surface of the implant behave as the carrier (Losic *et al.*, 2015). In this context, various drugs can be delivered through different methods on the surface of implants and they are summarised in Table 1.2.

Table 1.2: Classification of bacterial agents that can be used on the surface of implants

Type of antibacterial agent	Antibacterial agent	Examples of antibacterial agent	References
Inorganic	Metallic materials	Silver	(Wei <i>et al.</i> , 2015)
		Zinc	(Liu <i>et al.</i> , 2014)
		Copper	(Zhu <i>et al.</i> , 2007)
Organic	Antibiotics	Vancomycin	(Zhang <i>et al.</i> , 2013)
		Gentamicin	(Zhang <i>et al.</i> , 2013)
	Polymers	Chitosan	(Song <i>et al.</i> , 2016)
		Peptides	Cytokines
Mixture	Composites	DNA	
		Chitosan/HA	(Vaca-Cornejo <i>et al.</i> , 2017)
		Silver/TiO ₂	(Wei <i>et al.</i> , 2015)
		ZnO/TiO ₂	(Liu <i>et al.</i> , 2014)
		Silver/Chitosan	(Mishra, Ferreira & Kannan, 2015)

Most of the drugs can be delivered with help of TiO₂ nanotubes on titanium based implants. This in turn enhances the properties of the nanotubes with the addition of a drug delivery system (Gulati, Aw & Losic, 2011; Jia & Kerr, 2013). Among the different antibacterial agents (Table 1.2), the organic antibacterial agents can be easily degraded by changes in the surrounding

environment or by mechanical forces; and some of them are specific to a limited number of species of microorganisms and cannot combat multiple infections (Gallo, Holinka & Moucha, 2014; Gulati, Aw & Losic, 2011; Huang *et al.*, 2015b). Hence the choice for inorganic metallic antibacterial agents are preferred as the drugs to be loaded in TiO₂.

Before loading the nanotubes with the chosen drug, several factors have to be taken into consideration. The drug has to be mechanically and chemically stable, biocompatible and most importantly the nanotubes have to be able to load them first and release them in a systematic way (Gultepe *et al.*, 2010).

Nanoparticles can be very toxic depending on the size, surface chemistry, chemical component and dosage in which it is exposed to human cells. As such when loading the nanotubes with nanoparticles the distribution and attachment of the particles to the walls of the nanotubes have to be taken into consideration. There are two approaches through which the nanoparticles attach to the walls of the nanotubes namely physisorption and chemisorption out of which, physisorption is mainly caused by van der Waals force which is weak (Kwon *et al.*, 2013). Chemisorption involves ionic and covalent bonding which are stronger than physisorption. Depending on the release rate expected and the toxicity of the nanoparticle, the attachment method is chosen.

1.5 Nano-silver

Silver nanoparticles have been known for over 120 years (Chernousova & Epple, 2013). They are considered to be the best inorganic antibacterial

agent with the ability to combat many infecting agents (dos Santos *et al.*, 2014; Prabhu. & Poulouse, 2012). They have been studied as part of TiO₂ nanotubes matrix with the aim of forming antibacterial nanocomposite coatings on titanium based materials. There are several methods of synthesis of silver nanoparticles during which the particles formed are in different shapes such as spherical, bipyramids, discs, rods, cubes, prisms, rings, platelets, triangular prisms, and octahedral depending on the conditions used to grow them (Chernousova & Epple, 2013). The commonly used shape for antibacterial nano-silver is the spherical shape. The most common method of synthesis in solution is the chemical reduction method whereby there is a precursor of silver, a reducing agent and a stabilising agent (Wei *et al.*, 2015). However, when growing the silver nanoparticles on the walls of TiO₂ nanotubes photochemical reduction is mostly used along with several more methods which are summarised along with the microorganism targeted (Table 1.3).

Table 1.3: Method of silver nanoparticles synthesis on TiO₂ nanotubes and the bacteria against which their antibacterial properties were tested.

Method of synthesis	Bacteria	Reference
Silver mirror reaction	<i>Escherichia coli</i> <i>Bacteria</i>	(Li <i>et al.</i> , 2013)
Magnetron sputtering	<i>Staphylococcus aureus</i>	(Bai <i>et al.</i> , 2015)
Electrochemical	<i>Aggregatibater</i> <i>actinomycetemcomitans</i> <i>Tannerella forsythia</i> <i>Campylobacter rectus</i>	(Yeniyol <i>et al.</i> , 2014)

Electron beam evaporation	<i>Staphylococcus aureus</i>	(Uhm <i>et al.</i> , 2013)
Photochemical reduction	<i>Staphylococcus aureus</i>	(Zhao <i>et al.</i> , 2011)
Spin coating	<i>Escherichia coli</i>	(Chen <i>et al.</i> , 2013b)

Table 1.3 shows that silver nanoparticles synthesised using either method have exhibited antibacterial activity against various bacteria. From the various researches as mentioned in the table above, it was found that the antibacterial activity is dependent on the size and distribution of the nanoparticle, size and depth of the nanotubes and the attachment of the particles to the nanotubes (Cheng *et al.*, 2013). Their antibacterial properties are correlated with radical oxygen species (ROS) formation, silver ions release and internalisation of the silver nanoparticles (Manke, Wang & Rojanasakul, 2013). One more interesting aspect of silver nanoparticles is that it has the ability to inhibit biofilm formation as well (Besinis, De Peralta & Handy, 2014; Cheng *et al.*, 2013). Long term antibacterial activities from silver nanoparticles loaded in TiO₂ nanotubes have been demonstrated by many studies in the past, in-vitro (Yeniyol *et al.*, 2014; Zhao *et al.*, 2011) . However, toxicity to human cells remains an issue due to initial fast release of silver from the coating (Gao *et al.*, 2014).

In this context, all researches involving the fabrication of silver nanoparticle loaded titania nanotubes to be used on implants have to involve a toxicity test in the presence of the cells around which the silver is expected to

provide the antibacterial properties. Making the silver nanoparticles adhered to the nanotubes more stable and controlling the release of silver from the composite coating is one solution which has attracted the attention of researchers (Zhao *et al.*, 2011). Another solution is the use of another broad range inorganic antibacterial agent. From table 1.2, copper related nanomaterial was found to be another antibacterial agent with good antibacterial property and low toxicity to human cells (Hostynek & Maibach, 2004). Nonetheless they are not widely used because of the fast oxidation of the nanoparticles in air and the chemical and physical instability of the copper oxides formed at temperature below 200°C (Akhavan & Ghaderi, 2010). The other choice is ZnO nanoparticles which are considered to have good antibacterial properties and less toxicity than both silver and copper nanoparticles (Bondarenko *et al.*, 2013).

1.5.1 Chemical reduction of silver ions to silver nanoparticles

Silver nanoparticles can be synthesised using different methods. One example is the electrochemical method, whereby the source of silver is a piece of silver metal which is used as an electrode in an electrolysis procedure in the presence of a solvent (Khaydarov *et al.*, 2009). Another method of synthesis is thermal decomposition which involves the decomposition of a silver complex at a specific temperature (Navaladian *et al.*, 2006). Silver nanoparticles have been fabricated using laser ablation method also which involves the application of the a laser beam to a solvent containing silver (Valverde-Alva *et al.*, 2015). There are a few more methods using which silver nanoparticles can be successfully synthesised. However,

chemical reduction is one of the most common and simplest method of fabricating Ag-NPs (Lee & Meisel, 1982) and similar reduction of silver salts have been used to form Ag-NPs on the surface of TiO₂ nanotubes (Abou El-Nour *et al.*, 2010; Pinto *et al.*, 2010). Several types of reducing agents have been used such as ascorbic acid (Chekin & Ghasemi, 2014), sodium citrate (Gorup *et al.*, 2011), sodium borohydride (Dong *et al.*, 2010), hydrazine (Tatarchuk *et al.*, 2013) and hydroquinone (Pérez *et al.*, 2008). Glucose has also been shown to affect the reduction of silver nitrate into silver nanoparticles (Hussain *et al.*, 2011). In the latter study, detailed investigations on the redox reaction between Ag⁺, [Ag(NH₃)₂]⁺ and glucose were carried out. The silver nanoparticles were formed in the presence of glucose as per Figure 1.2. The researchers used silver ammonia to prevent colloidal formation of the nanoparticles.

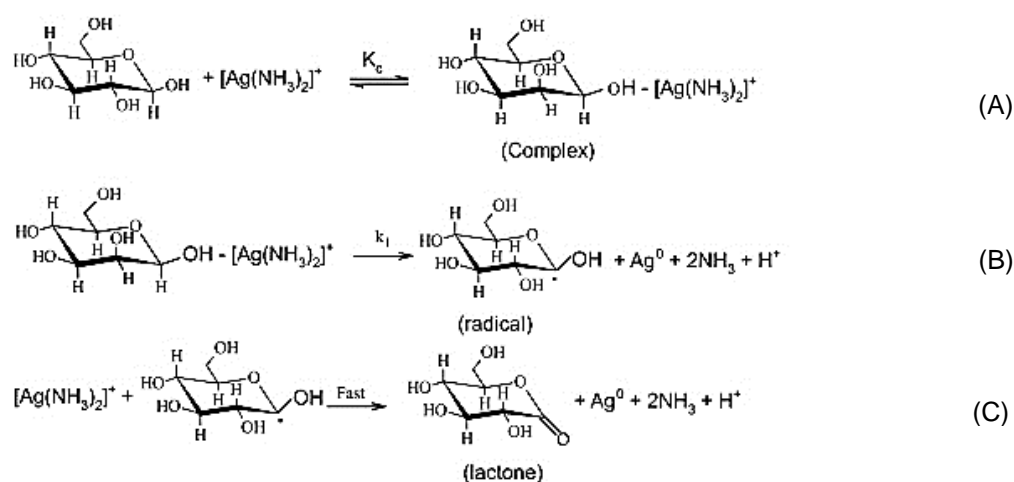


Figure 1.2: The reduction process of silver ammonia complex to silver nanoparticles in the presence of glucose starting with (A) the complex binding with the glucose molecule, (B) the formation of silver nanoparticles, ammonia and a radical ending with (C) a lactone molecule, ammonia and the nanoparticles. Note. From 'Time dependence of nucleation and growth of silver nanoparticles'(Hussain *et al.*, 2011).

To start with, the silver ammonia complex, formed by adding ammonia solution to silver nitrate, reacts with the glucose molecule and attaches to the –OH part. Subsequently, the resulting complex will break down to form silver nanoparticle and ammonia.

Once the silver ammonia is prepared, the reaction is simple and can be carried out at room temperature provided there is enough ventilation. The other reducing agents are either too toxic on their own or they release toxic chemicals that could affect the morphology of the TiO₂ nanotubes or make it unsafe to be used in the human body. As such, there is a need for reducing agents similar to glucose which is not toxic and does not produce toxic chemicals that can damage the nanotubes. Delta-gluconolactone is one such example which is widely available.

1.6 Nano-zinc oxide

Zinc oxide nanoparticles have antibacterial properties against both gram-positive and gram negative bacteria and because of low oral zinc toxicity to humans it has been successfully been used in food products or food related materials (Xie *et al.*, 2011). This antibacterial effect has been associated with zinc ions release, internalisation of ZnO nanoparticles in the bacteria, electrostatic interactions and ROS formation (Sirelkhatim *et al.*, 2015) . The mentioned processes disturbs the physiological biochemical pathways in the cells resulting in malfunction or death of cells. The shape and size of the nanoparticles are considered to have an effect on the degrees of antibacterial properties with smaller nanoparticles being more biocidal than bigger nanoparticles (Stankovic, Dimitrijevic & Uskokovic, 2013)

(Raghupathi, Koodali & Manna, 2011). The method of synthesis determines the morphology of the resulting zinc nanoparticle (Talebian, Amininezhad & Doudi, 2013).

There are several methods of growing ZnO nanoparticle on the surface of TiO₂ nanotubes which include hydrothermal method, electrodeposition, pyrolysis deposition, atomic layer deposition, self-assembled monolayer and many more (Bingqiang Cao and Weiping Cai and Yue Li and Fengqiang Sun and Lide, 2005; Liu *et al.*, 2014; Roguska *et al.*, 2014; X L Liu, 2012; Xiao, 2012). These methods give rise to nano-zinc oxide in different shapes and dimensions, such as flower-like, hexagonal rod-like and spherical-like (Talebian, Amininezhad & Doudi, 2013). All of the various shapes have been shown to have antibacterial properties, with the smallest sizes generally exhibiting the highest antibacterial properties. The surface defects of the zinc oxide are also proposed as a method of antibacterial activity due to mechanical effect and zinc ion dissolution at the defect (Rekha *et al.*, 2010). Hence manipulation of the shape, size and surface defects can be used to optimise the potential antibacterial activity.

Large amount of zinc oxide nanoparticles in the human body have been shown to be toxic to several cells including fibroblast cells, which is involved in wound healing and many more cells. Making the situation worse, systemic exposure led to neurological effects in the past (Vandebriel & De Jong, 2012). Hence there is a need to reduce zinc ion dissolution in the human body whenever zinc is being applied on surface coatings. As mentioned before localised drug delivery require small amount of the antibacterial agent in order to be effective. Even though, the zinc oxide nano composite coatings

would not release massive concentration of zinc or zinc oxide, toxicity test would be considered to ensure the prevention of overdose to the human body.

1.7 Nano-hydroxyapatite

Hydroxyapatite is a bioceramic material which has similar structure to bone but it does not have the mechanical strength required to work in load bearing application (Arifin *et al.*, 2014; Lugovskoy & Lugovskoy, 2014). Nonetheless when used in conjunction with titanium alloy, HA add to the properties of the alloy, hence increasing the osseointegration of the alloy in the body (Fernandes *et al.*, 2013; Lugovskoy & Lugovskoy, 2014). Hence using TiO₂ nanotubes as a scaffold for the growth of nano HA is a good combination for enhancing osseointegration. Several techniques have been used to grow or add nano-HA on the surface of metals and alloys such as sol-gel technique, plasma-spraying, biomimetic deposition, electrodeposition, laser ablation and so on (Gopi *et al.*, 2011; Huang *et al.*, 2013). Due to the similar chemical properties as bone, nano-HA can be added to the nano-ZnO and nano-Ag loaded TiO₂ nanotubes with the aim of reducing the toxicity of the antibacterial agent to the bone cells.

All nanomaterials have been known to have some levels of toxicity due to the small size which can enter cells and hence, even though HA is known to enhance biocompatibility, the toxicity aspect has to be analysed as well. Nano-HA has been shown to cause inflammation and induce oxidative stress of exposed human epithelial cells (Tay *et al.*, 2014). However for long term

use, nano-HA of size less than 50 nm has been shown to be non-toxic in rodents (Remya *et al.*, 2017).

In a recent study, toxicity of nano-HA has been shown against micro-organisms whereby antibacterial activity against *Escherichia coli*, *Pseudomonas aeruginosa*, *Klebsiella pneumonia* and *Salmonella typhi* has been observed in the presence of nano-HA (Baskar, Anusuya & Devanand Venkatasubbu, 2017) . Hence addition of nano-HA to nano-Ag or nano-ZnO coated TiO₂ nanotubes might also enhance the antibacterial activity of the composite coating.

1.8 Hypotheses

Various hypotheses were tested in this study which are as follows:

- ✓ The pH of the aqueous electrolytes and initial sweep rate of voltage applied for anodisation in the self-assembly of TiO₂ nanotubes affects the morphology of the resulting nanotubes (Chapter 2).
- ✓ Post-anodisation treatment of TiO₂ nanotubes and duration of exposure of Ti alloy to and concentration of silver source have an effect on the morphology and distribution of nano-Ag on the surface of the nanotubes (Chapter 3, 4, 5).
- ✓ Concentration of zinc nitrate used for nano-ZnO synthesis and annealing of nano-ZnO has an effect on the morphology and distribution of the resulting nano-ZnO coating and nano-HA formed on the coating (Chapter 6).
- ✓ Nano-ZnO coated TiO₂ nanotubes can exhibit the same level of antibacterial properties against *S. aureus* as nano-Ag coated TiO₂ nanotubes while being able to maintain biocompatibility (Chapters 5, 6, 7).
- ✓ Nano-HA coated on the surface of the nano-Ag and nano-ZnO coating can help reduce toxicity of the nanocomposite coating (Chapters 5, 6, 7).

1.9 Aim and Objectives

The overall aim of this study was to synthesis nano-silver or nano-zinc oxide particle in a matrix of TiO₂ nanotubes self-assembled on the surface of Ti-6Al-4V. Furthermore the resulting coating would be characterised in the presence of *S. aureus* for antibacterial properties and in the presence of primary human osteoblast cells for toxicological studies. Silver nanoparticles are known to be antibacterial but high levels of silver nanoparticles can be toxic to mammalian cells, hence the need for a method to synthesis uniformly distributes silver nanoparticles with a low toxicity to osteoblasts. Zinc is an essential metal that is homeostatically controlled by mammalian cells, and so is likely to be more biocompatible than silver as a non-essential metal. Zinc is not as strong a biocide as silver, so this offers a good trade of some biocidal activity but with good biocompatibility/safety for human tissue.

The specific objectives of the study were:

- ✓ To optimise the self-assembly of TiO₂ nanotubes on the surface of Ti-6Al-4V to achieve a uniformly distributed nanotubes coating on the surface of the alloy.
- ✓ To optimise the synthesis of uniformly distributed silver nanoparticles on the surface of the TiO₂ nanotubes matrix with the aim of having a good surface coverage and stability of the coating.
- ✓ To characterise nano zinc oxide coating in both the presence and absence of nano HA.
- ✓ To assess the antibacterial properties of the nano-Ag and nano-ZnO coated TiO₂ nanotubes on Ti-6Al-4V discs with respect to negative

and positive controls with and without nano-HA. This will be performed in the presence of *S. aureus*, the first line of infection during surgeries.

- ✓ To look into the biocompatibility of the latter coatings with respect to the controls. This will be performed by exposing the coatings and the controls to primary human osteoblast cells in DMEM media for specific number of days after which biochemical assays, PCR and microscopic imaging will be used to do the assessment.
- ✓ To analyse and compare all the properties of the various coatings (surface coverage, stability, antibacterial, biocompatibility, molecular biocompatibility).

Chapter 2

Optimisation of the anodisation process for the self-assembly of TiO₂ nanotubes on the surface of Ti-6Al-4V discs

2.1 Introduction

Among the various parameters affecting the anodisation process for the self-assembly of TiO₂, the initial change in voltage is known to affect the formation of the initial barrier oxide layer (Peremarch *et al.*, 2010; Taveira *et al.*, 2005). The barrier oxide layer is the building base for the final nanotubes formed. Nonetheless, there is less information about the effect on the initial sweep rate of voltage in the literature. The barrier layer is the initial uniform oxide layer formed during anodisation onto which etching occurs for the nanotube formation as per equation 1.2 in Section 1.4.1. The quality of the barrier layer determines the adhesive strength of the nanotubes and their bonding on to the substrate on which they are grown (Li, Yu & Yang, 2009; Paulose. *et al.*, 2007; Wang & Lin, 2008).

Using the theories behind the chemical and electrical reactions happening during the anodisation process, this chapter analyses the detailed growth of the nanotubes on the surface of Ti-6Al-4V alloy. It provides an insight in the initial stage of anodisation which is the major step determining the end result. This chapter also studies the effect of pH of electrolyte and the initial voltage sweep rate on the resulting current density and the resulting morphology of the nanotubes. Altogether, conclusions were made with respect to the effect of pH and initial voltage sweep rate on the initial etching sites of the nanotubes on the barrier layer.

2.2 Materials and methods

The experiment involved growing TiO₂ nanotubes on the surface of Ti-6Al-4V discs while monitoring the variation of current density over the anodisation time when pH and sweep rate was changed. All the chemicals used in this chapter were of analytical grade and were purchased from Sigma Aldrich, Irvine, UK. The resulting morphology and adhesive strength was analysed with respect to the change in pH and the optimum one was selected for further experiments. The same tests were performed with respect to the change in sweep rate and the optimum pH and the optimum initial sweep rate for anodisation was selected (see below).

2.2.1 Ti-6Al-4V disc pre-anodisation preparation

A sheet of medical grade Ti-6Al-4V alloy of 1 mm thickness (William Gregor Ltd, London, UK) were initially laser cut into 15 mm discs by Laser Industries Ltd (Saltash, UK). The alloy was then polished with #400, #800 and #1200 grit silicon carbide (SiC) paper (Elektron Technology Ltd, Torquay, UK) using a polisher-grinder (Buehler UK Ltd, Coventry, UK) with the aim of removing the naturally formed oxide layer on the surface of the discs. Subsequently the discs were polished with 6 micron and 1 micron diamond paste (Agar Scientific, Stansted, UK) to further reduce the roughness of the surface after which they were ultrasonicated (12 MHz) in a mixture of NaOH (1 M), NaHCO₃ (1M) and Na C₆H₇O₇ (1.5 M) in a ratio of 1 : 1 : 1.5 respectively, for 10 minutes. The latter cleaning process was expected to remove any contaminant from the polishing process and any

residual oxide parts. The roughness of the surface was measured using an OLS 3000 LEXT laser microscope before and after polishing.

2.2.2 Anodisation of Ti-6Al-4V discs

A dual output programmable power supply (Metrix electronics limited, Tadley, UK) was used for the anodisation process. A Labview program was designed as per Appendix A so that the initial sweep rate, voltage applied and the duration the voltage could be controlled via a laptop connected to the power supply. Ammonium fluoride was then prepared by dissolving 0.5 g of solid ammonium fluoride in 100 mL of ultrapure water.

The ammonium hydrogen phosphate, $\text{NH}_4\text{H}_2\text{PO}_4$ was prepared in deionised water at room temperature; for 1 L of solution, 115.03g of $\text{NH}_4\text{H}_2\text{PO}_4$ was added to 1 L of deionised water. Then, 100 mL of 0.5 wt % NH_4F (0.5 g of NH_4F per 100 mL of ultrapure water) was added to 100 mL of 1 M $\text{NH}_4\text{H}_2\text{PO}_4$ and the resulting mixture was made more acidic by adding drops of 3 M H_3PO_4 and more alkaline using 3 M NaOH and the pH was read using LabX pH meter (Mettler Toledo Ltd., Leicester, UK). A square-shaped copper sheet of 15 mm dimensions was used as a cathode and the 15 mm diameter Ti-6Al-4V discs were used as the anode. A schematic diagram of the electrochemical cell is shown in Figure 2.1. The laptop used stored the collected current values at 0.2 second intervals.

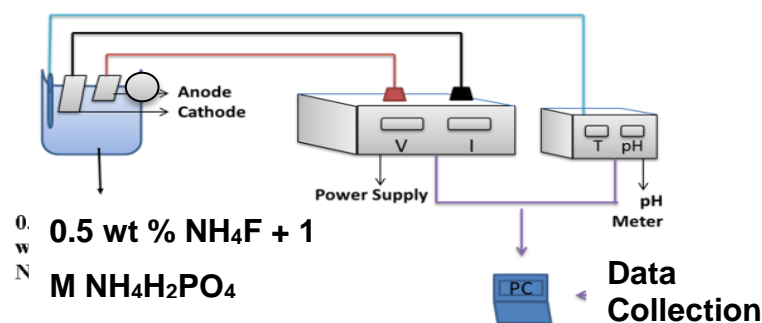


Figure 2.1: Electrochemical cell setup for anodisation

Anodisation was then performed for 3600 s with no initial ramp at 20 V with the pH of electrolytes being 3, 4 and 5 in 6 replicates ($n = 3$ for imaging, $n = 3$ for interfacial adhesion test). After optimising the pH with respect to the morphology, porosity and adhesive strength (details given below), anodisation was performed again using 0.2, 0.5, 0.8, 1.0 and 1.5 V/s as the initial sweep rate in 6 replicates (as above). The resulting anodising current was collected with respect to time and voltage every 0.2 seconds for the whole 3600 s under the different anodisation conditions. The current value was divided by the area of anodised surface to obtain current density values with mA/cm^2 as unit. The data from the 3 repeats were combined and presented using Matlab. The anodised samples were ultrasonicated in deionised water at 12 MHz for 10 min to remove the excess attached ions and then dried using an air dryer.

2.2.3 SEM imaging and measurements the of TiO_2 nanotubes

Three repeats of the anodised samples at different pH and voltage sweep rates were viewed under high resolution scanning electron microscope (SEM, JEOL7001F SEM, Plymouth Electron Microscopy Centre, Plymouth)

for surface imaging and the associated energy-dispersive X-ray spectroscopy (EDS) was used to analyse the elemental composition of the nanotubes with the help of AZtec analysis software supplied with the EDS attachment (Oxford Instruments, Oxford, UK). Once in the microscope vacuum chamber, each sample was viewed at 3 different areas and photographs and measurements averaged on each sample, before calculating mean values per treatment. In each area viewed, the diameter of 6 individual nanotubes were read.

The porosity of the coating was calculated using Matlab image analysis. The SEM images at magnification $\times 50\,000$ were used for porosity calculations. The program code created would first crop the image from the SEM, in .tiff format, to remove the labels. Then the contrast of the image was enhanced to adjust the pixel intensity. Subsequently a median and average filter was applied with the aim of smoothing the image. Otsu's Method of thresholding was performed to distinguish in between intensities (Liu & Yu, 2009). Last the image was converted to black and white after which the porosity was calculated by dividing the number of black pixels by the total number of pixels. It was assumed that the spacing between the tubes were similar in all images.

2.2.4 Interfacial adhesion test

The adhesion of the TiO₂ nanotubes to the titanium alloy was compared with respect to pH and sweep rate. The test was conducted using a universal testing 3345 machine (Instron, Buckinghamshire, UK). To start with, the end of a rod of 40 mm length and 3 mm diameter was roughened using a #150

silicon carbide sheet (SiC). It was then glued to the anodised Ti discs from the appropriate treatment ($n = 3$ each) and 3 non-anodised titanium alloy discs were used as a control each time the test was done. The glue was a two component SD 8824 epoxy resin (Matrix composites materials company, Bristol, UK), freshly prepared according to the supplier's protocol. Briefly, component A was mixed with component B a 100 to 22 ratio by weight. The rods were glued at a 90° angle with respect to the discs, with the help of a triangle ruler and the glue were allowed to harden. In order to maintain the same quantity of glue for every repeats, same type of plastic toothpicks were used with one layer of coating in the same direction at all times.

Subsequently, the rod was pulled off vertically at a rate of 1 N/s with the discs strongly held at the bottom of the instrument. The resulting load required to pull off the coating from the discs was recorded. The area that was successfully pulled off was measured using a microscope with an integrated digital camera (Olympus BX 61 M with Olympus Stream Software, Engineering Lab, Plymouth University, Plymouth, UK). The resulting pulled off load per unit area minus the controlled value was then calculated.

The pull-off test, not being completely optimised, at this stage was considered to be part of a pilot study for another student's PhD project as this study would provide the adhesive strength between the TiO_2 coatings on their own and as part of nanocomposite coatings.

2.2.5 Growth of TiO₂ nanotubes at different time interval

Using the optimum pH and initial sweep rate, anodisation was performed on the Ti-6Al-4V discs for several durations, with the aim of visualising the development of the nanotubes through time. At 5, 10, 15, 20, 25, 30 and 60 minutes the anodisation was stopped and the samples were cleaned and dried (n=3 each). They were then visualised under the high resolution microscope and the change in the nanostructure of the surface was observed and deductions on the growth of the nanotubes.

2.2.6 Statistical analysis

In this chapter, current density data was plotted using Matlab. The remaining data was plotted using SigmaPlot 13.0 and data were analysed using Statgraphics Centurion XVII (StatPoint Technologies, Inc.). The normally distributed data with equal variances (Levene's Test) were analysed using One-way ANOVA with the Fisher's LSD test post-hoc to identify the location of any differences. In case of unequal variances, the data were transformed before analysis by ANOVA. Where data were non-parametric and could not be transformed, the Kruskal-Wallis test was used. Data are presented as mean \pm S.E.M unless otherwise stated. The default 95.0 % confidence level was used for all statistics. Alphabets were the used to denote the various statistical difference between the samples being analysed.

2.3 Results

2.3.1 Effect of pH on anodisation current, nanotubes morphology and adhesive strength of nanotubes to Ti-6Al-4V alloy

The change in anodisation current due at different pH with respect to time and voltage are presented in Figure 2.2 and Figure 2.3 respectively. At all the different pH from 1 to 10 s the anodisation current increased gradually. Briefly, after 10 s the current density spiked to a maximum value per unit area of sample being anodised for the specific pH. From about 15 to about 25 s (12 V), the current decreased after which it remained almost constant till the 3600 s of anodisation where the voltage was maintained at 20 V. There is a transient rise of current density over time with the biggest increase at pH 4. Current density was also voltage-dependent with the greatest density at around 9 V, regardless of pH.

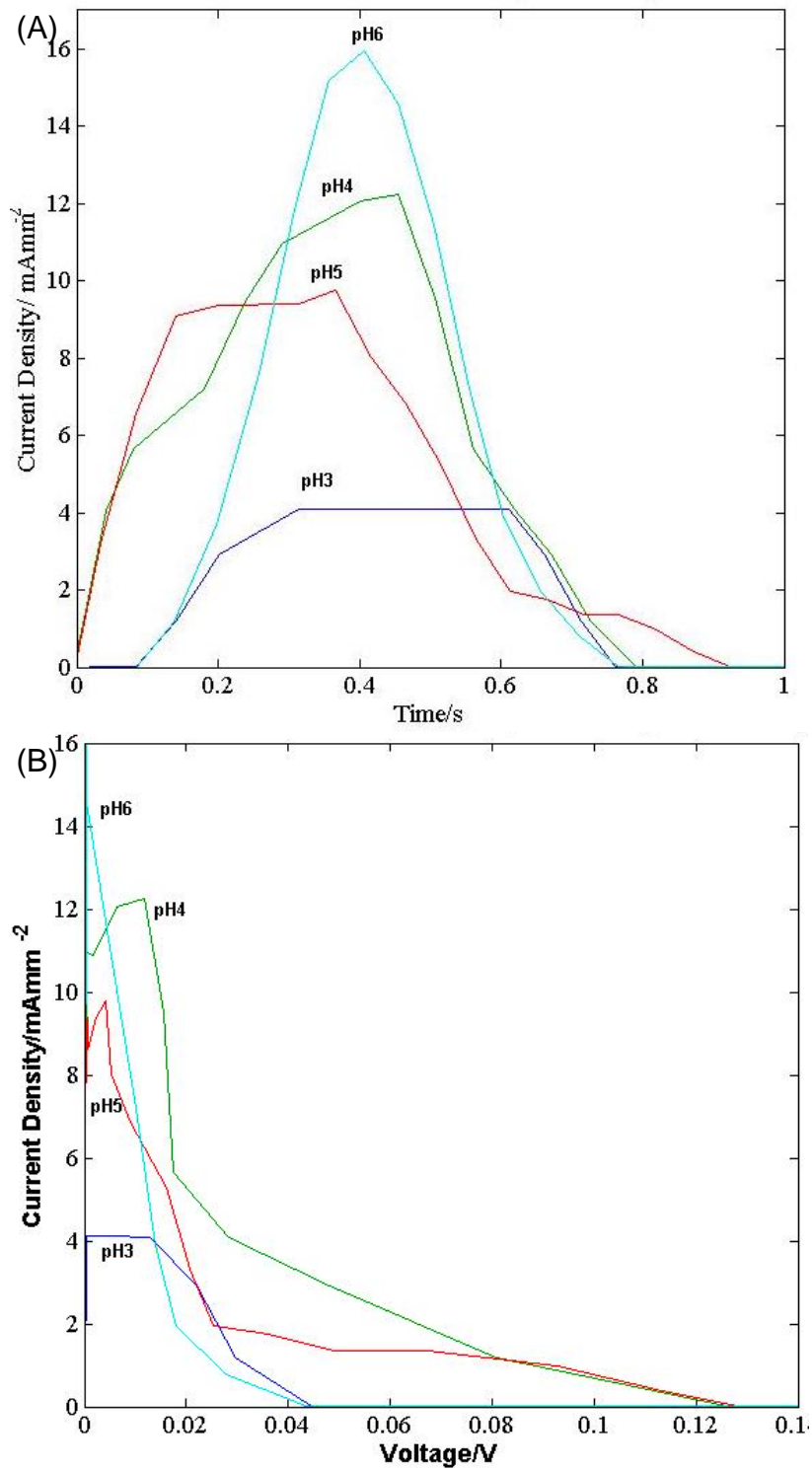


Figure 2. 2 : The effect of the change in pH on the (A) anodising current density with time in the first 1 second and (B) voltage in the first 1 second.

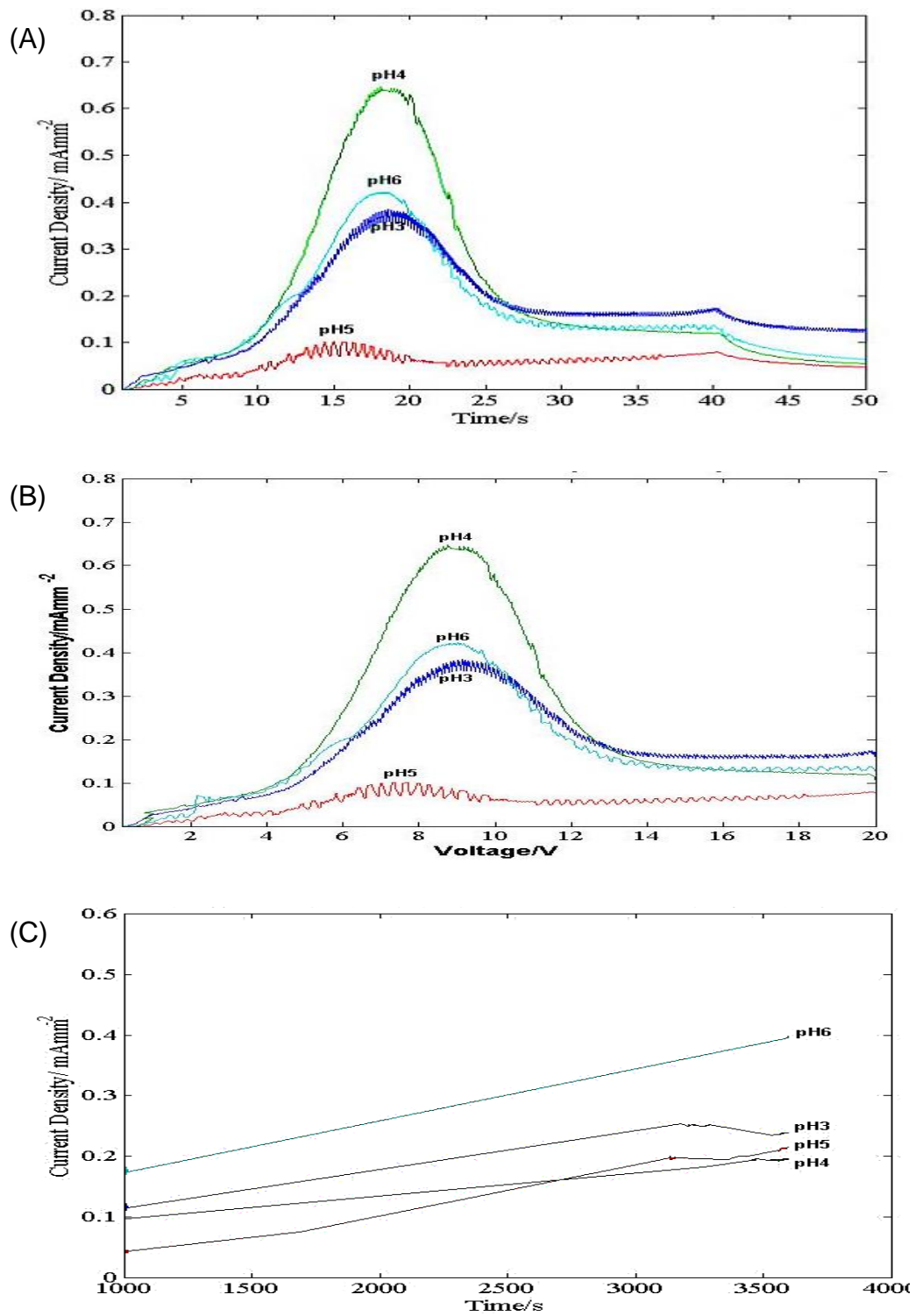
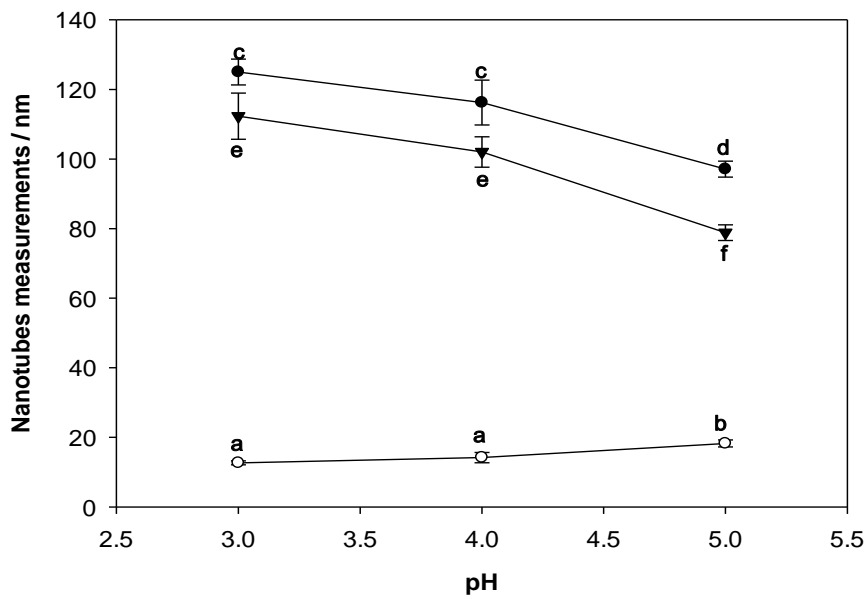


Figure 2.3: The effect of the change in pH on the (a) anodising current density with time during the first 50 s, (B) voltage during the first 50 s and (C) anodising current density with time between 1000 s and 3600 s of the anodisation process

The wall thickness of the nanotubes increased from pH 4 to 5 as seen in Figure 2.4 A. However the tube diameter decreased with increase in pH with a significant decrease at pH 5 (Transformed One-way ANOVA, $p < 0.05$, $n = 3$). Figure 2.4 B showed that anodisation performed in electrolytes at any pH (3-6) resulted in similar final current density at 3600 s (Kruskal-Wallis, $p = 0.73$, $n=3$). The porosity was significantly different from each other with the porosity at of the nanotubes at pH 4 having the lowest value (Kruskal-Wallis, $p = 0.003$, $n=3$).

(A)



(B)

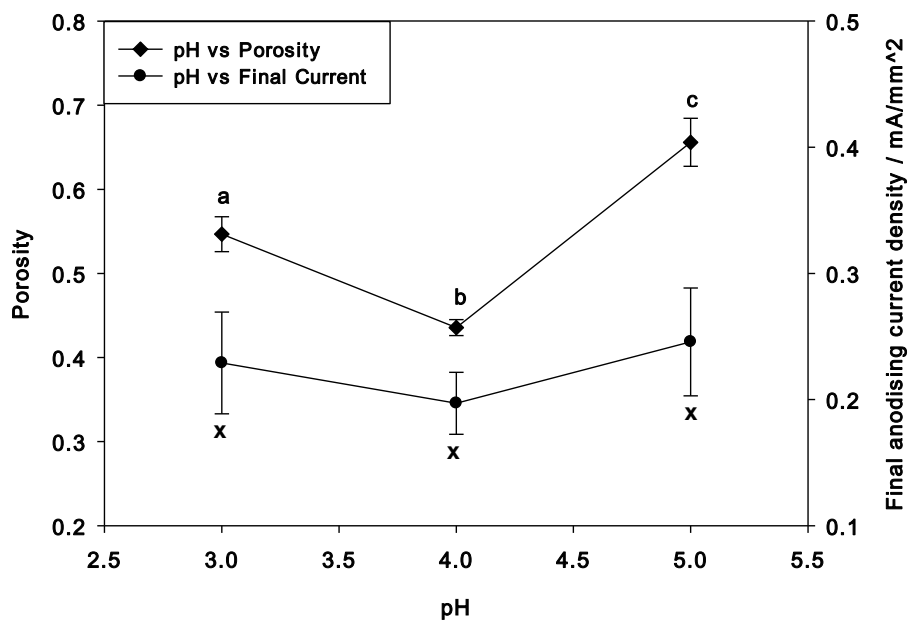


Figure 2.4: The effect of the change in pH on the (A) nanotubes pore diameter and wall thickness and (B) porosity of the nanotubes coating and the current density at the end of the anodisation. The alphabets present the significance in difference between the differently treated samples at 95 % confidence interval (Transformed One-Way ANOVA, n = 3)

The interfacial adhesion between the nanotubes and the substrate was found to be highest at pH 4 as shown in Figure 2.5 (Transformed One-way ANOVA, $p < 0.05$, $n=3$).

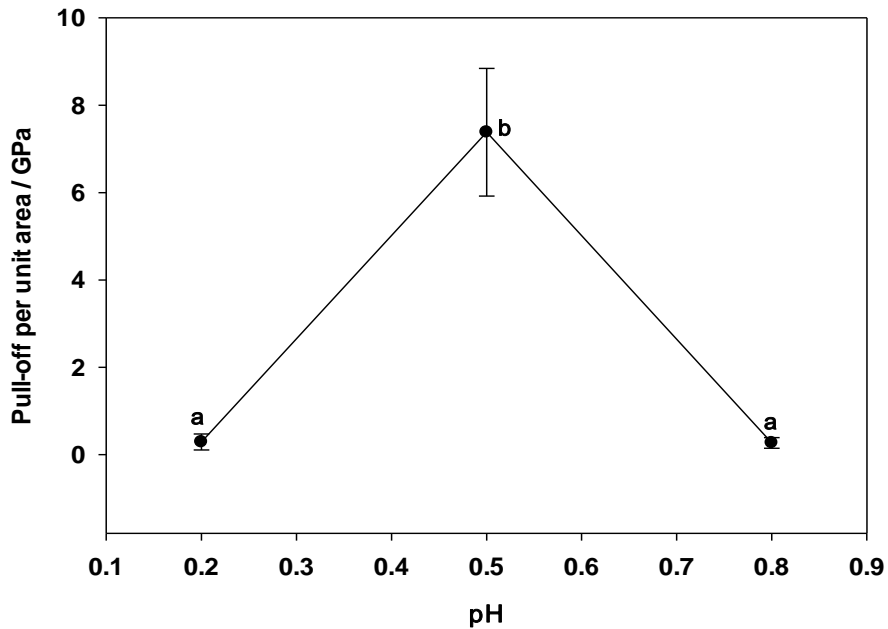
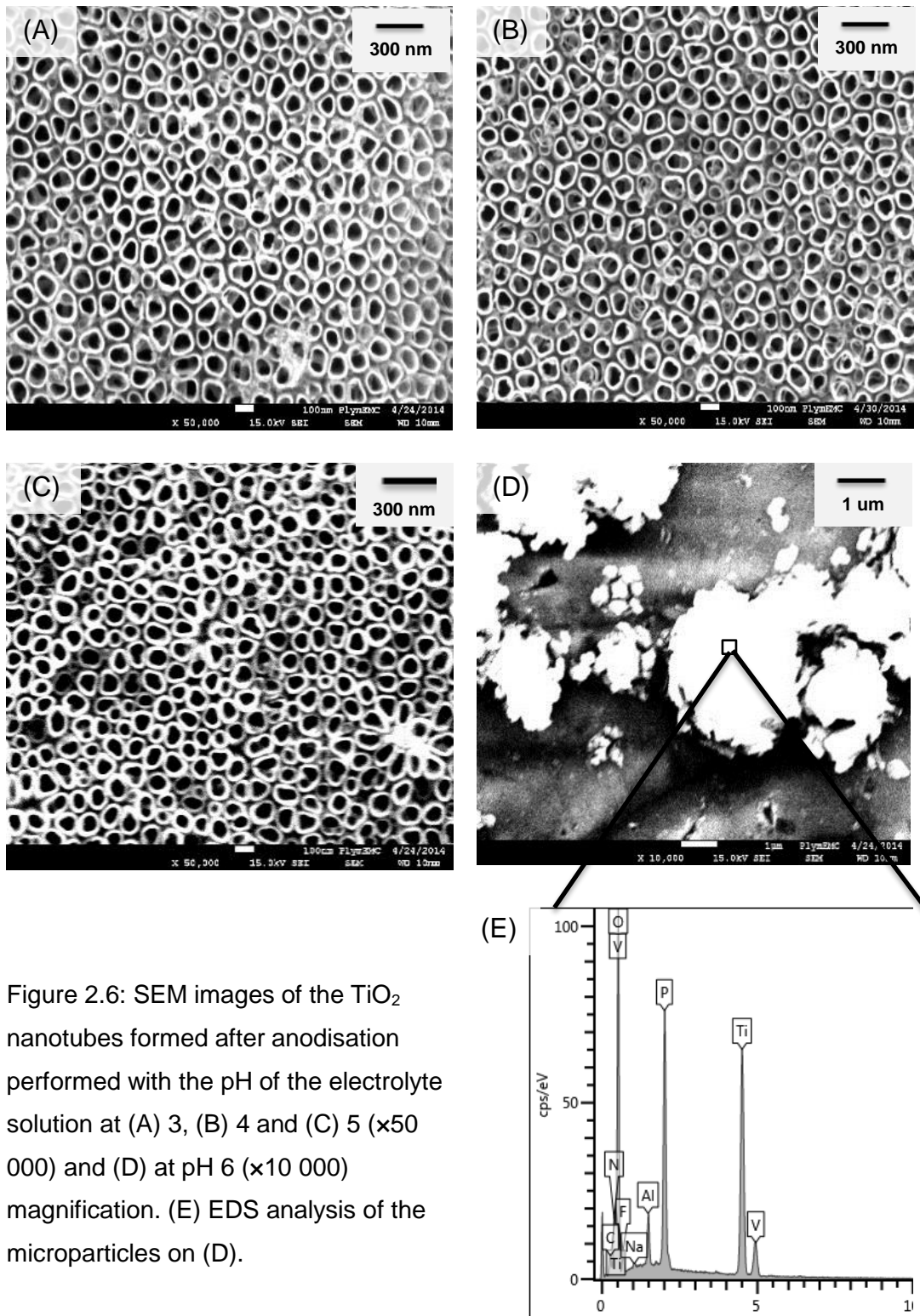


Figure 2.5: The effect of the change in pH on the pull off load per unit (for adhesion test) whereby the alphabets present the significance in difference between the differently treated samples at 95 % confidence interval (Kruskal-Wallis, $n = 3$).

The quantitative observations were visually confirmed by the SEM images in Figure 2.6. Another observation was that more nanotubes were grown at pH 5 (141 ± 6 nanotubes per square micrometer) as compared to pH 3 (71.5 ± 2 per square micrometer) ($n=3$).



2.3.2 Effect of initial sweep rate on anodisation current, nanotubes morphology and adhesive strength of nanotubes to Ti-6Al-4V alloy

Figure 2.7 A and B highlights the changes in anodising current density with respect to time and voltage. It was also observed that the maximum current density reached during the process increases with increase in voltage sweep rate as seen in Figure 2.8 A and B.

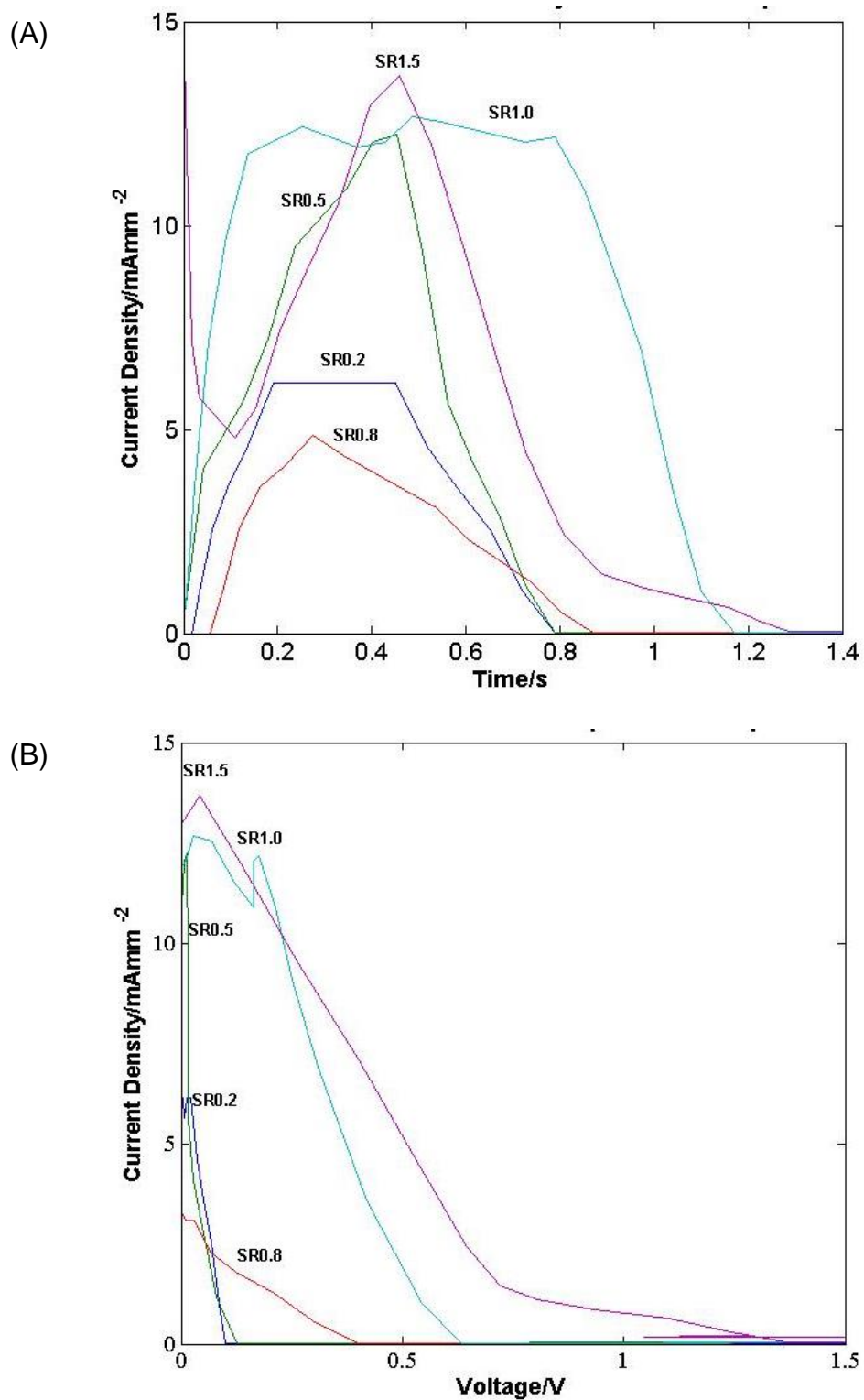


Figure 2.7: The effect of the change in initial sweep rate on the (A) anodising current density with time in the first 1 second and (B) voltage in the first 1 second of the anodisation process.

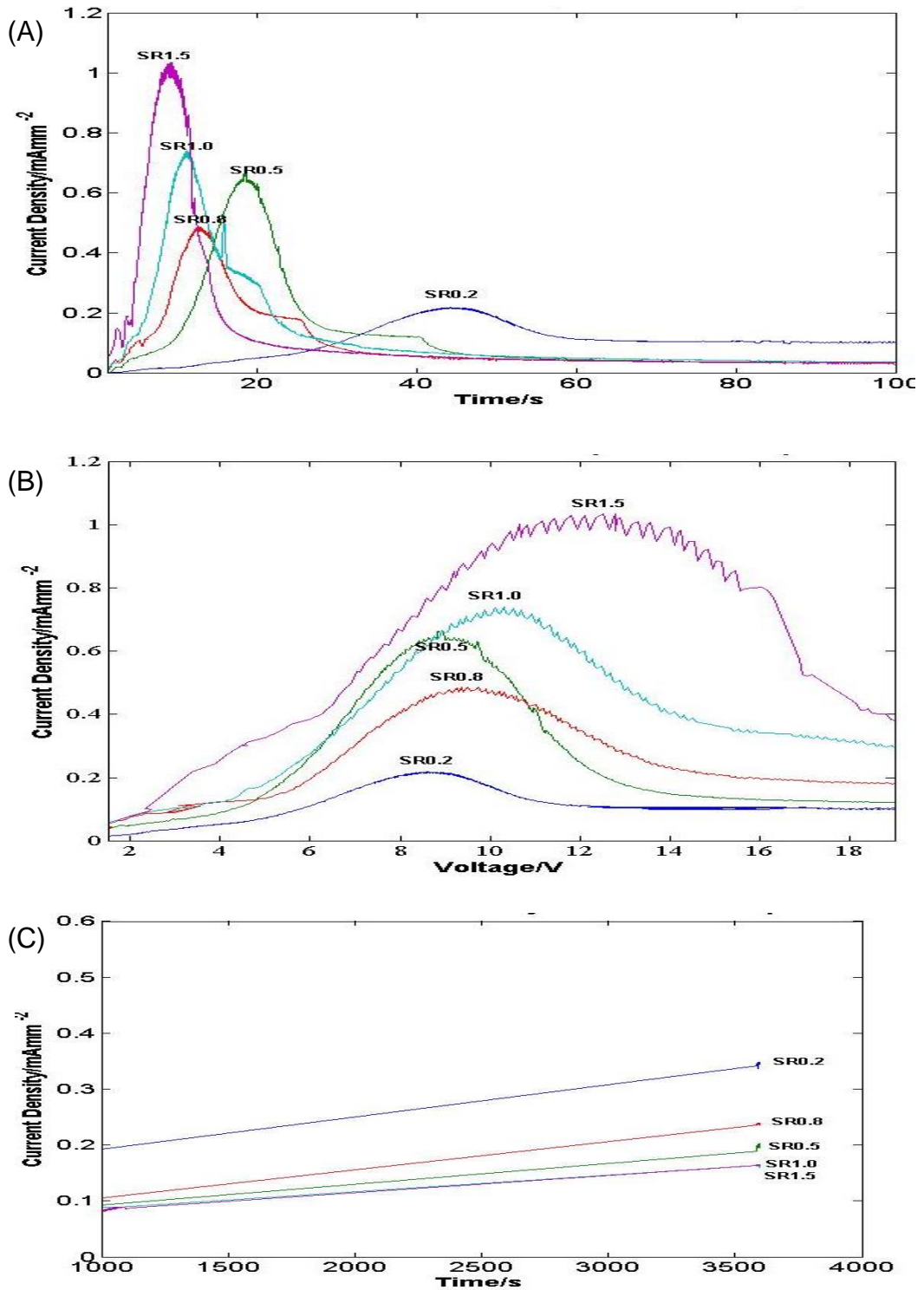


Figure 2.8: The effect of the change in initial sweep rate on the (A) anodising current density with time in the first 100 second, (B) with voltage in the first 100 second and (C) with time between 1000 s and 3600 s of the anodisation process.

The resulting nanotubes had smaller tube diameter with increasing sweep rate while the wall thickness remained unchanged as seen in Figure 2.9 A and B (Transformed One-way ANOVA , n=3).

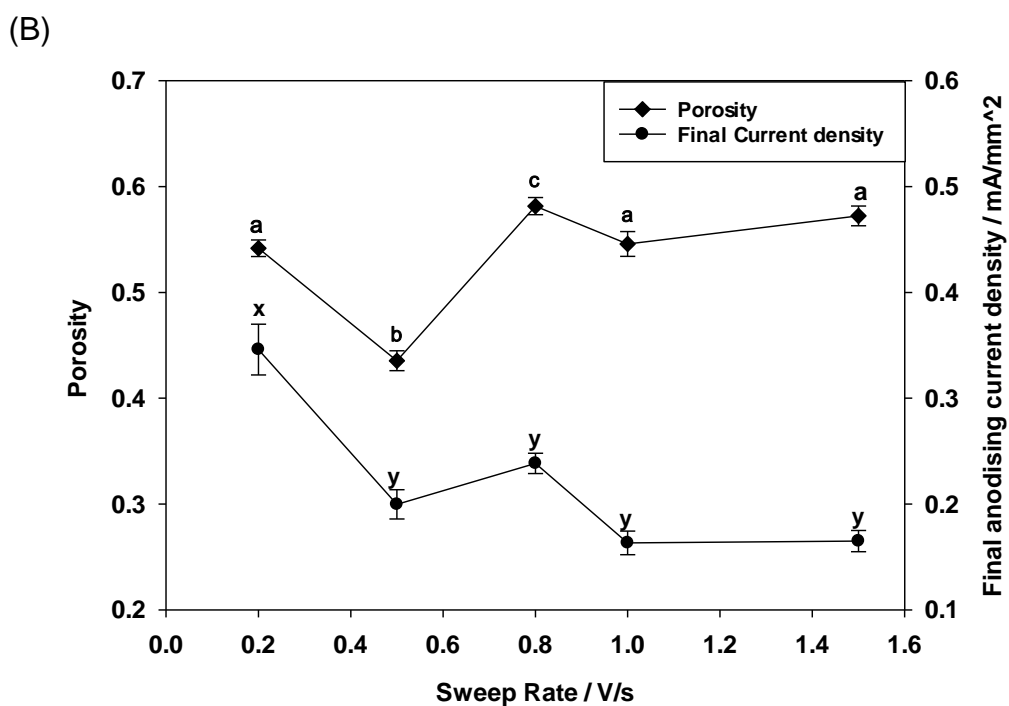
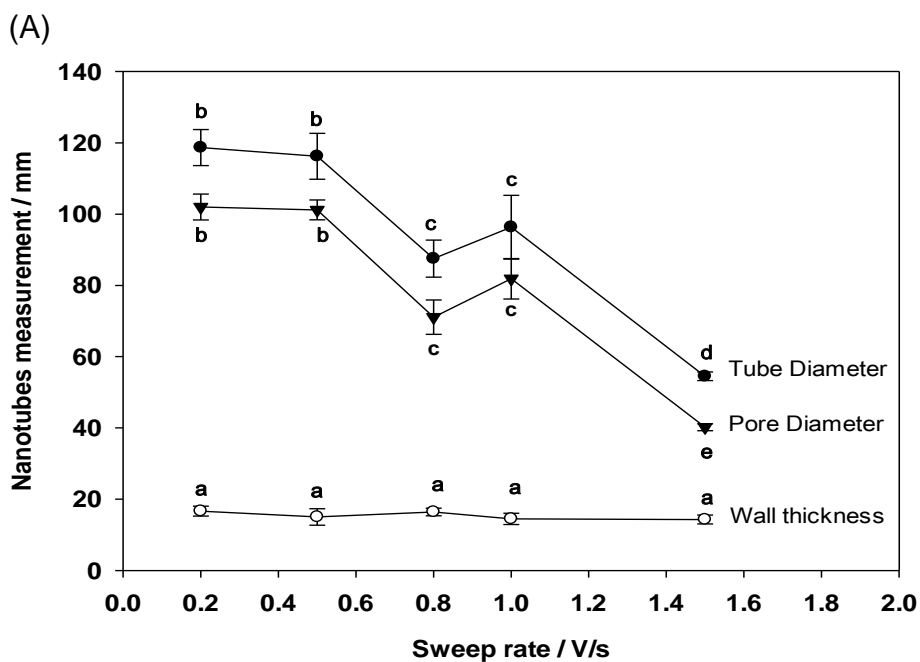


Figure 2.9: The effect of the change in initial sweep rate on the (A) nanotubes pore diameter and wall thickness and (B) porosity of the nanotubes coating and the current density at the end of the anodisation whereby the alphabets present the significance in difference between the differently treated samples at 95 % confidence interval (Transformed One-Way ANOVA, n=3).

The pull off test showed a variation in adhesion strength of the nanotubes to the coating with the maximum adhesion exhibited by the sample which underwent anodisation at an initial sweep rate of 0.5 V/s as shown below in Figure 2.10.

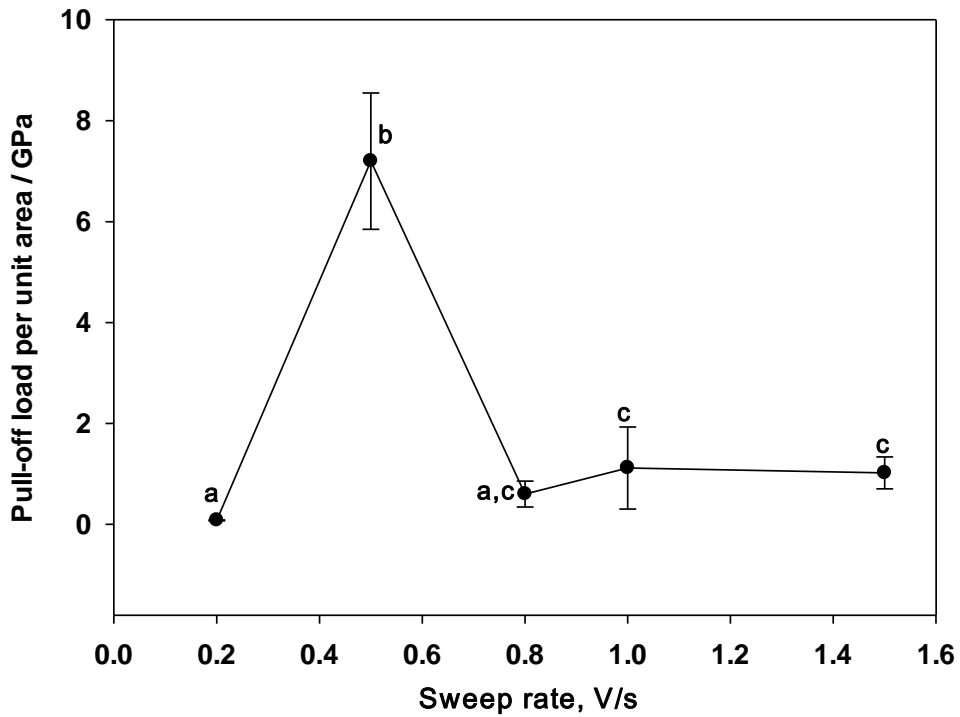


Figure 2.10: The effect of the change in initial sweep rate on the pull off load per unit area for adhesion test whereby the alphabets present the significance in difference between the differently treated samples at 95 % confidence interval (Transformed One-Way ANOVA, n=3).

Figure 2.11 provides the visual confirmation of morphology changes described above with respect to the initial sweep rate. With increasing sweep rate, the nanotubes look smaller and less uniform. It was also observed that there were more nanotubes per unit area with increasing sweep rate.

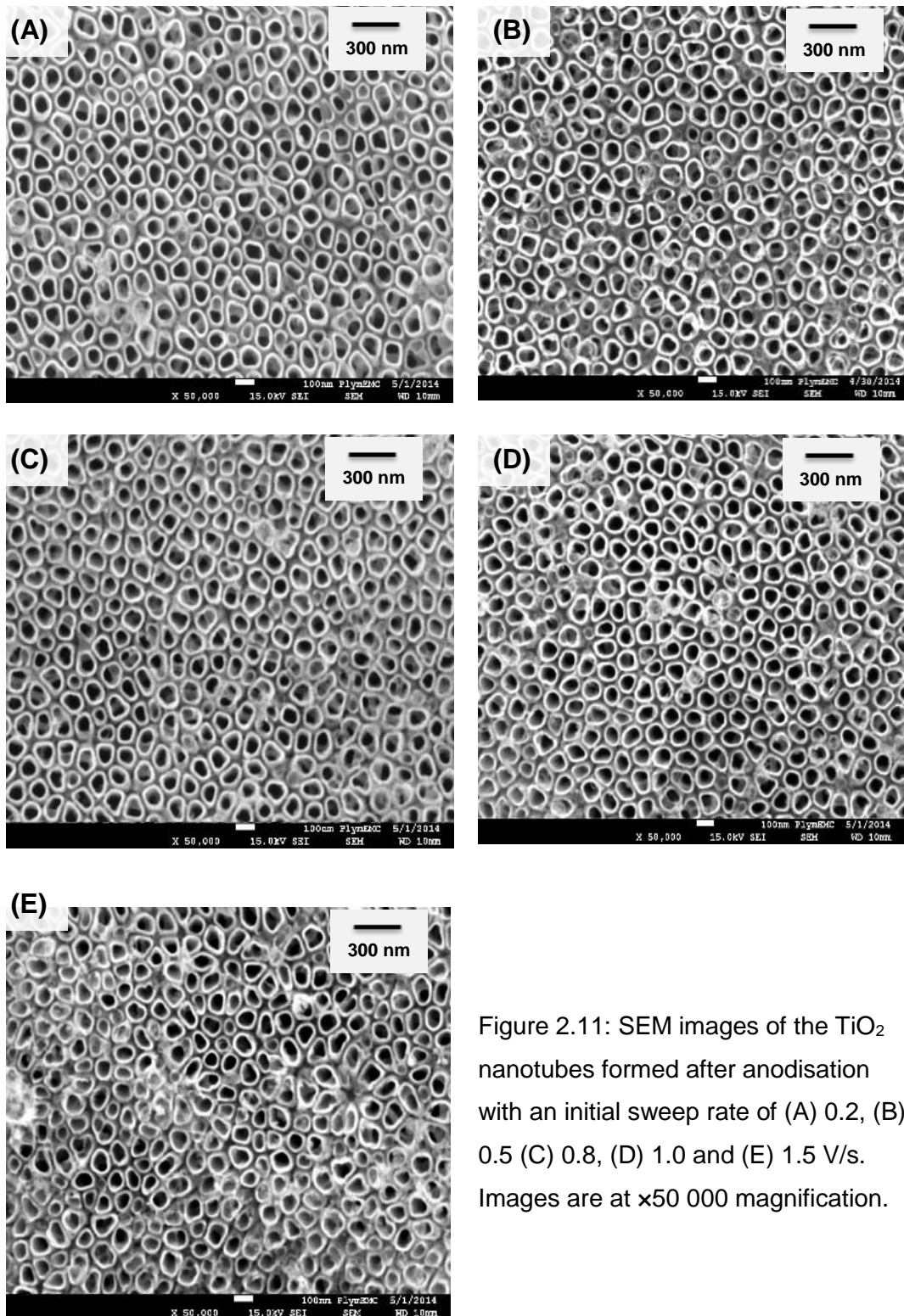


Figure 2.11: SEM images of the TiO₂ nanotubes formed after anodisation with an initial sweep rate of (A) 0.2, (B) 0.5 (C) 0.8, (D) 1.0 and (E) 1.5 V/s. Images are at x50 000 magnification.

2.3.3 Different stages of self-assembly of TiO₂ nanotubes

During the first 5 minutes the surface of the β alloy could be outlined from the α alloy as seen in figure 2.12 A. At the beginning of the process, the β alloy was etched quicker than the α alloy as seen in Figure 2.12. With time the nanostructures formed by etching developed into circular nanostructures. Fifteen minutes into the process, the nanostructures on the β alloy became uniform, only to lose the uniformity after another 5 minutes. Nonetheless the structures became uniform and porous after 30 minutes. The structure on the α alloy only became uniform from 30 minutes after which the uniformity of the nanotubes remained the same.

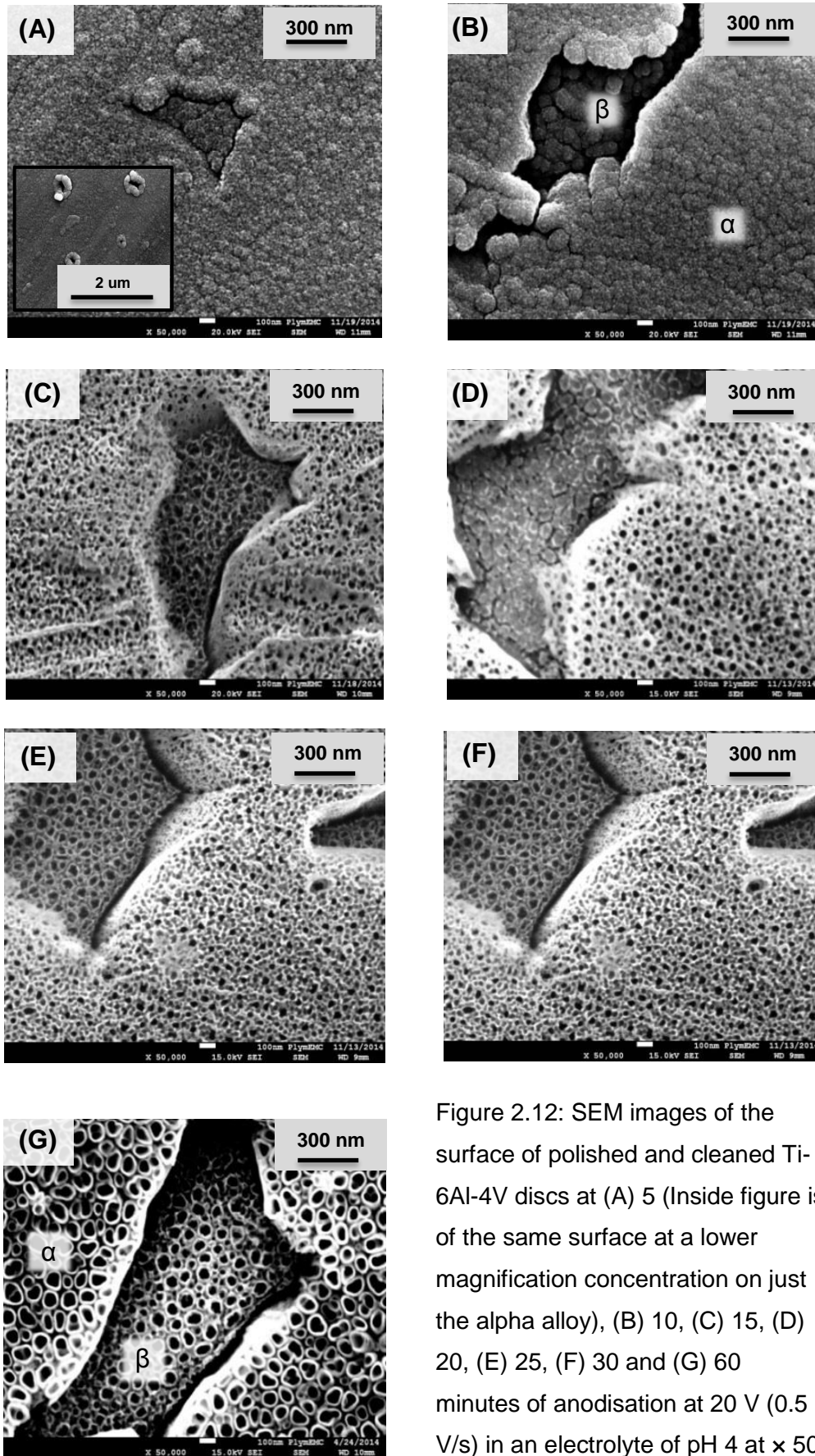


Figure 2.12: SEM images of the surface of polished and cleaned Ti-6Al-4V discs at (A) 5 (Inside figure is of the same surface at a lower magnification concentration on just the alpha alloy), (B) 10, (C) 15, (D) 20, (E) 25, (F) 30 and (G) 60 minutes of anodisation at 20 V (0.5 V/s) in an electrolyte of pH 4 at x 50 000 magnification.

Figure 2.13 below displays the EDS analysis of the elements present on the surface of the coating whereby the proportion of vanadium present was higher in the β - alloy than the α alloy while the other elements remained almost unchanged. The vanadium to aluminium ratio was in alpha alloy and 3.8 in beta alloy.

Spectrum 4 (α)			Spectrum 1 (β)		
	Wt%	σ		Wt%	σ
Ti	64.3	0.5	Ti	64.2	0.5
O	19.9	0.6	O	18.5	0.6
V	8.8	0.2	V	10.5	0.2
F	3.8	0.2	F	3.8	0.2
Al	2.8	0.1	Al	2.7	0.1
P	0.5	0.0	P	0.3	0.0

Figure 2.13: The EDS analysis of the α - and β - part of the coated discs surface after 60 minutes of anodisation from Figure 2.12 G.

2.4 Discussion

2.4.1 Current density variation during anodisation

Anodisation performed in an electrolyte of pH 4 was considered to provide the best uniformity and morphology of nanotubes with the best adhesive strength to the Ti-6Al-4V discs. The initial voltage sweep rate used for the best results was 0.5 V/s.

Roughly a model of the change in current density with respect to time, was built to emphasize on and discuss the different stages in the anodisation process as shown in Figure 2.14. The model helps understand the electrochemical process happening in details. The model was based on the anodisation curve for the experiment performed using the optimum conditions obtained in the study.

Within the first second of the electrochemical process, there is a big increase in current density as shown in Figure 2.14 A. This was associated with the development of an electrode potential at the anode as soon as a circuit was made. There was a fast rate of electron transfer between the electrolyte and the electrode during that second. This current was thus determined by the initial resistance of the electrolyte.

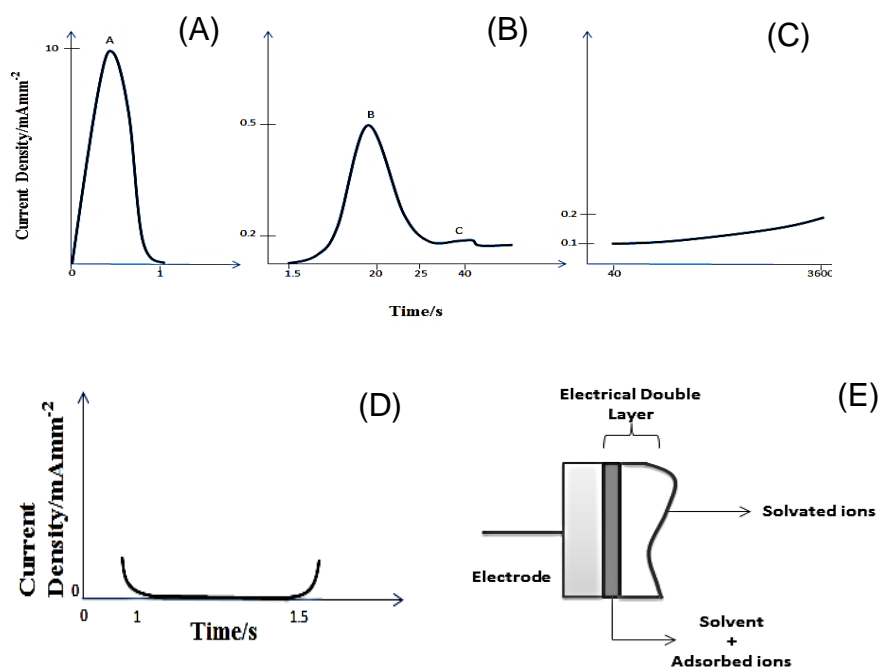


Figure 2.14: (A, B and C) Current density variation with respect to time during anodisation zoomed in for various time intervals. (D) Anodisation current density variation with time highlighting the part when there is no change in current density. (E) An illustration of the presence of the electrical double layer for the IPE effect.

Between the decrease from peak A to the increase to peak B, there was no detectable current for about 500 ms, (from 1 to 1.5 s) as shown in Figure 2.14 D. This was associated with the ideal polarisable electrode (IPE) as even though there was a change in voltage, no charge was flowing between the electrolyte and electrode. Therefore the electrical double layer at the solution/electrode interface acted as a capacitor. When the electrode potential was applied, some of the ions from the electrolyte got adsorbed on the surface of the electrode giving rise to desolvated ions (Chen, 2007). Hence the double layer was formed by firstly, the solvent molecules along with the adsorbed ions and secondly the solvated ions in the electrolyte as shown in Figure 2.14 E. In this situation the capacitance was dependent on

the potential applied and the effect was independent of the content of the electrolyte.

The current density increase to peak B was related to the resistance of the electrolytes and followed Ohm's Law of $V = I R$. as such, as the voltage was increasing the current density decreased as well. The current density stopped increasing when the potential for barrier formation was reached. Afterwards it decreased to a minimum point until 20V was reached which was the barrier formation stage as per equation 1.1 (Section 1.4.1). Such decrease agrees with equations 1.6 and 1.7. Then it increased slightly to point C as shown in Figure 2.14. This increase is owing to the increase in voltage and the polarization of the anode. The current density drops after the voltage reaches the maximum 20V and the polarization stops. The gradual increase in the current density after peak C was due to the etching of the oxide layer in the presence of the F^- ions which react with the TiO_2 layer forming soluble $[TiF_6]^{2-}$ ion as per equation 1.2.

Afterwards, the current density remained almost constant for the remaining 1 hour which was because of the equilibrium of the electrochemical process. Hence there was a balance between etching and oxidation. Following the theory mentioned by Macak *et al* (2007), the dissolution allowed the nanotubes to grow deeper in the oxide layer while the continuous oxidation helped the nanotubes to grow longer (Macak *et al.*, 2007). In the meantime small nanotubes would disappear leaving the larger nanotubes leading to a small increase in nanotube diameter and porosity with time accounting for the slight increase in current density in Figure 2.14 A.

This model provided an insight into the electrochemical reactions occurring during anodisation process with particular attention to the initial 40 seconds of the reaction. This 40 seconds is crucial in determining the barrier oxide formation and the etching process leading to the development of the nanotubes.

2.4.2 Effect of pH

While the pH value was varied, the sweep rate was maintained at a fixed value. As mentioned before, the barrier formation is dependent on the resistance of the electrolytes. As such, with increasing pH, the resistance is expected to decrease and considering Ohm's law, the current density is hence expected to increase. In this study, the resistance of the electrolytes decreased from pH 3 to 4 and from pH 5 to 6 as seen in Figure 2.8 B. Hence this part of the anodisation process in the specific electrolytes in this study agrees with Ohm's law, confirming the theory that the barrier oxide formation obeys Ohm's Law.

During the etching process, the rate of decrease of current density increased with a rise in pH. This was explained by the decrease in the concentration of H^+ ions. Following equation 1.2, when the concentration of H^+ decrease, the etching process is not favoured, hence accounting for the above mentioned observation.

After the etching process, the electrochemical cell reached equilibrium. Since the etching reaction (equation 2.2) is the slowest process among them, it

was chosen as the rate determining step and was used to explain the results with respect to pH and initial voltage sweep rate.

The lower the pH is, the higher the H^+ concentration becomes hence there is a higher current density involved. This accounted for the higher current density reached in pH 3 as compared to pH 4 and 5 when the reaction was in equilibrium as shown in Figure 2.8 C. Nonetheless, the reaction in electrolytes with pH 6, behaved differently. This was because, the concentration of H^+ was so low, that the etching reaction as per equation 2 was reduced and hence allowing more oxidation to take place. Likewise, reactions as per equations 1.3 to 1.5 could not happen in the right way resulting in the accumulation of the hydroxide of titanium which further decomposed to the oxide of titanium. Since there was less etching, the resulting current density was not dependent on the etching process only. Uncontrolled oxidation was happening resulting in the higher current density at the end of anodisation at pH 6.

An observation was a slight decrease in the diameter of the final nanotubes prepared in electrolytes of pH 3 -5. Theoretically, the height of nanotubes are increased with increase in pH as reviewed before. Since nanotubes diameter increases with increase in height, an increase in the nanotubes diameter is expected. However, when pH was changed, there was a slight decrease in nanotubes diameter from pH 3 to 5 with an increase in the number of nanotubes present per micrometre square. In the presence of more H^+ , there was more etching and as such, the initial etching site grew bigger resulting in the presence of less etching sites and hence less nanotubes. At the higher

pH, the oxidation process did not allow the etching process to create big etching sites and as such resulted in smaller and more nanotubes.

2.4.3 Effects of sweep rate

The increase in current density to peak B (Figure 2.8 A and B) with increase in initial sweep rate, followed Ohm's law such that when voltage was increased the resulting current density was increased. As soon as the barrier layer was formed, although the voltage kept increasing the current density did not increase. When a high sweep rate was used, the barrier layer was grown quicker as compared to when a lower one was used but the voltage required for a higher sweep rate was more than that at a lower sweep rate. This was because, a larger power density was applied at SR1.5 in order to form the oxide barrier layer as compared to SR0.2. As such a greater stress would be generated at the electrode/oxide interface at a higher sweep rate resulting in a higher current density. The equilibrium of the electrochemical reaction was maintained at a higher current density when a lower sweep rate was used. When a lower sweep rate was used, a lower impedance was encountered in the cell. Since similar voltage was used for all the processes, the current density increased when a lower sweep rate was used.

Figure 2.9A showed a decrease in the pore diameter of the nanotubes with increase in sweep rate with no change in porosity. This was explained as follows. Etching started and ended earlier than the others when a higher sweep rate was used. As such, when a lower sweep rate was used, more etching occurred resulting in bigger etching sites and hence nanotubes.

However since the number of etching sites increased with increase in sweep rate. Therefore, the porosity did not change much.

2.4.4 Stages of nanotube formation

Etching started earlier in the β alloy as compared to the α alloy because, the β alloy have more vanadium as compared to the α alloy as confirmed by the EDS analysis in Figure 2.13. Vanadium is the β -stabiliser in a Ti-6Al-4V alloy (Luo *et al.*, 2008; Sieniawski *et al.*, 2013; Zeng & Bieler, 2005). As such, the first oxide to form was that of vanadium which is soluble and as such accounted for the loss of initial porosity at 25 minutes of anodisation. This dissolution also accounts for the higher extent of etching in the β alloy. The nano-grains formed in the beta alloy at 20 minutes, was thus the underlying alpha alloy grains which developed into a thin layer of nanoporous layer five minutes later.

The step by step analysis has been first reported in this study whereby the mechanism behind the self-assembly of the nanotubes in the alpha alloy was as follows. First there was formation of nanoparticles followed by the development of 'doughnut-shaped' structures due to arrangement of the nanoparticles with pore diameter slightly bigger than 200nm. Nanopores with varying diameters are initially formed followed by the assembly of the uniformly distributed nanotubes all over the surface.

The nanoparticles formed, at the beginning, was due to the beginning of the etching process in the presence of fluoride ions. The latter led to the presence of the uniformly spread nanoparticles all over the surface of the

sample. Since nanoparticles have the tendency to stick to each other, they arranged themselves in such a way that the doughnut-shaped structures were formed as shown in Figure 2.12 A. Since there was oxidation and chemical dissolution at the same time, neighbouring, 'doughnut-shaped' structures grouped together so that the competition reactions and lateral forces resulted in the formation of the nanoporous surface. This process continued for 30 min whereby the pores were arranged uniformly with well-defined walls differentiating the pores from each other. It was observed that there was a space in between the walls of nanotubes. This followed the theory derived by Macak *et al* (2007) whereby it was explained that as the nanotubes grew longer, the pore diameter decreased, accounting for larger base and smaller opening (Macak *et al.*, 2007).

2.4.5 Theory of initial etching sites

In this study, Ti-6Al-4V alloy was used and as such, during the anodisation process, the oxides of aluminium and vanadium were formed along with titanium dioxide. Nonetheless, the discussion in this work was limited to the oxide of titanium only, due to the predominance of titanium over aluminium and vanadium on the coating (X-ray Analysis in Figure 2.13).

Following the observations at different pH and sweep rate, a new theory was deduced which related the growth of nanotubes to the etching sites at very early stage. The effect of pH and sweep rate could be illustrated using figure 2.15. Due to the large volumetric expansion in the oxidation process, the oxide layer is under large in-plane compressive stress. This could cause buckling or wrinkling according to Hutchinson and Suo (1992) (Hutchinson &

Suo, 1992). The valley of the wrinkles is under additional surface energy and becomes preferred sites for etching. At lower pH, etching started earlier so that the barrier layer was thinner and less stressed. Fewer etching sites per unit area were expected so that smaller number of nanotubes per unit area compared to a higher pH. Figure 2.15 A illustrated that there were fewer nanotubes at lower pH. The wall was thinner while pores were larger due to the ongoing etching of the walls at higher concentration of hydrogen ions and it also showed the growth of the nanotubes at a higher pH whereby the presence of lower concentration of hydrogen ions and hence higher $[\text{OH}^-]$, more oxide was deposited on the inner walls of the tubes. This caused the wall thickness to increase with time. Therefore nanotubes with thicker walls and smaller pores were obtained at a higher pH. This was in agreement with the images in Figure 2.6.

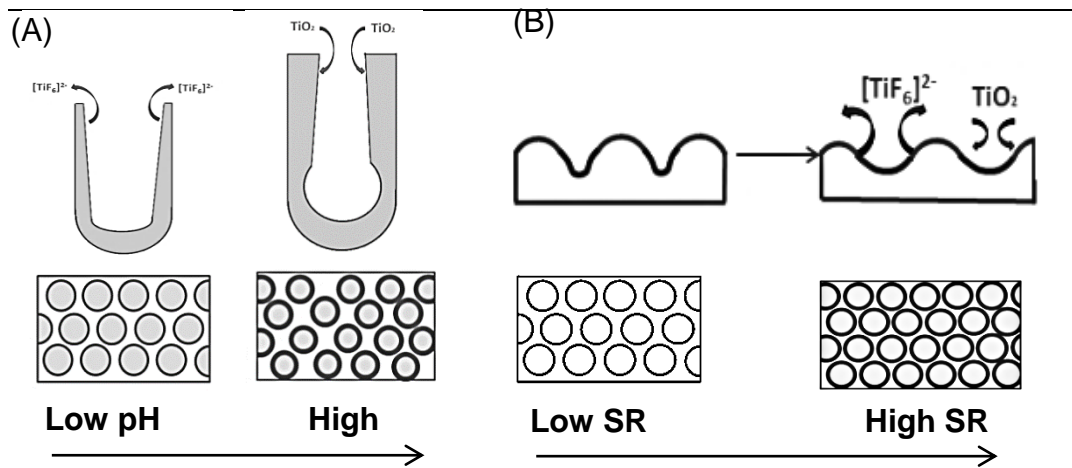


Figure 2.15: Vertical and horizontal cross sections of TiO₂ nanotubes models growing (A) in an electrolyte of low and high pH and (B) at an initial low and high sweep rates. The first part in both A and B highlights the changes happening on single nanotubes whereas the second part shows the distribution, size and quantity of the nanotubes grown in the various conditions.

At a higher sweep rate, the reaction was quicker, resulting in a higher stress being generated accounting for more bulging and as such the presence of more etching sites with smaller size. It was expected that the in-plane stress due to the oxidation expansion is proportional to the reaction rate. This was imaged by Figure 2.15 B whereby more nanotubes with much smaller pores were formed at higher sweep rate than at lower sweep rate. The final current density is determined by the etching rate which is determined by the impedance of the smaller pores. Therefore the final density decreased with increasing sweep rate due to higher impedance of the pores. Nevertheless the wall thickness was not significantly affected as shown in Figure 2.8 A.

2.5 Conclusion

This chapter proved that the initial sweep rate of the applied voltage did have a significant role to play in the self-assembly of titanium dioxide nanotubes as well as the pH of the electrolyte being used for anodisation. The resulting morphology was dependent on the rate at which the voltage was increased to the target value along with the concentration of hydrogen ions in the electrolytes. The interfacial adhesion between the formed nanotubes and the substrate was concluded to be dependent to some extent to pH and sweep rate. The optimum pH of electrolytes used for anodisation was concluded to be pH 4 and optimum initial voltage sweep rate 0.5 V/s. The conclusion was mainly due to the strongest interfacial adhesion between nanotubes and Ti-6Al-4V disc and the resulting morphology of the nanotubes with the absence of contaminants. As such, these were used for the further tests moving forwards. Furthermore, this research work provided a deeper insight to the different stages of the nano self-assembly which allowed a theory related to the initial etching sites to be derived involving the formation of titanium dioxide nanotubes on the surface of Ti-6Al-4V, in the presence of phosphate and fluoride ions. This would be beneficial in carrying antibacterial agents in the nanotubes providing a good surface coverage.

Chapter 3

Pilot study- Amorphous TiO₂ nanotubes as a scaffold for silver nanoparticles on titanium alloy

3.1 Introduction

In this study, δ -gluconolactone was employed to reduce silver ions to silver nanoparticles on the surface of TiO₂ nanotubes grown on Ti-6Al-4V. The aim was to impart some antibacterial properties by decorating the surface of the TiO₂ nanotubes with Ag-NPs, but also attaching the Ag-NPs in a way that would allow slow silver release or sustained antimicrobial properties during use as an implants. The as formed nanotubes during anodisation on titanium alloy are known to have an amorphous crystal structure and are considered to be hydrophilic and non-toxic (Roy, Berger & Schmuki, 2011). Therefore, they will provide the platform for silver ammonia complex to attach while being more interactive with bodily fluids. Hence this chapter concentrated on the analysis of the distribution of the silver nanoparticles reduced from silver ions through chemical reduction on the surface of amorphous TiO₂ nanotubes on Ti-6Al-4V.

3.2 Materials and Methods

TiO₂ nanotubes were initially self-assembled on Ti-6Al-4V discs using an anodization process lasting one hour in an electrolyte containing ammonium hydrogen phosphate and ammonium fluoride of pH 4 and an applied voltage of 20 V with an initial sweep rate of 0.5 V/s as per Chapter 2 (n = 12 discs). The as formed amorphous TiO₂ nanotubes coated on the titanium alloy discs were then exposed to silver ions in reducing conditions to promote the growth of Ag-NPs on them.

3.2.1 Growth of silver nanoparticles

The silver ammonia solution was initially prepared at room temperature using reagents bought from Sigma Aldrich, UK. For the preparation of 1L of 0.015 M of silver ammonia, 0.015 M of silver nitrate was first made with 2.545 g of silver nitrate and 900 mL of pure water. While the resulting solution was continuously stirred using a magnetic stirrer, 15 mL of 1 M of NaOH was added to it. The precipitate of silver oxide formed was continuously mixed for 15 minutes to ensure complete precipitation. Concentrated liquid ammonia of 13.4 M concentration and 0.910 density was then added dropwise to the mixture until all the oxide had dissolved back into solution. Pure water was then added to the mixture with the aim of reaching a volume of 1000 mL and the solution was allowed to stir for a further 10 minutes to ensure complete reaction and mixing. Afterwards, 0.002 M δ -gluconolactone solution was prepared in 0.012 M sodium hydroxide (prepared in deionised water), the volume of which was dependent on the need for the day.

Two different methods of reducing the silver ions were used. In the first method (Method 1), silver ammonia was added to the δ -gluconolactone solution first, after which aTiO₂ (Abbreviation for amorphous TiO₂ nanotubes coated Ti-6Al-4V discs) was exposed to the mixture. To optimise the reaction mixture, the concentration of silver ammonia was changed from 0.005 M to 0.015 M while the concentration of δ -gluconolactone solution was maintained at 0.002 M. The various concentrations of silver ammonia used were 0.005M, 0.010M and 0.015M resulting in the formation of silver nanoparticles on aTiO₂ and were labelled accordingly as follows: TiO₂-Ag0.005 , aTiO₂-

Ag0.01 and aTiO₂-Ag0.015 respectively (n = 6 discs for each). In Method 2, METHOD 2, aTiO₂ was exposed to 0.015M silver ammonia first for 1, 5 or 10 minutes to explore optimising the reaction duration. Samples were washed in deionised water, in order to remove the excess silver and reactants, air dried and then exposed to 0.002M the δ-gluconolactone solution for 5 minutes. The three different exposure times to 0.015M silver ammonia are nominally termed aTiO₂-Ag1G5, aTiO₂-Ag5G5 and aTiO₂-Ag10G5 respectively.

After the addition of silver nanoparticles to aTiO₂ using both methods, the coated discs were placed in 10mL of deionised water and then ultrasonicated in distilled water at 12 MHz with the aim of removing loosely attached nanoparticles. They were then finally dried at room temperature.

3.2.2 Morphological observations on TiO₂ nanotubes coated with Ag-NPs

The prepared discs aTiO₂-Ag0.005, aTiO₂-Ag0.01 and aTiO₂-Ag0.015 from METHOD 1 and aTiO₂-Ag1G5, aTiO₂-Ag5G5 and aTiO₂-Ag10G5 using METHOD 2 were examined by electron microscopy with the aim of analysing the distribution and morphology of the silver nanoparticles attached to the nanotubes. The nanotubes without any silver treatment was used as a negative control for the Ag-NPs. High resolution scanning electron microscope, JEOL7001F SEM was used in conjunction with energy dispersive spectroscopy (EDS) analysis to visualise and characterise the elements present on the discs respectively (in triplicate). Once in the microscope vacuum chamber, each replicate was viewed at 3 different locations and photographs were taken and saved in tiff format. Images were

then collected systematically from each specimen. A low magnification was used with the aim of confirming a full coverage and uniform distribution of any coating on the alloy, while a high magnification was used to analyse the morphology of the silver nanoparticles and whether or not they appeared attached to the TiO₂ nanotubes. The EDS was coupled with AZtec analysis software (Oxford Instruments, UK) with the aim of confirming the presence of the different elements present on the coating, especially the presence of silver.

3.2.3 Measurement of silver ion release after 24 hours

Silver ions and/or metals are known to be toxic in the human body. Since the coating is aimed to be used on implants, it was mandatory to assess the stability of the silver coating. In this section, the assessment was performed by measuring the concentration of silver ions released in a liquid medium having components similar to the human bodily fluid, known as simulated body fluid (SBF) for 24 hours. This experiment will give an indication on the stability of the different coatings and as such help in the selection of the best. First, the SBF was prepared in Milli Q water using Kokubo's recipe at 37 °C with the concentration of the ions being Na⁺ 426, K⁺ 15.0, Mg²⁺ 4.5, Ca²⁺ 7.5, Cl⁻ 443.4, HCO₃⁻ 12.6, HPO₄²⁻ 3.0, SO₄²⁻ 1.5 mM (Kokubo, 1997). The amount of the various salts used were hence as follows for 1 litre of SBF being made: 7.996 g NaCl, 0.350 g NaHCO₃, 0.224 g KCl, 0.228 g K₂HPO₄·3H₂O, 0.305 g MgCl₂·6H₂O, 0.278 g CaCl₂, 0.071 g Na₂SO₄, 6.057 g (CH₂OH)₃CNH₂, 40 cm³ 1 kmol/m³ HCl and more 1 kmol/m³ HCl to further adjust the pH.

Then 24 plastic containers of 50 mL were acid washed in 5 % nitric acid and allowed to dry at room temperature. To each containers, 25 mL of SBF was added followed by the samples aTiO₂-Ag0.005, aTiO₂-Ag0.01 and aTiO₂-Ag0.015 from METHOD 1 and aTiO₂-Ag1G5, aTiO₂-Ag5G5 and aTiO₂-Ag10G5 from METHOD 2 and aTiO₂ (n=3 for each category) and placed in an incubator at 37 °C for 24 hours. Three containers were left without any samples in them to act as a control for the SBF. The latter temperature was used with the aim of mimicking the temperature of a human body. After the 24 hours exposure, 5 mL from the SBF was taken and pipetted into 15 mL Falcon tubes. Two drops of 70 % nitric acid was added to the tube to ensure that the silver stays in the solution and is not adsorbed to the falcon tubes. Simultaneously this step helps with matrix matching with respect to the standards being used for the ion measurement. Inductively Coupled Plasma Atomic Emission Spectroscopy (ICP-OES) was used to measure the amount of silver released in the SBF. To start with, standards for the different ions were prepared in triplicates at 0, 10, 20, 40, 100 ppb for Ag which were prepared using the certified reference material (CRM) obtained from Sigma Aldrich, Irvine, UK in 5 % HNO₃. The instrument was then calibrated with the standards. Thenceforth the acidified samples were run through the instrument with 3 set of measurements being made per sample being read. After every 5 readings, the instruments were blanked and calibrated again to correct any instrument drift and prevent any side-effect of the nanomaterial, if any undissolved, on the instrument. After the readings were obtained the detection limits for each element was calculated as per section 4.6. Any value below the detection limit was considered to be zero. The ICP

measurements thus allowed the analysis of the attachment of silver nanoparticles to the coatings.

3.2.4 Statistical Analysis

The data obtained from measuring the amount of silver released from the various silver containing coatings were analysed with Statgraphics Centurion XVII (StatPoint Technologies, Inc.) and curves were fitted using SigmaPlot 13.0. The means of the replicates were investigated and the normally distributed data with equal variances (Levene's Test) were analysed using One-way ANOVA with Fisher's LSD test post-hoc. Data are presented as mean \pm S.E.M and the analysis used p-values of less than 0.05 for statistical significance.

3.3 Results

3.3.1 Silver nanoparticles synthesis using Method 1

Using Method 1, silver nanoparticles were successfully formed on the surface of the nanotubes and not inside the walls of the nanotubes. The resulting nanoparticles were spherical in shape and had diameters of 102 ± 21 nm on all the coatings. Nonetheless, they formed clusters which were uniformly distributed over the nanotubes surface and the cluster as a whole had varying dimensions. The space between the clusters varied between 1 to 10 μ m as seen in Figure 3.1. The spacing between the clusters remained the same, irrespective of the concentration of silver ammonia used in the reduction process.

Figure 3.1D showed a higher magnification of aTiO₂-Ag0.005 treatment. Assuming the clusters fitted in a 2D rectangle, the average dimensions of the latter rectangular space the latter occupied on aTiO₂-Ag0.005 was of approximately 1 by 0.5 μm. With increasing concentration of silver ammonia, the distribution and spacing of the clusters remained the same. Nonetheless, the size of the clusters increased with an average approximate dimension of 1 by 3 μm for the aTiO₂-Ag0.01 (Figure 3.11B and E) and 5 by 5 μm for the aTiO₂-Ag0.015 treatment (Figure 3.1C and F). The EDS analysis in Figure 3.1G confirmed the presence of silver on the surfaces with a slight increase in the silver present when a higher concentration of silver ammonia was used (Figure 3.1 H and I). The X-ray analysis also detected a high level of titanium, aluminium, vanadium and oxygen for all the treated samples.

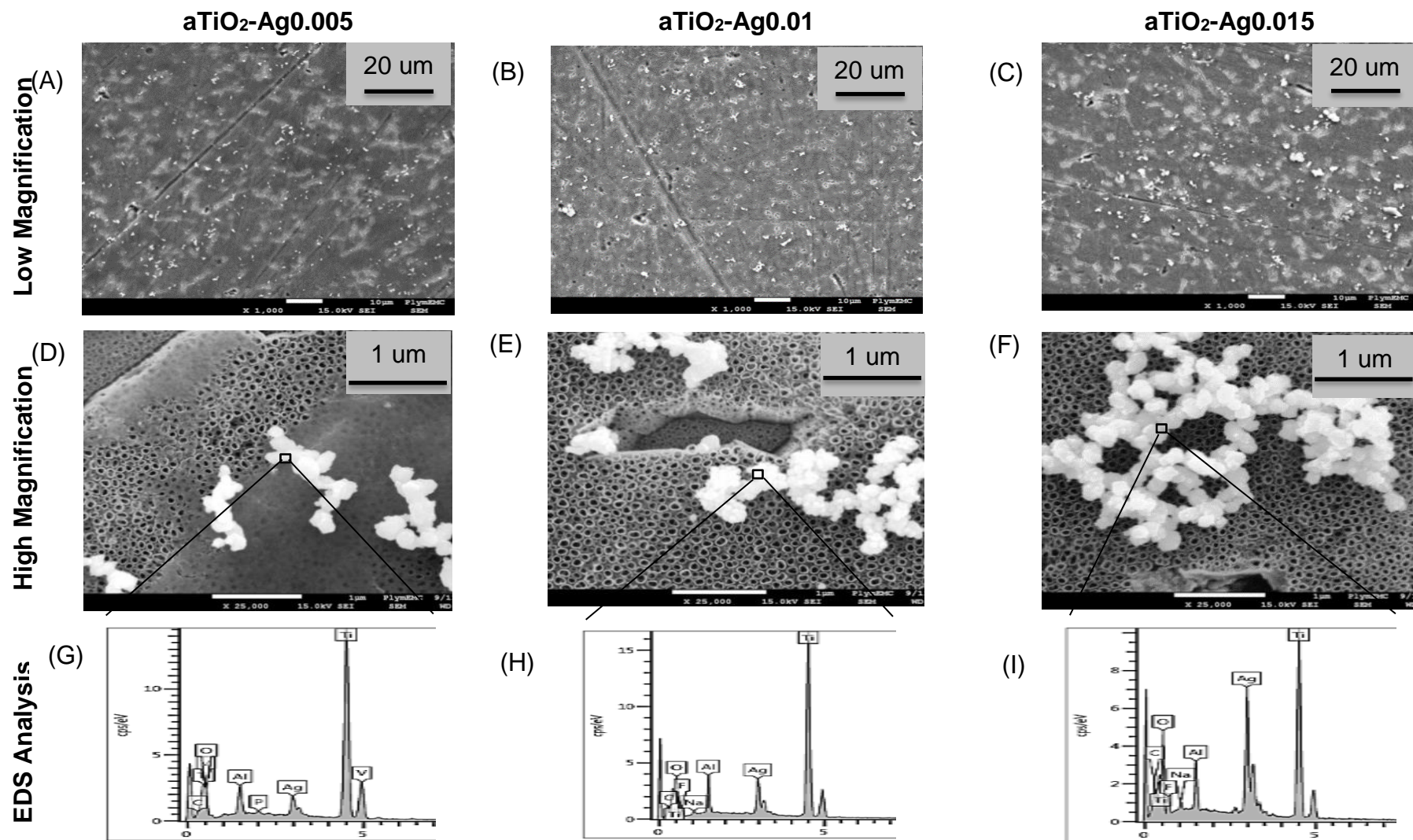


Figure 3.1. SEM images of silver nanoparticles forming micro-clusters on TiO₂ nanotubes (A) aTiO₂-Ag0.005, (B) aTiO₂-Ag0.01 and (C) aTiO₂-Ag0.015 being viewed at a low magnification of $\times 1000$. Panel D-F shows the respective coatings at a higher magnification of $\times 25\,000$. Panel (G-I) shows the respective EDS analysis of the silver nanoparticles.

3.3.2 Silver nanoparticles synthesis using Method 2

Using Method 2, nano-clusters were formed on the surface and the interior walls of the nanotubes on the Ti alloy as shown in Figure 3.2. The surfaces of the TiO₂ nanotubes were uniformly covered with the clusters of spherical silver nanoparticles. Figure 3.2 A, B and C showed the composite coating at a low magnification which provided evidence of surface coverage and distribution of the clusters. Figure 3.2 D, E and F showed the coating at a higher magnification which provided an insight on the morphology of the clusters and the nanoparticles. Figure 2G confirmed the presence of silver on the surface through EDS analysis of the nanoparticles clusters. Again, the analysis detected titanium, aluminium, vanadium and oxygen. In this method the incubation time in the δ -gluconolactone solution was fixed at 5 minutes, but the time of exposure to the silver ammonia complex was varied as 1, 5, and 10 minutes (left, middle, and right hand panels in Figure 3.2 respectively). Increasing the time in the presence of the silver ammonium complex from 1 to 10 minutes, resulted in a reduction in the size of the nano-clusters (cluster as a whole having at least one dimensions less than 100 nm) on the surface of the TiO₂ nanotubes (Figure 3.2). The nanotubes exposed to the silver ammonia for 1 minutes (aTiO₂-S1G5) created clusters varying from 200 nm to 500 nm. With increase in exposure times from 5 min (aTiO₂-S5G5) to 10 min (aTiO₂-S10G5), the size of the clusters as whole, decreased from 100 – 200 nm to less than 100 nm which were not visible enough on Figure 2C at lower magnification.

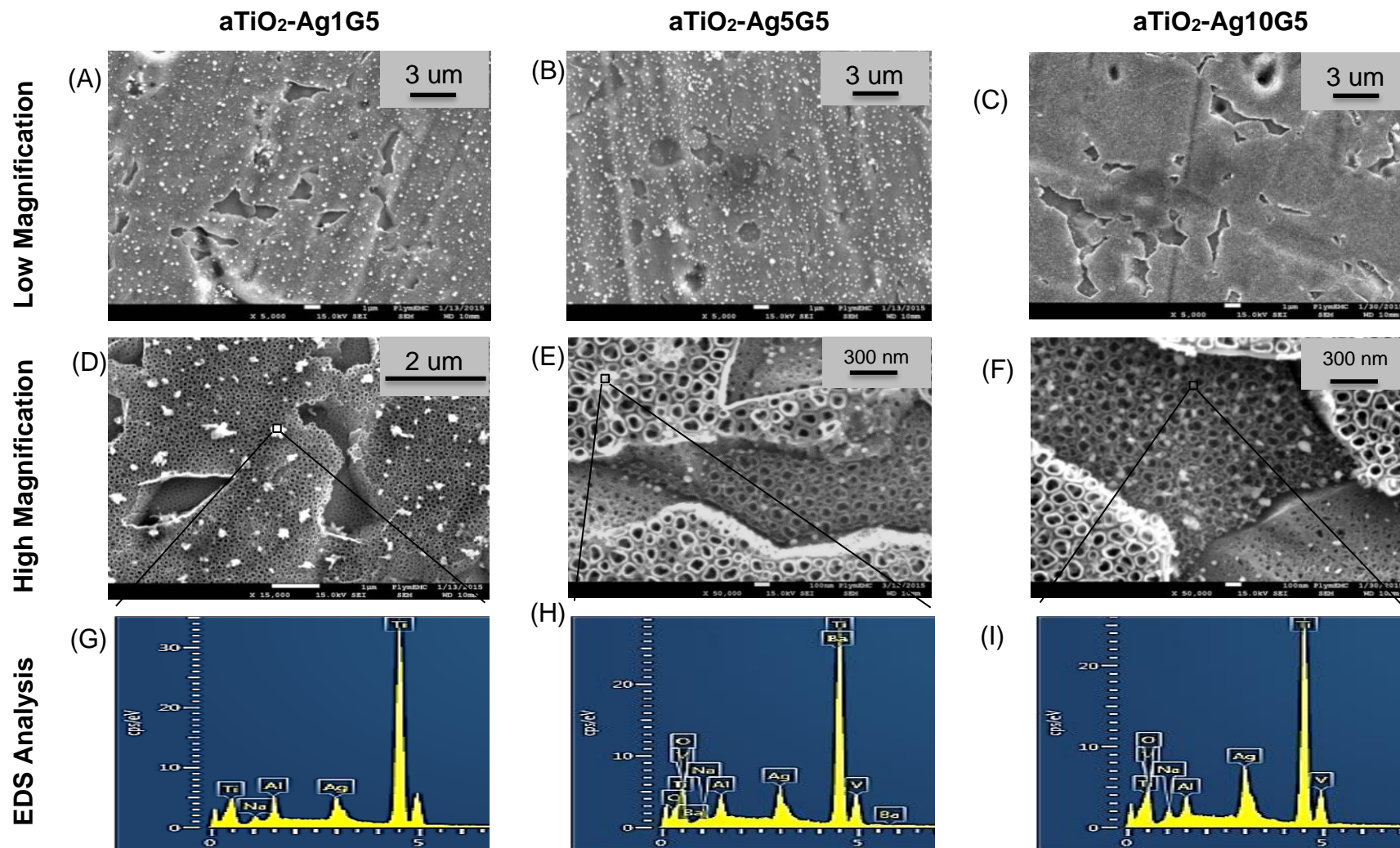


Figure 3.2: SEM images of nanoclusters of silver nanoparticles. The exposure time to silver ammonia was (A) 1 minutes, (B) 5 minutes and (C) 10 minutes and exposure to δ -gluconolactone was maintained at 5 minutes. (D), (E) and (F) shows a higher magnification SEM images of aTiO₂-Ag1G5, aTiO₂-Ag5G5 and aTiO₂-Ag10G5 respectively. (G-I) EDS analysis of the silver nanoparticles coated aTiO₂.

3.3.3 Total dissolved silver in SBF

The total amount of silver dissolved in SBF after 24 hours of exposure of the samples, from Method 1, to SBF was featured in Figure 3.3 A. The results for the blank successfully acted as the control for the SBF which did not have any silver. When aTiO₂ was exposed to SBF, again no silver was present in the exposed simulated body fluid. As compared to the controls, the concentration of silver dissolved in the SBF from aTiO₂-Ag0.005, aTiO₂-Ag0.01 and aTiO₂-Ag0.015 was significantly higher after 24 hours (One-way ANOVA, $p < 0.05$, $n = 3$).

Using Method 1, it was found that with increasing concentration of the silver ammonia solution used for the synthesis of Ag-NPs on amorphous TiO₂ nanotubes, the amount of silver dissolved in the SBF after 24 hours exposure increased. The lowest release from aTiO₂-Ag0.005 was 3.35 ± 0.17 ppm and the highest was from aTiO₂-Ag0.015 (14.6 ± 0.67 ppm).

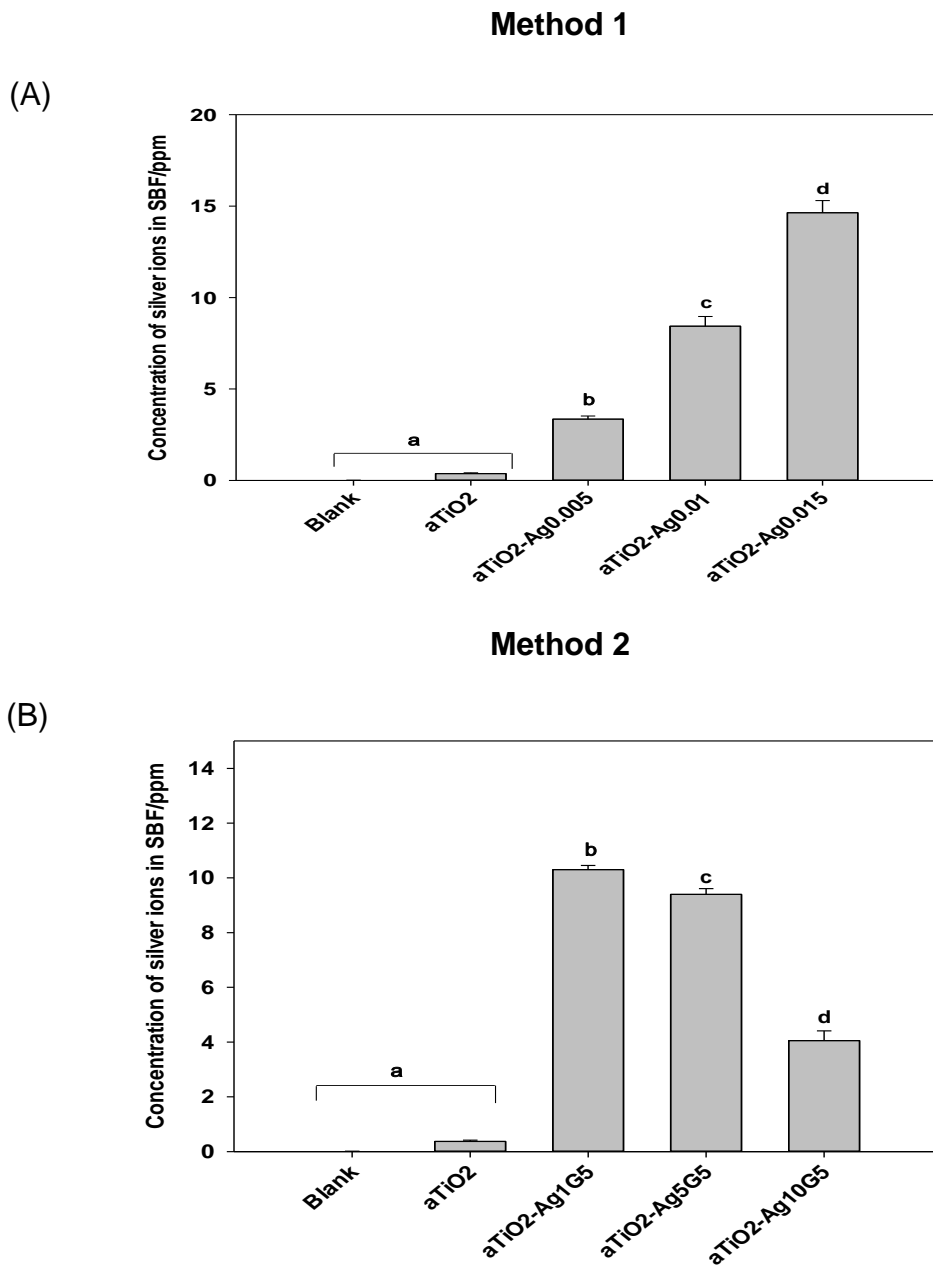


Figure 3.3: Concentration of total silver dissolved in acidified SBF measured by ICP-OES after 24 hour exposure of the aTiO₂ discs from (A) method 1 and (B) Method 2 of silver nanoparticles synthesis. The different letters indicate the statistically significant differences in between samples at a confidence interval of 95 % (One-way ANOVA, n=3)

Figure 3.3 B showed the total silver concentrations in the acidified SBF after the 24 hours exposure of the samples from Method 2 (aTiO₂, aTiO₂-Ag1, aTiO₂-Ag5 and aTiO₂-Ag10) to the simulated body fluid. Although aTiO₂-Ag10 was exposed to silver ammonia solution longer, the total amount of silver released from the coating was less (4.05 ± 0.36 ppm) than the release from aTiO₂-Ag1 and aTiO₂-Ag5. As such, there was less silver release from the Ag-NPs coated samples with increase in the exposure time to silver ammonia.

Another important observation made was that when 0.015 M silver ammonia solution was used in Method 1 (aTiO₂-Ag0.015), the total amount of silver dissolved in SBF after 24 hours was 14.6 ± 0.67 ppm. When the same concentration was used in Method 2, the highest amount of silver dissolved from the coating was 10.3 ± 0.15 ppm (aTiO₂-Ag1), which was lower than the release from Method 1.

3.4 Discussion

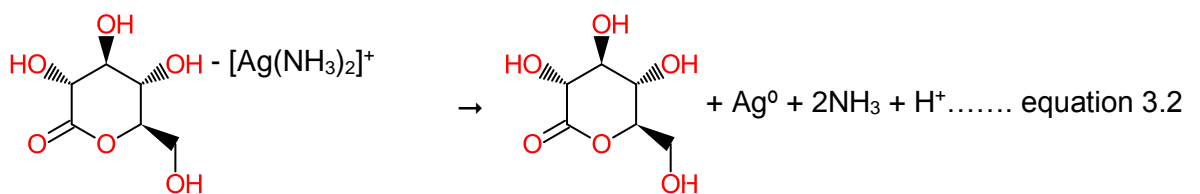
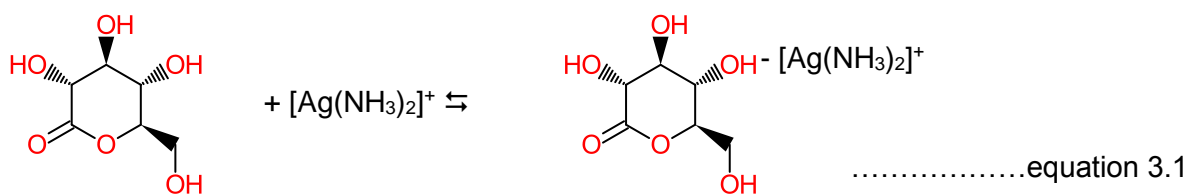
After the self-assembly of TiO₂ nanotubes, silver nanoparticles were successfully reduced on the latter surface using δ -gluconolactone as a reducing agent. The difference in the growth of silver nanoparticles on the surface of the TiO₂ nanotubes using the two different types of chemical reduction were then evaluated. The main findings were the synthesis of clusters of silver nanoparticles with the dimension of the clusters as wholes being in the nanometre and micrometre scale. The best coating was found to be aTiO₂-Ag10G5 with the right morphology and distribution of the nanoparticles.

3.4.1 Synthesis of micro-clusters (cluster as a whole within the micrometre scale) of Ag-NPs on amorphous TiO₂ nanotubes

Using Method 1, silver nanoparticles, were successfully formed on the nanotubes. This method shows that changes in the concentration of the silver ammonia, in the mixture of silver ammonia and δ -gluconolactone, does not affect the morphology of the spherical Ag-NPs formed. Instead, the change in the concentration of silver ammonia affects the distribution of the nanoparticles. That is more nanoparticles, are formed with an increase in the concentration of silver ammonia, resulting in the formation of clusters in the micrometre scale as shown in Figure 3.1. As such, the increased number of nanoparticles were attached to each other resulting in bigger clusters.

In section 3.2, the chemical reaction between glucose and silver ammonia was commented on. The results from this study agrees with the chemical reaction developed by Hussain *et al.* (2011) (Hussain *et al.*, 2011). Following that reaction,

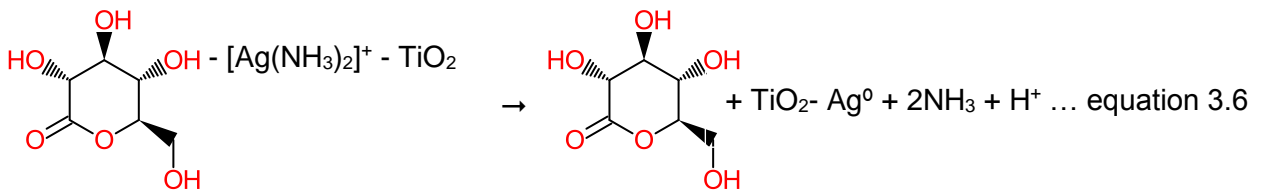
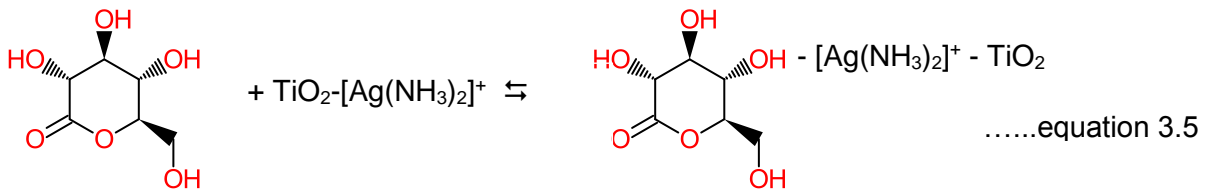
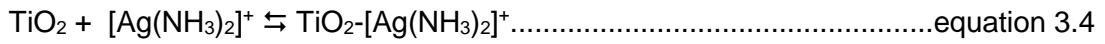
when δ -gluconolactone was mixed with the silver ammonia, the silver ions were assumed to be reduced to nanoparticles as per equation 3.1 and 3.2. The clustering at the micrometre scale observed in this part of the study was hence associated with the attachment of many silver ammonia complex to the $-OH$ parts of the δ -gluconolactone molecule. The dissolution of the silver from the coating to the SBF was very high within 24 hours. This dissolution increased with an increase in cluster size. This meant that the increase in cluster size did not enhance the attachment of the nanoparticles to the nanotubes or other nanoparticles. Since the silver ammonia was added to the reducing agent before exposure to the samples, the clustering could have happened before the attachment to the nanotubes wall. As such, this was associated with the fact that the silver nanoparticles, as clusters, attached to the TiO_2 nanotubes. Since the concentration of δ -gluconolactone remained unchanged throughout, the number of clusters did not increase with the increase in the concentration of silver ammonia. Nonetheless, the number of silver nanoparticles increased leading to an increase in the size of the micro-clusters formed on TiO_2 nanotubes.



3.4.2 Synthesis of nano-clusters (cluster as a whole within the nanometre scale) of Ag-NPs on amorphous TiO₂ nanotubes

In Method 2, the samples were first exposed to the silver ammonia complex solution for 1, 5 and 10 min followed by an exposure to the δ -gluconolactone. Since the samples were exposed to silver ammonia and δ -gluconolactone separately, the only way silver nanoparticles can form would be if the silver ammonia to attached to the nanotubes first as one whole complex, $[\text{Ag}(\text{NH}_3)_2]^+$ as per equation 3.3.

Subsequently, when exposed to δ -gluconolactone, the silver ammonia complex was reduced to silver nanoparticle as per equation 3.4 and 3.5. The clusters formed in this case were smaller but closer to each other as compared to the micro-clusters. Thus, a longer exposure time to the silver source yielded more nano-clusters closer to each other on aTiO₂. The longer aTiO₂ stayed in the silver ammonia solution, the more molecules would be able to attach to the walls of the nanotubes. Since the concentration of δ -gluconolactone and the exposure time to the latter remained 5 min for all the samples in Method 2, the resulting morphology and distribution of the Ag-NPs were dependent on the exposure time to silver ammonia only.



3.4.3 Comparison of clustering of nanoparticles on amorphous TiO₂ nanotubes

δ -gluconolactone successfully reduced silver ions to silver nanoparticles at room temperature. However, the nanoparticles were not distributed as individual particles on the surface of the nanotubes. Instead they formed clusters, the whole size of which was dependent on the concentration of silver ammonia being used and the exposure time to the latter. Method 1 highlights the change in clustering size with respect to the concentration of silver ammonia in the mixture of silver ammonia and δ -gluconolactone. Method 2 associated the clustering size with the exposure time to silver ammonia. The difference between Method 1 and Method 2 was the type of exposure of aTiO₂ to the chemical reagents. In order to compare Method 1 from Method 2, aTiO₂-Ag0.015 from Method 1 needs to be considered as the concentration of the silver ammonia used was similar to that use in Method 2. It was hence concluded that there was a big difference in the size of the cluster of Ag-NPs

as a whole when the samples were exposed to a mixture of silver ammonia and δ -gluconolactone as compared to when the samples were exposed to silver ammonia first and then δ -gluconolactone. The difference in size was from micrometre dimensions to nanometre dimensions. The latter difference in clustering size was associated with the way the nanoparticles were formed.

In Method 1, when the samples were exposed to the mixture, the nanoparticles would form in the solution first and then attach to the nanotubes. When considering Method 2, when the samples were exposed to silver ammonia first, the silver ammonia complexes would be attached to the nanotubes first and then be reduced by the δ -gluconolactone upon exposure to the latter. This was found to be the only way the reduction could happen when considering the chemical reaction involved. As such, formation of clusters before attachment to nanotubes was associated with the formation of bigger clusters as compared to nanoparticle formation directly on the walls on the nanotubes.

Still comparing aTiO₂-Ag0.015 from Method 1 to the resulting coatings from Method 2, it was observed that the total amount of silver dissolved from the coatings in Method 1 was higher than those from Method 2, irrespective of the exposure time to silver ammonia in Method 2. As such, it was concluded that the big clusters consisted of loosely attached silver nanoparticles which were dissolved easily in the presence of SBF. In comparison, the nanoparticles, in the nano-clusters from Method 2, were more strongly attached to the nanotubes wall or each other that the release was lower. From the samples in Method 2, aTiO₂-Ag1 had bigger nano-clusters as compared to aTiO₂-Ag10 and the total amount of silver dissolved from aTiO₂-Ag1 was higher than that from aTiO₂-Ag10. As such it could be concluded that since there were more nanoparticles attached to each other as compared to those attached to

the nanotubes wall in aTiO₂-Ag1. Hence, the nanotubes attached to each other with a weaker bond as compared to the bond between the nanoparticles and the nanotubes wall. Such conclusions could be made because the samples were washed in deionised water after the chemical reduction reactions and any loosely attached silver ammonia complex or nanoparticles would be removed. As such all the dissolved silver would be from the silver nanoparticles attached to the nanotubes. However the dissolved silver dissolved could be in both an ionic state and particulate state because titanium element was detected by EDS on the nanoparticles.

From all the results and discussion Method 2, involving exposure of samples to silver ammonia and then δ-gluconolactone, proved to provide the best coating with smaller sized clusters and less silver dissolution. From Method 2, aTiO₂-Ag10G5 had the most uniform coating with less clustering and less silver release from the coating and as such was considered to be the best coating.

In the human body, too much silver can cause severe toxicity. As such the ability to control the release of silver from an implant coating can provide the necessary antibacterial properties while being less toxic. In this study, the morphology and distribution of the silver nanoparticles and the release of silver from the coating were controlled in various ways. Also the chemistry behind the attachment of the nanoparticles to the nanotubes wall was investigated which provides the prospect for further research into Ag-NP containing composite coatings for implants using δ-gluconolactone as a reducing agent.

3.5 Conclusions

Silver nanoparticles forming clusters of dimensions as whole ranging from less than 100 nm to 5 μm was successfully synthesised in this study. The effect of the concentration of the silver source and the effect of the sequence of exposure to the silver source and the reducing agent used for the nanoparticle synthesis was analysed. Increasing the concentration of silver ammonia solution in the mixture of silver ammonia and δ -gluconolactone using Method 1, led to an increase in the size of the Ag-NPs clusters attached to aTiO_2 . Using Method 2, the increase in the duration of exposure of TNT to the silver ammonia solution led to a decrease in the size and increase in the quantity of the clusters. As such a better distribution of the nanoparticles and their clusters was provided when the nanotubes were exposed to the silver ammonia first and then the reducing agent, δ -gluconolactone. Method 2 also resulted in the release of less silver ions in the first 24 hours of exposure to SBF as compared to the release from the samples from Method 1. Nonetheless, there are more works to be done before this coating could be considered for application on implants. First, more data could be obtained during the 24 hours of exposure by measuring the silver dissolved in the SBF over various time intervals. And the exposure to SBF itself could be extended to more than 24 hours. The total amount of silver dissolved could be divided in a way to quantify the amount of silver particles dissolved as compared to silver ions. Such data would allow understanding the chemistry between the silver nanoparticles and the nanotubes better.

Chapter 4

General Materials and Methods

4.1 General materials and methods

In this study, two major types of composite coatings were synthesised. The first category was a silver nanoparticle-containing TiO₂ coating on Ti-6Al-4V with and without HA. The second category was nano zinc oxide-containing TiO₂ coating with and without HA. After the optimisation of the synthesis of the respective coatings, they were first tested for their stability using a dialysis experiment. Secondly, their antibacterial properties were tested against *S. aureus* using biochemical assays such as the Live/Dead assay, lactate production assay, and trace element analysis to determine composition. In addition to the latter, high resolution microscopy associated with surface X-Ray analysis was used to quantify the surface composition. Lastly their biocompatibility were tested in the presence of primary human osteoblast cells after which biochemical assays such as lactodehydrogenase (LDH), alkaline phosphatase (ALP), glutathione (GSH) and protein assays were utilised after which the electrolyte contents were analysed. At a molecular level, the expression of focal adhesion kinase (FAK), alkaline phosphatase (ALP), runt-related transcription factor 2 (RUNX-2), osteocalcin (OC), carbonic anhydrase 1 (CA1), cyclo-oxygenase 2 (COX-2), interleukin 6 (IL-6), tumour necrosis factor alpha (TNF- α), and superoxide dismutase (SOD) genes in the osteoblast cells exposed to the coated samples were compared to the uncoated TiO₂ discs. Focal adhesion kinase is a protein in cells which is associated with the cytoskeletal structure of the cells which helps in their adhesion and proliferation (Sista *et al.*, 2013). The gene RUNX-2 is the first transcription factor which determines the osteoblast lineage and as such a marker for differentiation (Komori, 2010). Osteocalcin is a calcium binding protein in the extracellular matrix (ECM) and its genes act as a differentiation marker (D'Alonzo *et al.*, 2002). Likewise ALP gene is a differentiation marker associated with the

synthesis of alkaline phosphatase (Pujari-Palmer *et al.*, 2016). Carbonic anhydrase 1 is a protein which promotes calcium salt formation and gives an indication whether the cells are ready to mineralise (Chang *et al.*, 2012). After confirming the adhesion, proliferation and differentiation ability of the cells, the inflammatory markers were investigated being COX-2 which is associated with pathological process in the human body (Crofford, 1997), IL-6 which inhibits differentiation (Kaneshiro *et al.*, 2014) and TNF α which inhibits differentiation and causes inflammatory reactions in the cells (Gilbert *et al.*, 2002). Last but not least, SOD is provides an antioxidant defence system in the cells (Niska *et al.*, 2015). As such the genetic analysis would provide an insight on the various processes mentioned at a molecular level.

At the end of the cells exposure, they were also visualised using SEM in association with energy-dispersive X-ray spectroscopy (EDS) analysis.

This chapter hence describes the core methodologies and those used in multiple chapters.

4.2 Synthesis of Ag-NP and nano-ZnO loaded TiO₂ nanotubes

4.2.1 Post anodisation annealing

TiO₂ nanotubes were initially grown on a polished and cleaned surface of the Ti alloy. Briefly, TiO₂ nanotubes of an internal diameter of 101.2 ± 2.8 nm (mean \pm S.E.M., n = 6) were grown on the surface of the Ti-6Al-4V alloy by anodisation. The electrochemical process was accomplished in 1 hour in 1M NH₄HPO₄ and 0.5 weight percent NH₄F maintained at pH 4 with an applied voltage of 20 V and an initial sweep rate of 0.5 V/s. The resulting coated discs with the freshly grown TiO₂ nanotubes was

then annealed at 350 °C for 2 hours in a furnace (Carbolite RWF 1200, Carbolite Engineering Services, Hope Valley, UK). Care was taken to provide an initial gradual increase in temperature, and gradual decrease back to room temperature during the annealing to ensure that the final crystalline phase of the nanotubes was anatase (Liu *et al.*, 2015). Afterwards, the TiO₂ tubes were functionalised with –OH groups by exposing them to 2M NaOH at 50 °C for 2 minutes (Parcharoen *et al.*, 2014). This provides a more reactive surface for other reactions to take place on the surface.

4.2.2 Addition of silver nanoparticles and nano zinc oxide

A chemical reduction method was used to fabricate silver nanoparticles on the surface of the TiO₂ nanotubes with the silver source being silver ammonia. Initially a pilot study was done whereby the nanoparticles were grown on the surface of the non-annealed nanotubes and the silver released from the surface after 24 hours in simulated body fluid (SBF) was measured. Chapter 3 gives more details about the synthesis, characterisation and silver release experiment. Afterwards, the nanoparticles were grown on the annealed TiO₂ nanotubes using the same chemical reduction process under different conditions, the details of which are described in chapter 5. The resulting samples after the optimisation study was known as TiO₂-Ag7. Afterwards nano-hydroxyapatite (HA) was sintered on the Ag-Np coated TiO₂ nanotubes resulting in a nanocomposite coating on the surface of the titanium alloy discs which was labelled as TiO₂-Ag7-HA.

A hydrothermal technique was used for the synthesis of nano zinc oxide structure on the annealed surface of TiO₂ nanotubes, the details of which are given in chapter 6. The final nanocomposite coating from the optimisation section was labelled as TiO₂-ZnO/350. Subsequently nano-HA was allowed to grow on the nano-ZnO coated TiO₂

nanotubes using a biomimetic method in the presence of concentrated simulated body fluid and the resulting samples was known as TiO₂-ZnO-HA/350.

After the synthesis of the composite coatings, TiO₂-ZnO/350 and TiO₂-ZnO-HA/350 and TiO₂-Ag7 and TiO₂-Ag7-HA (n=30 for each category), they were used for the dialysis experiment, antibacterial tests and biocompatibility tests.

4.3 Dialysis experiment and the release of dissolved metal

This experiment was conducted to aid the interpretation of the biological experiments with respect to the presence of dissolved zinc or silver toxicity, or not; but also to inform on the stability of the coatings in the simulated body fluid. The dialysis experiments were conducted according to Besinis *et al* (2013) in order to explore dissolved zinc or silver release, presumably derived from the nano-ZnO and Ag-Np part of the coatings, and also total Ca and P to reflect possible dissolution of the HA component (Besinis, De Peralta & Handy, 2014). The samples to be tested were the discs containing TiO₂ with Ag-NP, TiO₂ with Ag-NP and nano HA, TiO₂ with nano-ZnO and TiO₂ with nano-ZnO and nano HA. Discs containing TiO₂ nanotubes were used as controls for the coating. The SBF was prepared in deionised water using Kokubo's recipe whereby the concentration of the following ions were: Na⁺ 142, K⁺ 5.0, Mg²⁺ 1.5, Ca²⁺ 2.5, Cl⁻ 147.8, HCO₃⁻ 4.2, HPO₄²⁻ 1.0, SO₄²⁻ 0.5 mM (Kokubo, 1997). The amount of the various salts used were hence as follows for 1 litre of SBF being made: 7.996 g NaCl, 0.350 g NaHCO₃, 0.224 g KCl, 0.228 g K₂HPO₄.3H₂O, 0.305 g MgCl₂.6H₂O, 0.278 g CaCl₂, 0.071 g Na₂SO₄, 6.057 g (CH₂OH)₃CNH₂, 40 cm³ 1 kmol/m³ HCl and more 1 kmol/m³ HCl to further adjust the pH.

The pH was adjusted to 7.2 with a few drops of 1M HCl. Experiments were conducted in triplicate at room temperature in previously acid washed (5% nitric acid) and deionised glassware. Dialysis tubing (MW cut off, 12 000 Da, Sigma Aldrich, UK), was cut into 7 cm x 2.5 cm lengths pieces and sealed at one end using a mediclip, and then filled with one of Ti alloy discs as appropriate with 7 mL of SBF. Triplicates of dialysis bags with no titanium alloy in them were used as controls for the SBF. The dialysis bag was closed with another mediclip and the bag suspended in a 500 ml Pyrex beaker containing 243 mL of SBF. The beakers were gently stirred, and samples of 4 mL of SBF were collected at 0, 0.5, 1, 2, 3, 4, 6, 8, 24 hours. The samples were acidified with a drop of 70 % nitric acid and stored for metal analysis (see section 3.5). At the end of the 24 hours, the dialysis bags were carefully opened and 4 mL of the fluid therein collected for metal analysis. Dialysis curves were plotted from the initial elemental measurements for all 3 repeats (using all individual data points) using SigmaPlot 13.0 (Systat Software, Inc.), after deducting the background ionic concentrations of the SBF. A 1st order rectangular hyperbola function was used to fit dialysis curves to the raw data. The maximum initial slope of the curves informed on the maximum apparent dissolution rate of each substance.

4.4 Antibacterial test

The coated discs were exposed to *S. aureus* after which biochemical assays and microscopy were used to analyse the antibacterial properties of the coatings with respect to various controls. A summary of the whole antibacterial test is illustrated in Figure 4.1.

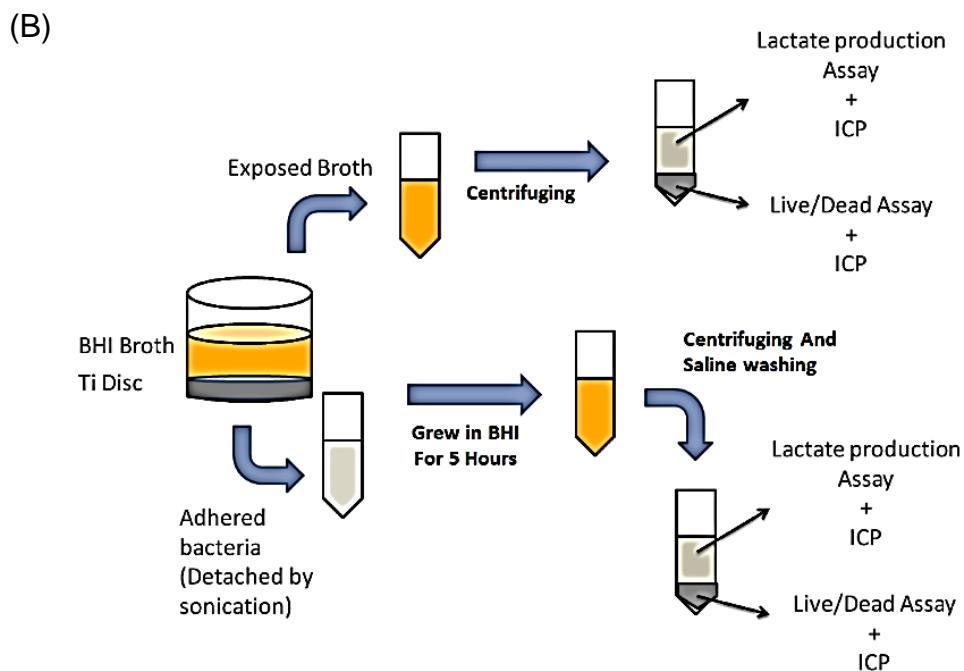
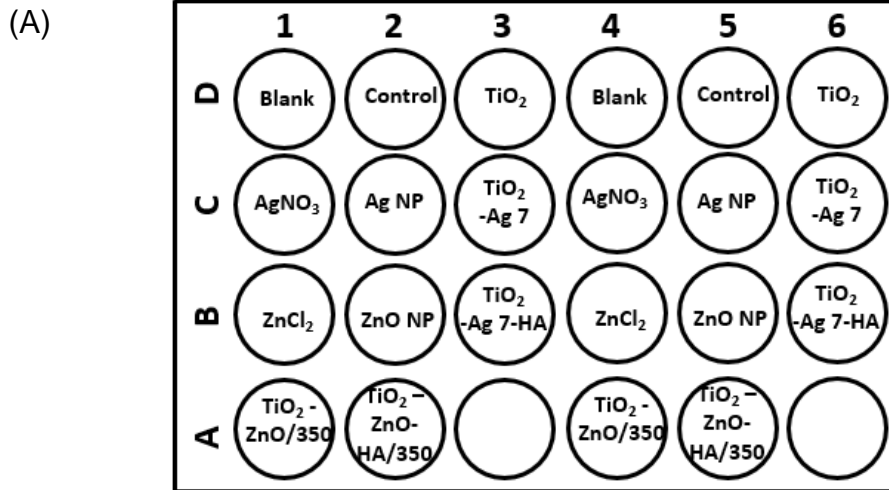


Figure 4.1 (A) Plate setup for the coated samples with the respective controls for biochemical assays and imaging (24-well plate) (B) Summary of biochemical assays performed for the antibacterial tests. The figure illustrates one well from the plate in (A) with the titanium alloy disc at the bottom covered with the BHI broth containing the *S. aureus*. Briefly after the overnight exposure, the exposed broth is centrifuged after which the supernatant is used for the lactate production assay and the pellets for Live/Dead assay. The bacteria which were attached to the disc were removed and allowed to grow in BHI broth for 5 hours. Then the resulting broth was centrifuged and the supernatant is used for the lactate production assay and the pellets for Live/Dead assay. All the supernatant and pellets were used for ICP as well.

4.4.1 Plate preparation and exposure to *S. aureus*

The experimental design involved exposing *S. aureus* to the coated samples TiO₂-ZnO/350 and TiO₂-ZnO-HA/350 and TiO₂-Ag7 and TiO₂-Ag7-HA in 24-well, flat-bottom sterile polystyrene plates (Thermo Fischer Scientific, Loughborough, UK). TiO₂ nanotubes-coated discs were used as a control for the coating, zinc chloride was used as a positive control for zinc ions and zinc oxide nanoparticles was used as a positive control for zinc oxide nanoparticle. *S. aureus* was allowed to grow on its own as a negative control. Nine repeats were used for each coated samples and the controls (n = 6 for biochemical assays and n = 3 for SEM). Following the approach by Besinis *et al* (2014), the materials were exposed to *S. aureus* for 24 hours and the proportion of live to dead cells and the amount of lactate produced were evaluated and the concentration of zinc, calcium and phosphorus ions released from the coating in the fluid were measured using inductively coupled plasma optical emission spectrometry (ICP-OES) (Besinis, De Peralta & Handy, 2014). *S. aureus* was chosen as it is considered to be one of the main causes of infection in orthopaedic and dental implants (Swank & Dragoo, 2013; Tsikandylakis, Berlin & Branemark, 2014). To start with, *S. aureus* was cultured in brain heart infusion (BHI) broth (Lab M Ltd, Bury, UK) at 37 °C. A bacterial suspension having optical density 0.018 at 595 nm absorbance (Spectrophotometer Genesys 20, Fisher Scientific, Loughborough, UK) was prepared in the BHI broth at a concentration of 1 × 10⁷ cells/mL. Two mL of the bacterial culture of *S. aureus* was pipetted in each well of the 24-well plate containing TiO₂, TiO₂-ZnO/350, TiO₂-ZnO-HA/350, TiO₂-Ag7, TiO₂-Ag7, ZnCl₂ (0.001M), ZnO nanoparticles (0.001M), AgNO₃ (0.001M) and Ag nanoparticles (0.001M) (n = 9 wells for each category distributed over a few plates). For the positive controls, 0.001M of chemicals was used as it was found that 0.001M was the maximum amount of trace

metal that could be released from the coatings. In addition, 2 mL of the same culture media with the bacteria were pipetted in 9 empty wells as well for the negative control and another 9 wells were filled with 2 mL of BHI broth on its own as the positive control. Each 24 well plates had only 2 repeats of the samples and controls as shown in Figure 4.1A so that the treatments were the only influence on the bacterial growth. Four plates were hence prepared with similar composition as Figure 4.1A and one more plate with just one set of samples and controls, thus resulting in 9 repeats for each sample and control. The resulting 5 plates were incubated at 37°C on a shaking table. At the end of the overnight exposure, for 6 repeats of the various categories (that is 3 plates), the broth from each well were pipetted out and the ratio of live to dead cells was analysed using a LIVE/DEAD® kit and the quantity of lactate in the latter was measured. The remaining broth was acidified with 70 % HNO₃ and used for metal analysis by ICP-OES.

Bacterial pellets were obtained using the same protocol as Besinis *et al.* (2013) whereby the samples from the wells were sonicated (12 MHz) for 60 s in 2 mL of sterile saline. The bacterial pellets obtained using this technique was considered to be the bacteria that were able to attach to the surface of the samples. As such, performing the biochemical assays on the latter would help characterise the attached bacteria. One mL of the resulting suspension were allowed to grow in 5 mL of BHI broth for 5 hours at 37°C on a shaking table with the aim of increasing the amount of live cells in order to reduce error for the Live/Dead assay (Besinis, De Peralta & Handy, 2014). The viability of the cells and the amount of lactate in the suspension was assessed followed by the measurement of the ionic content of the latter. For the remaining 3 repeats, the supernatant was removed and the samples were prepared for microscopic imaging the details of which are given in section 4.7.

4.4.2 Cell viability

The cell viability of *S. aureus* in both, the exposed broth and incubated adherent bacteria from the coated samples and controls were assessed using the L7012 LIVE/DEAD® Backlight™ Kit (Invitrogen Ltd, Paisley, UK). One hundred µL of the exposed broth and 100 µL the incubated adhered bacteria from each replicate for the different categories were transferred to a V-bottom 96-well microplates (Corning, UK). The microplates were centrifuged at 4000 rpm for 10 minutes in a 2040 Rotors microplate centrifuge (Centurion Scientific Ltd, Chichester, UK), after which the pellets in each well were washed with 1 mL of sterile NaCl saline and centrifuged at 4000 rpm for another 10 minutes. The final washed pellets were resuspended in 1 mL of saline out of which 100 µL were pipetted into another 96 well plate flat bottom microplate. Then, 100 µL of freshly mixed dyes from the LIVE/DEAD kit was added to those wells and mixed thoroughly. The microplate was then incubated in the dark at room temperature for 15 min after which the fluorescence of the wells were immediately measured on the Cytofluor II, fluorescence plate reader at an excitation wavelength of 485 nm and emission wavelength of 530 nm and 645 nm respectively. The readings at 530 nm were divided by the readings at 645 nm in order to obtain the percentage of live to dead cells in the exposed broth and the incubated cell suspension from the different samples and controls. The kit was calibrated against 0, 10, 20, 30, 40, 50, 60, 70, 80, 90 and 100 percentage of live to dead cells, the results of which are illustrated in Figure 4.2 A.

4.4.3 Lactate production

The metabolic activity of *S. aureus* was assessed by measuring the amount of lactate using the approach utilised by Besinis *et al* (2013). The presence of lactate would

suggest the presence of metabolically active bacterial cells. To start the test, the lactate assay reagent was prepared by pipetting 1 μL of 1000 units/ml lactate dehydrogenase (Sigma-Aldrich Ltd, UK) to wells in a flat bottom 96-well plate followed by 10 μL of 40 mM nicotinamide adenine dinucleotide (NAD) (Melford Laboratories Ltd, UK) and 200 μL of 0.4 M hydrazine prepared in a glycine buffer of pH 9. Then, 100 μL of the exposed broth and 100 μL of the incubated adherent cells from the samples and controls were transferred to a V-bottom 96-well microplate and were centrifuged at 2000 rpm for 10 minutes. Then 10 μL of the resulting supernatant was added to the 211 μL lactate assay reagent mixture in the flat bottom 96 well plate. The microplate was then placed in an incubator at 37°C for 2 hours in order to allow the reduction of NAD to happen if lactate was present. The absorbance was then read at 340 nm using the microplate reader with the aim of proving that lactate was present and this presence was quantified using the calibration data obtained from the triplicates of 10 μL lactic acid as standards (0, 0.25, 0.5, 1.0, 2.0, 4.0, 8.0 mM) reacting with the 211 μL of the lactate assay buffer illustrated in Figure 4.2 B.

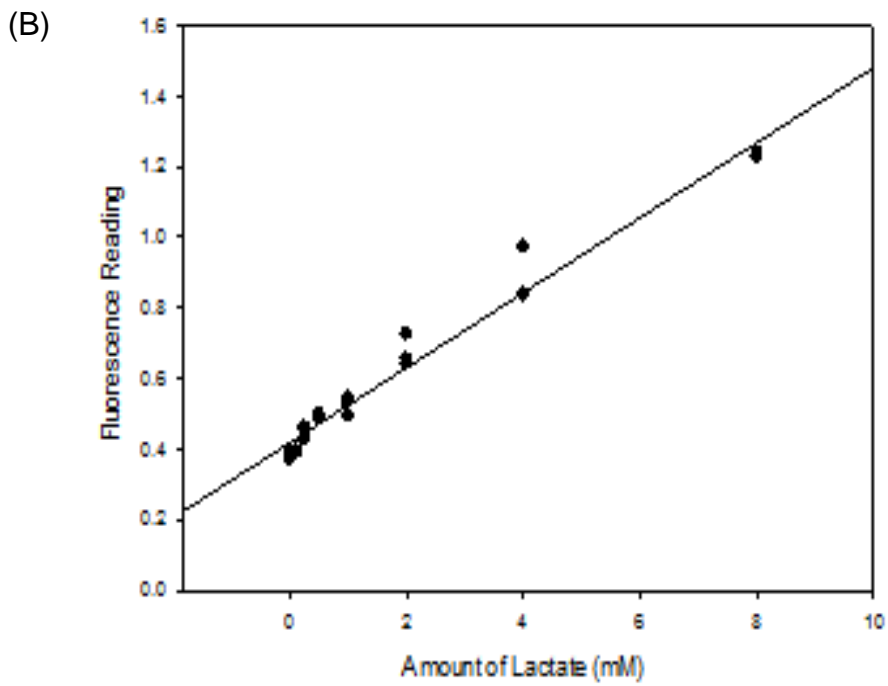
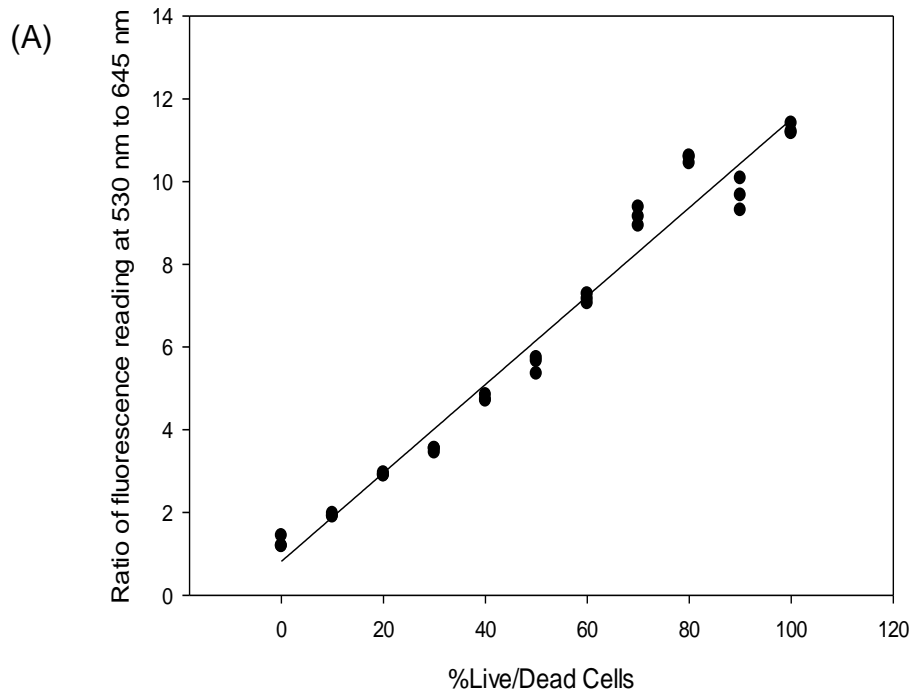


Figure 4.2: Example calibration curve for the (A) Live/Dead[®] Backlight[™] Kit following the protocol from Invitrogen and (B) Lactate production assay with respect to the standards used in the respective protocols.

4.5 Biocompatibility test

The nano silver and nano zinc oxide coated discs were exposed to primary human osteoblast cells after which, biochemical assays were performed on the media exposed and the cell homogenate and PCR was done on the extracted RNA from the attached cells. The results were then analysed with the aim of understanding the biocompatibility of the nanocomposite coatings. The cell culturing and biochemical assays were done using similar protocols to what was used by (Hadi, 2014).

4.5.1 Osteoblast cell culture

Primary human osteoblast cells (Hob) were obtained from ECACC (European Collection of Cell cultures). They were initially cultured at a density of 1×10^6 cells/cm² in 75 cm² flasks (Sterilin, Newport, UK) which contained 15 mL of DMEM (Dulbecco's Modified Eagle's medium) with L-glutamine, 10% foetal bovine serum (FBS), and 1% penicillin-streptomycin (100 IU Penicillin- 100 µg/ ml Streptomycin) (Fisher Scientific, Loughborough, UK). The media were changed every 3 days and the cells sub-cultured when confluence reached 80-85 %. For sub-culturing, the cells were washed twice with phosphate buffer saline, D-PBS, (Fischer scientific, without added calcium and magnesium), then trypsinized (2 ml of 0.1% trypsin and 1 mM EDTA) and resuspended in fresh media and counted with a haemocytometer. The cell viability was checked with trypan blue. All cells were kept at 37 °C in 5 % CO₂ and 95 % air. In this study passage 4, 5 and 6 were used on for the different replicates with the aim of reducing errors.

4.5.2 Plate preparation for osteoblast cells exposure to samples

A few 24-well plates were used for this part whereby, the sterile coated TiO₂ discs were placed in each well as per Figure 4.3.

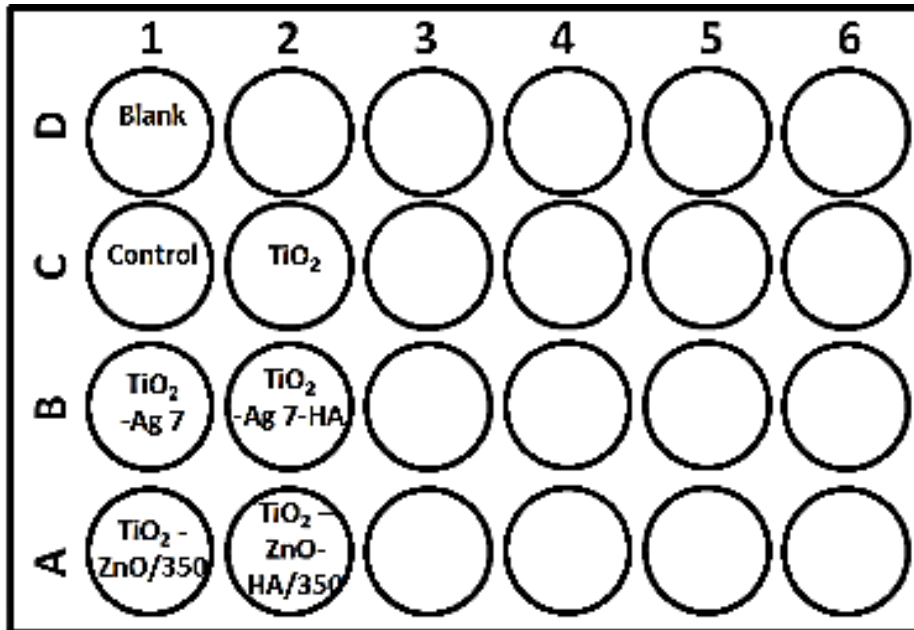


Figure 4.3: Plate preparation for samples exposure to primary osteoblast cells grown in DMEM media in triplicates exposed on different plates

	Replicate 1	Replicate 2	Replicate 3
Bioc hemi cal Assays	Plate 1 : 4 th Passage	Plate 4: 5 th Passage	Plate 7: 6 th Passage
PCR for RNA detection	Plate 2 : 4 th Passage	Plate 5: 5 th Passage	Plate 8: 6 th Passage
SEM analysis	Plate 3 : 4 th Passage	Plate 6: 5 th Passage	Plate 9: 6 th Passage

Figure 4.4: Different 24-well plates' setup for biocompatibility tests with each plate at a different passage number per replicate. Plate 1-3 was the first replicate with the 4th passage number being used for the biochemical assays, PCR and SEM analysis.

There were 3 replicates for each sample and control with each replicate being done in separate plates as shown in Figure 4.4. The cultured media were then pipetted in

the wells at a concentration of 35 000 cells per well and incubated at 37 °C for 10 days. The cultured media was changed at day 1, 4 and 7 after which the lactate dehydrogenase activity (LDH), alkaline phosphatase activity (ALP) and the trace elements and electrolytes concentration were measured using the protocols detailed in the following sections.

For another 3 repeats, the RNA were extracted from the cells in each well using the protocols from Qiagen with respect to the RNease Kit and RNase free DNase kit (Qiagen, Manchester, UK). Afterwards, reverse transcriptase PCR was performed on the extracted RNA using Quantinova SYBRGreen RT Kit and its protocol with respect to specific primers. The remaining 3 repeats were used for high resolution electron microscopy after the media was removed after day 10 and cells washed with sucrose buffer.

4.5.3 Biochemical Assays

The first part of the biocompatibility testing involved biochemical assays which brought forward an insight about the biochemical reactions that took place in the cells after exposure to the coated samples.

4.5.3.1 Homogenate and media collection

At day 4 and 10, the media in the wells was removed and the attached cells were washed twice with sucrose buffer (300 mmol/l sucrose, 0.1 mmol/l EDTA, 20 mmol/l HEPES buffered to 7.4 with few drops of Trizma base). Subsequently, 1 ml of lysis buffer (30 mmol/l sucrose, 0.1 mmol/l EDTA, 0.01 % of Triton-X, 20 mmol/l HEPES buffered to 7.4 with few drops of trizma base) was pipetted to the wells. The resulting cell homogenate were further diluted with milliQ water, with the aim of reducing the

effect of Triton-X on the enzyme activity after which they were sonicated for a few seconds. The cell homogenates were then used to measure cellular LDH activity, ALP activity, protein content using BCA, and metal analysis (n = 3 per treatment).

4.5.3.2 Protein assay on homogenate

The concentration of protein in the homogenate was measured using the Bicinchoninic acid (BCA) method (Pierce, Rockford, USA). Using the protocol from the BCA kit, 190 μ l of BCA reagent was added to a 96-well plate followed by 10 μ l of the cell homogenate from the respective wells from section 4.5.2. The resulting microplates were then incubated at 37 °C for 30 min. Using a series of bovine 97 serum albumin standards (1.25, 0.625, 0.312, 0.156 and 0 mg/l) obtained with the BCA kit, the assay was calibrated at a wavelength of 592 nm using a plate-reader (VersaMax Molecular Devices, Berkshire, UK) and presented in Figure 4.5 A and B for day 4 and day 10 respectively. Subsequently the absorbance of the incubated plate was read at the same absorbance.

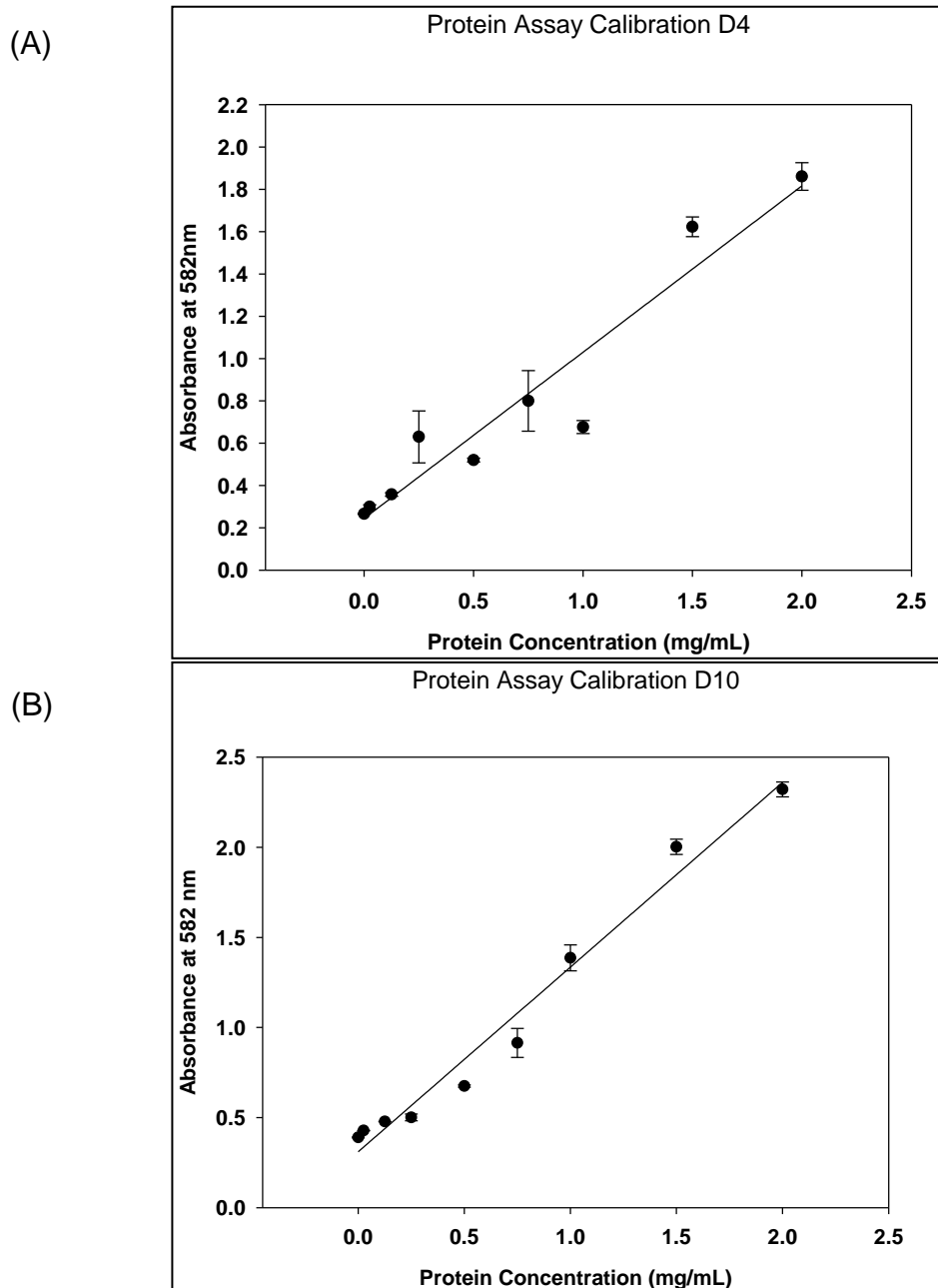


Figure 4.5: Example calibration data for protein assay on (A) day 4 and (B) day 10 with respect to the standards provided with the kit.

4.5.3.3 Lactate dehydrogenase assay on homogenate and media

Lactate dehydrogenase leak is known to be a biomarker for cell injury and has been widely used to quantify cell health or toxicity (Gitrowski, Al-Jubory & Handy, 2014).

In the present work LDH activity in the media and the homogenate was measured at

day 1, 4 and 10. To start the assay, 1 ml of a reaction mixture containing 0.6 mM of pyruvate in 50 mM phosphate buffer at pH 7, was added to a 1 ml cuvette, followed by 0.035 μ l of 0.6 mM of NADH after which 0.035 μ l of the test sample (cell culture media/ cell homogenate) was added at the end with rapid mixing using the pipette. The oxidation of NADH was read at a wavelength 340 nm using a Helios β Spectrophotometer (Thermo Fisher, Loughborough, UK) for 2 minutes. The resulting LDH activity (μ mol/min/ml) was calculated using an extinction coefficient of 6.3 mM for a path length of 1 cm. Finally, the intracellular LDH (From homogenate) was normalized with intracellular protein content (μ mol/min /mg protein).

4.5.3.4 Alkaline phosphatase assay on cell homogenate and media

Alkaline phosphatase is a known biochemical marker for osteoblast activity (Sabokbar *et al.*, 1994). In this study the activity of the ALP enzyme was measured in the external media and the cell homogenate, with the aim of analysing the effect of the composite coatings on osteoblast function. To start with, 0.665 of the reagent assay consisting of 0.265 ml of 0.1 M glycine buffer plus 0.330 ml of 0.5 mM p-Nitrophenylphosphatase (pNPP) in glycine buffer was pipetted to the well of a 96-well plate. Then 0.065 μ l of the sample (external media or cell homogenate) was added to the wells. The presence of pNitrophenol was measured using a spectrophotometer at a wavelength of 405 nm (Helios β Spectrophotometer, Fisher Scientific, Loughborough, UK). The final ALP activity of from each well was calculated using an extinction coefficient of 18.3 mM for a path length of 1 cm. The ALP activity present in the media was expressed as nmol/min/ml and for cell homogenate, the ALP activity was normalised with respect to the protein content and as such expressed as nmol/min/mg cell protein.

4.5.3.5 Glutathione assay on cell homogenate

Glutathione is an intracellular antioxidant and a good indicator of oxidative stress and associated reactions and as such is considered to be crucial in toxicity studies (Čapek *et al.*, 2017). In this study, the cell homogenates were first treated with dithionitrobenzoic acid (DTNB) by mixing them at a 1:1 ratio with buffered DTNB which consisted of 10 mM DTNB in 100 mM potassium phosphate at pH 7.5 with containing 5 mM EDTA. The resulting mixtures were transferred to a 96-well microplate in triplicates (40 μ L each well) to which 20 μ L of 2U/mL glutathione reductase (Sigma, Irvine, UK) was added followed by 260 μ L of the assay buffer consisting of 100 mM of potassium phosphate and 5mM EDTA at a pH of 7.5. After 1 min of equilibration the reaction was started by the addition of 20 μ l of 3.63 mM NADPH. The absorbance for the different wells were read at a wavelength of 412 nm using a microplate reader over 15 minutes. The total glutathione content per protein (μ mol g^{-1}) was determined using the calibration data obtained from standards of 0, 4, 8, 12, 16 and 20 mg/mL of GSH as shown in Figure 4.6 and 4.7.

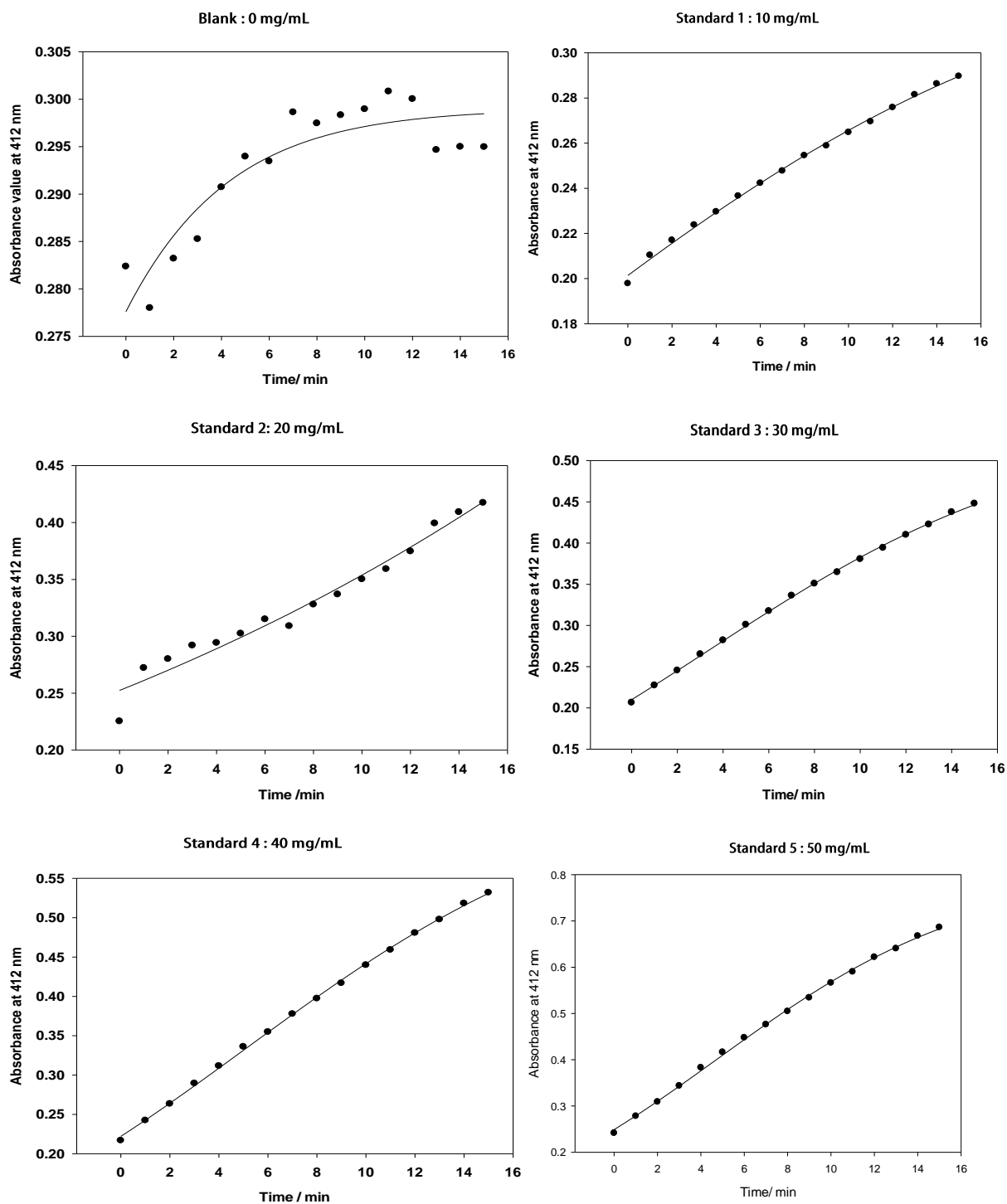


Figure 4.6: Absorbance readings for standards used in the calibration of the glutathione assay read at a wavelength of 412 nm. The concentration of glutathione standards used were (A) 0 mg/mL ($R^2=0.8999$), (B) 10 mg/mL ($R^2= 0.9978$), (C) 20 mg/mL ($R^2= 0.9652$), (D) 30 mg/mL ($R^2=0.9994$), (E) 40 mg/mL ($R^2 = 0.9993$) and (F) 50 mg/mL ($R^2= 0.9991$) and the data was made to fit a sigmoidal shape of 3 parameters using SigmaPlot with the R^2 value representing the line fit.

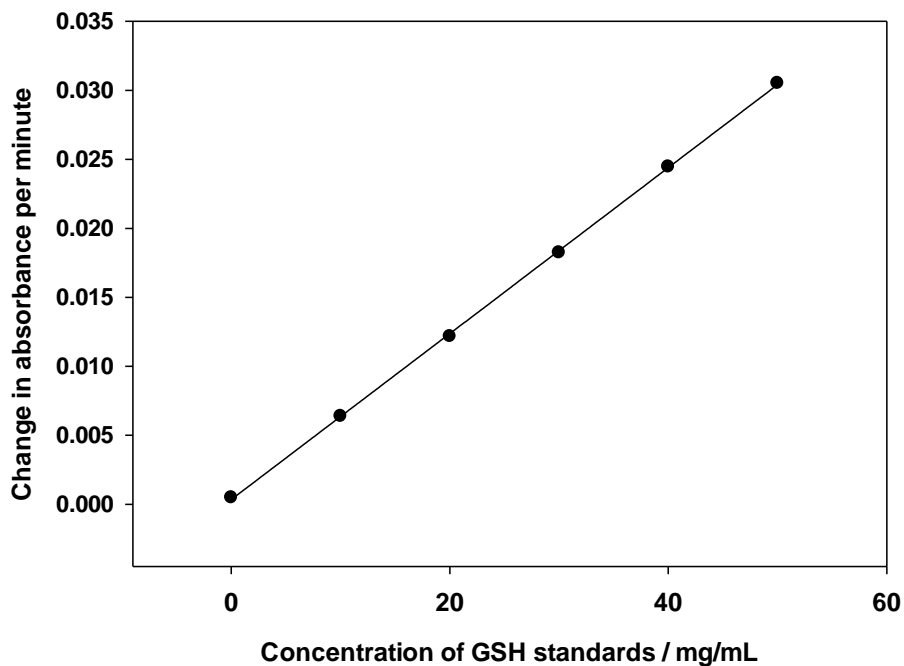


Figure 4.7 : Calibration data for GSH assay at 0-50 mg/mL GSH standards with absorbance read at 412 nm over 15 min ($R^2 = 0.9998$ for polynomial linear fit).

4.5.4 Relative gene expression using comparative Ct method

A molecular insight about the biocompatibility and toxicity of the composite coatings to osteoblast cells was provided by genetic analysis, reverse transcriptase polymerase chain reaction (RT-PCR) combined with comparative Ct. PCR was performed on day 4 and day 10 of exposure of the cells to the coated samples and controls.

4.5.4.1 RNA extraction using RNeasy Kit

Using Qiagen's RNeasy Kit and RNase free DNase protocols (Qiagen, Manchester, Uk), the RNA from the exposed cells were initially extracted. Briefly, the media was removed from the wells and the cells were lysed using 350 μ L of the lysis buffer

provided by the kit. After 1 min of homogenisation of the lysate by vortexing, 70% of ethanol was added to the latter followed by mixing. Afterwards, 700 μ L of the resulting mixture was transferred to the RNeasy spin columns which were centrifuged at 10 000 rpm for 15 s after which the liquid was discarded. This step was repeated with Buffer RW1 supplied with the kit with the aim of washing the columns. Using RNase free DNase kit, DNase was digested if present by the addition of 80 μ L DNase 1 incubation mix to the spin column followed by an incubation period of 15 min at 25 °C. The spin columns were then centrifuged at 10 000 rpm for 15 s after which the flow through was discarded. The columns were washed with Buffer RPE through centrifuging twice (First time for 15 s and second time for 2 min). To complete the extraction, 40 μ L of RNase free water was added to the spin column membrane after which they were centrifuged at 10 000 rpm for 1 min with the aim of eluting the RNA from the membrane. Using Nanodrop 2000 (Thermo Fisher, Loughborough, UK), the concentration of RNA was finally measured for each repeat of exposed cells to the samples and controls.

4.5.4.2 Block preparation using QuantiNova SYBR Green RT Kit

In this study the PCR was performed on a 384-well block and as such the quantities of the various components used was tailored to the latter. Using the Quantinova SYBR Green RT Kit, an initial reaction mixture containing 5 μ L of 2 \times QuantiNova SYBR Green RT-PCR Master Mix, 0.05 μ L of QN Rox Reference Dye, 0.1 μ L QN SYBR Green RT-Mix and 3.85 μ L of RNase free water were prepared for each well in the 384-well block. Subsequently, 0.5 μ L of the diluted forward primer (diluted $\times 10$) and 0.5 μ L of the diluted reverse primer (diluted $\times 10$) of the target genes and control genes were then placed in the wells in duplicates for each RNA sample. To finalise

the block preparation for PCR, 10 ng of the extracted RNA from each samples were pipetted into the wells in the PCR block. Figure 4.8 shows the final plate preparation with a clearer distribution of the PCR primers and sample RNA with the reagents for 1 day and 1 replicate. A second plate of similar preparation was done for the same day.

		Control			TiO ₂			TiO ₂ -Ag7			TiO ₂ -Ag7- HA			TiO ₂ -ZnO			TiO ₂ -ZnO- HA			Media			Water		
		1	2	3	4	5	6	7	8	9	10	11	12	13	14	15	16	17	18	19	20	21	22	23	24
B-Actin	A																								
GAPDH	B																								
FAK	C																								
ALP	D																								
RUNX2	E																								
OC	F																								
CA 1	G																								
COX 2	H																								
IL-6	I																								
TNF - α	J																								
SOD	K																								
	L																								
	M																								
	N																								
	O																								
	P																								

Figure 4.8: A sample 384-well block preparation for PCR with the 3 replicates per samples included. One more similar plates was prepared and used as a technical replicate for the experiment.

The target and control RNA used are listed in Table 4.1.

Table 4.1: Primers used for PCR in this study

Gene	Primer	Reference
B-Actin (Internal Control)	F: CCAAGGCCAACCGCGAGAAGATG R: GTCCCGGCCAGCCAGGTCCAGA	(Cheng <i>et al.</i> , 2015)
GADPH (Internal Control)	F: GCTCTCCAGAACATCATCC R: TGCTTCACCACCTTCTTG	(Lotz <i>et al.</i> , 2016)
FAK	F: GGTGCAATGGAGCGAGTATT R: GCCAGTGAACCTCCTCTGA	(Dasari <i>et al.</i> , 2010)
ALP	F: GACAATCGGAATGAGCCCACAC R: GTACTTATCCCGCGCCTTCACCAC	(Cheng <i>et al.</i> , 2015)
OC	F: AGCCCAGCGGTGCAGAGTCCA R: GCCGTAGAAGCGCCGATAGG	(Cheng <i>et al.</i> , 2015)
RUNX2	F: TGCGGCCGCCACGACAA R: ACCCGCCATGACAGTAACCACAGT	(Cheng <i>et al.</i> , 2015)
CA 1	F: AAATGAGCATGGTTCAGAACATACA R: ACTTTGCAGAATTCCAGTGAGCTA	(Tarun, 2003)
TNT-α	F: 5-AGCCCCCAGTCTGTATCCTT-3 R 5- CTCCCTTTGCAGAACTCAGG-3	(Neacsu <i>et al.</i> , 2014)
IL 6	F; 5-AGTTGCCTTCTTGGGACTGA-3 R: 5-TCCACGATTTCCAGAGAAC-3	(Neacsu <i>et al.</i> , 2014; Tsaryk <i>et al.</i> , 2013)
COX 2	F: 5-TGCATTCTTTGCCAGCACT-3 R: 5-AAAGGCGCAGTTTACGCTGT-3	(Tsaryk <i>et al.</i> , 2013)
SOD 2-16	F:5 '-CCAGCAGGCAGCTGGCACCG-3' R:5'-TCCAGGGCGCCGTAGTCGTAGG-3'	(Chistyakov <i>et al.</i> , 2001)

4.5.4.3 Comparative Ct for quantitative PCR

After the plate preparation, they were immediately placed in a Quantstudio 12K Flex Real-Time PCR system (ThermoFisher Scientific, Loughborough, UK). After assigning the different wells in the different blocks their name and content, Comparative Ct was selected as the computational procedure to be performed. At the end of the experiment Ct data was collected which were used according to

Schmittgen and Livak's protocol (2008) with the aim of calculating the final relative gene expression (Schmittgen & Livak, 2008). The calculations for the fold change in change expression was as follows:

$$dCt = Ct (\text{target gene}) - Ct (\text{internal control})$$

$$\text{Fold change, } ddCt = dCt (\text{coated sample}) - dCt (\text{uncoated sample})$$

Fold change was related to ddCt so that the downregulation and upregulation of gene expression was comparable on one chart.

4.6 Change in ionic concentration of media after

Measurements of the relevant trace metals in the media and cells during the experiments is an important aspect to confirm the exposure to the materials. In addition, trace metals can cause disturbances to ionic regulation, and thus measuring the electrolytes in the cells can inform on this mode of toxicity as well as the general health of the cells. Consequently, trace metals and electrolytes in samples of cells and media from the exposure to TiO₂, TiO₂-ZnO/350, TiO₂-ZnO-HA/350, TiO₂-Ag7 and TiO₂-Ag7-HA to bacterial and human cells were determined. The measurements of zinc and calcium in the media also informed on metal leaching from the coatings and the stability of the latter. An increase in the concentration of zinc in the exposed media/broth would suggest leakage from the coating while a change in calcium and phosphorus would give an indication of the stability of the HA part of the coating. Sodium and potassium measurements provide an insight into the cells physiology and would give an indication about the health of the osteoblast cells (Francis *et al.*, 2002). Hence ICP-OES was used to measure trace metals such as Ag and Zn while ICP-MS was used to measure Ca, P, Na and K.

To start with, standards for the different ions were prepared in triplicates at 0, 10, 20, 40, 100 ppm for Ca, P, Na and K and 0, 10, 20, 40, 100 ppb for Zn and Ag which were prepared using the certified reference material (CRM) obtained from Sigma Aldrich, Irvine, UK in 5 % HNO₃. The instrument was then calibrated with the standards before any readings were taken. Thenceforth the acidified samples were run through the instrument with 3 set of measurements being made per sample being read. After every 10 readings, the instruments were blanked and calibrated again to correct any instrument drift and prevent any side-effect of the nanomaterial, if any undissolved, on the instrument. After the readings were obtained the detection limits for each element was calculated as follows:

$$\text{Detection limit} = \frac{C1 - C0}{I1 - I0} (3 \sigma) \quad , \text{ where}$$

$C1$ = concentration of the high sample

$C0$ = concentration of the blank

$I1$ = raw intensity of the high sample (cps)

$I0$ = raw intensity of the blank (cps)

3 is a confidence factor

σ (sigma) = standard deviation obtained from the readings from blank.

Subsequently, any value obtained below the detection limit was considered to be too low to be taken into consideration.

4.7 Imaging coated samples using SEM

The triplicates of TiO₂, TiO₂-ZnO/350, TiO₂-ZnO-HA/350, TiO₂-Ag7 and TiO₂-Ag7-HA and the controls were imaged using high resolution SEM after the exposure to bacterial culture or osteoblast cells media with the aim of providing visual

confirmation of the attached cells/bacteria. After the exposure, the broth/media from the 24-well plate was removed after which the samples were washed with sterile saline (0.85% NaCl) twice in the case of bacterial exposure and sucrose buffer in the case of osteoblasts exposure. Then 2 mL of 3% glutaraldehyde in 0.1 M cacodylate buffer was added to each well and was allowed to stay overnight at 4 °C. The next day, the glutaraldehyde was removed and the samples were washed with 0.1 M cacodylate buffer. An increasing concentration of ethanol (30%, 50%, 70%, 90% and 100%) was added to the wells containing the samples and controls with the aim of dehydrating *S. aureus* attached to the samples and controls. The samples were then coated with carbon for viewing under JEOL7001F SEM. Once in the microscope vacuum chamber, each sample was viewed at 3 different locations and photos were taken and saved in tiff format. Out of the 3 locations in the 3 repeats per sample, the common denominator in all of them was selected to be compared to the others. Comparable low and high magnification was used for all of them so that the coverage of the surface with the cells/bacteria could be visually compared.

4.8 Statistical Analysis

The collected data from the biochemical assays were analysed using Statgraphics Centurion XVII (StatPoint Technologies, Inc.) and SigmaPlot 13.0. The analysis done was similar to the one used in section 2.3.6. The normally distributed data with equal variances (Levene's Test) were analysed using One-way ANOVA with Fisher's LSD test post-hoc. In the case of unequal variances, the data was transformed first and then analysed using One-way ANOVA. When there was non-normality in the distribution of data, then the Kruskal-Wallis test was used. At the end of the analysis, the data were presented as mean \pm S.E.M and the analysis was done at a 95.0 %

confidence level. At the end of the analysis, the data were presented as mean \pm S.E.M and the analysis was done at a 95.0 % confidence level. Alphabets were the used to denote the various statistical difference between the samples and controls being analysed.

Chapter 5

TiO₂ nanotubes embedded with silver nanoparticles on Ti-6Al-4V alloy and their respective antibacterial properties and biocompatibility

5.1 Introduction

Silver nanoparticles are known to be toxic to mammals through the dissolution of silver ions and the oxidative stress caused by silver nanoparticle. Loosely attached silver nanoparticles of TiO₂ nanotubes are known to act as an antibacterial coating for implants. The dissolved silver is of no good as they are washed away. As such, there is a need for stronger attachment of the nanoparticles to implants. Integrating the latter into composites is one solution which can provide the long term antibacterial properties. Even though the right composite coating is obtained, maintaining the balance between the antibacterial properties and toxicity level for silver containing composite coatings for implants is the issue at the moment. The addition of hydroxyapatite on the silver nanoparticles coated TiO₂ could have an impact on the biocompatibility of the coating. At the same time, the HA might prevent the release of Ag ions and/or prevent direct contact of the biocidal component with any infection. Ideally, a HA coating with some porosity or tiny gaps is one possible solution. In Chapter 3, clustering of silver nanoparticles was observed on the surface of the amorphous nanotubes. The latter coating resulted in massive release of silver when exposed to SBF within 24 hours. Hence the aim of this chapter was to grow individual silver nanoparticles on the surface of TiO₂ nanotubes with a uniform distribution. Assuming that the clustering of the nanoparticles resulted in the huge release of silver ions, this chapter aims at obtaining a more stable composite coating with the uniformly distributed individual nanoparticles. Once the stability of the coating is obtained and the silver release is controlled, the biocompatibility of the coatings will have to be confirmed in the presence of human osteoblast cells.

5.2 Materials and Methods

In this Chapter, the nanotubes have been annealed at 350 °C for 2 hours and then exposed to 2M NaOH for 2 min as explained in Section 4.2.1, following which silver nanoparticles were grown on the latter.

5.2.1 Silver nanoparticles composite coating synthesis

For the synthesis of silver nanoparticles on the treated TiO₂ nanotubes, 0.05M of silver ammonia solution was prepared in ultrapure water and the pH was adjusted to 12 with 1 M NaOH. Then 0.002 M of δ -gluconolactone (Sigma Aldrich, Irvine, UK) was prepared in 0.0012M of aqueous NaOH as described in Chapter 3. The Ti-6Al-4V disc with the treated nanotubes, was immersed in silver ammonia first. This was expected to allow the silver ammonia to attach to the –OH part of the nanotubes (Escada *et al.*, 2012; Hussain *et al.*, 2011). After this exposure, the samples were ultrasonicated in deionised water at 12 MHz for 5 minutes to remove any loosely attached silver ammonia; after which the disks were air dried at room temperature. The sample was then exposed to the δ -gluconolactone solution for 5 minutes. Depending on the exposure time to silver ammonia, the samples were identified as TiO₂-Ag3, TiO₂-Ag7 and TiO₂-Ag10 for an exposure of 3, 7 and 10 minutes in silver ammonia respectively, and all treated for 5 minutes in δ -gluconolactone solution (n = 3 each). Δ -gluconolactone was expected to reduce the silver ammonia to silver nanoparticle which form attached on the surface of the TiO₂ nanotubes (as seen in Chapter 3). The samples were again ultrasonicated at 12 MHz in 10 mL of deionised water for 5 minutes with the aim of removing the loosely attached silver nanoparticles. This step ensured the presence of only strongly attached

nanoparticles to the nanotubes coating. Subsequently the surface of TiO₂, TiO₂-Ag₃, TiO₂-Ag₇ and TiO₂-Ag₁₀ were characterised in terms of morphology and the distribution of the nanoparticles on the nanotubes coating as described in section 2.3.3. SEM was used to aid the analysis of the surface coating as detailed out in Section 4.7 along with EDS analysis. Once the different silver nanoparticle coatings were synthesised, the morphology and distribution of the latter were analysed and compared in order to obtain the optimum coating for this Chapter. Once the optimum silver nanoparticle coating was selected, nano-HA was added the latter.

5.2.2 Addition of hydroxyapatite

After the optimisation of the synthesis of silver nanoparticles composite coated Ti alloy discs, hydroxyapatite was added to the latter coating by the sintering method described by Hadi (2014) (Hadi, 2014). Briefly, the selected Ag-Np coated discs were placed in 24-well plates after which, 70 % ethanol was added to the latter for sterilisation (n = 27, n = discs). Afterwards, 20 µL of 10 wt% nano-hydroxyapatite solution (Sigma Aldrich, UK) was evenly pipetted on top of the discs after which they were left to dry at room temperature for 48 hours. Subsequently, the discs were placed in a porcelain dish and put in the furnace (Carbolite, Hope, UK) with the setting of gradual increase of 10 °C per min to 500 °C. The final temperature was maintained for 10 minutes after which the temperature was gradually reduced to room temperature. The 500 °C temperature was chosen as it was high enough to cause sintering while being below the melting point of silver. The change in temperature was gradual with the aim of maintaining the crystallinity of the nano HA. The resulting discs were finally labelled as TiO₂-Ag_x-HA.

Finally a dialysis experiment was performed as per Section 4.3 to analyse the stability of the coating in details.

5.2.3 Antibacterial test of the silver composite coating

The antibacterial properties of the Ag-Np composite coating with and without HA was then exposed to *S. aureus* at 37 °C in BHI broth as explained in Section 4.4.1 with various positive and negative controls (n=15 per treatment). Different biochemical assays were performed in order to confirm the bactericidal properties of the coated alloy against the bacteria. First, a Live/Dead assay was used to test for the viability of the bacteria as described in Section 4.4.2 (n=6 per treatment). Subsequently, the concentration of lactate produced by the bacteria attached to the surface of the coating and the bacteria exposed to the coated discs was tested using a lactate production assay as described in Section 4.4.3 (n=6 per treatment). The concentration of silver ions released from the coating in the exposed bacteria and the attached bacteria were then measured using ICP-MS using the methods explained in Section 4.6. Afterwards, the discs were viewed under high resolution microscope as explained in Section 4.7 whereby the presence of bacteria that were attached to the coatings were visually confirmed.

5.2.4 Biocompatibility test of the AgNp composite coating

Once the antibacterial properties of the composite coatings were analysed, the coated discs were exposed to primary human osteoblast cells in DMEM media at 37 °C for 10 days , with the aim of testing the biocompatibility properties of the latter coatings as per Section 4.5.1 (n=12 per treatment). In this context, biochemical assays and genetic analysis were performed. In terms of biochemical assays

(Section 4.5.3), protein assays, ALP assay and LDH assay were performed to test the viability and metabolic activity of the osteoblast cells exposed to the coatings and controls (n=3 per treatment). For the genetic analysis, comparative Ct was used to analyse the genetic expression of FAK, RUNX2, CA1, ALP, OC, COX2, IL6, TNF α and SOD in osteoblast cells exposed to the coatings with respect to β -actin which was measured against the latter expression in the control (TiO₂ Nts) (n=6 per treatments). The details of the experiment are explained in Section 4.5.4. The change in ionic concentration of Ag, Na, Ca, P, K and Mg was measured in the cell homogenate and exposed media, using ICP on day 1, 4, 7 and 10 of exposure of the coatings to the cells (Section 4.6). Last the attached cells to the coated and uncoated discs were viewed under high resolution microscope as per Section 4.7.

5.3 Results

5.3.1 Imaging and analysis of Ag-Np containing nanocomposite coating

The high resolution microscopic images of the coated discs TiO₂, TiO₂-Ag3, TiO₂-Ag7 and TiO₂-Ag10 were analysed and presented through Figures 5.1, 5.2 and 5.3 with their associated EDS analysis.

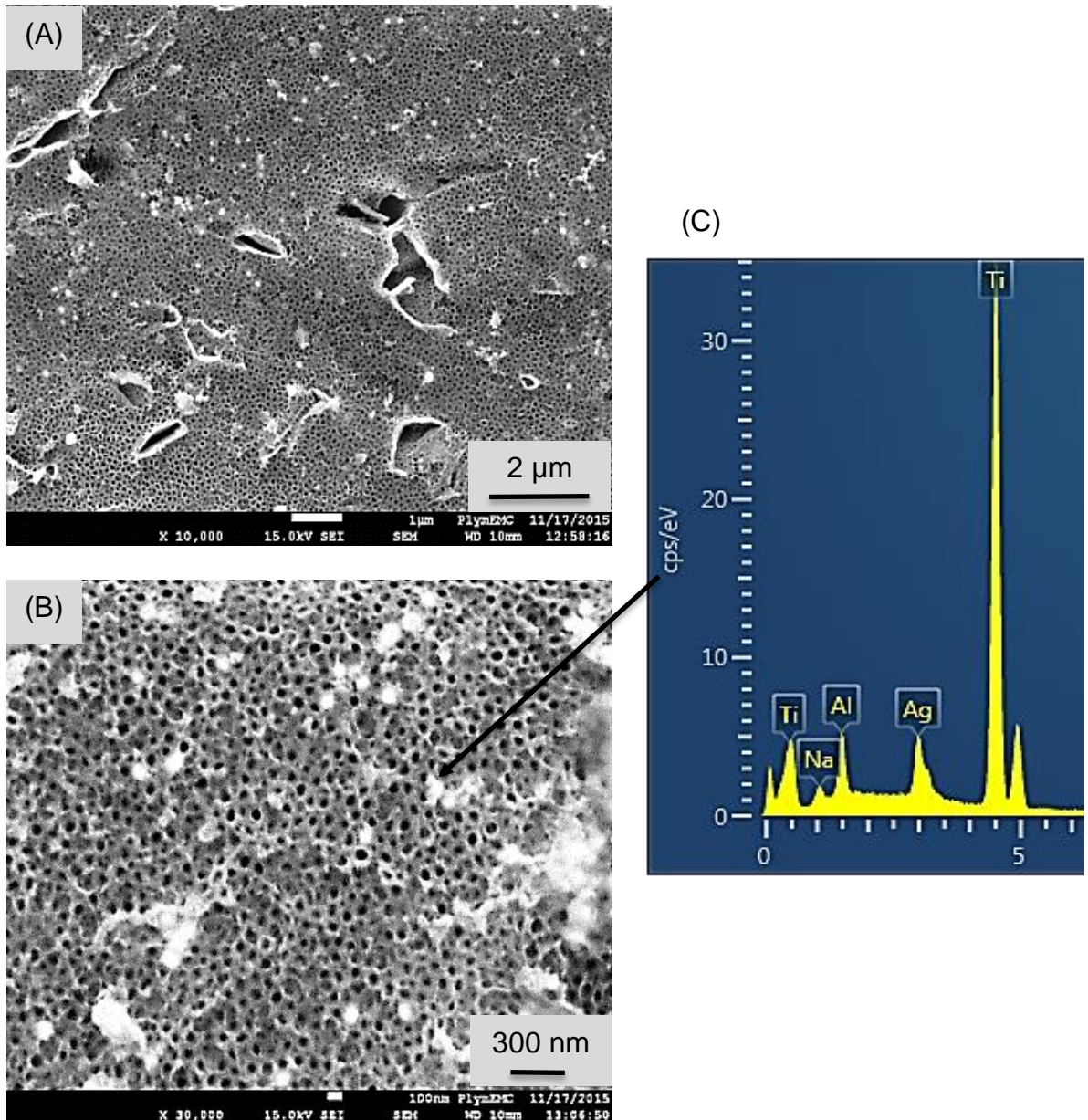


Figure 5.1: SEM images of Ti-6Al-4V discs coated with TiO₂-Ag₃ at (A) ×10 000 and (B) ×30000 magnification. The spherical white structures in 5.1 B are considered to be the silver nanoparticles, the EDS analysis of which is shown in (C).

From Figure 5.1, it was observed that there was less or no clustering of silver nanoparticles on the TiO₂ after the reduction of silver ammonia on the latter surface. When 3 minutes incubation time was used (TiO₂-Ag₃), the surface had less spherical nanoparticles on the surface as seen in Figure 5.1 B and F with the average diameters shown in Table 5.1 (Mean ± S.E.M, n= 3; Table 5.1).

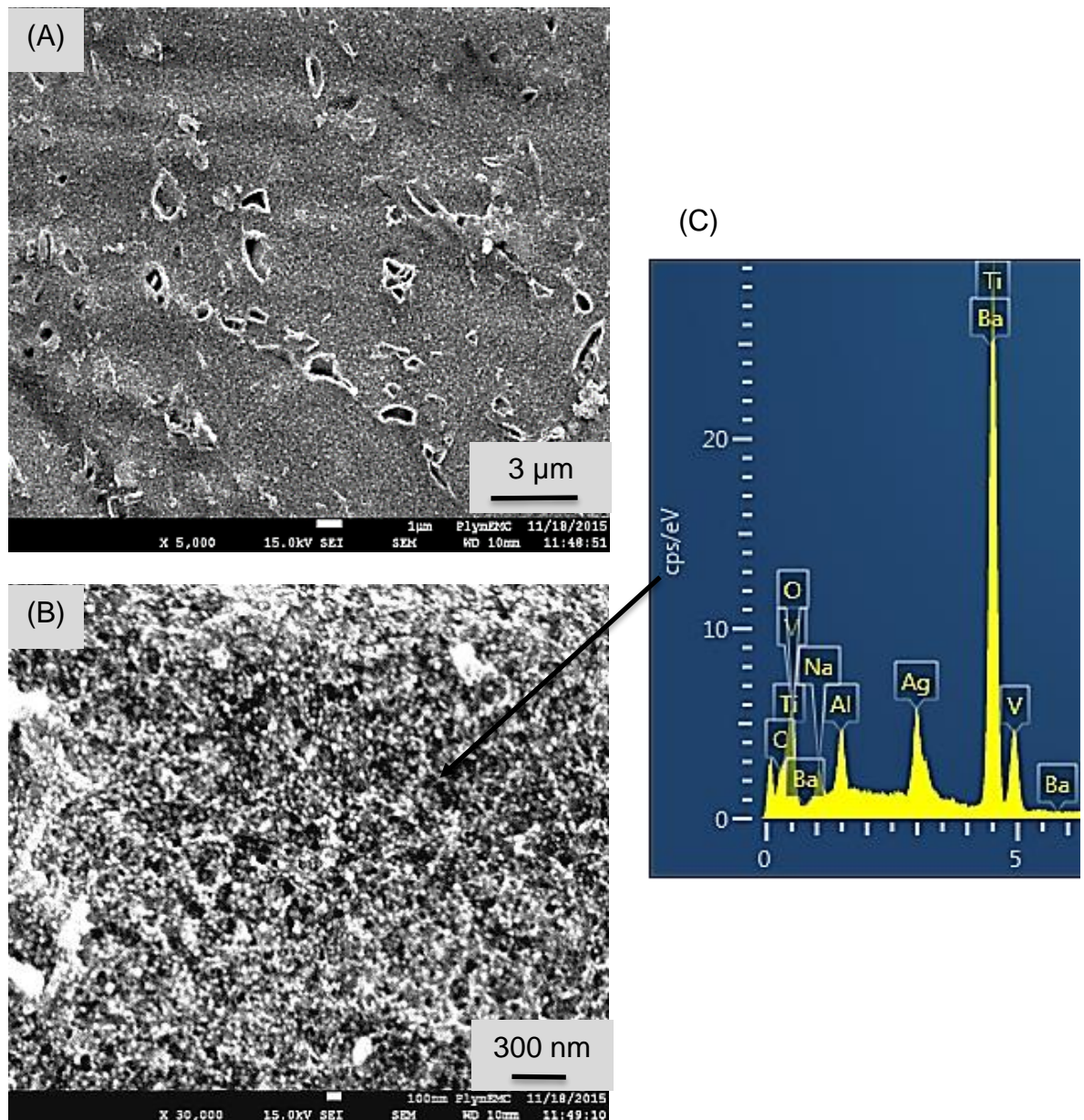


Figure 5.2: SEM images of Ti-6Al-4V discs coated with TiO₂-Ag7 at (A) ×5 000 and (B) ×30000 magnification. The spherical white structures in 5.2 B are considered to be the silver nanoparticles, the EDS analysis of which is shown in (C).

The samples exposed to an incubation time of 7 min (TiO₂-Ag7) had more uniformly distributed nanoparticles with significantly smaller diameters (One-way ANOVA , $p < 0.05$) than those on TiO₂-Ag3. In both TiO₂-Ag3 and TiO₂-Ag7, the nanotubular characteristic of the TiO₂ was still visible after the growth silver nanoparticles.

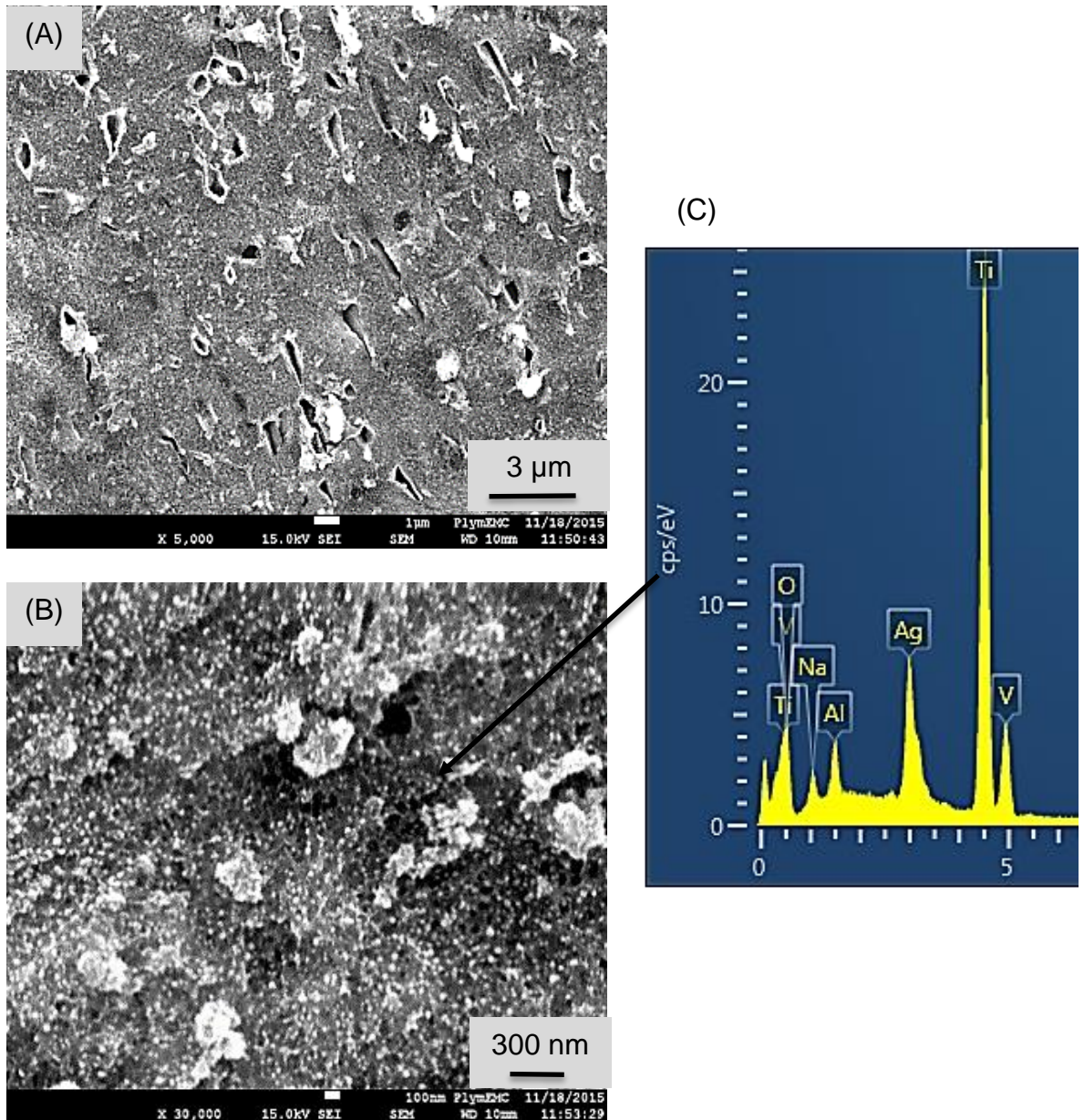


Figure 5.3: SEM images of Ti-6Al-4V discs coated with TiO₂-Ag10 at (A) ×5 000 and (B) ×30000 magnification. The spherical white structures in 5.3 B are considered to be the silver nanoparticles, the EDS analysis of which is shown in (C).

In TiO₂-Ag10, the nanoparticles grown covered the whole surface of TiO₂ with some clustering observed (Figure 5.3 A and B).

Table 5.1: Diameter of silver nanoparticles grown on TiO₂ shown as mean \pm S.E.M, n=3 with the alphabets indicating the statistical difference between the samples using One-way ANOVA at a confidence interval of 95 %.

Samples	Incubation time in silver ammonia / minutes	Silver nanoparticle diameter / nm
TiO₂-Ag3	3	88.25 \pm 5.1 ^a
TiO₂-Ag7	7	47.5 \pm 1.7 ^b
TiO₂-Ag10	10	30 \pm 2.4 ^c

The EDS analysis of the white spherical nanoparticles on the discs confirmed the presence of silver with the weight percentage of the latter over the coating increasing from TiO₂-Ag3 to TiO₂-Ag10 (5-8 wt%) to the contrary of Ti, Al and O which were found to be decreasing.

The increase in the number of nanoparticles was associated with the duration of exposure to silver ammonia. With increasing time of exposure to the latter, it was assumed that the amount of silver ammonia being able to attach to the surface increased, hence accounting for the increase in the amount of nanoparticles on TiO₂. With increasing incubation time in silver ammonia, the size the particles was observed to be decreasing with the number of the nanoparticles increasing. The concentration of the reducing agent, δ -gluconolactone, used was maintained at 0.002 M. Nonetheless, in the case of TiO₂-Ag3, due to less silver ammonia being able to attach, the concentration of the reducing agent exposed to individual silver ammonia

attached on TiO₂ was more as compared to TiO₂-Ag10. EDS analysis provides an overview of the elements present at the specific location pointed as shown in part C of Figures 5.1, 5.2 and 5.3. For a coating to provide the required properties, it has to be uniformly distributed so that the whole implant has the same property. Out of the three coatings fabricated, TiO₂-Ag7 provided the most uniform coating with almost no clustering of and full surface coverage of the nanoparticles. In the latter coating, the nanotubular structure of the nanotubes provided the platform for tissue engineering. Thus moving forwards in this chapter, TiO₂-Ag7 would be used for further analysis.

5.3.1.1 Imaging of coating after addition of nano HA

The nanocomposite coatings were viewed under the high resolution scanning electron microscope as used in Chapter 2 and 3, with the aim of demonstrating the surface morphology and coverage of the coatings (n=3 each). The imaging of the TiO₂-Ag7 with the HA coating is shown in Figure 5.2 B and D, where a full surface coverage was observed. However, micro-cracks were present on the latter coating.

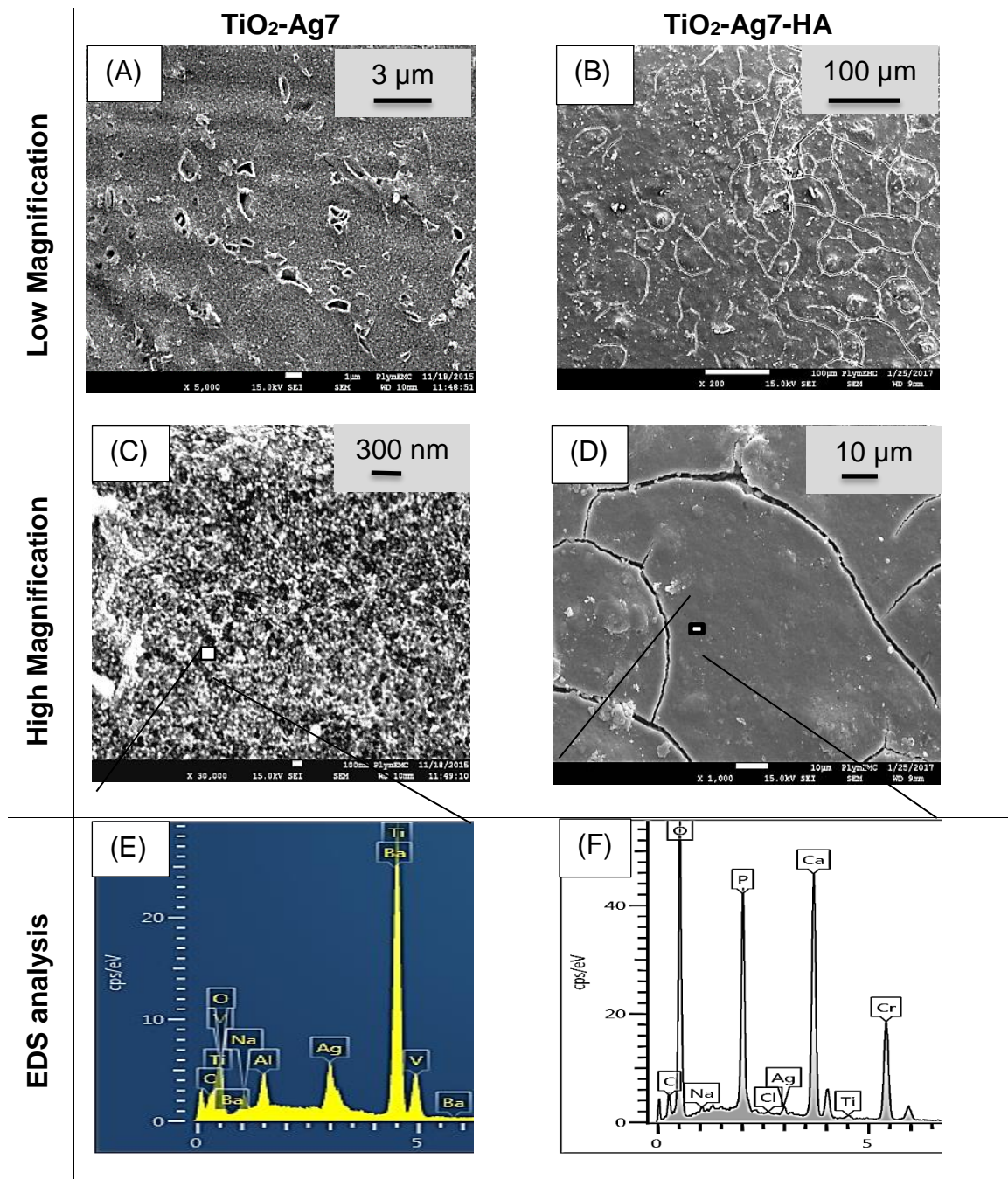


Figure 5.4: SEM images of (A) TiO₂-Ag7 (×5000) and (B) TiO₂-Ag7-HA (×200) at low magnifications and their magnified versions in (C, ×30 000) and (D, ×1000) respectively (n=3). (E) and (F) represents the EDS analysis of TiO₂-Ag7 and TiO₂-Ag7-HA respectively.

The EDS analysis shown in Figure 5.4 F confirms the presence of Ca and P as part of the hydroxyapatite. Nonetheless, the amount of silver detected on the HA surface was less as compared to TiO₂-Ag7 (Less than 5 wt %).

5.3.2 Dialysis Experiment

From the dialysis experiment, the release of silver, calcium and phosphorus ions from the nanocomposite coatings to the SBF in the beaker followed a rectangular hyperbola consistent with diffusion from the particle into a fixed volume of media as seen in Figure 5.5.

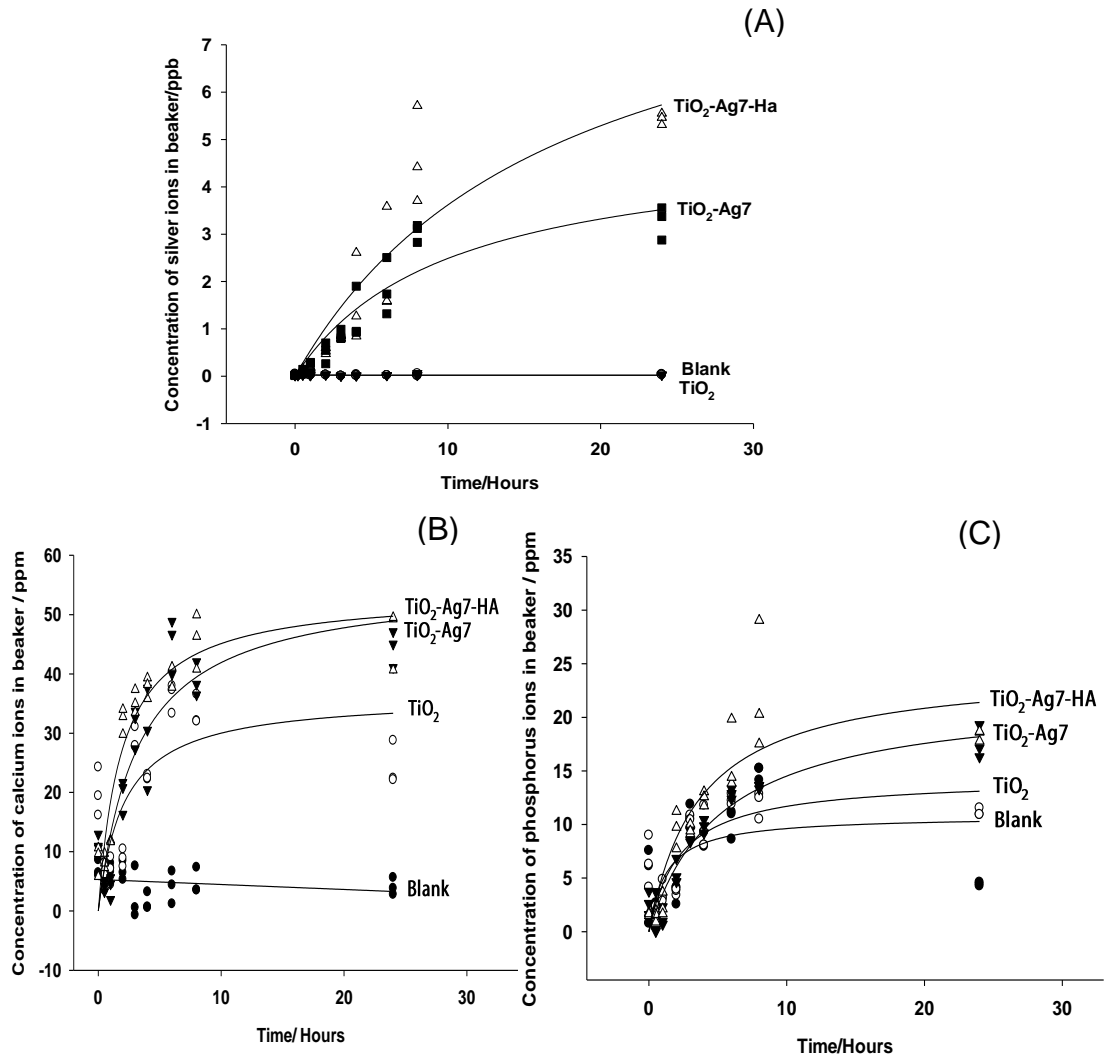


Figure 5.5: Concentration of (A) silver ions in the acidified SBF from the dialysis beakers (external media) as measured by the ICP-MS instrument, (B) calcium ions and (C) phosphorus ions in the acidified SBF from the dialysis beakers as measured by the ICP-OES instrument.

The maximum concentration of silver released in the beaker from both coatings was considered to be low (TiO₂-Ag7 :5.44 ± 0.06 ppb, TiO₂-Ag7-HA: 3.27 ± 0.11 ppb). However, the concentration of silver collected in the dialysis bag that could not go through the bag was significantly higher than that present in the beaker after the 24 hours experiment in both the results from TiO₂-Ag7 (62.6 ± 3.0 ppb) and TiO₂-Ag7-HA (29.7 ± 2.2) (Figure 5.6,

Kruskal Wallis, $p = 0.015$ and $p = 0.021$, respectively; $n=3$). As such, in the dialysis bag, the material to which silver was attached was not dissolved.

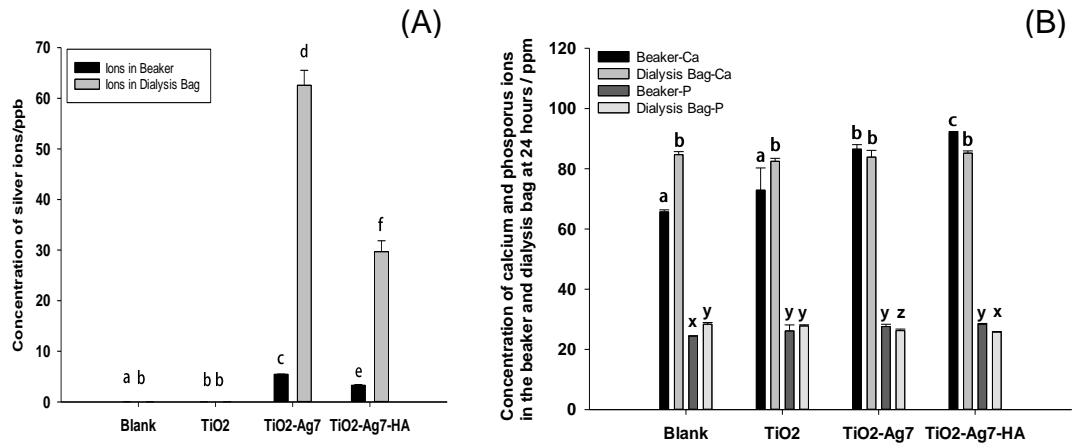


Figure 5.6 : Concentration of (A) silver ions in the acidified SBF from the beaker and the dialysis bag after 24 hours of dialysis (Mean \pm S.E.M, Kruskal-Wallis, $n=3$) and (B) calcium and phosphorus ions in the acidified content of the beaker (external media) and the dialysis bag after 24 hours of dialysis (Kruskal-Wallis, $n=3$). The alphabets show the significance in differences in the concentration of the ions between the differently coated samples and their respective locations at 95.0 % confidence level.

Since simulated body fluid already contains calcium and phosphorus, the concentration of calcium and phosphorus present in SBF has been negated from the data obtained from ICP and then presented in Figure 5.5 B, C and Figure 5.6 B.

5.3.3 Antibacterial Properties of nanocomposite coating

5.3.3.1 Cell viability of *S. aureus*

The media containing the cells exposed to TiO₂-Ag7 and TiO₂-Ag7-HA were found to have almost no live cells as illustrated in Figure 5.4 A. This was similar to the low/no percentage of live to dead bacterial cells in the presence of silver nitrate and silver nanoparticles (Kruskall-Wallis, $p=0.000007$, $n=6$). Similar observations were made with regards to the incubated adhered *S. aureus* with the percentage of live cells being about 100 % in the control and very low survival rates in the presence of the coatings and positive controls as shown in Figure 5.7 B.

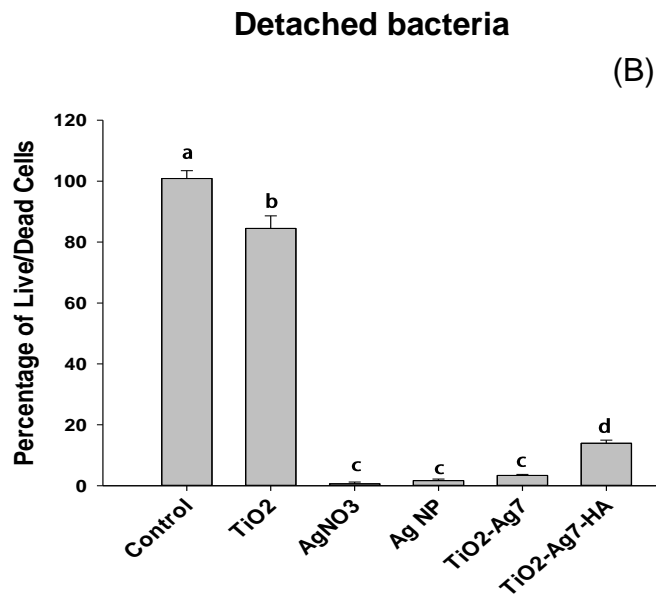
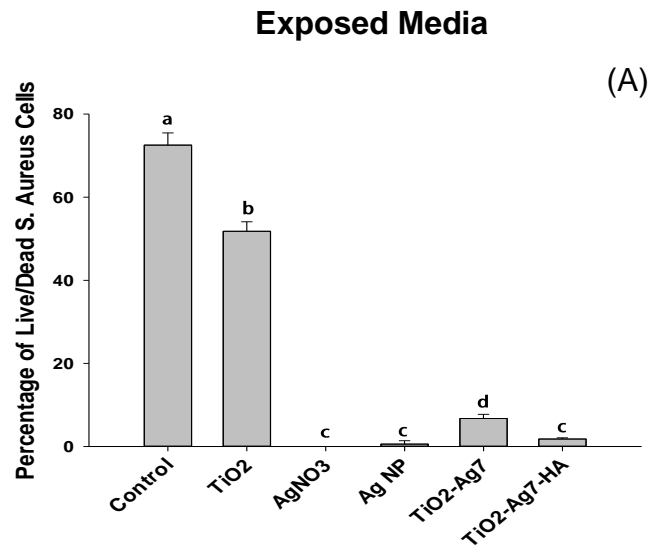


Figure 5.7 Percentage of live to dead *S. aureus* cells in (A) exposed media and (B) incubated detached cells presented as Mean \pm S.E.M (Kruskal-Wallis, n=6). The different alphabets represent the statistically significant differences between the different samples at a confidence interval of 95 %.

5.3.3.2 Lactate production of exposed *S.aureus*

The lactate produced by *S. aureus* was measured after the 24 hour exposure to the coatings and controls and presented in Figure 5.8 A and B. The amount of lactate produced by the bacteria in the exposed media in the case

of both TiO₂-Ag7 and TiO₂-Ag7-HA and the positive controls was significantly lower than that in TiO₂ and the control which is the bacteria growing in BHI media in the absence of any sample (Kruskal-Wallis, p=0.000007, n=6). Similar observations were made in the amount of lactate produced by the incubated attached bacteria (Kruskal-Wallis, p=0.000006, n=6).

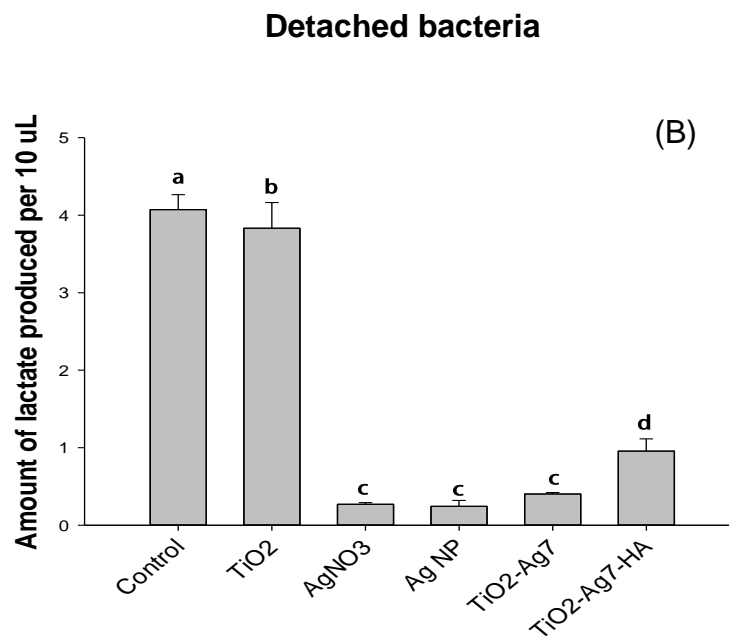
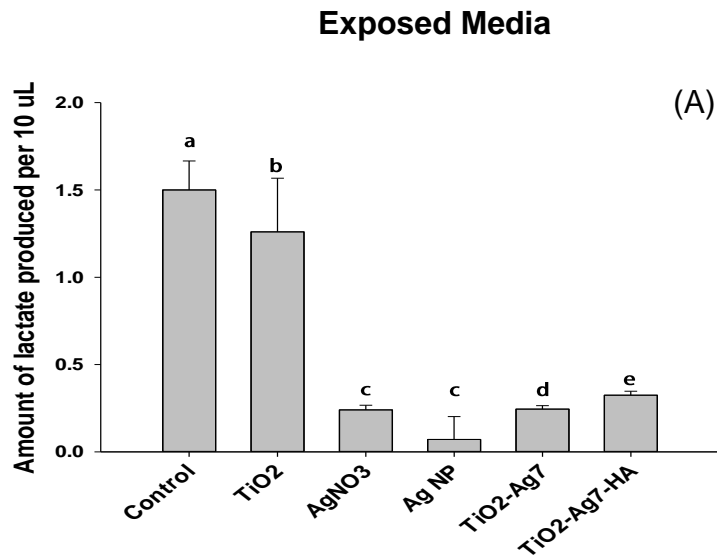


Figure 5.8 Amount of Lactate produced by *S. aureus* in (A) exposed media and (B) incubated adhered cells. Data are presented as mean \pm S.E.M (Kruskal-Wallis, $n=6$). The different alphabets represent the statistically significant differences between the different samples at a confidence interval of 95 %.

5.3.3.3 Silver ions release in broth from coating

The concentration of silver released in the broth from both TiO₂-Ag7 and TiO₂-Ag7-HA were 2.1 ± 0.2 ppm and 0.5 ± 0.1 ppm respectively as shown in Figure 5.9 A. They were hence higher than the silver that was released in the SBF from the dialysis experiment with a maximum release of 62.6 ± 3.0 ppb and 29.7 ± 2.2 respectively as shown Figure 5.5 A and 5.6 A.

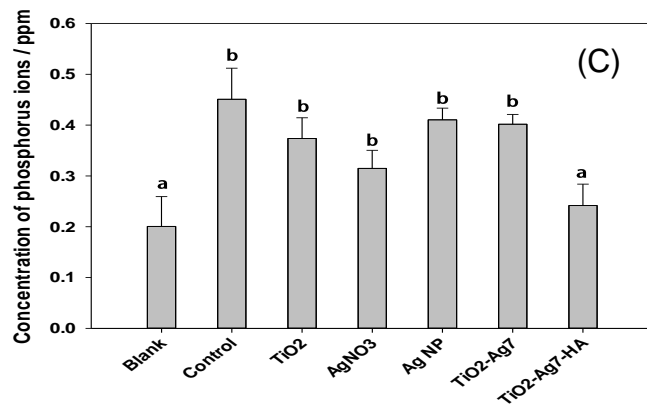
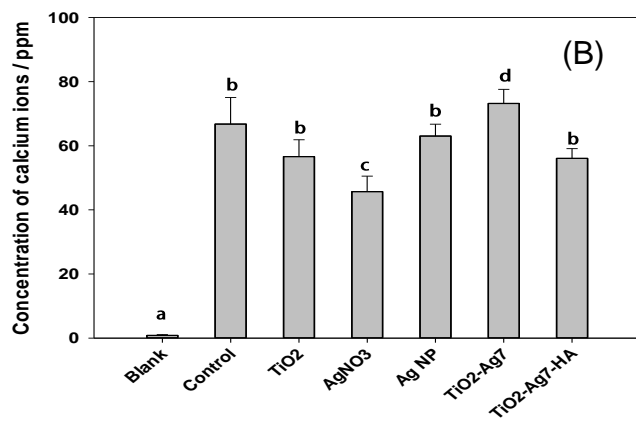
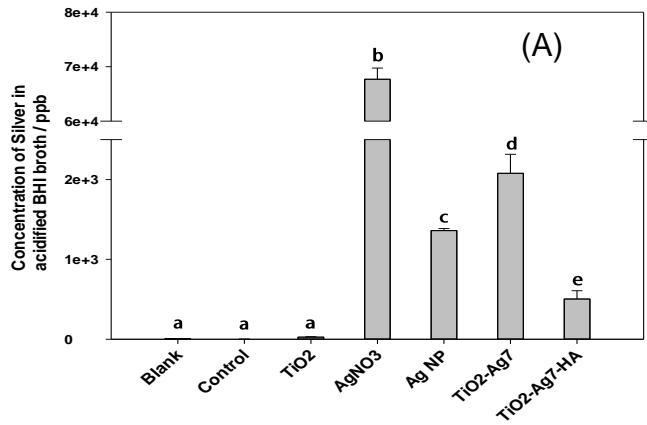


Figure 5.9: Concentration of (A) silver, (B) Calcium and (C) Potassium ions present in exposed media after 24 hours exposure of samples to *S. aureus* in BHI broth. The data are presented as Mean \pm S.E.M with the different alphabets representing the statistically significant differences between the different samples at a confidence interval of 95 %, (n=6).

5.3.3.4 Bacterial Adhesion of bacteria - Microscopic imaging

The microscopy provided a visual confirmation of the presence of a large amount of bacteria on the surface of the control and TiO₂ as seen in Figure 5.10 A and B.

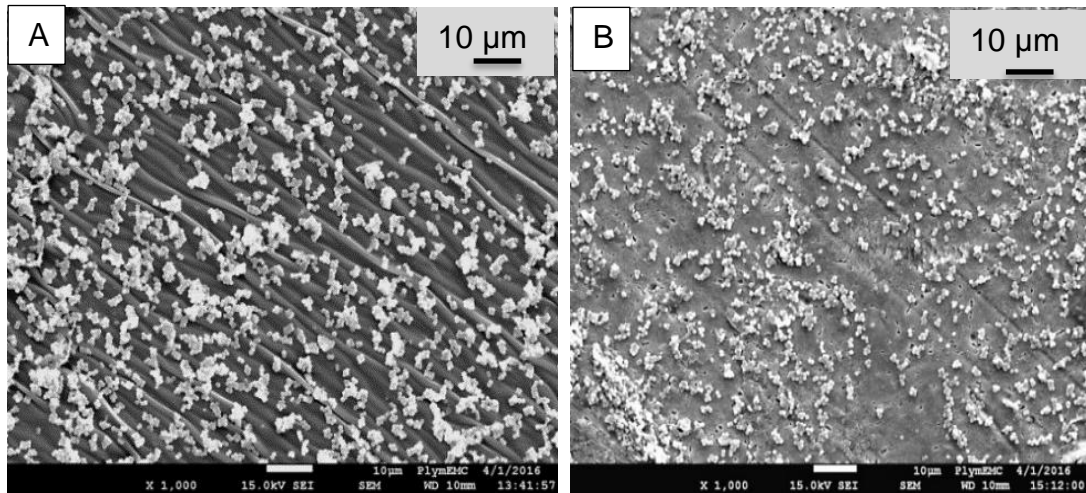


Figure 5.10: SEM images (JEOL 7001) at a magnification of $\times 1000$ of *S. Aureus* grown (A) in just media as a control and (B) on uncoated TiO₂.

Figure 5.11 A and B show the surface of a well containing silver nitrate and silver nanoparticles respectively, whereby no bacteria could be seen with the white parts representing the silver salt and silver nanoparticles.

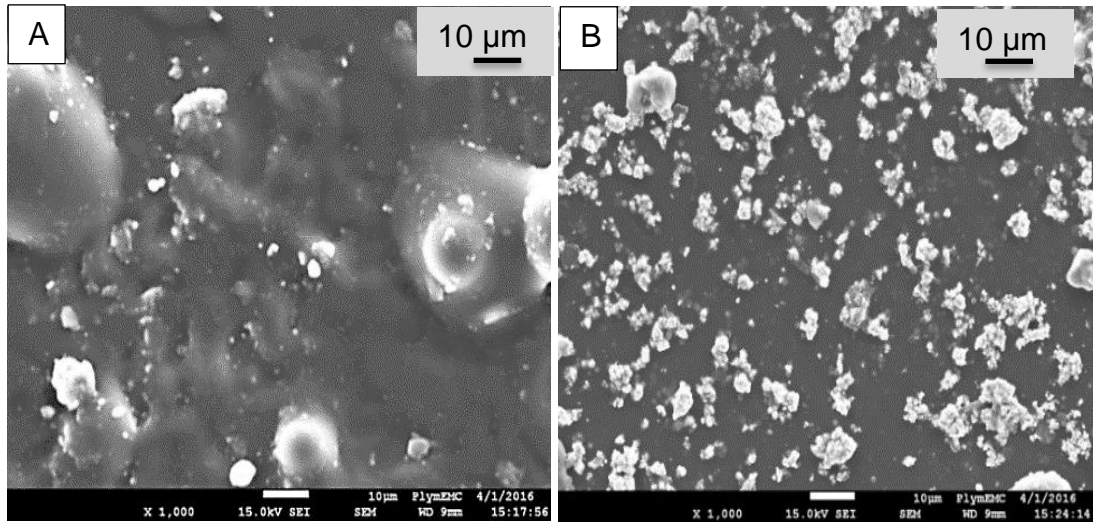


Figure 5.11: SEM images (JEOL 7001) at a magnification of $\times 1000$ of *S. Aureus* grown (A) in aqueous Silver Nitrate and (B) in the presence of Silver nanoparticles

TiO₂-Ag7 and TiO₂-Ag7-HA treatments exhibited similar observations (Figure 5.12 A and B) with no bacterial film observed.

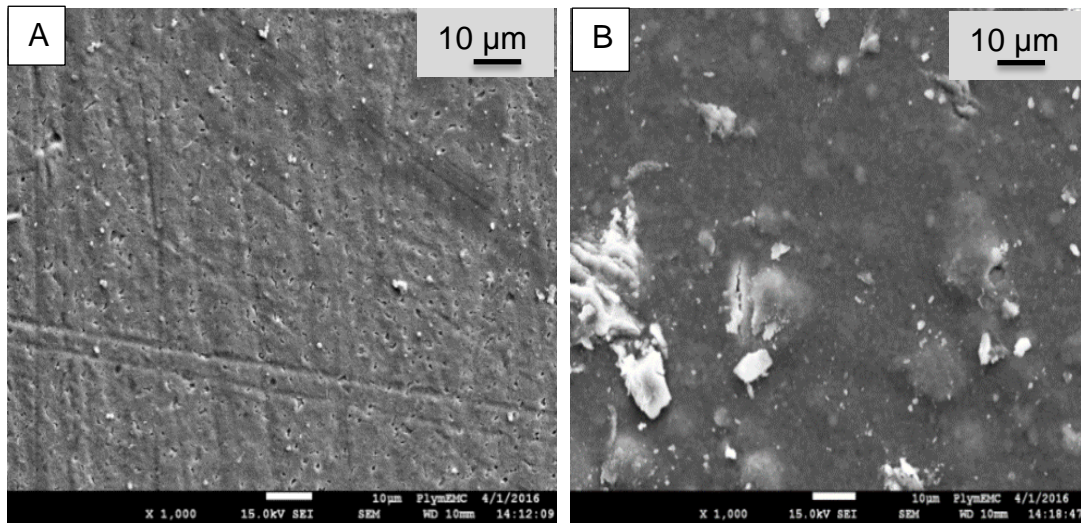


Figure 5.12: SEM images (JEOL 7001) at a magnification of $\times 1000$ of *S. Aureus* grown (A) on TNT-nAg and (B) on TNT-nAg/Ha.

5.3.4 Biocompatibility of nanocomposite coating

The biocompatibility of the coatings were assessed in the presence of primary human osteoblast cells as described in section 4.5. Biochemical assays were used to quantify the biocompatibility properties of the coatings in comparison to specific controls. Molecular diagnostics were used to assess the molecular biocompatibility of the coatings.

5.3.4.1 Protein Assay

Figure 5.13 showed the distribution of the concentration of the protein in the cell homogenates exposed to the different samples on day 4 and day 10. There was more protein on day 10 than on day 4. On day 4, the protein content for TiO₂-Ag7 and TiO₂-Ag7-HA were similar to that of the control and TiO₂. However by day 10, the concentration of protein reduced significantly on both TiO₂-Ag7 and TiO₂-Ag7-HA as compared to the control and TiO₂ (Kruskall-Wallis, $p= 0.015$, $n=3$).

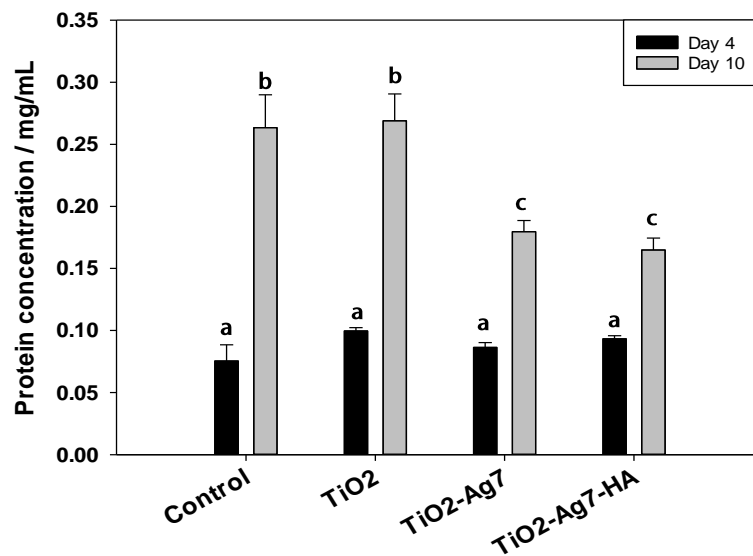


Figure 5.13: Concentration of protein in cell homogenates from attached osteoblast cells on TiO₂-Ag7 and TiO₂-Ag7-HA disks and the controls at day 4 and 10 of exposure. The data are presented as Mean \pm S.E.M with the alphabets represent the significance in difference among the various parameters involved at a confidence interval of 95 % (Kruskal-Wallis, $n=3$).

5.3.4.2 Alkaline phosphatase

The ALP data were presented in Figure 5.14 A. The ALP activity was the same on both day 4 and 10 for the TiO₂-Ag7 treatment which was similar to the control. However for TiO₂-Ag7-HA, the specific activity of ALP on day 10 was significantly lower than on day 4 in the homogenate (Kruskall-Wallis, n=3). Similar observations were made for the homogenates from TiO₂ as well. The alkaline phosphatase activity in the media of the cells exposed to all the sample was higher than that in the homogenate as seen in Figure 5.14 A and B. In TiO₂ and TiO₂-Ag7 media, the highest activity was visible on day 10 as compared to the control which was on day 4 (Figure 5.14B). The main difference between TiO₂-Ag7 and TiO₂-Ag7-HA was that the ALP activity in media was seen to be increasing for osteoblast cells exposed to TiO₂-Ag7 as compared to TiO₂-Ag7-HA which was decreasing from day 1 to day 10.

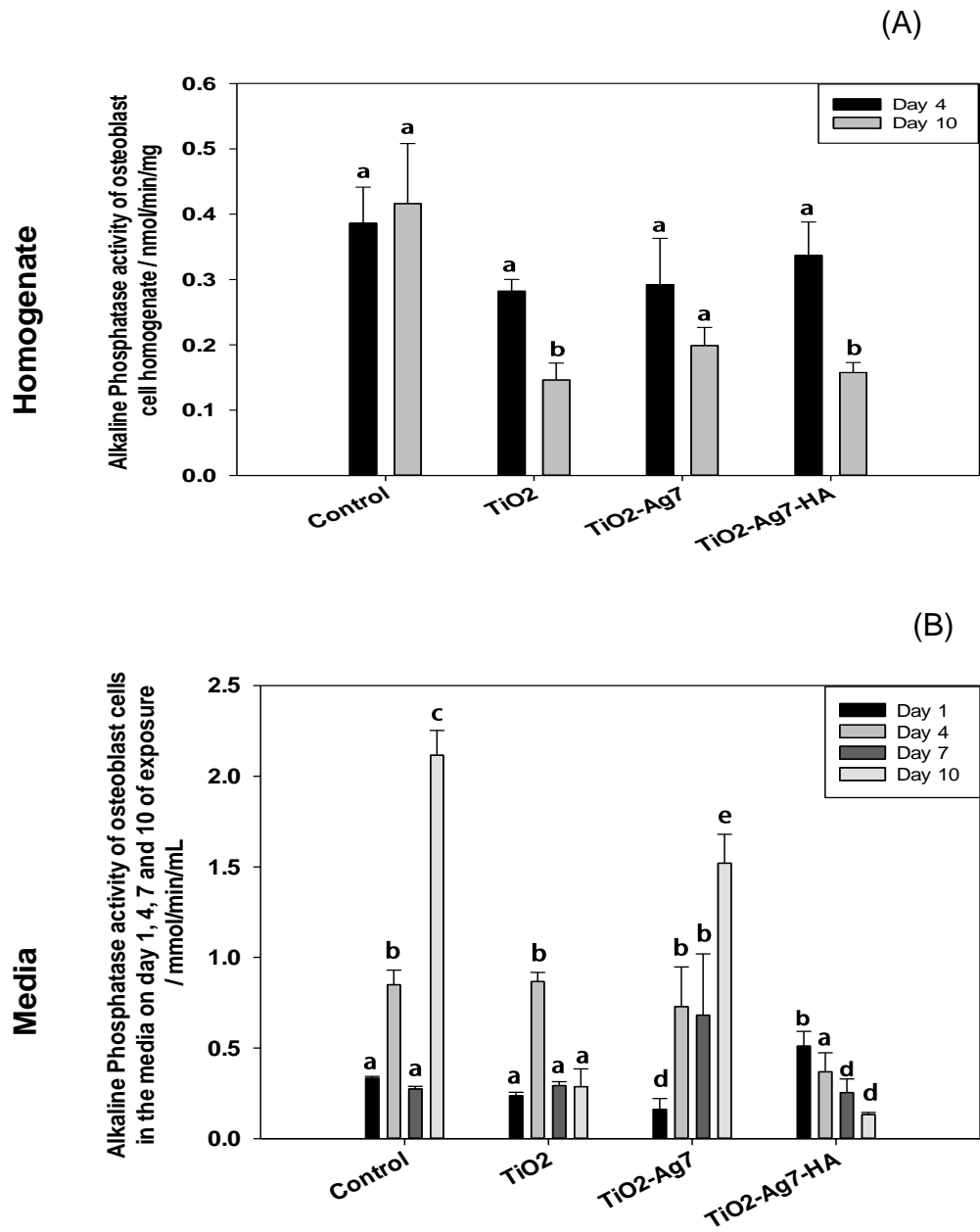


Figure 5.14: ALP activity of osteoblast cells in (A) homogenate and (B) exposed media. The values are represented as Mean \pm S.E.M. The different alphabets represent the statistically significant differences between the different samples on different days at a confidence interval of 95 % (Kruskal-Wallis, n=3).

5.3.4.3 Lactate dehydrogenase assay

The LDH assay data was presented in Figure 5.15. There was more LDH activity on day 10 as compared to day 4 in the homogenate of the cells exposed to both samples and controls as seen in Figure 5.15 A.

Nonetheless, the LDH activity was highest in the media as compared to the homogenate as viewed in Figure 5.15 B. On Day 1 the media of cells exposed to both control and TiO₂ expressed the highest LDH activity with the activity decreasing as from day 4.

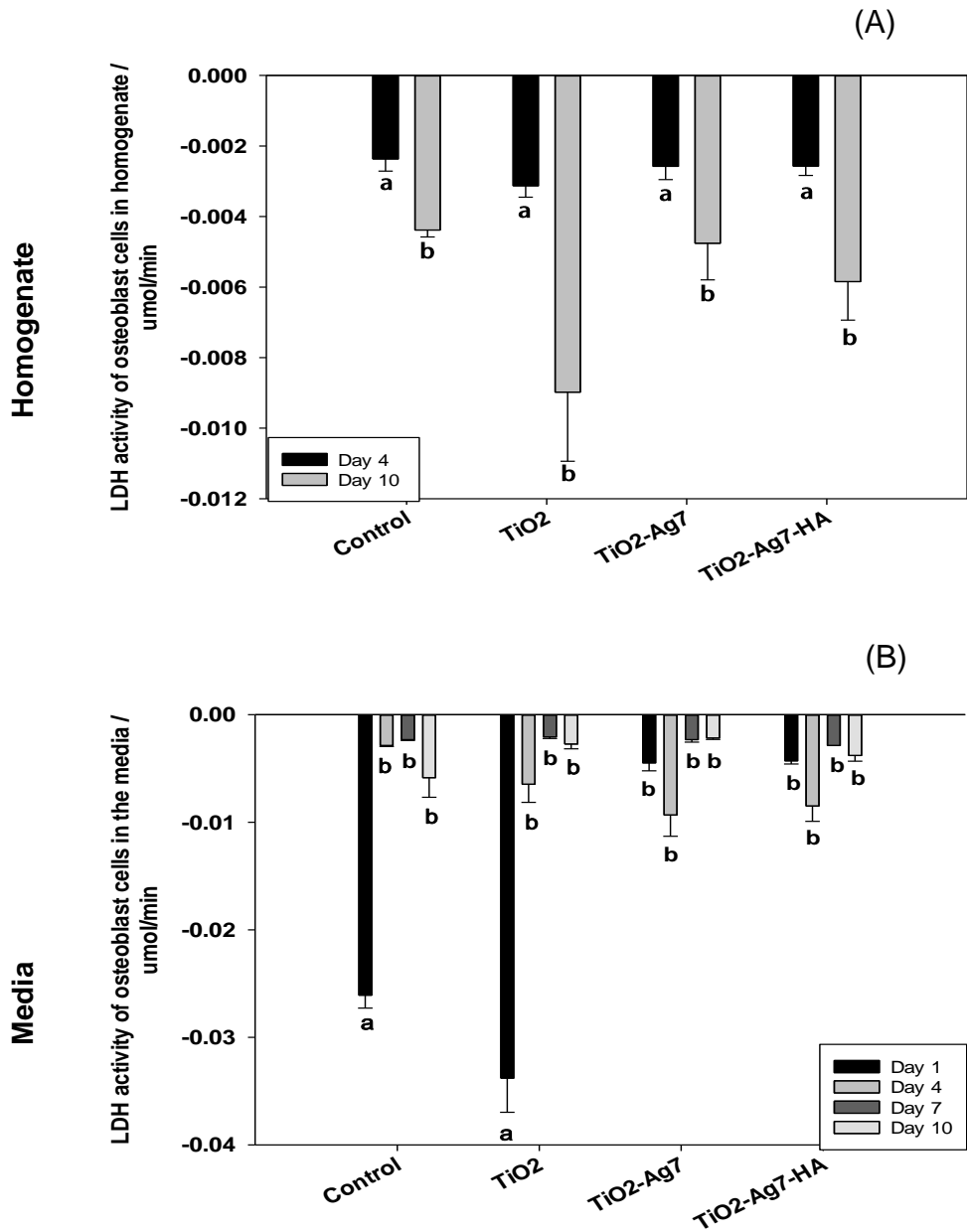


Figure 5.15: LDH activity of osteoblast cells in (A) homogenate and (B) exposed media. The values are represented as Mean \pm S.E.M. The different alphabets represent the statistically significant differences between the different samples on different days at a confidence interval of 95 % (Kruskal-Wallis, $n=3$).

5.3.4.4 Glutathione Assay

The total glutathione in the homogenates is shown in Figure 5.16. The concentration of glutathione present was the same for the coated samples and controls on day 4 with a lower amount than on day 10. However on day 10, the cell homogenates from TiO₂ exhibited the highest concentration of glutathione as compared to the rest.

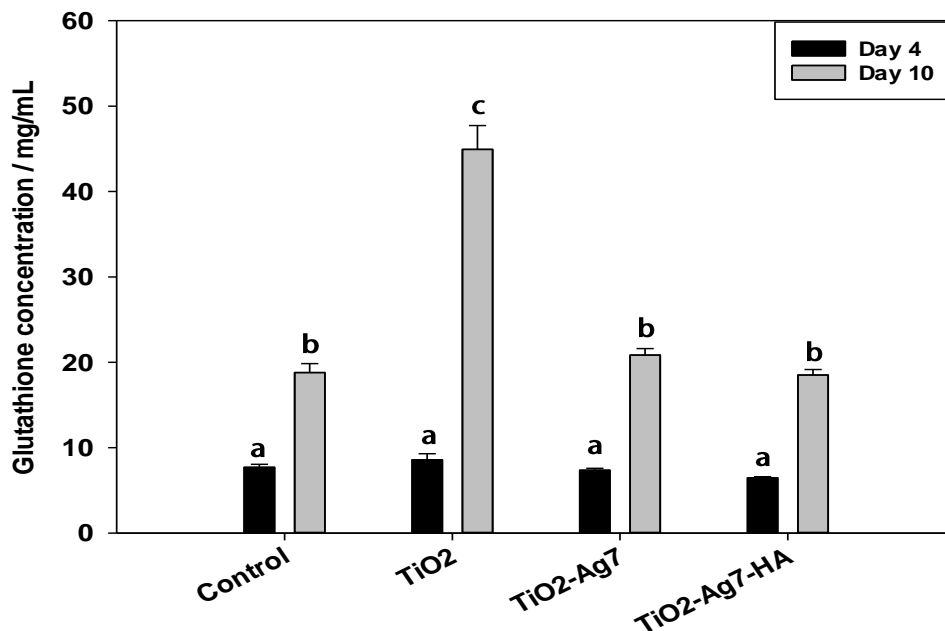


Figure 5.16: Glutathione concentration in homogenate of cells exposed to samples and controls on day 4 and day 10. The data are presented as Mean \pm S.E.M. The different alphabets represent the statistically significant differences between the different samples on different days at a confidence interval of 95 % (Kruskal-Wallis, n=3).

5.3.4.5 Trace Element Analysis

The release of silver from the coatings to the media was lower (Figure 5.17 B) than that observed in the presence of bacteria as observed in section 5.5. The concentration of silver in the cell homogenate as well were low as observed in Figure 5.17 A.

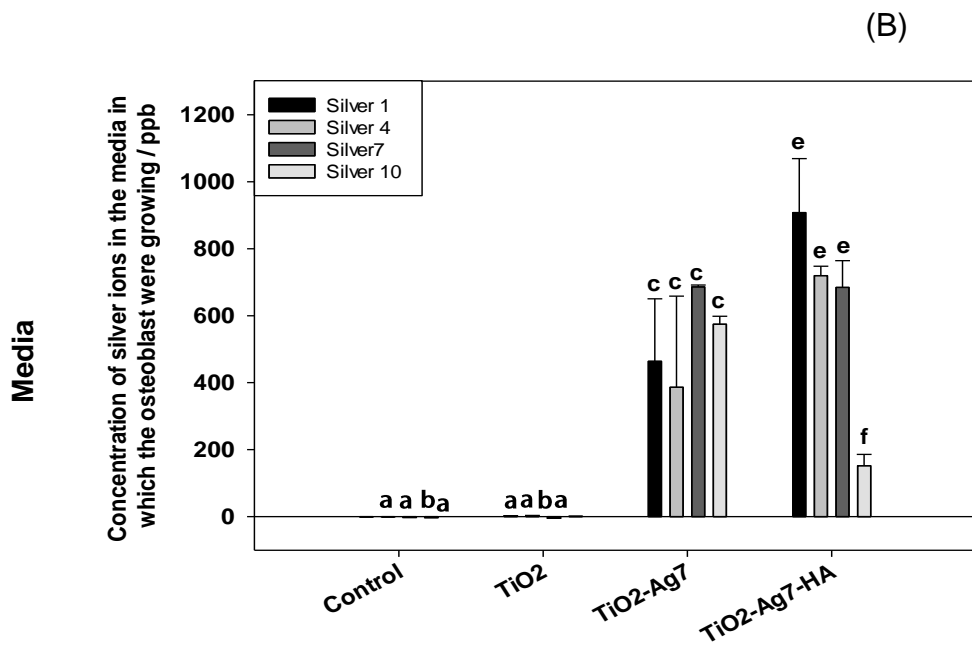
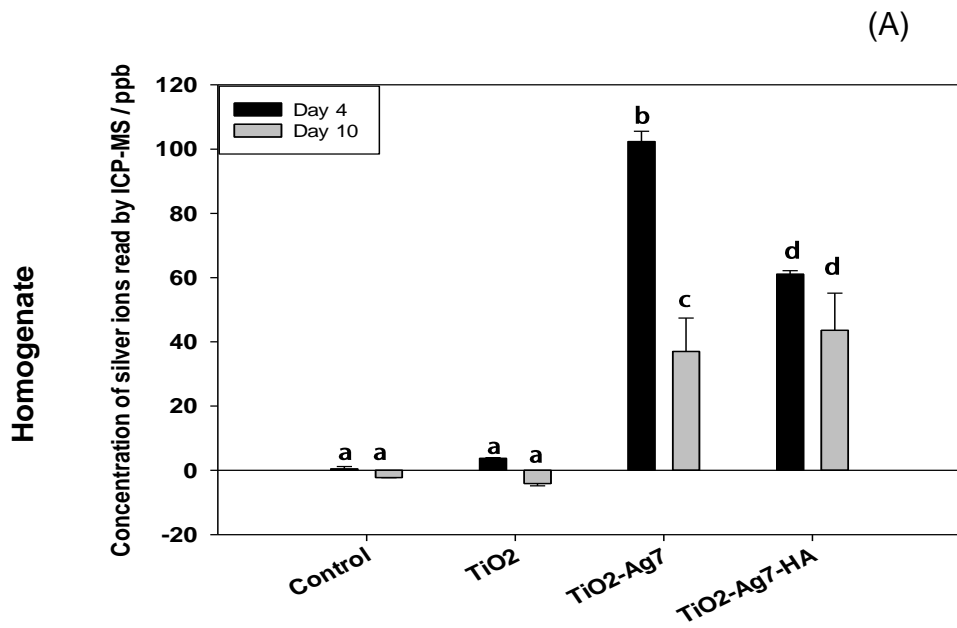


Figure 5.17: ICP readings for silver in the (A) Homogenate and (B) exposed media of the osteoblast cells grown on the samples and controls. The data are presented as Mean \pm S.E.M

5.3.4.5 Microscopic imaging of adhered cells

Visual confirmation of the presence of osteoblast cells attached to the coatings was provided by SEM which are presented in Figure 5.18. The highest amount of cells were present on the uncoated TiO₂ (Figure 5.18 A). The magnified image of the cells showed the presence of filopodia extending from the cells to each other. The amount of filopodia was more on TiO₂ than on TiO₂-Ag7 and TiO₂-Ag7-HA. However, the cells on TiO₂-Ag7 were the most granular as seen in Figure 5.18 D. TiO₂-Ag7-HA had scarce cells and it was also observed that the HA coating was pulled off during the exposure to osteoblast cells. Hence of the HA coating was missing on all the TiO₂-Ag7-HA discs.

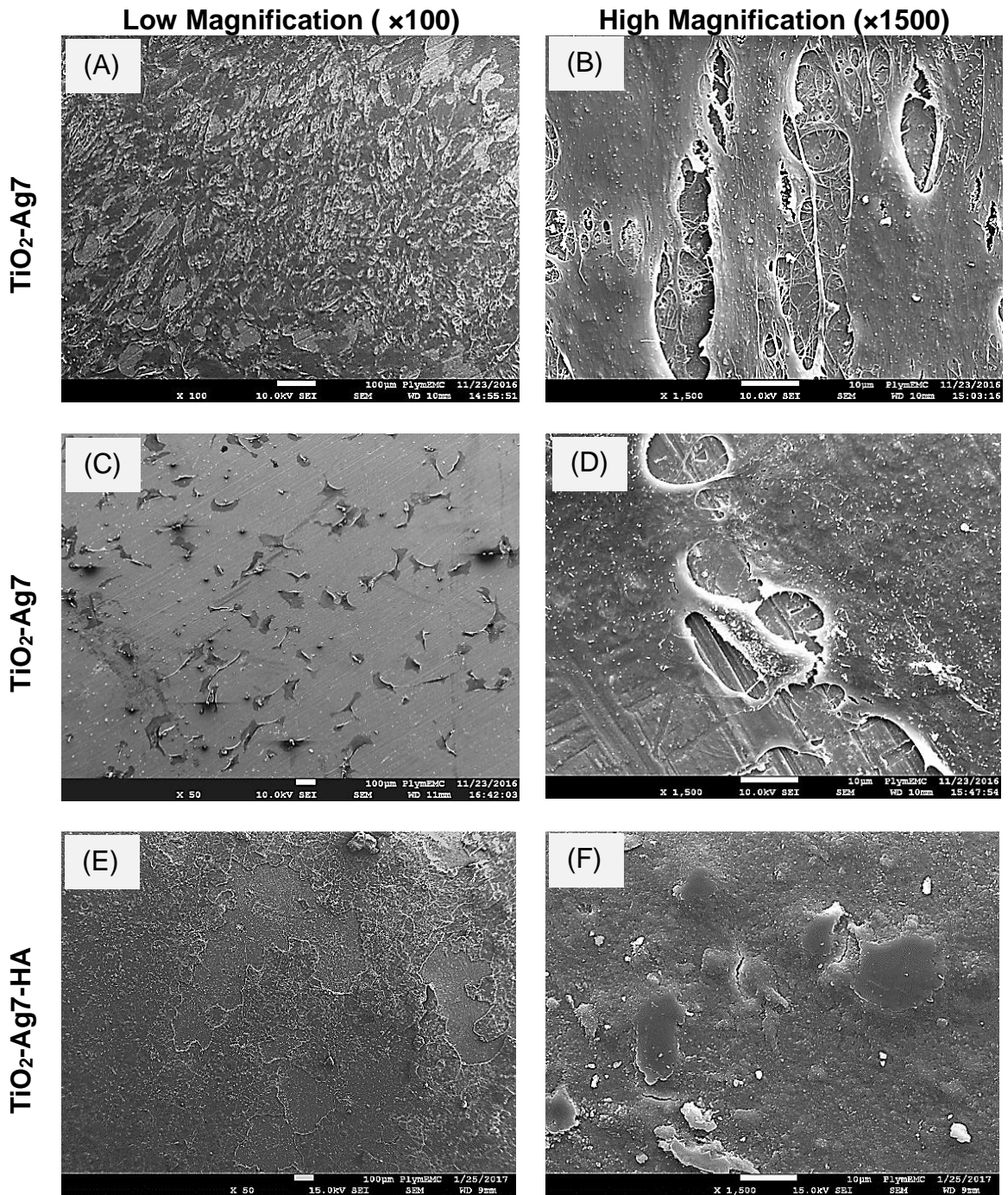


Figure 5.18 : SEM images of (A) and (B) TiO₂, (C) and (D) TiO₂-Ag7 and (E) and (F) TiO₂-Ag7-HA viewed at low (×100) and high magnifications (×1500) respectively.

5.3.4.6 Electrolytes measurement

The total concentration of electrolytes were measured using ICP-OES as described in chapter 4 and the readings from the acidified homogenates are presented in Table 5.2 and the acidified media in Table 5.3.

Table 5.2: Electrolytes' ions concentration in homogenate.

Electrolyte	Treatment	Day 4	Day 10
Sodium	Control	0.28 ± 0.12 a	0.75 ± 0.17 b
	TiO ₂	0.31 ± 0.02 a	0.70 ± 0.37 b
	TiO ₂ -Ag7	1.00 ± 0.28 b	1.59 ± 0.65 c
	TiO ₂ -Ag7-HA	0.64 ± 0.12 b	1.82 ± 0.37 c
Potassium	Control	1.13 ± 0.01 a	0.88 ± 0.25 a
	TiO ₂	0.94 ± 0.05 a	1.22 ± 0.82 b
	TiO ₂ -Ag7	1.10 ± 0.02 a	1.43 ± 0.42 b
	TiO ₂ -Ag7-HA	1.23 ± 0.06 a,b	0.91 ± 0.02 a
Magnesium	Control	0.00 ± 0.00 a	0.00 ± 0.00 a
	TiO ₂	0.00 ± 0.00 a	0.00 ± 0.00 a
	TiO ₂ -Ag7	0.01 ± 0.01 a	0.00 ± 0.00 a
	TiO ₂ -Ag7-HA	0.06 ± 0.00 a	0.04 ± 0.00 a
Calcium	Control	0.01 ± 0.00 a	0.02 ± 0.01 a
	TiO ₂	0.06 ± 0.01 b	0.02 ± 0.01 a
	TiO ₂ -Ag7	0.11 ± 0.03 c	0.02 ± 0.00 a
	TiO ₂ -Ag7-HA	0.67 ± 0.02 d	0.83 ± 0.08 e
Phosphorus	Control	0.05 ± 0.01 a	0.09 ± 0.02 a
	TiO ₂	0.06 ± 0.00 a	0.07 ± 0.01 a
	TiO ₂ -Ag7	0.03 ± 0.01 a	0.02 ± 0.00 a
	TiO ₂ -Ag7-HA	0.33 ± 0.02 b	0.54 ± 0.07 c

Total sodium, potassium, magnesium, calcium and phosphorus in homogenates of osteoblast cells grown on the TiO₂-Ag7, TiO₂-Ag7-HA and

TiO₂ and the control on day 4 and 10. The alphabets show the significance in differences among the different treatments involved and the different days at a 95 % confidence interval, per ion being measured. (Transformed One-way ANOVA, n=3) (The different ions are not compared with each other)

Table 5.3: Electrolytes' ions concentration in media

Ions	Samples	Day 1	Day 4	Day 7	Day 10
Sodium	Control	466.50 ± 11.50 a	213.51 ± 16.31 b	215.96 ± 7.04 b	317.47 ± 3.78 c
	TiO ₂	431.52 ± 14.64 d	221.97 ± 6.19 b	202.96 ± 9.55 b	286.85 ± 20.60 c
	TiO ₂ -Ag7	409.67 ± 6.89 e	231.95 ± 0.65 b	95.78 ± 4.99 f	275.93 ± 6.89 c
	TiO ₂ -Ag7-HA	527.32 ± 16.16 g	197.77 ± 4.08 b	540.95 ± 45.90 g	274.25 ± 18.31 c
Potassium	Control	36.01 ± 0.56 a	16.93 ± 1.35 b	18.02 ± 0.48 b	27.47 ± 0.30 c
	TiO ₂	34.16 ± 3.04 a	17.88 ± 0.53 b	16.40 ± 4.19 b	23.81 ± 1.68 d
	TiO ₂ -Ag7	32.69 ± 0.69 a	18.65 ± 0.12 b	6.90 ± 0.45 e	23.25 ± 0.36 d
	TiO ₂ -Ag7-HA	40.27 ± 2.10 f	16.03 ± 0.28 b	50.26 ± 6.46 g	24.73 ± 2.17 d
Magnesium	Control	3.03 ± 0.06 a	1.52 ± 0.12 b	1.45 ± 0.07 b	2.18 ± 0.03 c
	TiO ₂	2.72 ± 0.26 a	1.60 ± 0.05 b	1.12 ± 0.17 d	1.95 ± 0.15 e
	TiO ₂ -Ag7	2.58 ± 0.05 a	1.63 ± 0.02 b	0.75 ± 0.04 f	1.92 ± 0.08 e
	TiO ₂ -Ag7-HA	3.06 ± 0.16 a	1.32 ± 0.02 b	2.03 ± 0.04 e	1.64 ± 0.11 b
Calcium	Control	8.71 ± 0.19 a	3.56 ± 0.30 b	6.49 ± 0.66 c	6.40 ± 0.24 c
	TiO ₂	7.58 ± 0.64 c	3.64 ± 0.12 b	4.09 ± 0.60 d	5.41 ± 0.51 e
	TiO ₂ -Ag7	7.09 ± 0.09 c	3.58 ± 0.04 b	2.75 ± 0.24 e	5.54 ± 0.24 e
	TiO ₂ -Ag7-HA	3.62 ± 0.16 b	1.40 ± 0.03 f	1.88 ± 0.07 f	2.05 ± 0.29 f
Phosphorus	Control	4.30 ± 0.11 a	2.51 ± 0.21 b	2.90 ± 0.12 b	3.25 ± 0.04 c
	TiO ₂	3.80 ± 0.36 c	2.60 ± 0.08 b	2.29 ± 0.09 b	2.84 ± 0.21 b
	TiO ₂ -Ag7	3.55 ± 0.08 c	2.60 ± 0.01 b	2.36 ± 0.03 b	2.65 ± 0.14 b
	TiO ₂ -Ag7-HA	2.13 ± 0.09 b	1.03 ± 0.02 d	1.12 ± 0.05 d	1.05 ± 0.11 d

5.3.5 PCR data of markers in exposed osteoblast cells

The adhesion marker, FAK, was less expressed in the presence of silver nanoparticle as compared to uncoated TiO₂ on day 4. By day 10 the expression increased as seen in Figure 5.19 A.

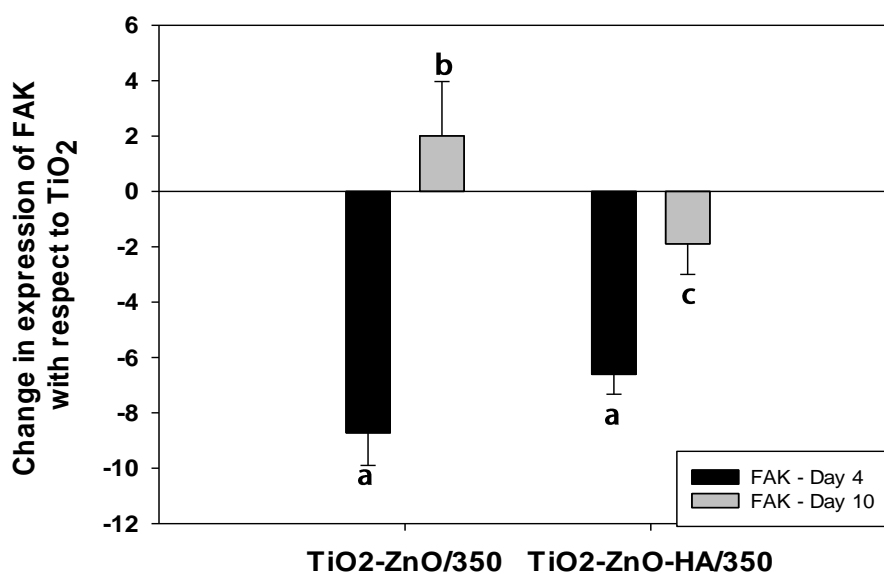


Figure 5.19: Change in gene expression of FAK in osteoblast cells grown on TiO₂-Ag7 and TiO₂-Ag7-HA on day 4 and 10 of exposure, with respect to the cells grown on TiO₂ after normalisation with respect to β -actin (Mean \pm S.E.M, Kruskal-Wallis, $p=0.05$, $n=3$). The different alphabets represent the statistically significant differences between the different samples on different days at a confidence interval of 95 %.

On day 4, RUNX-2, ALP and OC were downregulated as compared to day 10 when they were upregulated, all with respect to the expression on TiO₂ as illustrated in Figure 5.20 A, B and C. The cells on TiO₂-Ag7 expressed the latter genes more than TiO₂-Ag7-HA on both days.

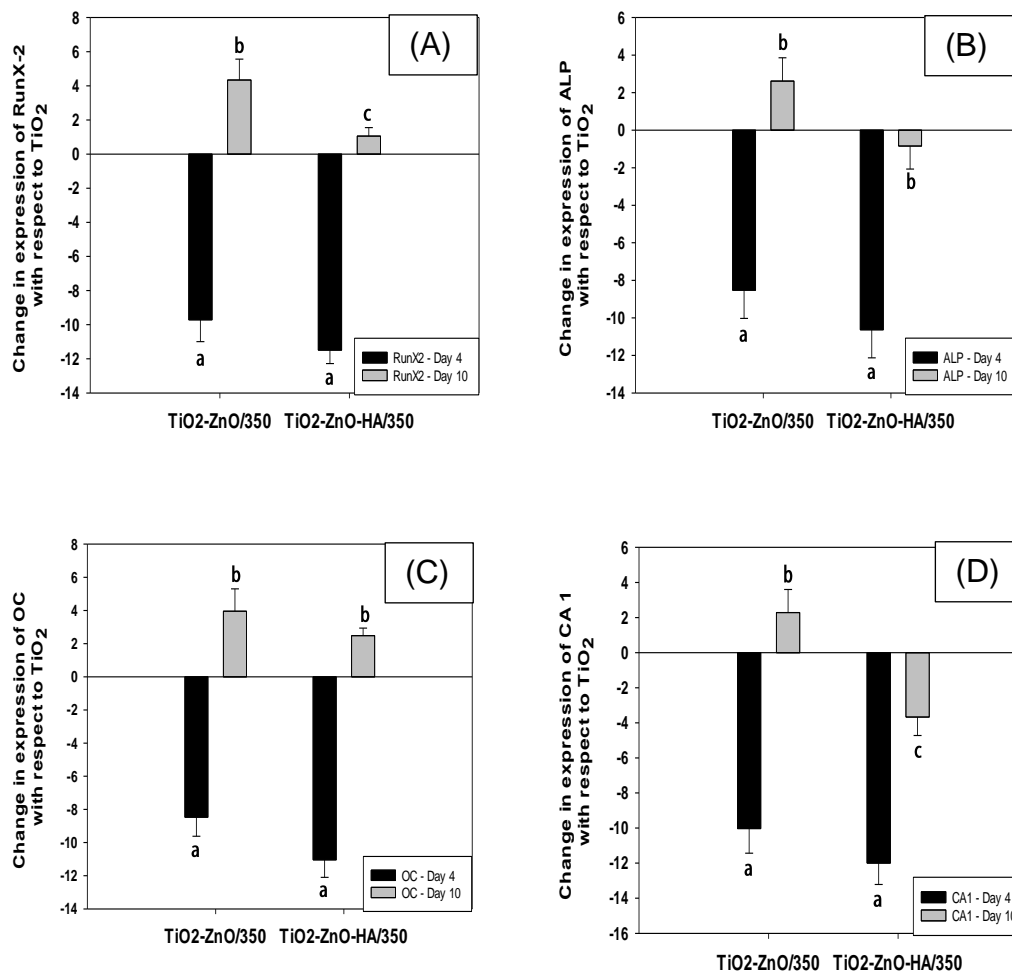


Figure 5.20: Change in gene expression of (A) RunX-2, (B) ALP, (C) OC and (D) CA1 in osteoblast cells grown on TiO₂-Ag7 and TiO₂-Ag7-HA on day 4 and 10 of exposure, with respect to the cells grown on TiO₂ after normalisation with respect to β -actin (Mean \pm S.E.M, Kruskal-Wallis, $p=0.05$, $n=3$). The different alphabets represent the statistically significant differences between the different samples on different days at a confidence interval of 95 %.

The inflammatory markers behaved similar to the genes for osteoblast proliferation and differentiation on day 4 and 10 as shown in Figure 5.21.

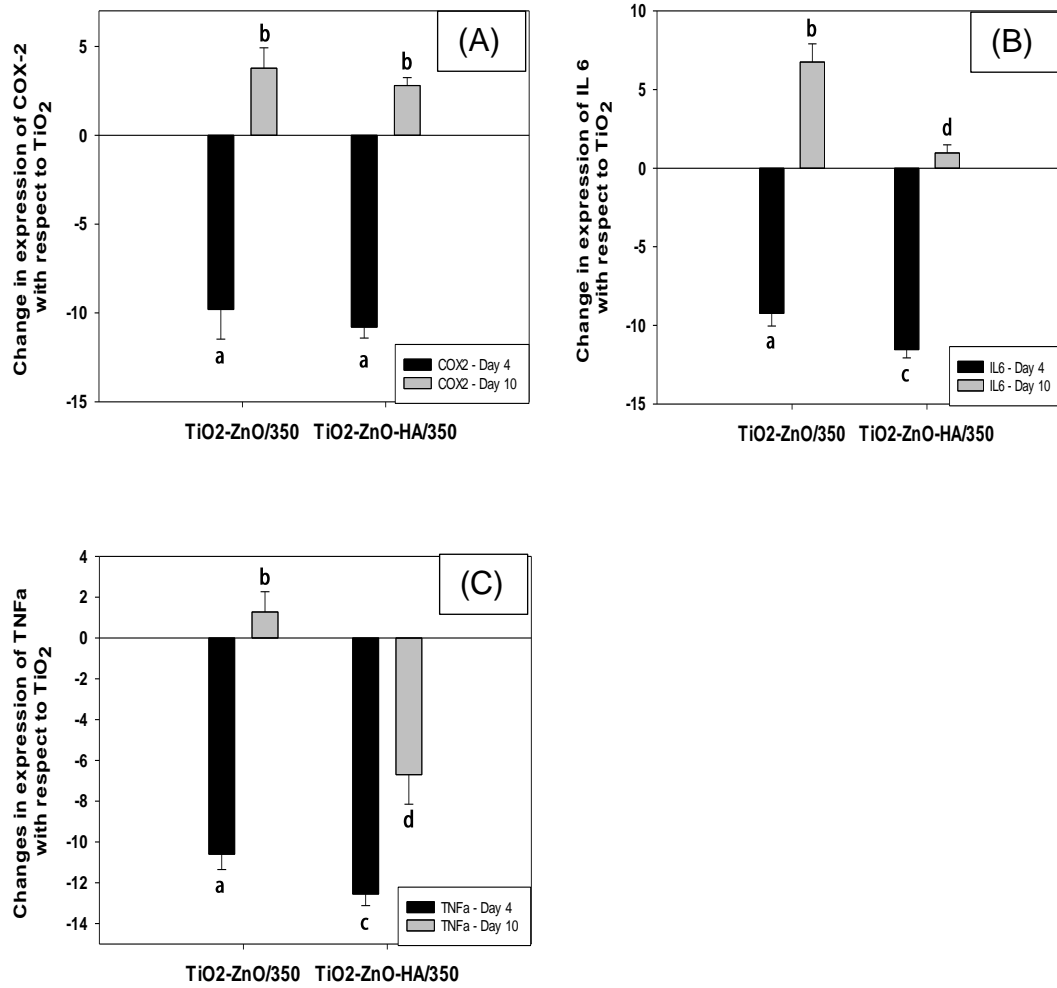


Figure 5.21: Change in gene expression of (A) COX 2, (B) IL 6 and (C) TNFa in osteoblast cells grown on TiO₂-Ag7 and TiO₂-Ag7-HA on day 4 and 10 of exposure, with respect to the cells grown on TiO₂ after normalisation with respect to β -actin (Mean \pm S.E.M, Kruskal- Wallis, p=0.05, n=3). The different alphabets represent the statistically significant differences between the different samples on different days at a confidence interval of 95 %.

Finally, SOD was downregulated on day 4 and upregulated on day 10 but the cells on both coatings had similar level of expression as shown in the figure below.

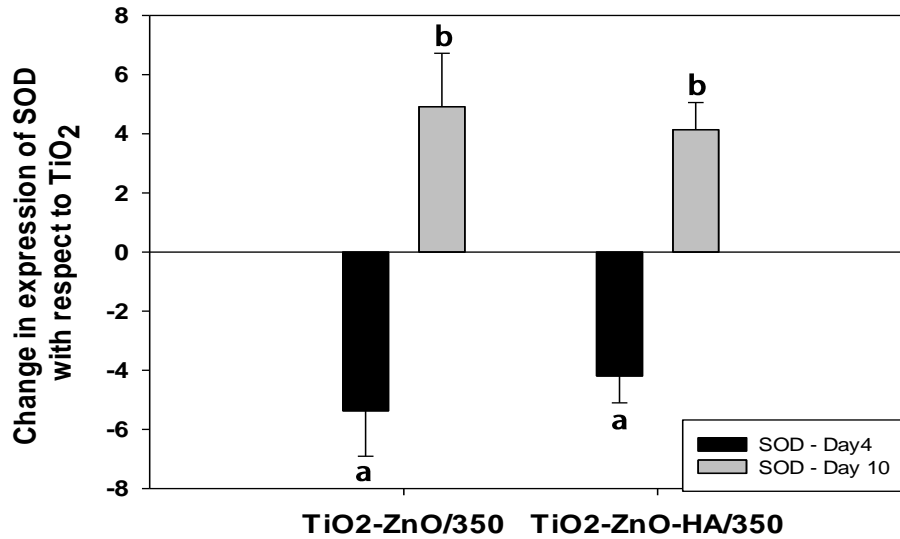


Figure 5.22: Change in gene expression of SOD in osteoblast cells grown on TiO₂-Ag7 and TiO₂-Ag7-HA on day 4 and 10 of exposure, with respect to the cells grown on TiO₂ after normalisation with respect to β -actin (Mean \pm S.E.M, Kruskal-Wallis, $p=0.05$, $n=3$). The different alphabets represent the statistically significant differences between the different samples on different days at a confidence interval of 95 %.

5.4 Discussion

The amorphous TiO₂ nanotubes in Chapter 3 was a poor surface for the attachment of Ag NPs. In this current chapter, the post-anodisation treatment of the titanium alloy discs allowed the nanotubes to be more bioactive with the change in crystalline structure and presence of -OH. The reduction of the silver solution in the presence of δ-gluconolactone successfully formed silver nanoparticles which were attached to the titanium dioxide nanotubes. Upon the addition of nano-HA, the silver nanoparticles were covered with a layer of nHA, but this was not complete with some cracks being present; possibly enabling the release of silver and the biocidal properties of the composite.

5.4.1 Antibacterial properties

Silver nanoparticles attached to TiO₂ nanotubes on Ti-6Al-4V alloy is known to be bactericidal with high level of toxicity. In this study, TiO₂-Ag7 confirmed its antibacterial properties whereby almost all the bacteria coming in contact with the coating or those bacteria which were able to attach to the coating died in the process. This was confirmed by the high level of metabolically inactive bacterial cell and high percentage of cell death as shown in section 5.5. However, even though the release of silver were less than 100 ppb in SBF, the release increased drastically to over 1 ppm in the presence of BHI broth and the bacteria within 24 hours. Moreover, in the presence of human osteoblast cells and DMEM media, the release exceeds 1 ppm in total as from day 7 as shown in Figure 5.12. Hence, the release of silver from the coating was controlled depending on the environment it is exposed to. In the

presence of bacteria and the broth, the high release of Ag as measured by ICP-MS, should help in eliminating the presence of bacteria hence resulting in the prevention of infection on implants coated with such coatings. The bactericidal effect was similar to both silver ions (from results of silver nitrate) and silver nanoparticles as whole. This agrees with Reidy (2013) where the bactericidal activity of the nanoparticles were associated with both the nanoparticle from contact action and as dissolved silver which attacks the walls of the bacteria (Reidy *et al.*, 2013).

As explained in Chapter 1, the presence of silver nanoparticle would result in the release of reactive oxygen species which would be toxic to the bacteria. This would prevent the bacteria from functioning normally and this was observed in this study by the significantly lower activity of lactate production by the bacteria in the presence of the coating as compared to the control and uncoated TiO₂. The extreme reduction in live bacteria in the broth indicated that the bacteria exposed as well were killed. Hence, they will not have the ability to produce the biofilm which protects the micro-organisms from being attacked by the body's immune system.

Both TiO₂-Ag7 and TiO₂-Ag7-HA exhibited a high level of antibacterial activity against *S. aureus* as measured by the Live/Dead and lactate production assay in section 5.5. The presence of HA did not hinder the antibacterial properties of the silver nanoparticles but did not improve it as well. Hence TiO₂-Ag7-HA could be considered as an antibacterial coating for implants. As such, the addition of HA did help improving the properties of the silver composite coating.

5.4.2 Biocompatibility

The biocompatibility of the coatings were tested in the presence of primary human osteoblast cells in DMEM media. Using the SEM, a majority of human osteoblast cells were visible on the uncoated TiO₂ as compared to TiO₂-Ag7 and TiO₂-Ag7-HA. In the case of TiO₂-Ag7-HA, delamination of the HA coating was seen. It was assumed to have happened during the samples preparation of the titanium alloy discs for viewing under the microscope. This was because osteoblast cells were obtained from the surface of the discs and the protein determination assay showed confirmed the presence of similar concentration of protein on TiO₂-Ag7-HA as that on TiO₂-Ag7. Hence the healthy cells were concluded to be able to remain attached to the surface of the coating as compared to the unhealthy cells which died due to unfavourable surface morphology and/or toxicity from the coating. As such, during the samples preparation for viewing under the microscope, the unhealthy/dead cells got delaminated and because of their big size, the HA coating as well was lost.

Both coatings, TiO₂-Ag7 and TiO₂-Ag7-HA, were less biocompatible than the uncoated TiO₂. The cells on the coatings on day 4 contained more ALP than on day 10 which is the contrary from the controls. As such, the cells attached to the coatings could be affected by the long term release of silver from the coatings. Hence the presence of silver nanoparticles reduced the ALP activity after day 4 leading to the conclusion that the cells were no longer healthy. Nonetheless the presence of a higher level of glutathione on day 10 indicated that the cells were able to provide antioxidant effect counteracting

the effect of the silver nanoparticles. The presence of less LDH in the media as compared to the controls suggested that there were only a few cells attached to the surface of the coatings that were able to allow big proteins to come out of the cell membrane. Hence, the cell membranes of the majority of the cells attached were not damaged and as such, healthy. However there was a significantly high level of silver ions in the cell homogenate after the 10 days of exposure to the coated samples with the level of sodium to potassium ratio increased from day 4 to day 10. As such the presence of silver in the cells created a slight imbalance in the electrolytes level in the cell. However since the ratio of sodium to potassium ions did not change much from day 1 to day 10 in the media, the imbalance in the cells can be neglected.

When comparing the antibacterial assays to the biocompatibility assays, the lactate production assay from Section 5.3.3.2 and the LDH assay from Section 5.3.4.3 followed similar principles whereby the activity of lactate was analysed. However, the results from the antibacterial assay (Section 5.3.3.2) were positive while the results from biocompatibility assay was negative (Section 5.3.4.3). This was because both assays involved one of the metabolic redox reactions happening in cells whereby the NAD is converted to NADH and vice versa through redox reactions. For *S. aureus*, the final amount of lactate produced by the cells were measured, hence accounting for the positive results. For the biocompatibility assay, the activity of the enzyme LDH was measured whereby NADH was converted to NAD through oxidation. The measurements were based on the decrease in NADH, hence accounting for the negative results as seen in Figure 5.15.

5.4.3 PCR data for markers in osteoblast cells

The genetic analysis of the osteoblast cells exposed to the coatings provided a deeper insight into the molecular changes in the cells for the synthesis of various proteins. Hence the markers used in this study provided an overview of what was being expressed in the cells before the respective biochemical reaction took place.

On day 4, the genes representing the physiological activity of the cells (ALP, RUNX2, OC) on TiO₂-Ag7 and TiO₂-Ag7-HA were downregulated with respect to those on TiO₂ as shown in Figure 5.20. And by day 10 they were upregulated. The cells that were attached on the coatings expressed also a high level of adhesion markers, FAK by day 10 which suggested that the cells on that day behaved similarly to those on TiO₂ (Figure 5.19). The inflammatory markers as well were downregulated on day 4 which lead to a conclusion that on exposure, TiO₂ caused the cells to express more inflammatory markers as compared to the coated samples (Figure 5.21). However the contrary was observed on day 10 which led to the conclusion that with time, the cells on TiO₂-Ag7 and TiO₂-Ag7-HA were faced with a higher inflammatory attack as compared to those on TiO₂. Nonetheless the cells were able to recuperate before day 10 due to the lower expression of inflammatory markers and higher expression of SOD on day 10 than on day 4 as seen in Figure 5.22. If the cells were left longer they might have had the chance to grow more.

Both TiO₂-Ag7 and TiO₂-Ag7-HA exhibited high level of antibacterial properties with TiO₂-Ag7 being better. The presence of nano HA did not

affect the biocompatibility of the coating significantly as compared to TiO₂-Ag7. Besides, the HA part of the coatings got delaminated after exposure to cells, during handling in the laboratory. Several future works can be derived from this stage. First the experiment should be repeated with the aim of confirming the delamination. Another option is to optimise the adhesion strength of the nano HA coating to TiO₂-Ag7 using a modified version of the technique used in Chapter 2 and then repeat the experiment. Reducing the toxicity level expressed by the cells on TiO₂-Ag7 is another future work as well.

5.5 Conclusion

Silver nanoparticle containing composite coatings were successfully fabricated on the surface of Ti-6Al-4V discs in this chapter. The silver nanoparticles formed were uniformly distributed with no clustering and full coverage. The addition of nano HA to the latter coating resulted in another uniform coating but with micro-cracks. Both coatings exhibited a high level of bactericidal activity but the biocompatibility of the coatings were compromised slightly at the beginning. As from day 10, the cells improved physiologically.

Chapter 6

TiO₂ nanotubes embedded with zinc oxide nanostructures on Ti-6Al-4V alloy and their respective antibacterial properties and biocompatibility

6.1 Introduction

Zinc oxide nanoparticles are considered to have more antibacterial properties than zinc oxide on its own due to the higher volume to surface area ratio which may facilitate a more reactive surface and/or the release of biocidal zinc ions (Xie *et al.*, 2011). The antibacterial properties of Zn NPs have been assigned to both free zinc ions and the size of the nanoparticle on as a whole and various mechanisms of action have been explored (Sirelkhatim *et al.*, 2015). Zinc oxide nanoparticles are proposed for use in food products and are considered to be safe when used within limit (Xie *et al.*, 2011). Zinc oxide has been successfully used in the food industry and hence is being considered for use on implants with the aim of providing targeted drug delivery.

Several studies have investigated the use of zinc oxide embedded in the nanotubes of TiO₂ as an antibacterial coating on what titanium based metal (Liu *et al.*, 2014; Roguska *et al.*, 2014). And there are various methods that can be used to synthesise the zinc oxide on the nanotubes as described in Chapter 1. Nonetheless, the required uniformity and coverage of the zinc composite coating has not been achieved yet. While being able to deliver antibacterial properties to some extent, the coatings were toxic to human cells (Liu *et al.*, 2014). Hence this chapter investigates the synthesis of the ZnO/TiO₂ nano-composite coating followed by the characterisation of the latter using various techniques. Furthermore nano-Ha was added to the latter coating and characterised as well. Afterwards, the antibacterial properties and biocompatibility of the coatings were assessed using various techniques.

6.2 Materials and Methods

Again in this chapter, the treated nanotubes, at high temperature and pH, were used for the scaffold for the growth of nano ZnO coating.

6.2.1 ZnO composite coatings synthesis

A modified version of the protocol used by Liu *et al.* (2014) was used for the synthesis of nano-ZnO on TiO₂ nanotubes (Liu *et al.*, 2014). The Ti alloy with the functionalised TiO₂ nanotubes was immersed in a 1 : 2 mixture of 0.075 M analytical grade ZnNO₃ (prepared in ultrapure deionised water) and 0.1 M hexamethylenetetramine, with 2 mg of analytical grade citric acid (Liu *et al.*, 2014). The concentration of zinc nitrate was optimised in a pilot study first as shown in Appendix B. The mixture was subsequently heated to 80 °C with continuous stirring using a magnetic hot plate. After 2 hours in the mixture, the alloy discs of TiO₂ nanotubes, now with the ZnO nanocoating present, were sonicated in deionised water for 10 minutes to wash the coatings and remove any loosely bound materials and dissolved zinc.

The next step involved stabilising the crystalline structure of the nano zinc oxide onto the TiO₂ (hereafter, called TiO₂-ZnO). Little is known about the formation of ZnO crystals on the surface of novel structures such as TiO₂ nanotubes and so this step was performed at three different annealing temperatures (350, 450 and 550 °C) in order to explore the resulting material morphology, surface roughness, and chemical composition. The annealing was performed in triplicate, by gradual heating of the samples to the required temperature in a furnace (Carbolite RWF 1200). The samples were

maintained at the desired final temperature for 1 hour, before being allowed to gradually cool to room temperature. The resulting coatings are hereafter termed as TiO₂-ZnO/350, TiO₂-ZnO/450 and TiO₂-ZnO/550 in relation to the annealing temperatures of 350, 450 and 550 °C respectively. A control for the annealing included unheated TiO₂-ZnO discs for comparison. The resulting discs were examined for morphology and elemental composition of the surfaces (in triplicate) by scanning electron microscope (JEOL7001F SEM) coupled with energy-dispersive X-ray spectroscopy (EDS). The EDS composition was described using the AZtec analysis software supplied with the EDS attachment (Oxford Instruments, Oxford, UK). In addition, surface roughness was measured using an Olympus Laser Microscope LEXT OLS3100.

6.2.2. Addition of hydroxyapatite on TiO₂-ZnO

Another composite coating was synthesized by allowing hydroxyapatite to grow on TiO₂-ZnO with the aim of improving the biocompatibility of the composite. Each of the zinc oxide-coated materials from the step above (from all annealing temperatures) were separately immersed in 3 times the normal concentration of a simulated body fluid (3SBF) which was prepared using Kokubo's recipe whereby the concentrations of the ions used were (in mM): Na⁺ 426, K⁺ 15.0, Mg²⁺ 4.5, Ca²⁺ 7.5, Cl⁻ 443.4, HCO₃⁻ 12.6, HPO₄²⁻ 3.0, SO₄²⁻ 1.5 mM (Kokubo, 1997). 3SBF was used instead of SBF in order to prevent the loss of extra zinc from the nano ZnO coating while giving the nano HA to form on the latter surface. The exposure was maintained at 37 °C for 24 hours with the aim of growing hydroxyapatite (HA) crystals on the

surface of the samples (Kokubo, 1997). After 24 h, the resulting HA-coated composites were removed, washed in deionised water, then air dried and examined by electron microscopy for morphology, and for surface roughness as above. The 3SBF media were retained for metal analysis to determine any losses of Zn from the discs and the expected decrease of Ca and P in the media during this final step of the synthesis. The spent 3SBF media were acidified with 1-2 drops of 70 % nitric acid and stored until required for trace metal analysis.

6.2.2 Antibacterial test of the nano ZnO composite coating

The antibacterial properties of the nano ZnO composite coating with and without HA was then exposed to *S. aureus* at 37 °C in BHI broth as explained in Section 4.4.1 (n=15 per treatment). A Live/Dead assay was used to test for the viability of the bacteria as described in Section 4.4.2 (n=6 per treatment). Then, the concentration of lactate produced by the bacteria attached to the surface of the coating and the bacteria exposed to the coated discs was tested using a lactate production assay as described in Section 4.4.3 (n=6 per treatment). The concentration of zinc ions released from the coating in the exposed bacteria and the attached bacteria were then measured using ICP-MS using the methods explained in Section 4.6. Afterwards, the discs were viewed under scanning electron microscope as explained in Section 4.7 whereby the presence of bacteria on the coatings were visually confirmed.

6.2.3 Biocompatibility test of the nano ZnO composite coating

Once the antibacterial properties of the composite coatings were analysed, the coated discs were exposed to primary human osteoblast cells in DMEM media at 37 °C for 10 days , with the aim of testing the biocompatibility properties of the latter coatings as per Section 4.5.1 (n=12 per treatment). In this context, biochemical assays and genetic analysis were performed. In terms of biochemical assays (Section 4.5.3), protein assays, ALP assay and LDH assay were performed to test the viability and metabolic activity of the osteoblast cells exposed to the coatings and controls (n=3 per treatment). For the genetic analysis, comparative Ct was used to analyse the genetic expression of FAK, RUNX2, CA1, ALP, OC, COX2, IL6, TNFa and SOD in osteoblast cells exposed to the coatings with respect to β -actin which was measured against the latter expression in the control (TiO₂ Nts) (n=6 per treatments). The details of the experiment are explained in Section 4.5.4. The change in ionic concentration of Ag, Na, Ca, P, K and Mg was measured in the cell homogenate and exposed media, using ICP on day 1, 4, 7 and 10 of exposure of the coatings to the cells (Section 4.6). Last the attached cells to the coated and uncoated discs were viewed under high resolution microscope as per Section 4.7.

6.3 Results

6.3.1 Microscopic imaging and surface analysis

The morphology and chemical composition as measured by SEM/EDS of the TiO₂ at each step of the synthesis (i.e., addition of ZnO and then HA) is

shown in Figure 6.1-6.5. The surface of the coatings were viewed at a low magnification first with the aim of confirming the surface coverage while the higher magnification highlighted the morphology of the nanostructures. Figure 6.1A and B show the TiO₂ nanotubes on the surface of the titanium alloy with Figure 6.1 C being the EDS analysis of the nanotubes. The growth of the TiO₂ NTs gave generally good coverage (Figure 6.1A) of the alloy. The material is known to consist of two different phases (Refer to chapter 2); the alpha-phase (α , the majority of the coating) and the beta phase (β , the depressions in Figure 6.1A). The additions of ZnO, regardless of the annealing temperature, gave complete coverage (Figures 6.2-6.5). After the exposure to 3SBF, nano-HA was grown on the nanotubes in clusters as seen in Figure 6.1D. The presence of Ca and P was confirmed by EDS analysis in Figure 6.1 E.

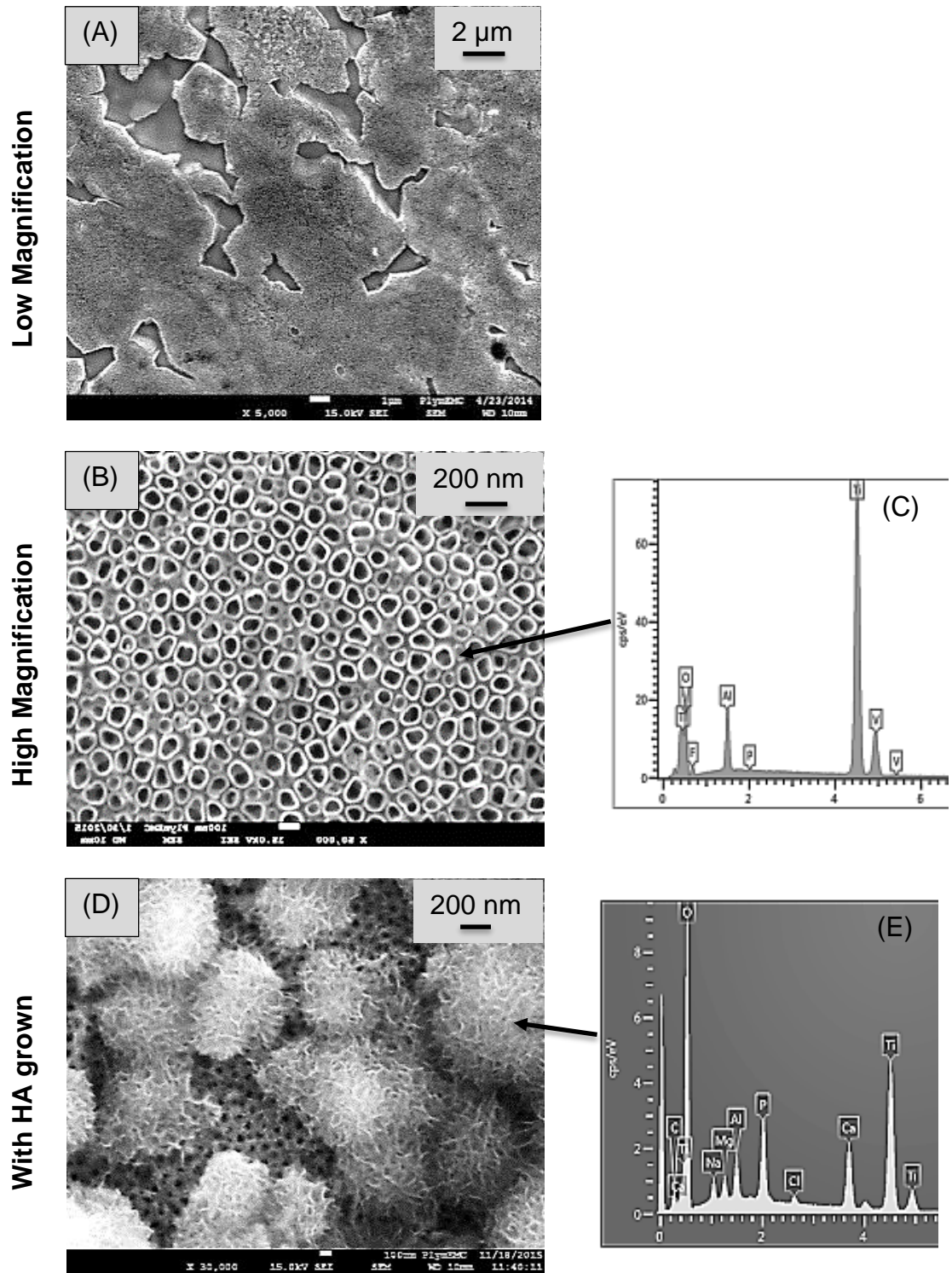


Figure 6.1: SEM images of Ti alloy with (A) the self assembled titania nanotubes (TiO_2) at (A) $\times 5000$ and (B) $\times 50000$ magnification with the (C) the EDS analysis of part of 6.1 B. (D) TiO_2 with HA on the surface with (E) the EDS analysis of the HA particle shown.

Once ZnO was grown on the nanotubes, the nano-porous structure of the surface was maintained as shown in Figure 6.2 A and B. TiO₂-ZnO had a nano-needle structure with a thickness of less than 100 nm and length less than 1 μm and uniform distribution over the surface of the nanotubes. The EDS analysis confirms the presence of zinc, oxygen, titanium, vanadium and aluminium as expected as shown in Figure 6.2 C. Once HA was grown on the ZnO, the nano-needle structure was lost as seen in Figure 6.2 D, with the underlying ZnO not exposed. The presence of Ca and P was confirmed by EDS analysis as shown in Figure 6.2 E.

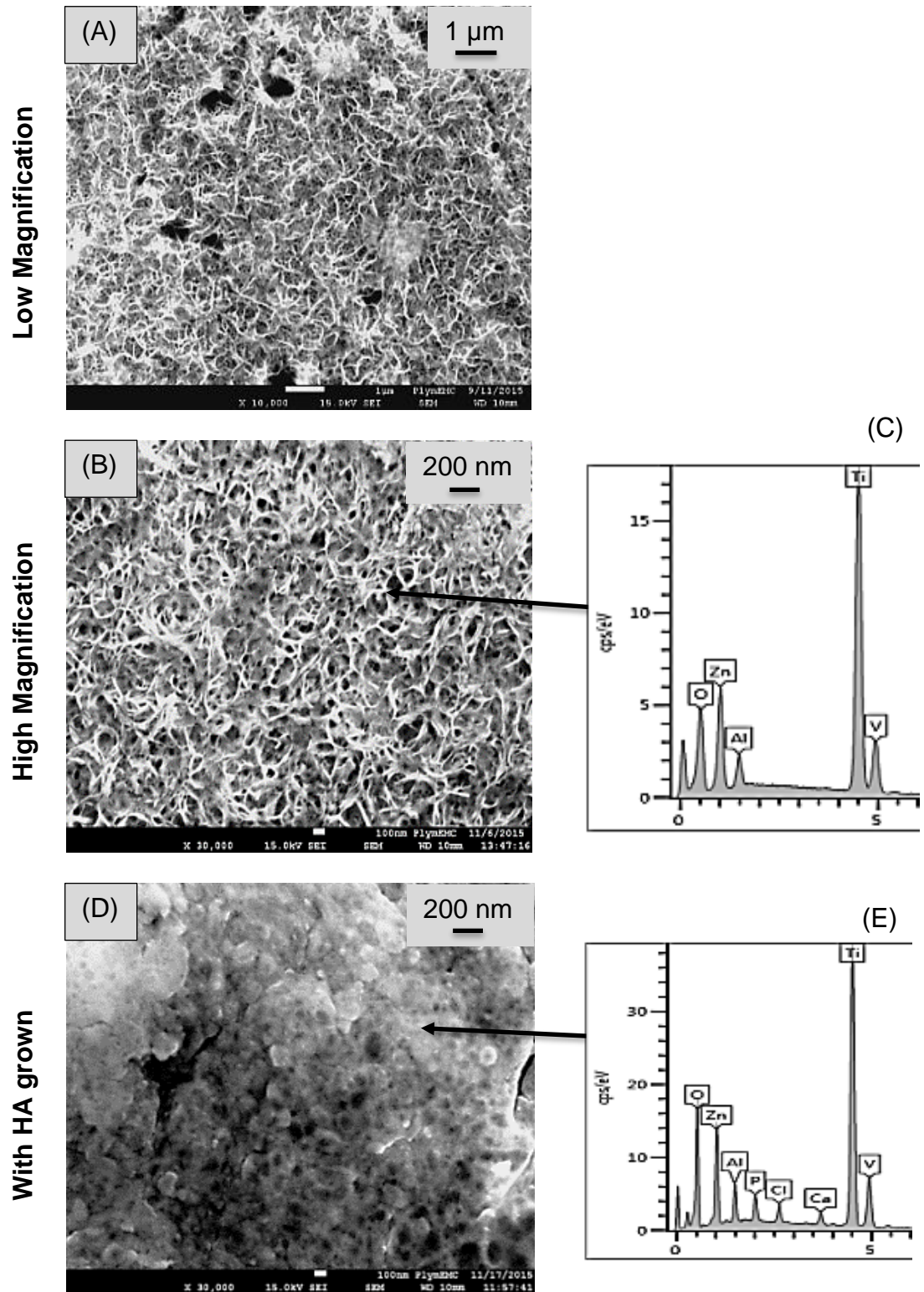


Figure 6.2: SEM images of Ti alloy with (A) ZnO grown on the TiO₂ without any heat treatment at (A) ×10000 and (B) ×30000 magnification with the (C) the EDS analysis of part of 6.2 B. (D) TiO₂-ZnO with HA on the surface with (E) the EDS analysis of the HA particle shown.

When TiO₂-ZnO was heated to 350 °C, the uniformity and coverage of the coating was maintained with similar morphology as shown in Figure 6.3 A and B with more density. However the level of zinc on the surface as measured by EDS reduced as seen in Figure 6.3 C. The nano-HA grown on the surface had a porous structure as shown in Figure 6.3 D with the presence of Ca and P confirmed by EDS (Figure 6.3 E).

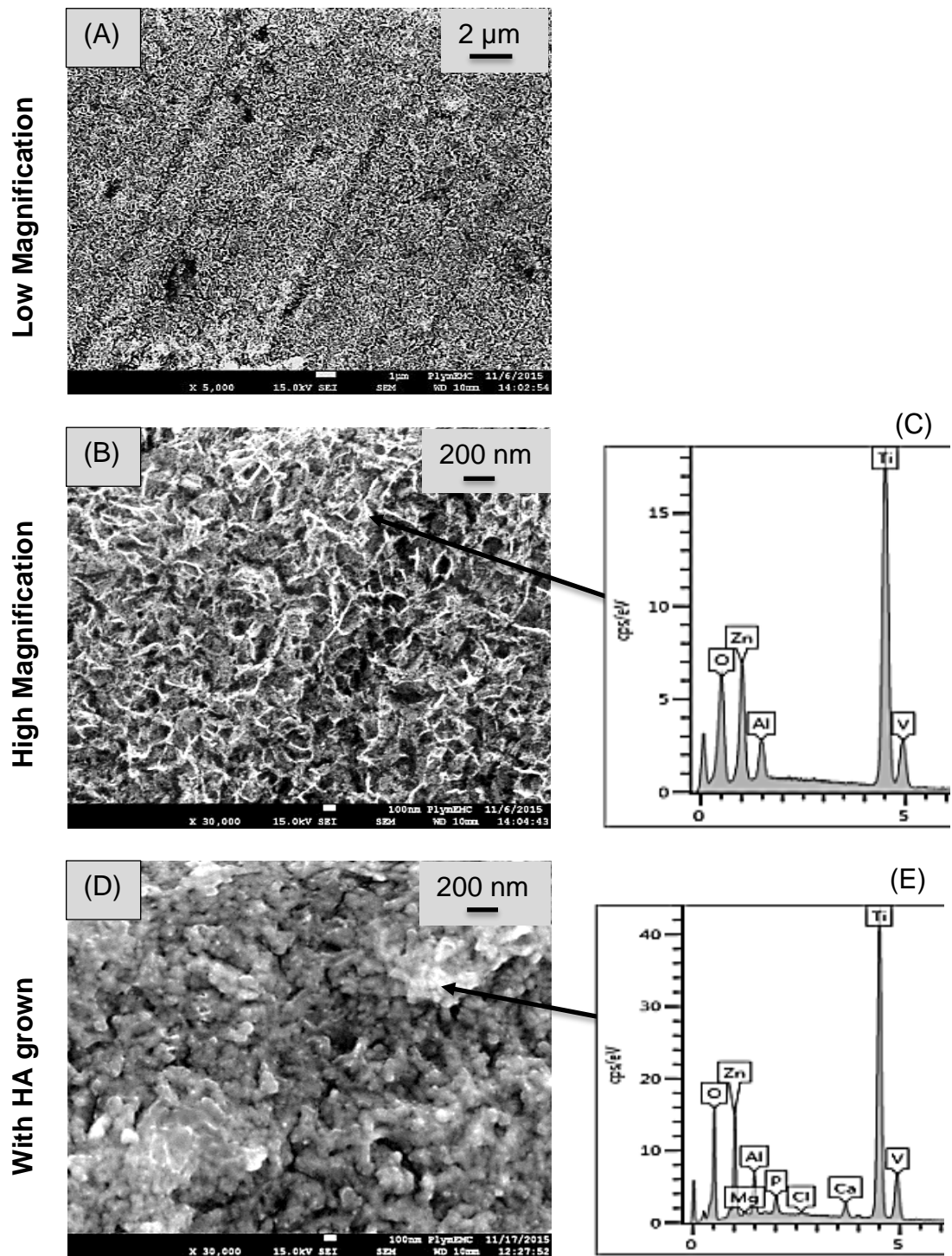


Figure 6.3: SEM images of Ti alloy with (A) ZnO grown on the TiO₂ after 350 °C heating viewed at (A) ×5000 and (B) ×30000 magnification with (C) the EDS analysis of part of 6.3 B. (D) TiO₂-ZnO/350 with HA on the surface with (E) the EDS analysis of the HA particle shown.

When heated to 450 °C, the ZnO started losing its nanostructures as seen in Figure 6.4 A and B. However there was still a uniform and full surface coverage (Figure 6.4 A). It was also observed that the porosity of the ZnO was maintained. The crystals of HA became cubic in shape with more clustering as seen in Figure 6.4 D.

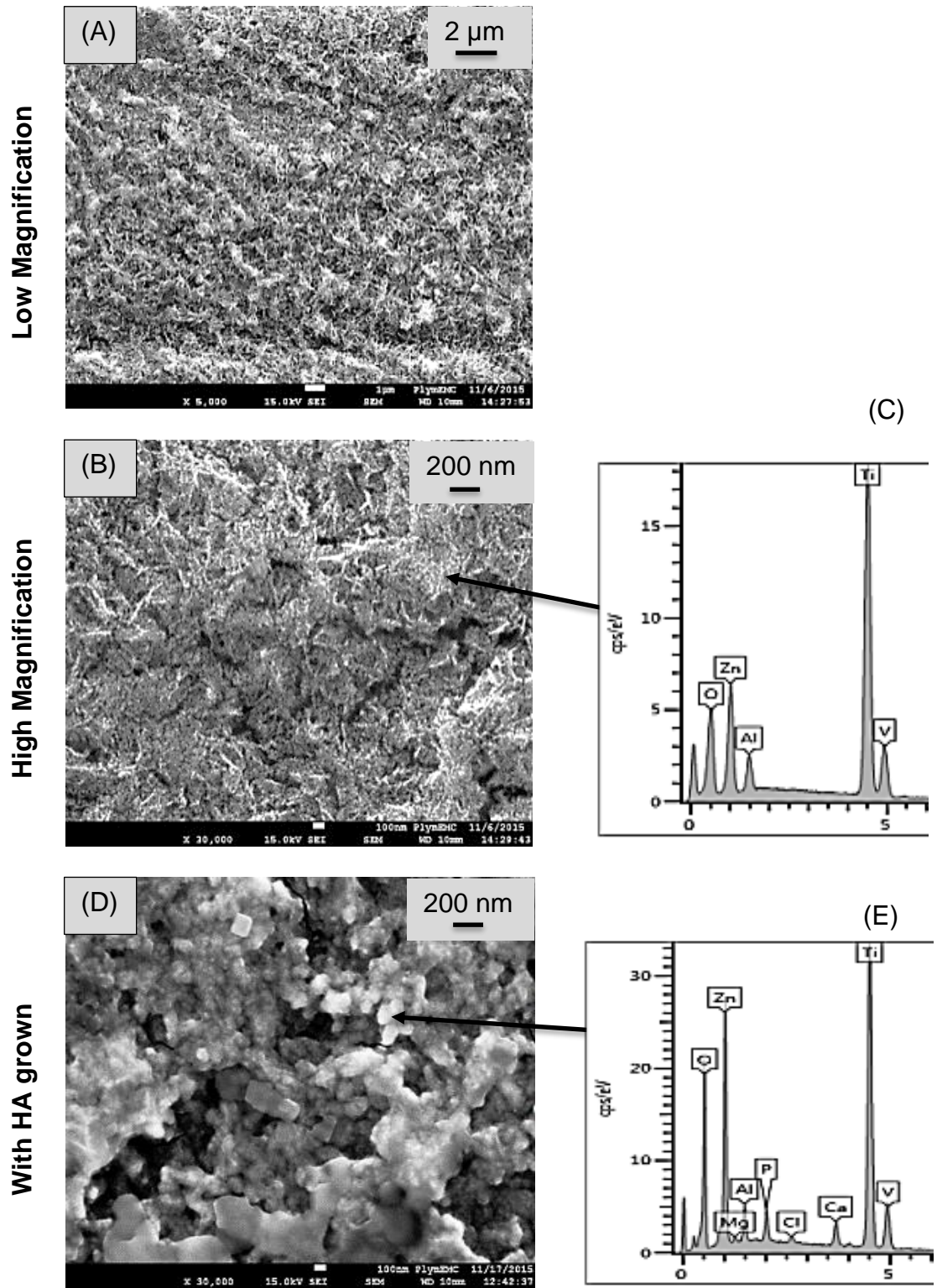


Figure 6.4: SEM images of Ti alloy with (A) ZnO grown on the TiO₂ after 450 °C heating viewed at (A) ×5000 and (B) ×30000 magnification with (C) the EDS analysis of part of 6.4 B. (D) TiO₂-ZnO/450 with HA on the surface with (E) the EDS analysis of the HA particle shown.

Heating the zinc oxide to 550 °C caused the coating to become denser with the lack of full surface coverage as seen in Figure 6.5 A. The porosity of the coating was also reduced (Figure 5.6 B). The clustering of the HA particles on the surface of TiO₂-ZnO/550 was even higher with almost no gaps in between as seen in Figure 5.6 D.

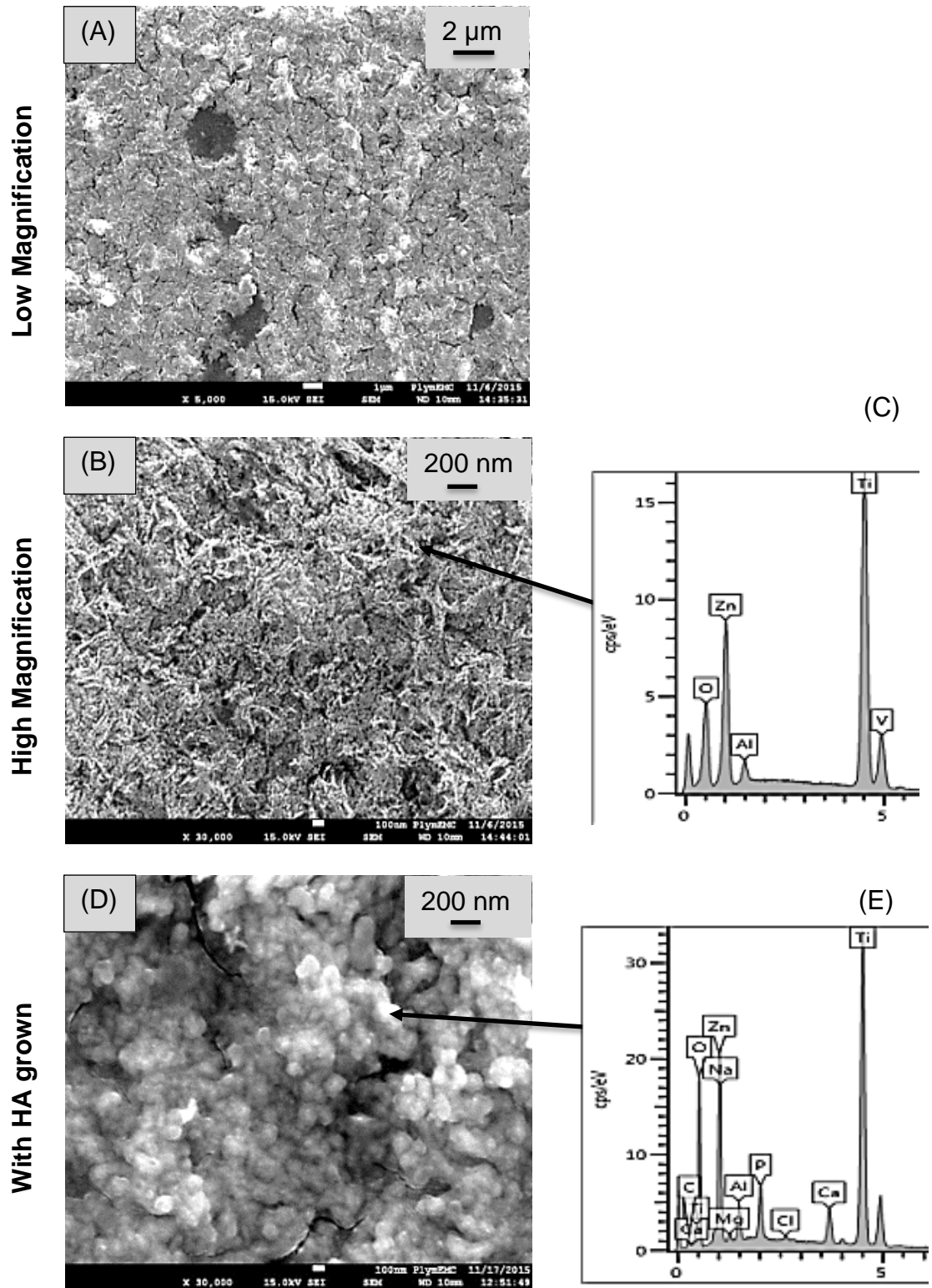


Figure 6.5: SEM images of Ti alloy with (A) ZnO grown on the TiO₂ after 550 °C heating viewed at (A) x5000 and (B) x30000 magnification with (C) the EDS analysis of part of 6.5 B. (D) TiO₂-ZnO/550 with HA on the surface with (E) the EDS analysis of the HA particle shown.

One of the concerns regarding the incubation of the partially made composite in 3SBF was that, while a HA layer might be evolved, this would be at the expense of considerable Zn leaching from the material surface. This was not the case (Figure 6.6 and 6.7). In Figure 6.6A, the EDS measurements of the composite before and after incubation in the 3SBF media are shown. While there was a loss of some Zn from the surface as measured by EDS, this was only about 1/5 of the total Zn present regardless of the previous annealing temperature. The visual observation of the final surface morphology in Figure 6.1-6.5 were confirmed by surface roughness measurements (Figure 6.6B). The presence of zinc oxide nanostructure on the coating increased the roughness, compared to the TiO₂ nanotubes coating alone (One-way ANOVA , $p < 0.05$). The annealing temperature at the ZnO addition step of the synthesis also influenced the final outcome on surface roughness; with the greatest roughness values associated with the higher annealing temperatures (One-way ANOVA , $p < 0.05$). However, the final step of HA additions tended to also decrease the surface roughness of each composite (One-way ANOVA , $p < 0.05$, Figure 6.6 B).

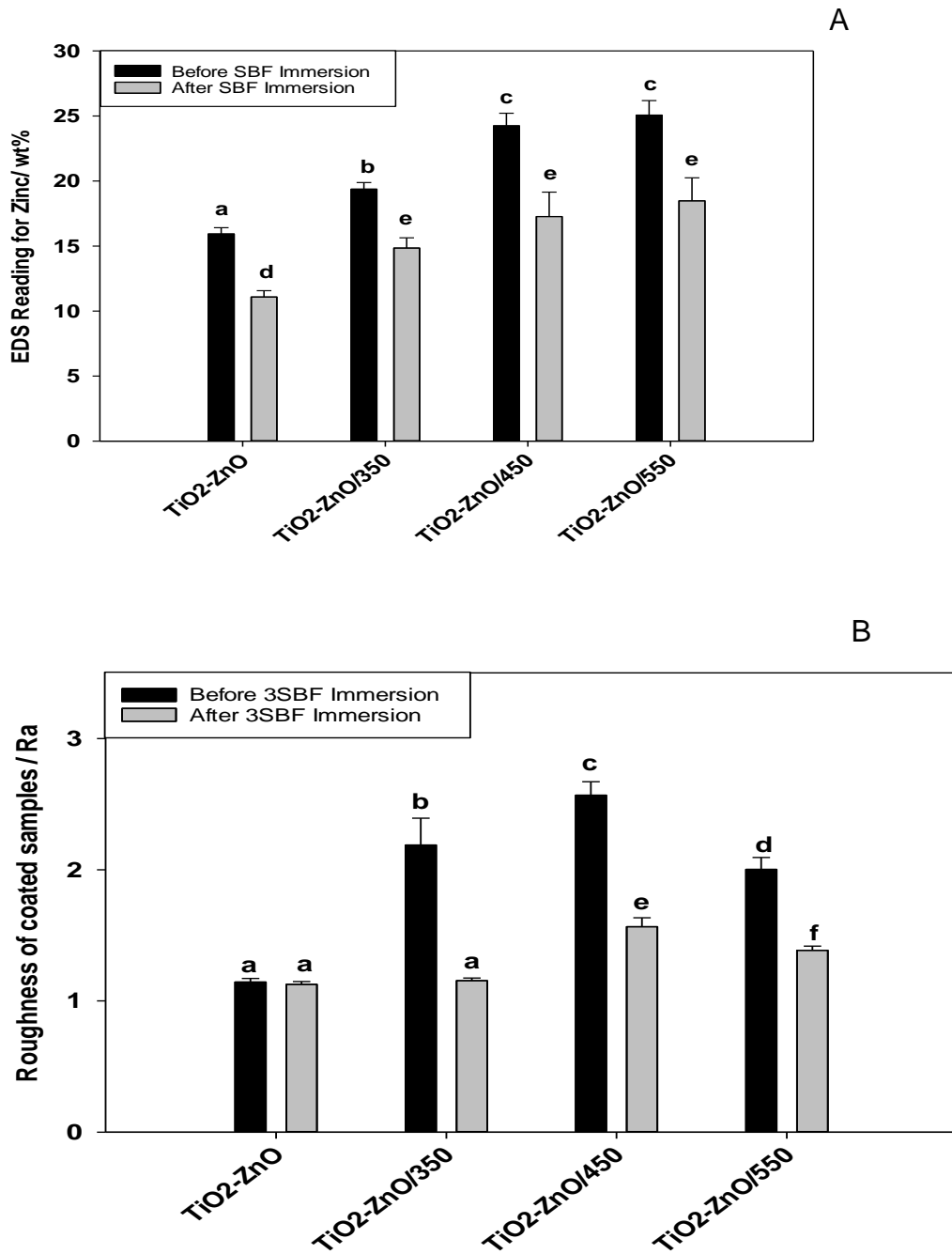


Figure 6.6: (A) EDS reading for Zinc from the coatings and (B) Roughness of the resulting coating.

In terms of total Zn metal lost to the external medium (Figure 6.7 A, One-way ANOVA , $p < 0.05$), there was a clear relationship with the annealing temperature in the ZnO addition step; with the highest temperatures resulting

in less Zn leaching. The 3SBF media showed the expected trend of decreasing Ca and phosphate concentrations following the incubation (Figure 6.7 B), consistent with ion adsorption to the surface during HA formation on the composite. The samples at the highest annealing temperature for ZnO coating addition, resulted in the greatest decreases in Ca concentration in the 3SBF media (One-way ANOVA , $p < 0.05$).

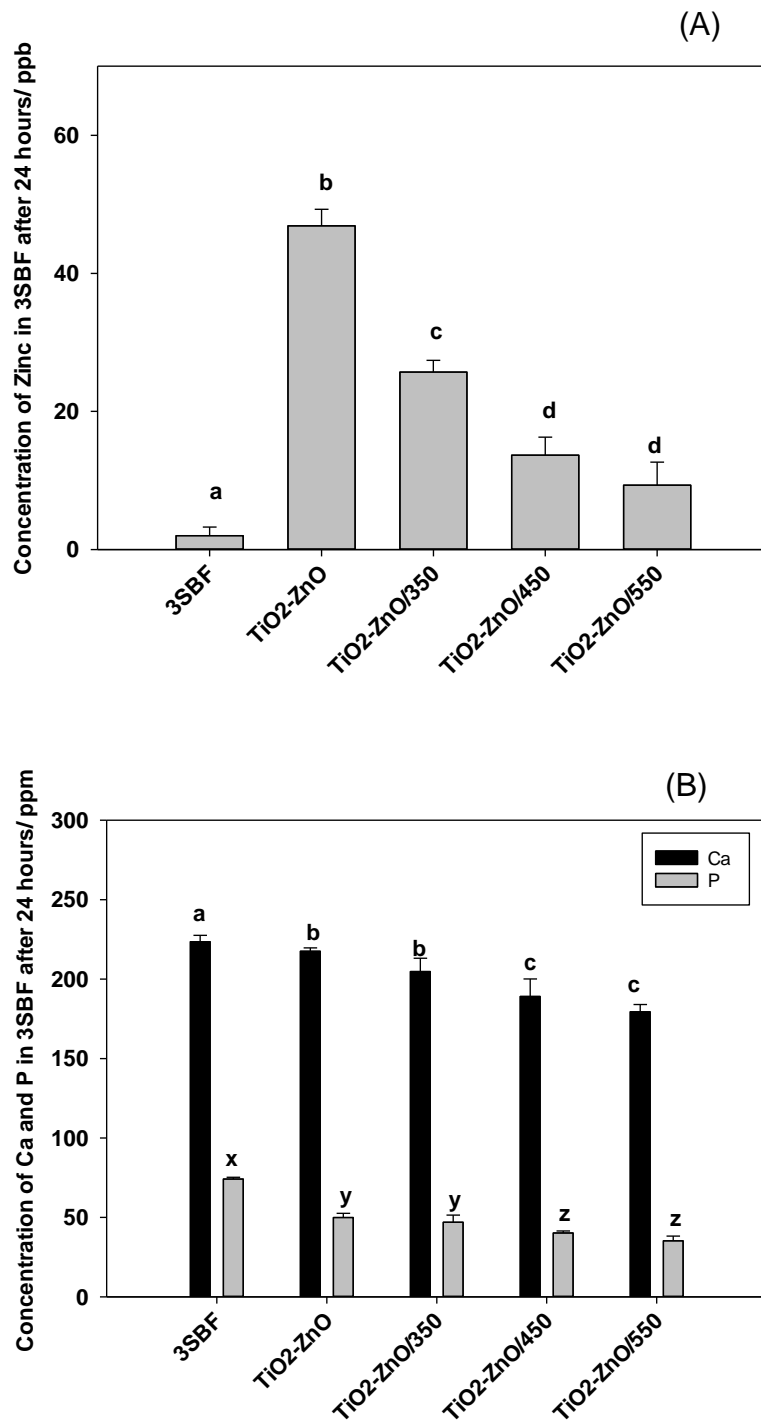


Figure 6.7: ICP readings of the 3SBF after 24 hours exposure for (A) zinc and (B) calcium and phosphorus

For the logistics for biological testing, one 'best' composite had to be selected for experimental work. After considering all the characterisation

information, TiO₂-ZnO /350 and TiO₂-ZnO-HA /350 were chosen as the coated samples to be taken forward for further testing. This was selected on the basis that the ZnO coating was uniformly structured covering the whole surface, and while the deposition of HA was also good, the gaps in the HA would allow some direct access to the biocidal ZnO coating. Subsequently, further batches of titanium alloy discs coated with the composite using the 350 °C annealing temperature were prepared. The composites were then sterilised under 36.42-40.72 kGy gamma radiation (Becton, Dickinson and company, Swindon, UK), as we have done previously with nano-coated Ti alloys (Besinis, De Peralta & Handy, 2014).

6.3.2 Dialysis Experiment

The dialysis experiment was performed with the aim of analysing the dissolution of zinc ions from the TiO₂-ZnO/350 and TiO₂-ZnO-HA/350 coating in the presence of simulated body fluid. As a control for the SBF, the dialysis bag without any samples maintained a low or no zinc ions in the beaker and the same was observed for the control for the samples, TiO₂ as shown in Figure 6.8A. Hence the dialysis data for the samples were independent of changes in the SBF content throughout the 24 hours of the dialysis. Figure 6.8A also shows that the rate of release of zinc ions released from the TiO₂-ZnO/350 was higher than that from TiO₂-ZnO-HA/350 due to the steeper rise to the maximum value in the diffusion curve for TiO₂-ZnO/350. The initial amount of zinc present in both coatings were the same and although during the growth of HA for TiO₂-ZnO-HA/350, some zinc ions were lost, the presence of the HA reduced the release of zinc from the coating. The curves

from the dialysis data became stable at about 4 ppb for TiO₂-ZnO-HA/350 as compared to 8 ppb for TiO₂-ZnO/350 as shown in Figure 6.8A. Figures 6.8B and C illustrated the diffusion curve for calcium and phosphorus respectively for the 24 hours. Since the SBF itself contains calcium and phosphorus, the diffusion curve for calcium and phosphorus was normalised with respect to the concentration of calcium and phosphorus in the simulated body fluid. The diffusion rate of calcium from the dialysis bag to the beaker was the same for the coated samples and the controls. The diffusion of the ions reached stability in the controls within 10 hours while for both TiO₂-ZnO/350 and TiO₂-ZnO-HA/350, stability was not reached within 24 hours.

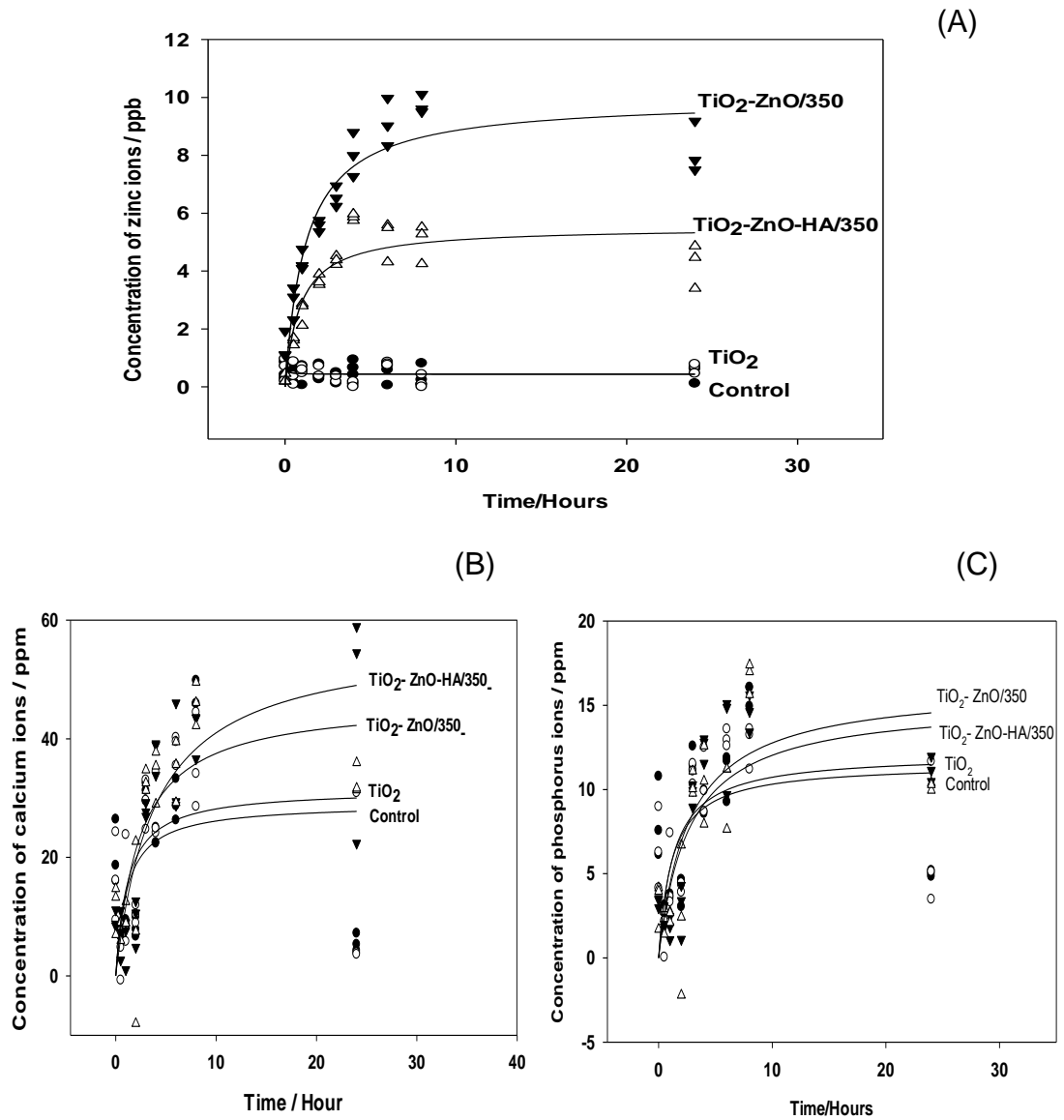


Figure 6.8: Concentration of (A) zinc ions in the acidified SBF from the dialysis beakers as measured by the ICP-MS instrument, (B) calcium ions and (C) phosphorus ions in the acidified SBF from the dialysis beakers as measured by the ICP-OES instrument.

There was no significant difference in the concentration of zinc in the dialysis bag and the beaker (One-way ANOVA, $p > 0.05$, $n = 3$) after 24 hours at the end of the dialysis experiment displayed in Figure 6.9A. At the end of the 24-hours experiment, the concentrations of calcium in the bag and the beaker were similar as seen in Figure 6.9B (Transformed One-way ANOVA, $p > 0.05$, $n = 3$). Similar observations were made in the case of phosphorus ions diffusion as shown in Figures 6.9 B. The dialysis experiment showed a higher release of zinc from $\text{TiO}_2\text{-ZnO}/350$ as compared to $\text{TiO}_2\text{-ZnO-HA}/350$. The majority of the zinc released had less than 12 KDa mass.

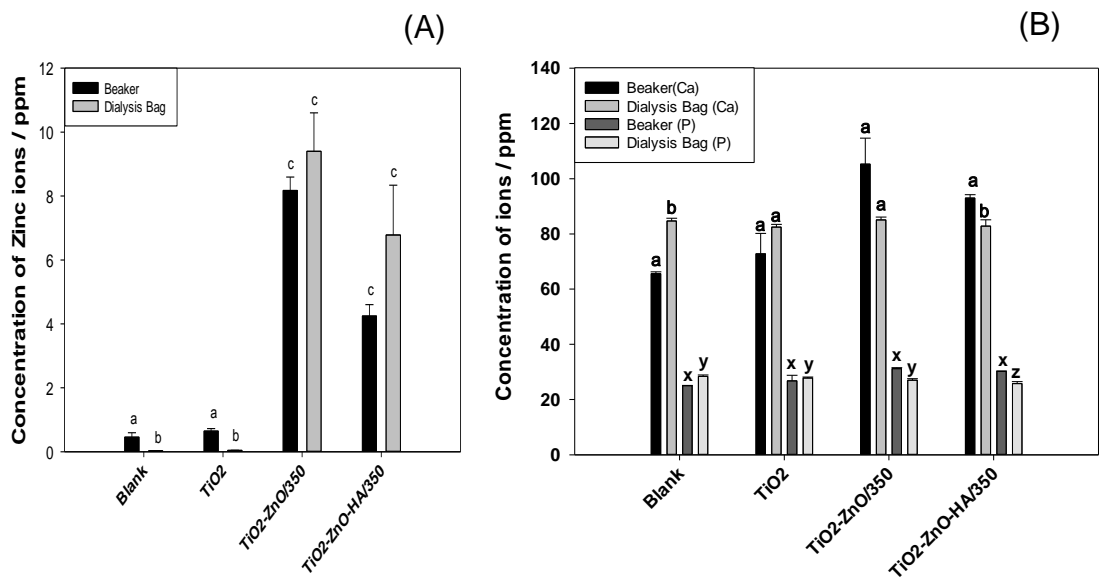


Figure 6.9: Concentration of (A) zinc ions in the acidified SBF from the beaker and the dialysis bag after 24 hours (Mean \pm S.E.M, Transformed One-way ANOVA, $n = 3$) and (E) calcium and phosphorus ions in the acidified content of the beaker and the dialysis bag after 24 hours (Kruskal-Wallis, $n = 3$). The different alphabets show the significant differences in between the different samples on different days at 95.0 % confidence level.

6.3.3 Antibacterial Properties of nanocomposite coating

6.3.3.1 Viability of *S. aureus*

S. aureus had a good viability when grown in BHI alone as a negative control with a percentage of live cells being 100 ± 2.6 % (% mean \pm S.E.M, n = 6) and the viability was significantly higher than the other controls and the samples (Kruskal-Wallis, $p < 0.05$) as illustrated in Figure 6.10 A. ZnCl_2 showed significantly lower cell viability than the negative controls with still 49.9 ± 1.1 % live cells, while the nZnO treatment had even lower cell viability than ZnCl_2 with 1.3 ± 0.3 % live cells (Kruskal-Wallis, $p < 0.05$, n=6). The $\text{TiO}_2\text{-ZnO}/350$ and $\text{TiO}_2\text{-ZnO-HA}/350$ treatments had 22.0 ± 2.0 % and 30.9 ± 3.0 % live cells respectively (Figure 6.10 A). *S. aureus* had lower viability in the exposed media in general as shown in figure 6.10 B with the control having 72.5 ± 2.9 % live cells and the nZnO treatment having the lowest viability with 1.8 ± 0.2 % live cells. In the exposed media, the percentage of live cells in ZnCl_2 (6.7 ± 1.6 %) was different than that in nZnO (Figure 6.10B, Kruskal-Wallis, $p < 0.05$; n=6). $\text{TiO}_2\text{-ZnO}/350$ and $\text{TiO}_2\text{-ZnO-HA}/350$ showed lower percentage of cells alive as compared to the control and lower than that of the cells incubated for 5 hours (19.9 ± 0.2 and 24.9 ± 2.0 % respectively). During the 24 hours exposure to *S.aureus*, $\text{TiO}_2\text{-ZnO}/350$ and $\text{TiO}_2\text{-ZnO-HA}/350$ had significantly lower percentages of live cells as compared to the negative controls but significantly higher than the positive controls in the exposed media as shown in Figure 6.10 B. $\text{TiO}_2\text{-ZnO}/350$ and $\text{TiO}_2\text{-ZnO-HA}/350$ did have lower percentage of live *S.aureus* in both the

exposed media and homogenate as compared to the negative controls
(Kruskal-Wallis, $p < 0.05$, $n = 6$).

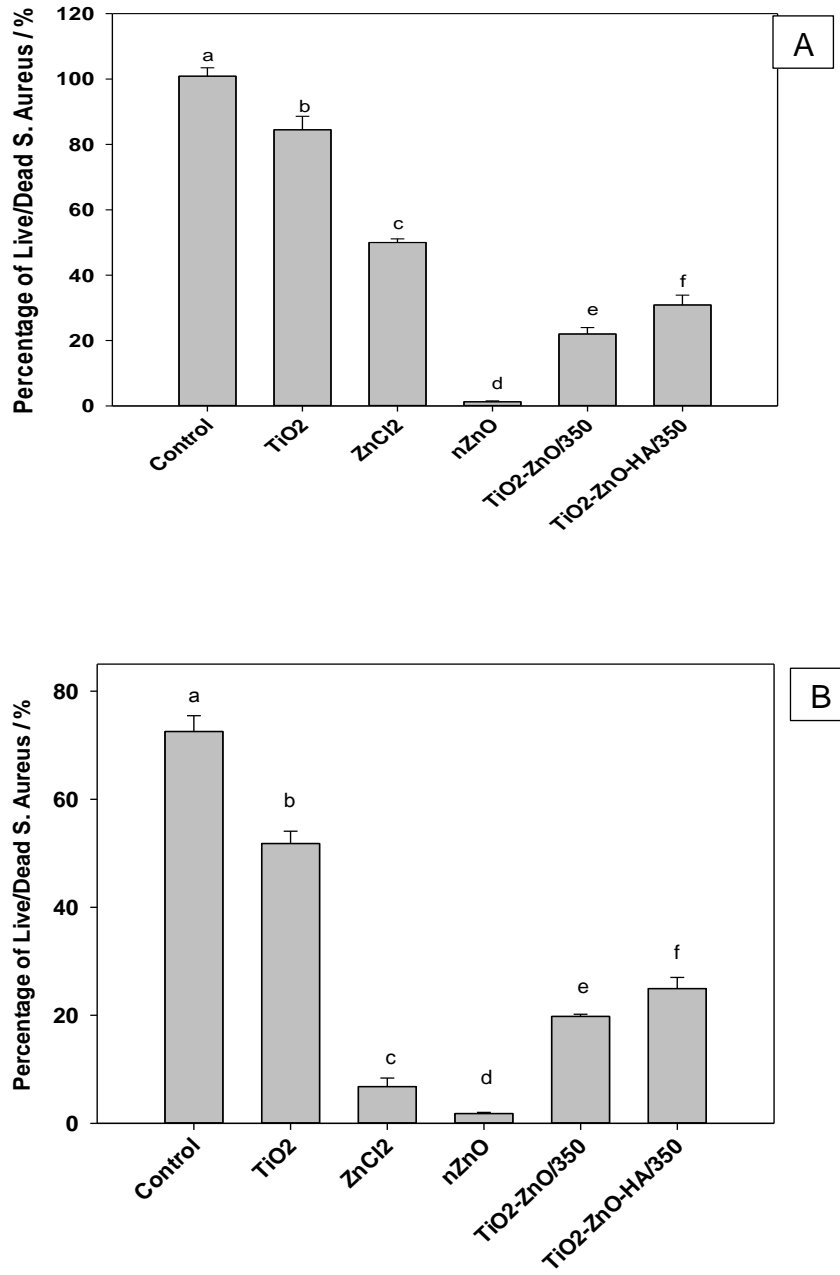


Figure 6.10 : Percentage of live to dead cells in (A) the incubated bacteria and (B) exposed media read from the calibration curve for the BacLight Live/Dead Assay (Mean \pm S.E.M, Kruskal-Wallis, $n = 6$). The different alphabets represent the statistically significant differences between the different samples at a confidence interval of 95 %.

6.3.3.2 Lactate production of exposed *S. aureus*

The microplate readings, after being analysed with respect to the calibration obtained from the standards value readings, were presented in Figure 6.11 A and B. It was observed that the negative controls, Control and TiO₂, had significantly higher amount of lactate in the exposed media (1.33 ± 0.2 mM and 1.09 ± 0.3 mM respectively; $p < 0.05$, $n = 6$) as compared to the positive controls and samples as shown in Figure 6.11 B. There was no difference in the amount of lactate produced from *S. aureus* on TiO₂ as compared to the control (Kruskal-wallis, $p > 0.05$, $n = 6$). Bacteria growing on ZnCl₂ produced more lactate as compared to nZnO and the samples. Figure 6.11 B also showed that TiO₂-ZnO/350 produced similar amount of lactate in the exposed media as compared to nZnO on its own (0.13 ± 0.03 mM and 0.37 ± 0.1 mM respectively; Kruskal-Wallis, $p > 0.05$; $n = 6$). However TiO₂-ZnO-HA/350 had 0.37 ± 0.1 mM lactate produced in the exposed media which was higher than TiO₂-ZnO/350 as seen in Figure 6.11 B (Kruskal-Wallis, $p < 0.05$, $n = 6$). Figure 6.11 A showed the lactate production observed in the different samples and controls by the bacteria which were incubated in broth for 5 hours after the overnight exposure. Similar observations to the lactate production by *S. aureus* in the supernatant were observed with higher amount of lactate present in all of them. The maximum amount of lactate produced by the bacteria were those exposed to just the Control and TiO₂ and the quantities were 3.9 ± 0.2 mM and 3.66 ± 0.3 mM respectively. The least amount of lactate was produced by the micro-organisms exposed to nZnO (0.07 ± 0.05 mM) and TiO₂-ZnO/350 (0.33 ± 0.04 mM). *S. aureus*

exposed to TiO₂-ZnO/350 and nZnO produced the least amount of lactate in both the supernatant and the incubated broth after 5 hours.

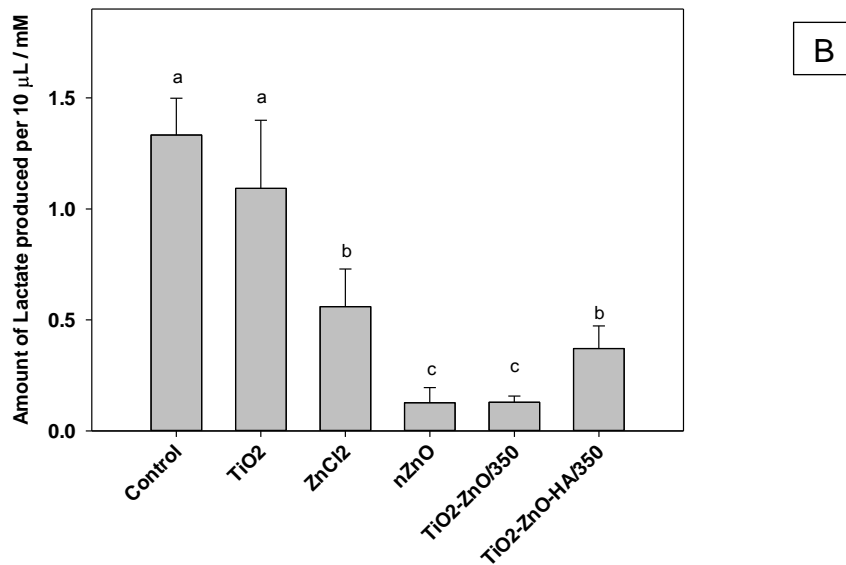
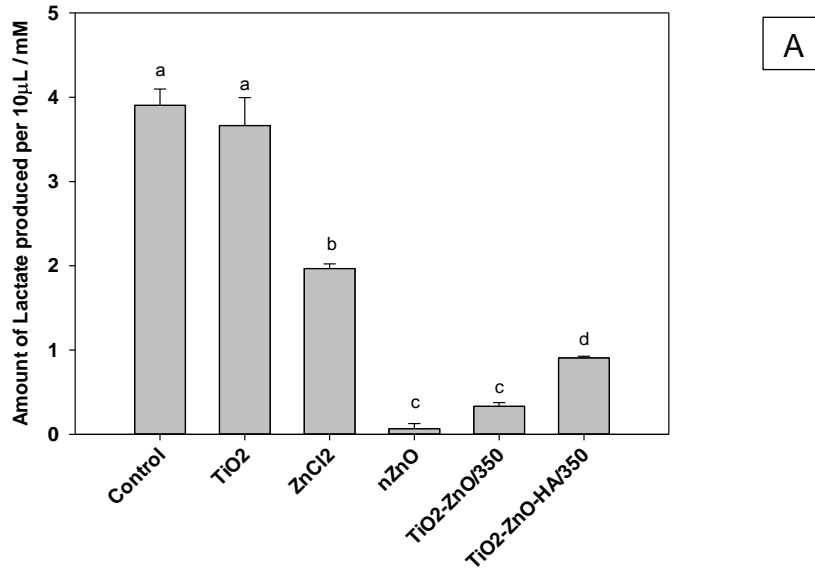


Figure 6.11: Concentration of lactate in (A) the incubated adhered bacteria and (B) exposed media after calibration (Mean ± S.E.M, Kruskal-Wallis, n=6). The different alphabets represent the statistically significant differences between the different samples at a confidence interval of 95 %.

6.3.3.3 Zinc ions release into the culture media from the coatings

Since BHI broth had some amount of zinc, the data from Control, TiO₂, TiO₂-ZnO/350, TiO₂-ZnO-HA/350, ZnCl₂ and nZnO had the concentration of zinc ions present in BHI broth deducted before any comparison was made. After the normalisation process, the results obtained were analysed and presented in Figure 6.12 A. After confirming that both negative controls did not release any extra zinc ions, the amount of zinc in the supernatant measured by ICP in TiO₂-ZnO/350 was found to have double the amount of zinc (45.0 ± 7.2 ppb) in the acidified broth as compared to TiO₂-ZnO-HA/350 (22.6 ± 0.9 ppb) (Kruskal-Wallis, $p < 0.05$; $n = 6$). These were significantly lower than the amount of zinc in the broth from ZnCl₂ and nZnO (Kruskal-Wallis, $p < 0.05$; $n = 6$). Figure 6.12 A showed the presence of lower amount of zinc in broth exposed TiO₂-ZnO/350 and TiO₂-ZnO-HA/350 as compared to the amount present in the broth exposed to the positive controls (Kruskal-Wallis, $p < 0.05$; $n = 6$).

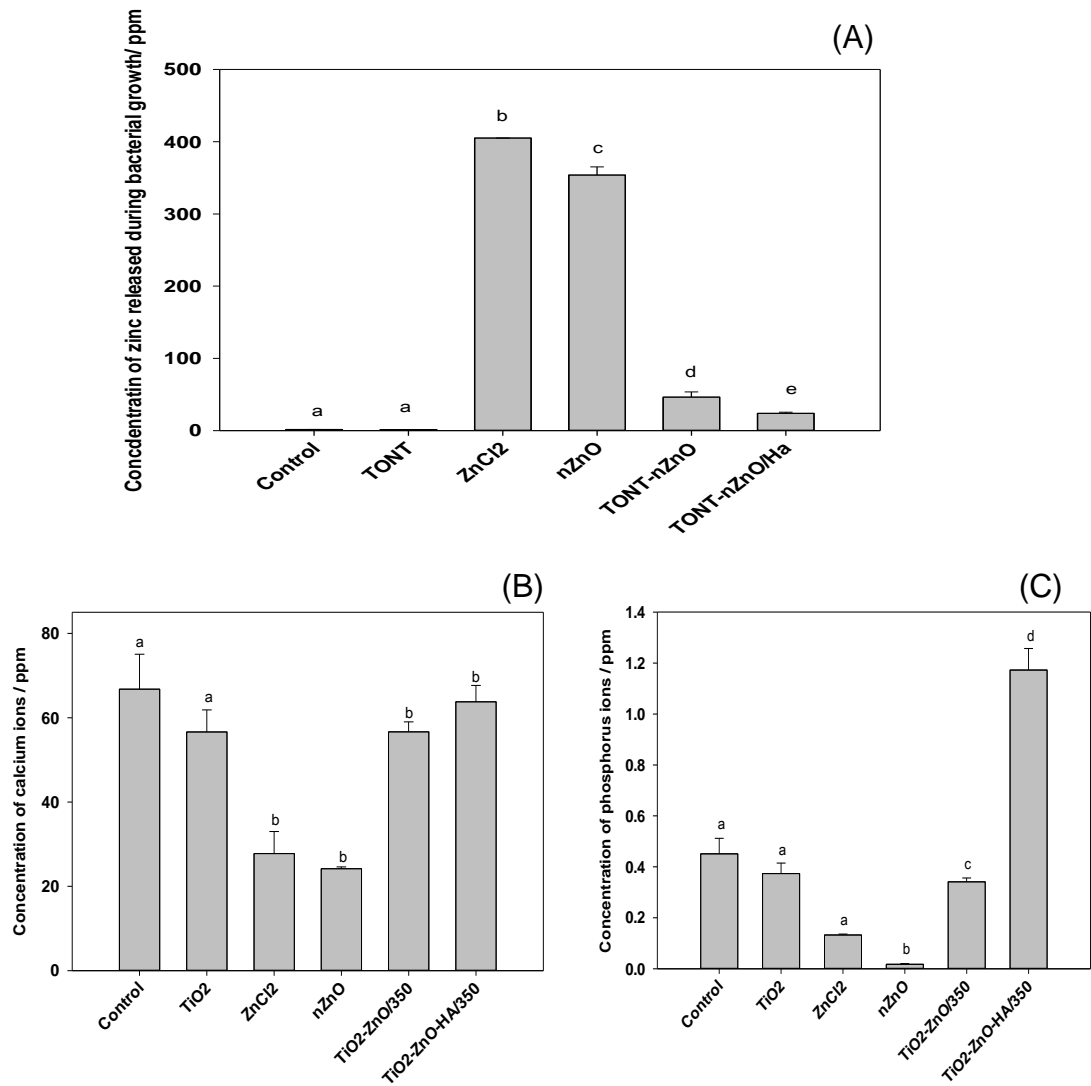


Figure 6.12 Concentration of (A) zinc ions, (B) calcium ions and (C) phosphorus ions in the acidified exposed media after overnight growth of *S.aureus* on the samples and controls read from ICP-OES (Mean \pm S.E.M, Kruskal-Wallis, n=6). The different alphabets represent the statistically significant differences between the different samples at a confidence interval of 95 %.

6.3.3.4 Bacterial Adhesion – Microscopic imaging

At the end of the incubation period, Control, TiO₂, TiO₂-ZnO/350, TiO₂-ZnO-HA/350, ZnCl₂ and nZnO were viewed under the microscope at high resolution. The wells without any sample and the sample without any zinc coating (Control and TiO₂ respectively), had micro-clusters of *S. aureus* all over the surface exposed to the micro-organism as shown in Figure 6.13A and B.

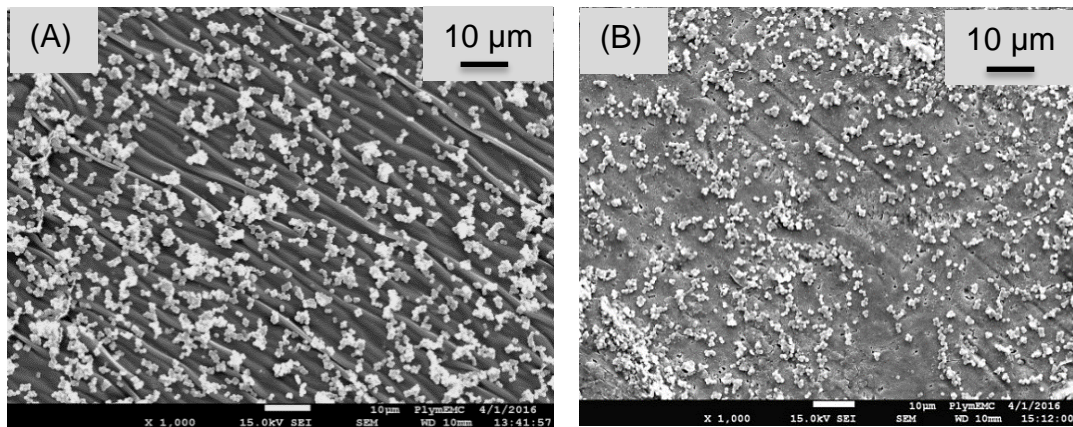


Figure 6.13: SEM images of attached *S.aureus* after overnight culture on (A) 24 well plate plastic surface [Control] (B) Ti alloy with TiO₂ nanotubes on the surface [TiO₂].

The ZnCl_2 treatment had a few clusters of *S. aureus* spread far from each other on the surface exposed, while the nZnO treatment had less individual bacterial cells lying on the surface (Figure 6.14 A and B).

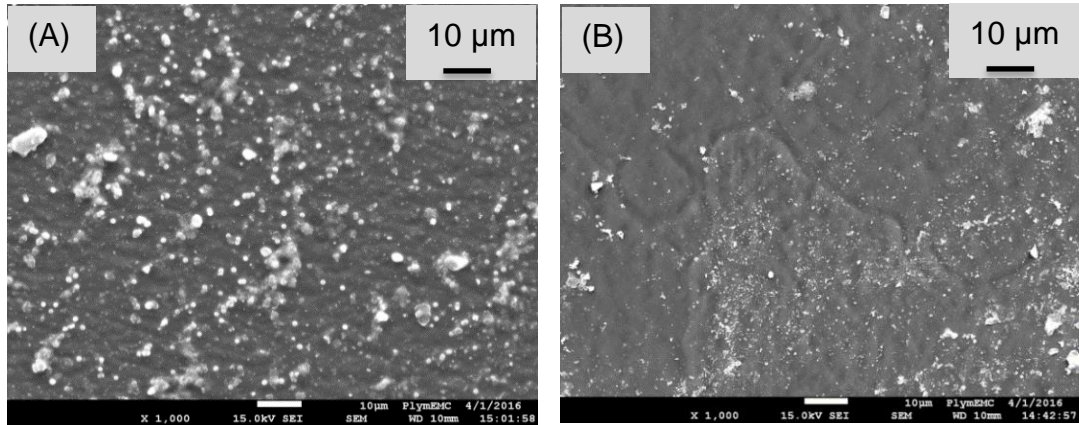


Figure 6.14: SEM images of attached *S.aureus* after overnight culture on (A) 24 well plate plastic with zinc chloride on the latter as a negative control for zinc ions [ZnCl_2] (B) 24 well plate plastic with zinc oxide nanoparticles on the latter as a negative control for nano zinc [nZnO].

The TiO₂-ZnO/350 and TiO₂-ZnO-HA/350 treatments had similar amount of clusters and individual *S. aureus* attached on the surface of the coated Ti alloy as shown in Figure 6.15 A and B. The bacterial adhesion observed on the TiO₂-ZnO/350 and TiO₂-ZnO-HA/350 composites was similar to the positive controls.

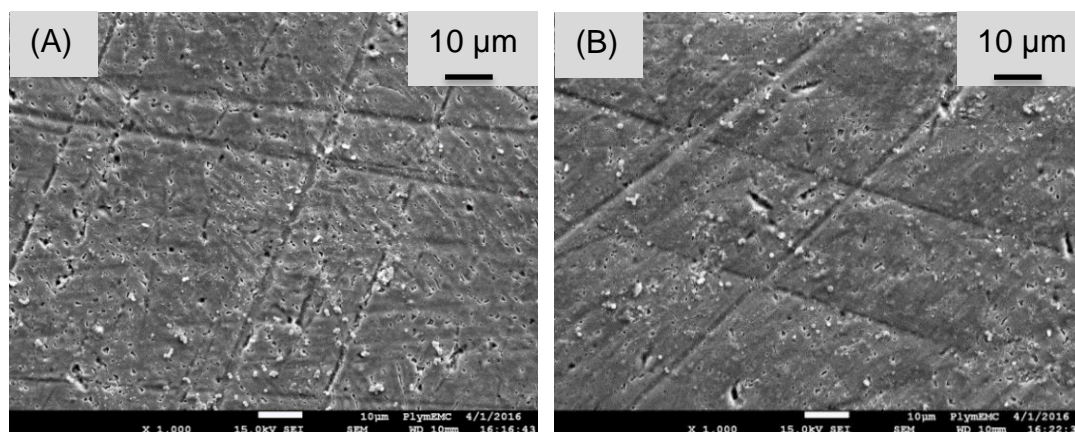


Figure 6.15: SEM images of attached *S.aureus* after overnight culture on (A) Ti alloy with nZnO embedded in TiO₂ nanotubes as a coating [TiO₂-ZnO/350] (B) Ti alloy with nZnO and Ha embedded in TiO₂ nanotubes as a coating [TiO₂-ZnO-Ha/350]

6.3.4 Biocompatibility of the nanocomposite coatings

The biocompatibility of the coatings was assessed in the presence of primary human osteoblast cells in the conditions described in section 4.5.1. In this section the controls were osteoblast cells grown in media without any sample and uncoated TiO₂ exposed the osteoblast cells in media. The media was changed on day 1, 4, 7 and 10 so that the cells are provided with the right nutrients to grow and the removed media was taken out and used for the biochemical assays. On day 4 and 10, the attached cells were removed

from the wells and converted to homogenate which were used in the biochemical assays mentioned below.

6.3.4.1 Protein concentration of cell homogenates

With respect to the calibration curve, the concentration of protein was found to be higher on day 10 as compared to day 4 for all the categories as seen in Figure 6.16. The concentration of the protein on TiO₂-ZnO/350 was observed to be similar to that on the control and TiO₂ on both day 4 (One-way ANOVA , p=0.06, n=3) and day 10 (One-way ANOVA , p=0.22, n=3). However, in the case of TiO₂-ZnO-HA/350 the protein concentration was higher than the others on day 4 (One-way ANOVA , p=0.03, n=3) and lower on day 10 (One-way ANOVA , p=0.01, n=3). That is, the cell protein increased over time as expected with cell growth. Only the TiO₂-ZnO-HA/350 treatment caused some depression of protein compared to controls.

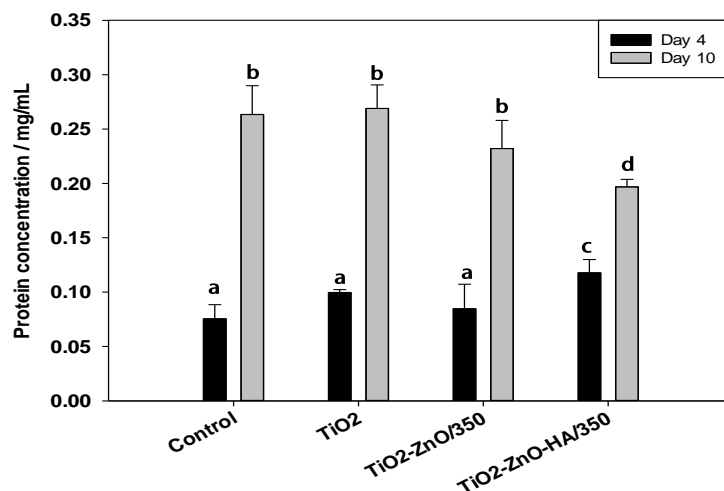


Figure 6.16: Concentration of protein in cell homogenate from attached osteoblast cells on TiO₂-ZnO/350 and TiO₂-ZnO-HA/350 and the controls at day 4 and 10 of exposure (Mean ± S.E.M, n=3). The different alphabets represent the statistically significant differences between the different samples on different days at a confidence interval of 95 %.

6.3.4.2 Alkaline phosphatase assay

The alkaline phosphatase activity was measured in the homogenate per unit protein on day 4 and 10 while in the media per mL of media on day 1, 4, 7 and 10. The results for the homogenate are illustrated in Figure 6.17 A. In the homogenate, no big difference was observed in the ALP activity between the coated samples and the controls and between day 4 and 10. In the media, the ALP activity was peak on day 10 for control and day 4 for TiO₂. Nonetheless, for TiO₂-ZnO/350 and TiO₂-ZnO-HGA/350 the ALP activity stayed constant from day 4 to day 10.

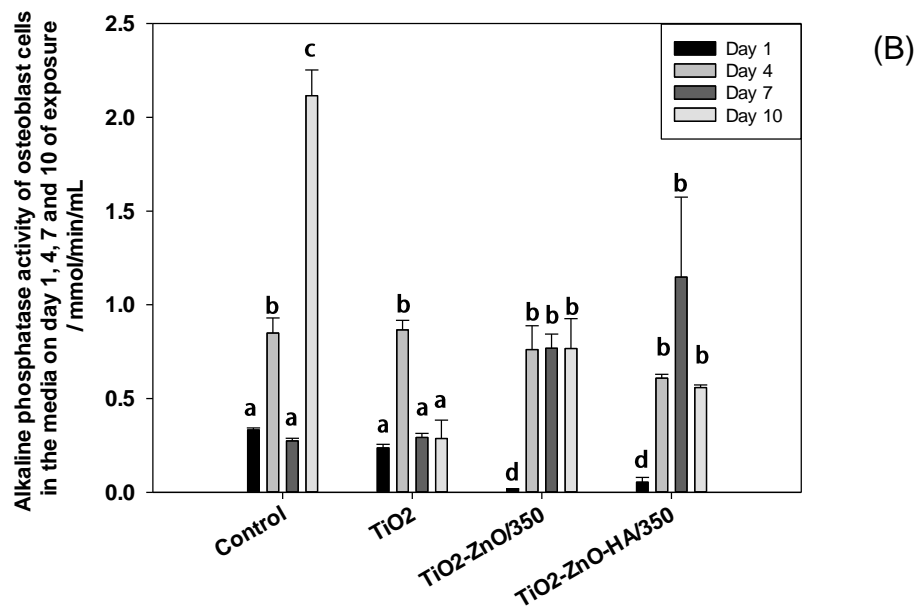
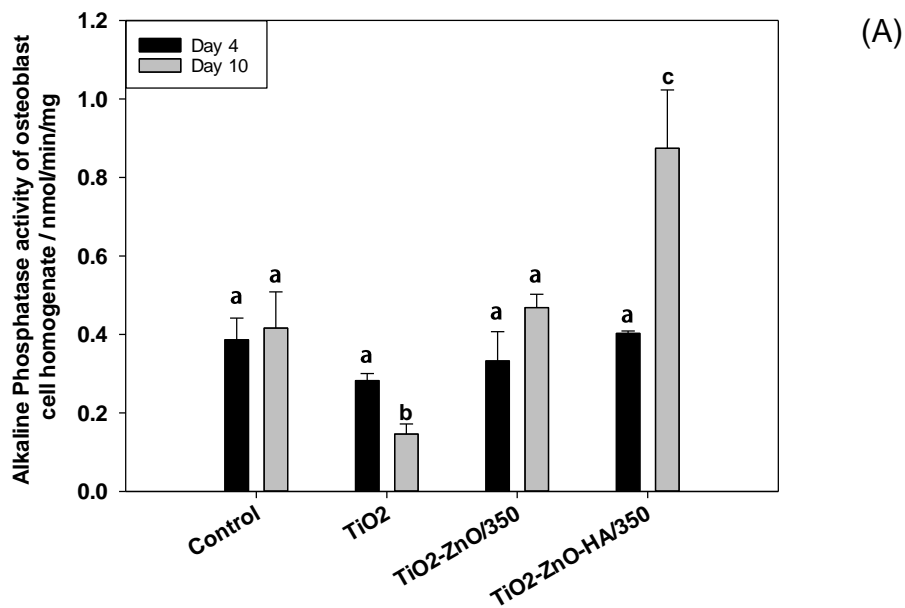


Figure 6.17: ALP activity of (A) osteoblast cells' homogenate grown on the coatings and controls on day 4 and 10 (B) the media in which they grew on day 1, 4, 7 and 10 (Mean \pm S.E.M, Kruskal-Wallis, n=3). The different alphabets represent the statistically significant differences between the different samples on different days at a confidence interval of 95 %.

6.3.4.3 Lactate dehydrogenase assay

The LDH assay was conducted on the same days with respect to similar parameters as for ALP activity. The LDH activity in the homogenate was less as compared to that in the media. In the homogenate, the LDH activity was higher on day 10 than on day 4 for all the samples except for TiO₂-ZnO-HA/350. For the latter, the LDH activity was the same on both days as seen in Figure 6.18 A. Figure 6.18 B shows the LDH activity in the media. In the media from the control and TiO₂ treatments, the LDH activity was maximal on day 1 as compared to TiO₂-ZnO/350 and TiO₂-ZnO-HA/350. However, as from day 4, the activity was higher on TiO₂-ZnO/350 and TiO₂-ZnO-HA/350 as compared to control and TiO₂ as seen in Figure 6.18 B. When comparing TiO₂-ZnO/350 to TiO₂-ZnO-HA/350 the activity was found to be higher on day 10 for the latter as compared to TiO₂-ZnO/350.

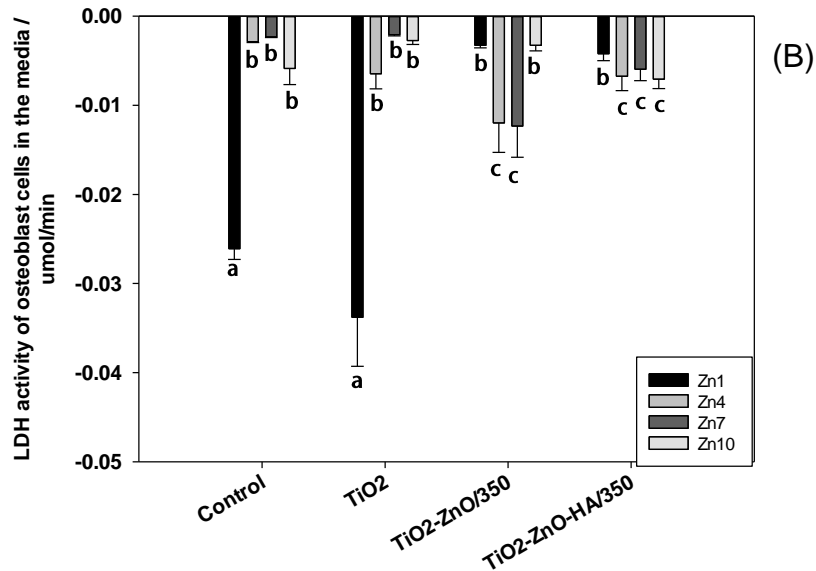
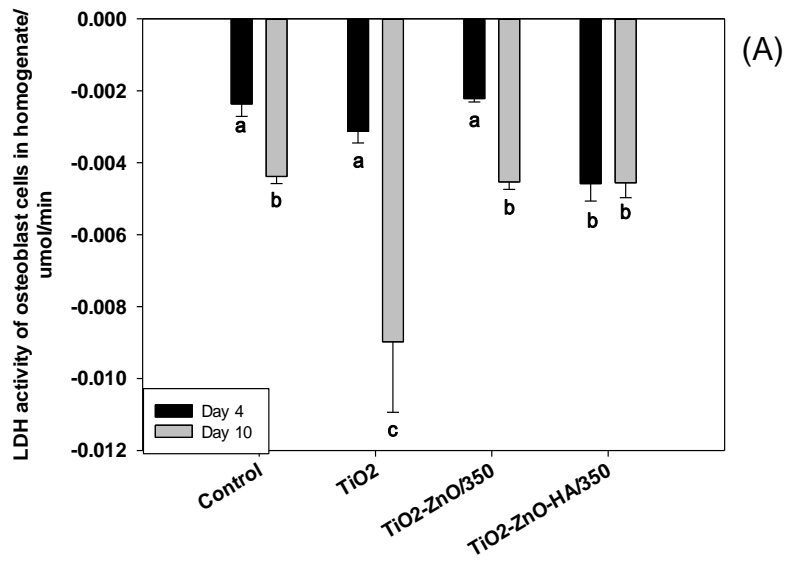


Figure 6.18 : LDH activity of osteoblast cells in the homogenate on day 4 and 10. (D in the media on day 1, 4, 7 and 10 (Mean \pm S.E.M, Kruskal-Wallis, $n=3$). The different alphabets represent the statistically significant differences between the different samples between different days at a confidence interval of 95 %.

6.3.4.4 Trace element analysis

Trace element analysis performed on both the homogenate and media are presented in Figure 6.19 A and B respectively. Only those coatings having zinc containing coating showed elevation in zinc in the cells. On day 4 the homogenates from both the TiO₂ and control presented with almost no zinc ions as compared to day 10. The homogenate on TiO₂-ZnO/350 had the highest amount of zinc ions reaching a concentration of 1 ppm on day 4 as compared to TiO₂-ZnO-HA/350, TiO₂ and control and to the values on day 10. On the latter day, both TiO₂-ZnO/350 and TiO₂-ZnO-HA/350 contained the same amount of zinc ions. The presence of zinc ions in the media on day 1 was minimum in the both TiO₂-ZnO/350 and TiO₂-ZnO-HA/350. However the concentration spikes to more than 6 ppm for TiO₂-ZnO/350 as from day 4 to day 10 which was significantly more than that present in TiO₂-ZnO-HA/350 on day 4, 7 and 10 (Kruskal-Wallis, n=3).

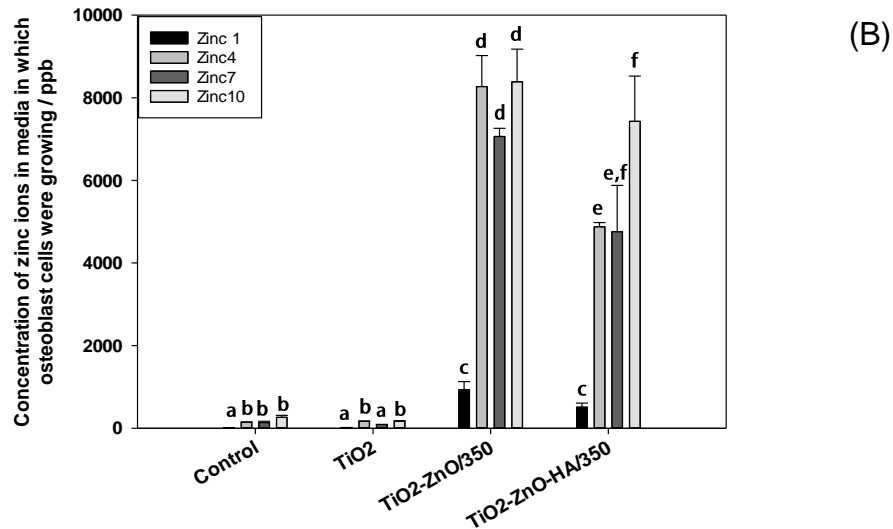
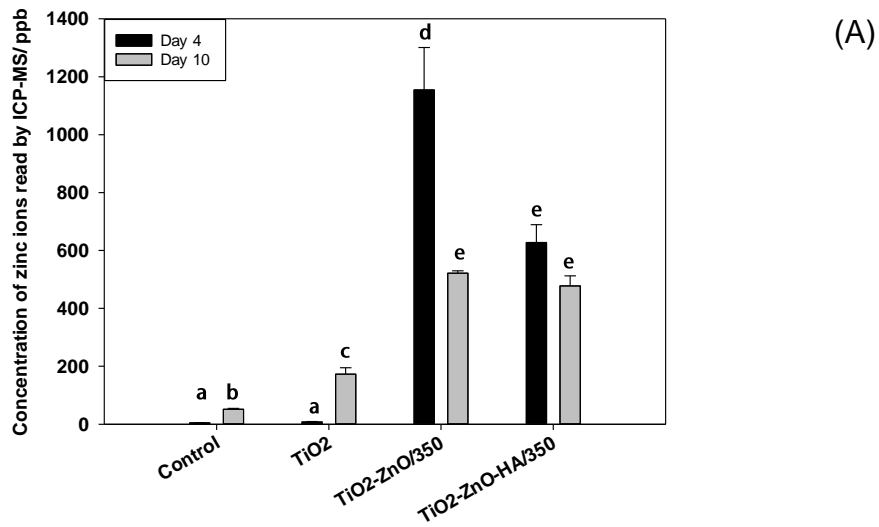


Figure 6.19: Trace element analysis for zinc read by ICP-OES of (A) homogenate of osteoblast cells on day 4 and 10. (B) media in which osteoblast cells were grown on day 1, 4, 7 and 10 (Mean \pm S.E.M, Kruskal-Wallis, n=3). The different alphabets represent the statistically significant differences between the different samples between different days at a confidence interval of 95 %.

6.3.4.5 Glutathione Assay

The glutathione assay was performed on homogenate of osteoblast cells on day 4 and 10 only, the results of which are presented in Figure 6.20. The concentration of glutathione per unit protein was higher on day 10 than on day 4 for all the cells. There was a steady measurable total GSH similar in all treatments at day 4. And on day 10 TiO₂-ZnO-HA/350 and TiO₂ contained more glutathione than TiO₂-ZnO/350 and control (Mean \pm S.E.M, Kruskal-Wallis, n=3).

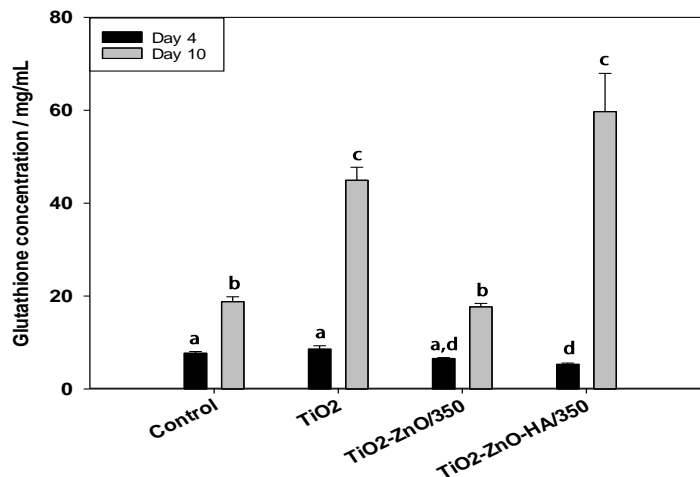


Figure 6.20: Glutathione assay results of homogenates of osteoblast cells on day 4 and day 10. All data are presented as mean \pm S.E.M (Kruskal-Wallis, n=3). The different alphabets represent the statistically significant differences between the different samples between different days at a confidence interval of 95 %.

6.3.4.6 Electrolyte concentration

The electrolytic concentrations in the acidified homogenate were presented in Table 6.1. The concentration of sodium was higher on day 4 than day 10 for all the samples. The concentration of magnesium in the homogenate was almost negligible on both days.

Table 6.1: The concentrations of different ions in the homogenate

Ions	Samples	Day 4	Day 10
Sodium	Control	0.28 ± 0.12 a	0.75 ± 0.17 b
	TiO ₂	0.31 ± 0.02 a	0.70 ± 0.37 b
	TiO ₂ -ZnO/350	0.40 ± 0.05 c	1.64 ± 0.24 d
	TiO ₂ -ZnO- HA/350	0.48 ± 0.09 c	2.05 ± 0.46 d
Potassium	Control	1.13 ± 0.01 a	0.88 ± 0.25 a
	TiO ₂	0.94 ± 0.05 a	1.22 ± 0.82 a
	TiO ₂ -ZnO/350	1.51 ± 0.01 a	1.33 ± 0.15 a
	TiO ₂ -ZnO-	1.79 ± 0.24 a	1.50 ± 0.15 a
	HA/350		
Magnesium	Control	0.00 ± 0.00 a	0.00 ± 0.00 a
	TiO ₂	0.00 ± 0.00 a	0.00 ± 0.00 a
	TiO ₂ -ZnO/350	0.01 ± 0.00 a	0.04 ± 0.01 b
	TiO ₂ -ZnO-	0.04 ± 0.00 b	0.03 ± 0.00 b
	HA/350		
Calcium	Control	0.01 ± 0.00 a	0.02 ± 0.01 a
	TiO ₂	0.06 ± 0.01 b	0.02 ± 0.01 a
	TiO ₂ -ZnO/350	0.10 ± 0.01 c	0.17 ± 0.04 d
	TiO ₂ -ZnO-	0.21 ± 0.02 d	0.21 ± 0.01 d
	HA/350		
Phosphorus	Control	0.05 ± 0.01 a	0.09 ± 0.02 a
	TiO ₂	0.06 ± 0.00 a	0.07 ± 0.01 a
	TiO ₂ -ZnO/350	0.11 ± 0.01 a	0.15 ± 0.00 b
	TiO ₂ -ZnO-	0.15 ± 0.00 b	1.79 ± 0.02 c
	HA/350		

The concentration of electrolytes ions in the acidified homogenate on day 4 and day 10 as measured by ICP-OES are presented as mean ± SEM. The

alphabets show the significance in differences among the different treatments involved and the different days at a 95 % confidence interval. There is no comparison being made between the different ions.

The concentration of the ions in the media are presented in Table 6.2 whereby all the ions reduced from day 1 to day 4 from all the samples. The decrease of both sodium and phosphorus ions from day 1 to day 10 was higher for TiO₂-ZnO/350 and TiO₂-ZnO-HA/350 as compared to the decrease seen for control and TiO₂. Similar observations were made for phosphorus ions as well. However there was no big difference in the ratio of sodium to potassium between the media from the coated samples and the controls. Similar observations were made for the ratio of calcium to phosphorus ions.

Table 6.2: The concentration of electrolytes ions in the acidified media on day 1, 4, 7 and 10 as measured by ICP-OES presented as mean \pm SEM. The alphabets show the significance in differences among the different treatments involved and the different days at a 95 % confidence interval. The different ions were not compared between each other.

Ions	Samples	Day 1	Day 4	Day 7	Day 10
Sodium	Control	466.50 \pm 11.50 a	213.51 \pm 16.31 b	215.96 \pm 7.04 b	317.47 \pm 3.78 c
	TiO ₂	431.52 \pm 14.64 a	221.97 \pm 6.19 b	202.96 \pm 9.55 b	286.85 \pm 20.60 c
	TiO ₂ -Ag7	488.69 \pm 19.57 a	203.98 \pm 14.64 b	448.01 \pm 13.37 a	160.28 \pm 21.56 b
	TiO ₂ -Ag7-HA	496.16 \pm 88.55 a	212.97 \pm 11.63 b	340.81 \pm 53.42 c	135.05 \pm 7.57 d
Potassium	Control	36.01 \pm 0.56 a	16.93 \pm 1.35 b	18.02 \pm 0.48 b	27.47 \pm 0.30 c
	TiO ₂	34.16 \pm 3.04 a	17.88 \pm 0.53 b	16.40 \pm 4.19 b	23.81 \pm 1.68 c
	TiO ₂ -Ag7	38.19 \pm 3.89 a	16.21 \pm 1.20 b	42.30 \pm 1.26 a	13.53 \pm 2.46 b
	TiO ₂ -Ag7-HA	37.87 \pm 2.10 a	17.12 \pm 0.82 b	30.54 \pm 5.32 a	11.20 \pm 0.60 b
Magnesium	Control	3.03 \pm 0.06 a	1.52 \pm 0.12 b	1.45 \pm 0.07 b	2.18 \pm 0.03 c
	TiO ₂	2.72 \pm 0.26 a	1.60 \pm 0.05 b	1.12 \pm 0.17 b	1.95 \pm 0.15 c
	TiO ₂ -Ag7	3.03 \pm 0.34 a	1.41 \pm 0.11 b	2.11 \pm 0.04 c	2.26 \pm 0.16 c
	TiO ₂ -Ag7-HA	3.10 \pm 0.19 a	1.44 \pm 0.08 b	1.89 \pm 0.19 c	2.04 \pm 0.14 c
Calcium	Control	8.71 \pm 0.19 a	3.56 \pm 0.30 b	6.49 \pm 0.66 a	6.40 \pm 0.24 a
	TiO ₂	7.58 \pm 0.64 a	3.64 \pm 0.12 b	4.09 \pm 0.60 b	5.41 \pm 0.51 c
	TiO ₂ -Ag7	8.28 \pm 0.82 a	3.01 \pm 0.23 b	5.01 \pm 0.10 c	2.69 \pm 0.26 b
	TiO ₂ -Ag7-HA	8.57 \pm 0.45 a	2.96 \pm 0.16 b	4.84 \pm 0.47 c	2.44 \pm 0.12 b
Phosphorus	Control	4.30 \pm 0.11 a	2.51 \pm 0.21 b	2.90 \pm 0.12 b	3.25 \pm 0.04 c
	TiO ₂	3.80 \pm 0.36 a	2.60 \pm 0.08 b	2.29 \pm 0.09 b	2.84 \pm 0.21 b
	TiO ₂ -Ag7	4.04 \pm 0.44 a	2.14 \pm 0.16 b	2.43 \pm 0.01 b	2.26 \pm 0.16 b
	TiO ₂ -Ag7-HA	4.14 \pm 0.25 a	2.13 \pm 0.14 b	2.46 \pm 0.11 b	2.04 \pm 0.14 b

6.3.4.7 Microscopic imaging of adhered cells

Figure 6.21 illustrates the SEM images of the osteoblast cells attached to the titanium alloy discs under a low and high magnification after 10 days of exposure. The TiO₂ coated Ti alloy alone had a full coverage of osteoblast cells as shown in Figure 6.21 A with filopodia extending from the cells as seen in Figure 6.21 B. However, patches of the discs could be seen in between the cells. TiO₂-ZnO/350 coating showed a full coverage of cells and with less patches of the discs visible without cells. In the case of TiO₂-ZnO-HA/350 neither the titanium disc underneath the cells nor the coating were visible (Figure 6.21 E). More granulation of the cells were visible on TiO₂-ZnO/350 and TiO₂-ZnO-HA/350.

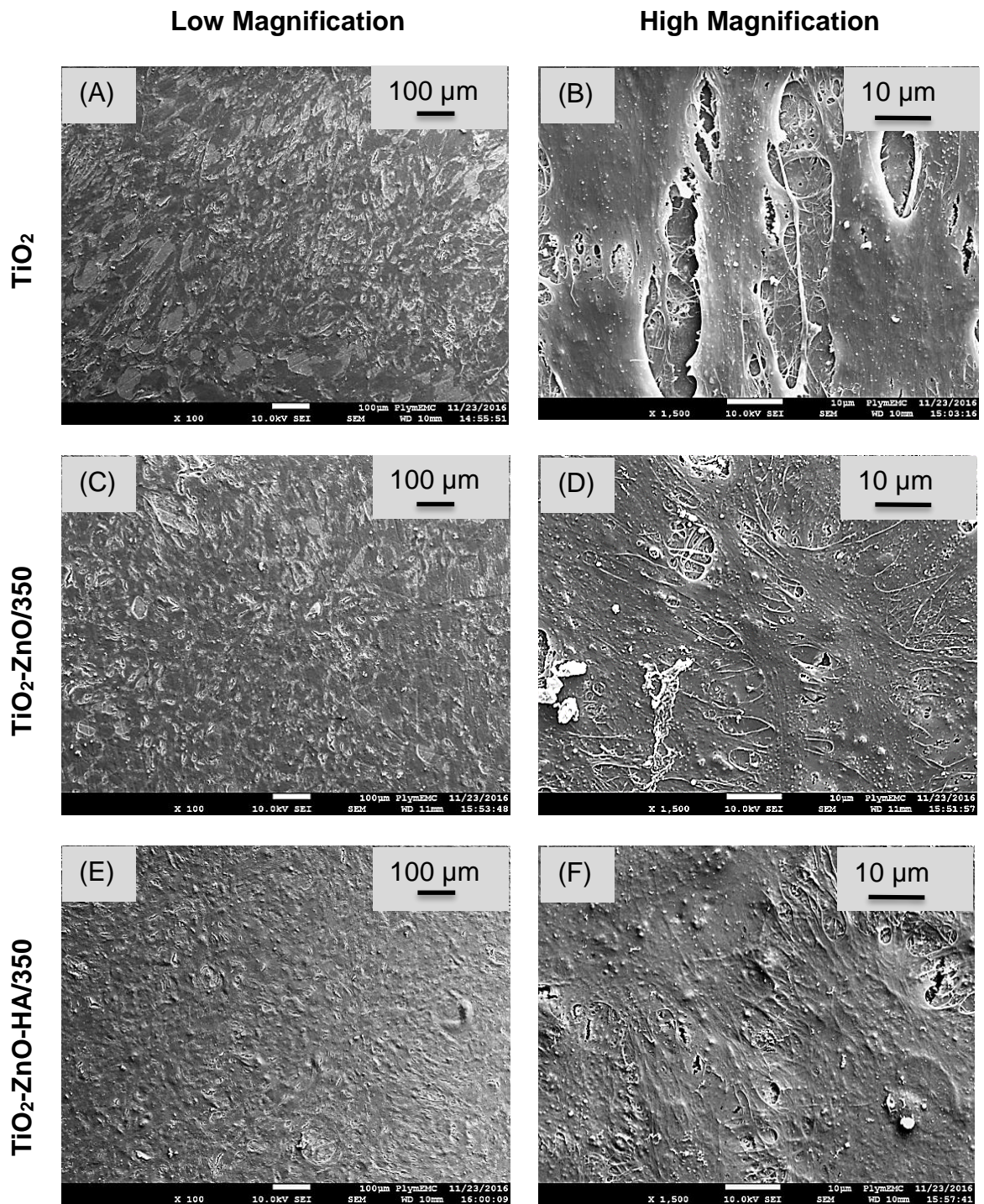


Figure 6.21 : SEM images of (A) and (B) TiO₂, (C) and (D) TiO₂-ZnO/350 and (E) and (F) TiO₂-ZnO-HA/350 at low (×100) and high magnifications (×1500) respectively.

6.3.5 PCR data for markers in exposed osteoblast cells

Figure 6.22 - 6.25 shows the expression of the genes in the cells on the TiO₂-ZnO/350 and TiO₂-ZnO-HA/350 coatings compared to the expression in the cells on uncoated TiO₂. As compared to TiO₂, FAK was downregulated on both day 4 and day 10 for both coatings as seen in Figure 6.22. However, cells on the TiO₂-ZnO/350 coating expressed less FAK as compared to those on TiO₂-ZnO-HA/350 on day 4 and on day 10 both expressed more FAK on day 10 as compared to day 4.

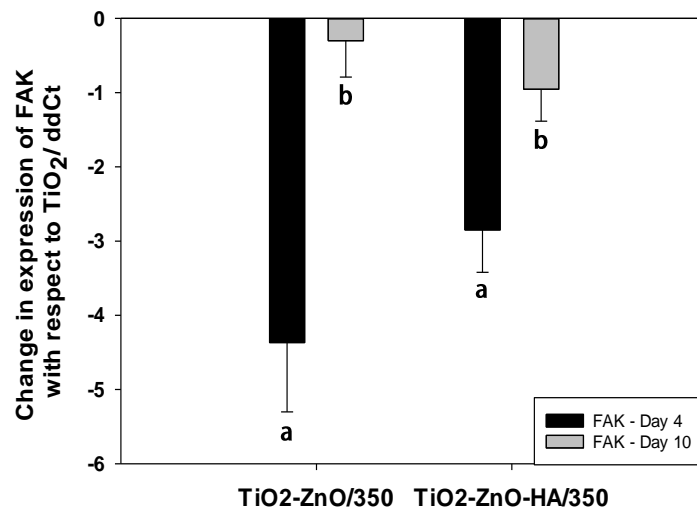


Figure 6.22: Change in gene expression of FAK in osteoblast cells grown on TiO₂-ZnO/350 and TiO₂-ZnO-HA/350 on day 4 and 10 of exposure, with respect to the cells grown on TiO₂ after normalisation with respect to β -actin. The different alphabets represent the statistically significant differences between the different samples between different days at a confidence interval of 95 %.

Figure 6.23 A shows the downregulation of RUNX-2 on day 4 as compared to the upregulation on day 10 with more expression of the latter on TiO₂-ZnO/350. ALP, OC and CA 1 were found to exhibit similar observations as seen in Figure 6.23 B, C and D respectively.

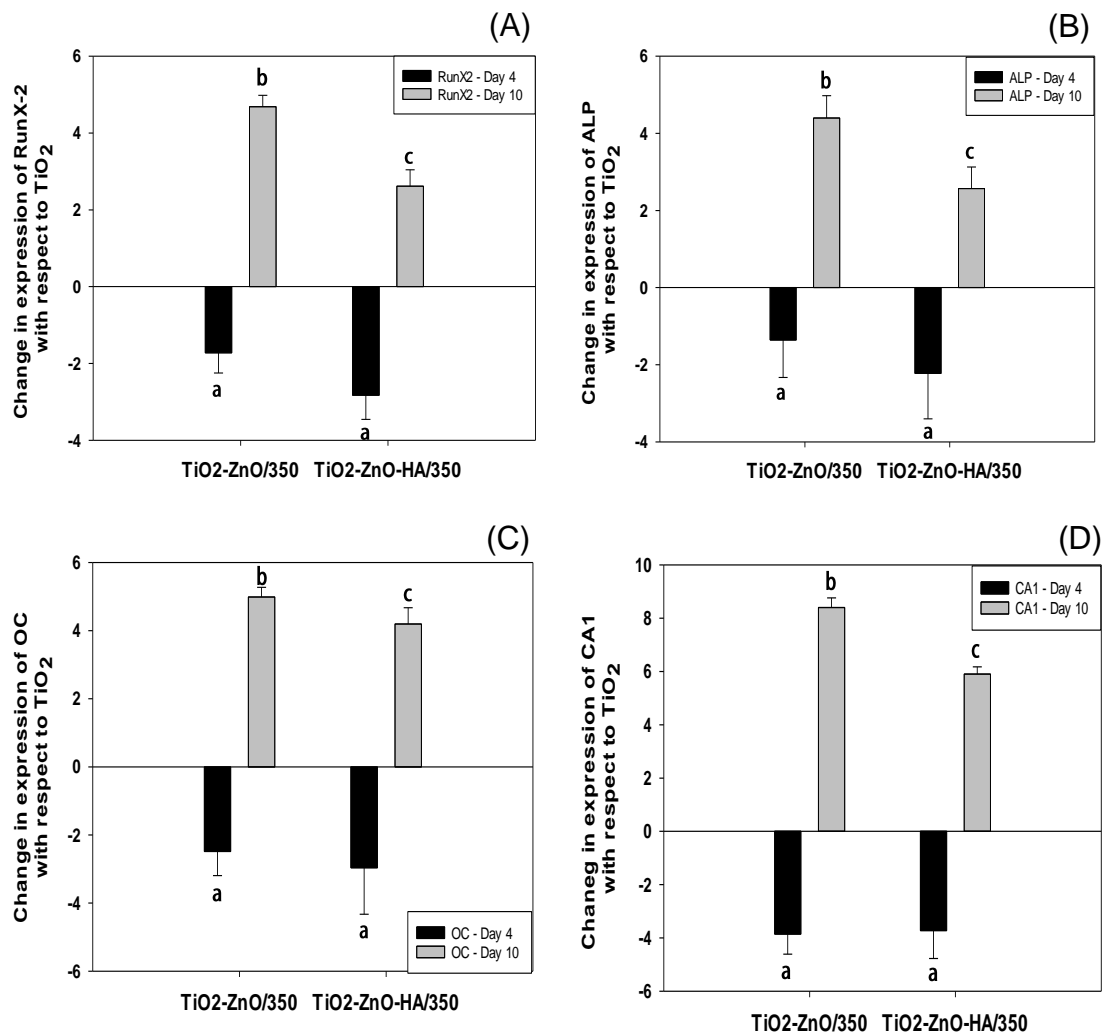


Figure 6.23: Change in gene expression of (A) RunX-2, (B) ALP, (C) OC and (D) CA1, in osteoblast cells grown on TiO₂-ZnO/350 and TiO₂-ZnO-HA/350 on day 4 and 10 of exposure, with respect to the cells grown on TiO₂ after normalisation with respect to β -actin. The different alphabets represent the statistically significant differences between the different samples between different days at a confidence interval of 95 %.

COX-2 was downregulated on day 4 and upregulated on day 10 for both TiO₂-ZnO/350 and TiO₂-ZnO-HA/350. Nonetheless, on day 4, the expression was more downregulated for TiO₂-ZnO/350 than TiO₂-ZnO-HA/350 (Figure 6.24 A). Both IL6 and TNF- α were downregulated on day 4 and upregulated on day 10 with more expression for TiO₂-ZnO-HA/350 (Figure 6.24 B and C respectively).

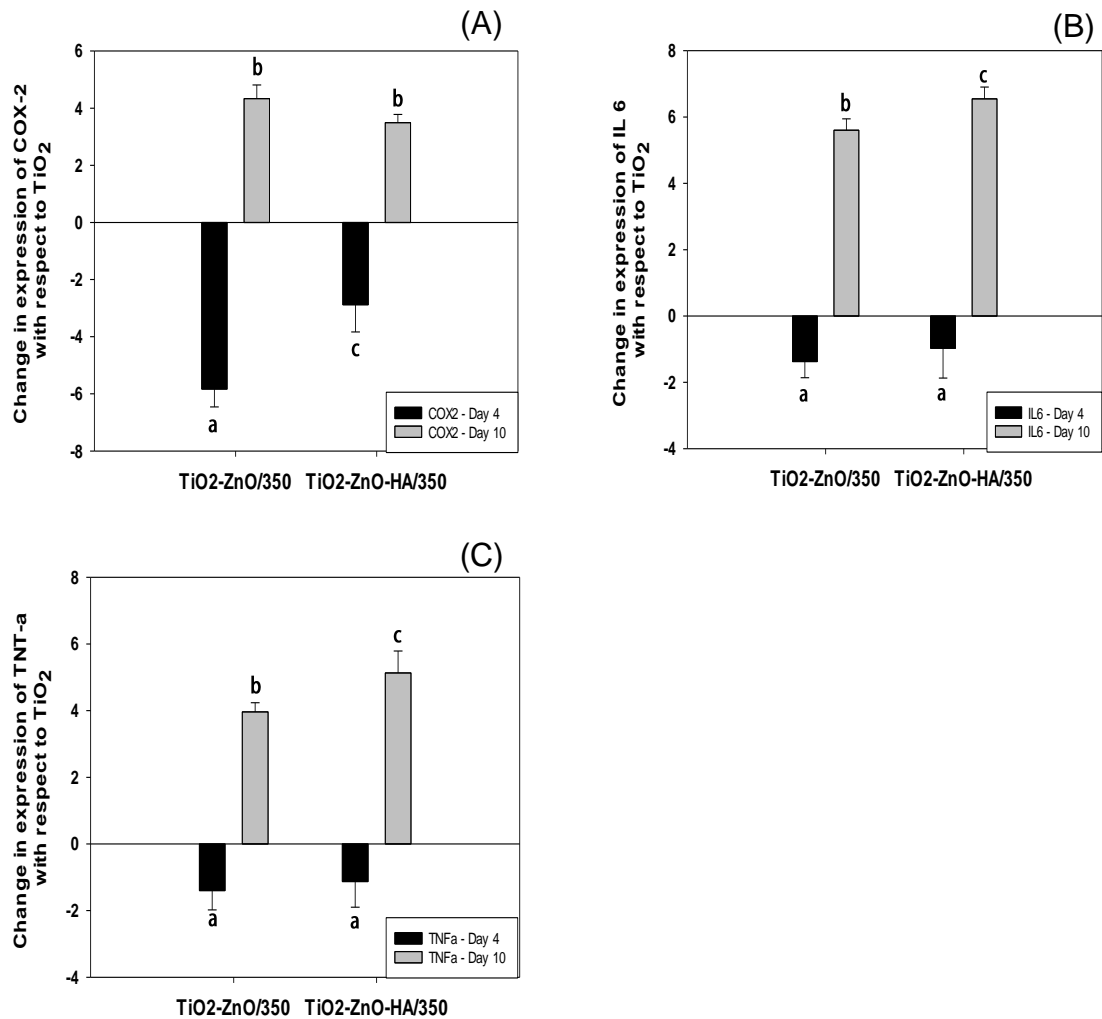


Figure 6.24: Change in gene expression of (A) COX 2, (B) IL 6 and (C) TNF α , in osteoblast cells grown on TiO₂-ZnO/350 and TiO₂-ZnO-HA/350 on day 4 and 10 of exposure, with respect to the cells grown on TiO₂ after normalisation with respect to β -actin. The different alphabets represent the statistically significant differences between the different samples between different days at a confidence interval of 95 %.

Finally the expression of SOD was lower for TiO₂-ZnO-HA/350 as compared to TiO₂-ZnO/350.

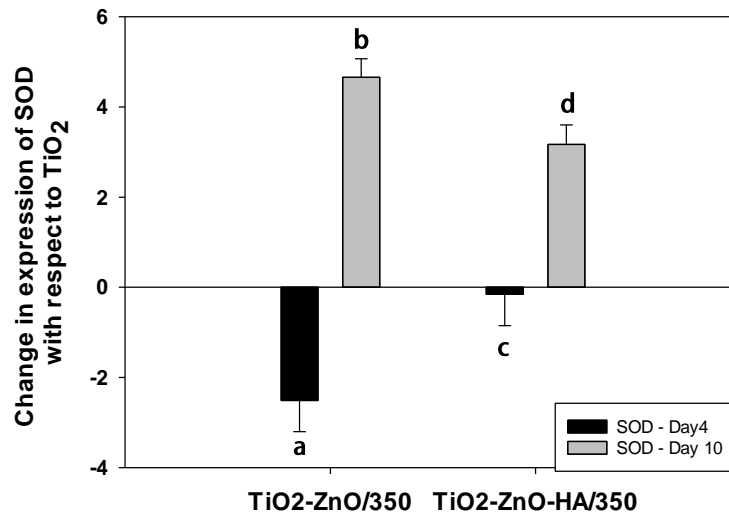


Figure 6.25: Change in gene expression of SOD in osteoblast cells grown on TiO₂-ZnO/350 and TiO₂-ZnO-HA/350 on day 4 and 10 of exposure, with respect to the cells grown on TiO₂ after normalisation with respect to β -actin. The different alphabets represent the statistically significant differences between the different samples between different days at a confidence interval of 95 %.

6.4 Discussion

The optimisation process of the nano-ZnO coated TiO₂ was based on the concentration of zinc nitrate used at first (Appendix B), followed by the temperature for crystallisation of the resulting coating (Section 6.3.1). The resulting the morphology and distribution of the ZnO and ZnO-HA coating also helped with the optimisation process. The nano-ZnO had the shape of nanorods which agreed with the study by Liu *et al* (2014) and review by Sirelkhatim *et al* (2015) whereby hydrothermal synthesis of ZnO resulted in nanorod-shaped particles (Liu *et al.*, 2014; Sirelkhatim *et al.*, 2015). In this study, heating the nano-ZnO resulted in the thickening of the nanoparticles as shown in Figure 6.2-6.5. This observation agreed with Gunawan and Johari (2008) whereby they concluded that annealing of the nano-ZnO on TiO₂-NTs resulted in the expansion of the nanoparticles due to the expansion of the ZnO shell (Gunawan & Johari, 2008). Selecting TiO₂-ZnO/350 over TiO₂-ZnO was partially because of the improved crystallinity of the ZnO coating upon annealing as compared to non-annealed ones (Elkady *et al.*, 2015). One of the objectives of this study was to provide antibacterial properties by the action of zinc and the final layer of HA over the ZnO coating was intended to enhance biocompatibility with osteoblast cells. It was also imperative that the zinc from the zinc oxide nano-coating could reach the external environment. As such, it was imperative that the nano-porous structure of the HA allow zinc oxide to be exposed by enhancing cell attachment and proliferation (see Chapter 1, section 1.7). In addition to the morphology and distribution of the coating obtained, there has been studies which concluded that too much annealing, resulting in increased volume to surface area ratio can reduce the antibacterial properties of the coatings ZnO (Elkady *et al.*, 2015). As

a result, TiO₂-ZnO/350 and TiO₂-ZnO-HA/350 was selected for further analysis in this Chapter.

6.4.1 Antibacterial properties

In the presence of *S. aureus*, both the TiO₂-ZnO/350 and TiO₂-ZnO-HA/350 coatings exhibited significant antibacterial properties within 24 hours of exposure to the microbial broth. Both TiO₂-ZnO/350 and TiO₂-ZnO-HA/350 coatings were able to kill more than 50 % of the bacteria as compared to the TiO₂ treatment and controls which killed less than 20 % to none in the Live/Dead assay as seen in Figure 6.10. This finding was confirmed by both the Live/Dead assay and the lactate production assay. However, the presence of HA hindered the antibacterial activity of the ZnO coating underneath it with the percentage of live to dead cells being lower than those on TiO₂-ZnO/350. There were two possible explanations for this observation. The first one was that the zinc ions or zinc oxide was not able to reach the bacteria because of the presence of the HA. The second reason could be that the antibacterial action was due to the shape and structure of the zinc oxide crystals which was then hidden by the presence of HA (Navale *et al.*, 2015; Roguska *et al.*, 2015).

In the case of the incubated attached bacteria, with respect to the concentration of zinc ions present in the broth after the bacterial exposure to the coatings, the bactericidal activity of TiO₂-ZnO/350 was more similar to that of nZnO than that of ZnCl₂. The reason behind this conclusion was that TiO₂-ZnO/350 released less zinc ions than nZnO and ZnCl₂ but still managed to provide a significant level of bactericidal activity proved by the Live/Dead assay, lactate production assay and SEM. And even though nZnO released less zinc ions than ZnCl₂, its

antibacterial properties were better than the latter. Moreover, the coated samples provided a better antibacterial action against *S. aureus* than $ZnCl_2$. Thus an antibacterial activity due to the action of zinc ions can be abandoned in the case of the bacteria which were attached to the surface of the material. Hence the surface morphology and properties of the ZnO coating was assumed to have an effect on the bacterial growth and proliferation. ZnO nanoparticles have been shown to be bactericidal in the literature (Roguska *et al.*, 2016). Since the amount of lactate present in the bacterial cells were low as well, the normal biochemical reaction such as metabolic activity was disturbed by the presence of the zinc oxide. Thus the bacteria that were able to attach to the coating were still not metabolically stable. This corroborated one of this study's hypothesis that nano zinc oxide coating was antibacterial.

The reason behind the antibacterial property of the coating against the bacteria in the exposed broth was considered to be different though. In the case of the exposed broth, zinc ions was considered to be the reason for the bacterial cell death. To start with, the dialysis experiment showing a balance between the concentration of zinc ions in the bag and beaker confirms that anything coming out of the coating which is different from TiO_2 which can be antibacterial was zinc ions. This is because, all the zinc ions that came out of the bag were able to pass through the pore of the dialysis bag, ZnO nanoparticle too big to go through the pores of the dialysis bag. As such, it will be only ions that were released from the coating. Moreover, $ZnCl_2$ had a lower live/dead cell ratio in the exposed broth as compared to the attached bacteria which were incubated. Thus the exposed bacteria in the media was considered to be affected by the presence of zinc ions. The exposed media has been associated with biofilm formation during which the biofilm forms a protective layer for bacteria attached

on a surface (Besinis *et al.*, 2017). Hence, it was concluded that biofilm formation was reduced due to the action of the zinc ions.

The presence of HA hindered the antibacterial activity of the coating even though they were significantly more bactericidal than TiO₂ and control. As such, TiO₂-ZnO-HA/350 could still be considered as an antibacterial coating for bone/dental implants made of titanium alloy.

6.4.2 Biocompatibility of the composite coatings with osteoblasts

The two methods used to assess the biocompatibility of the coatings in this study provided similar conclusions at different levels that the osteoblast cells survive.. Both the biochemical assays and the PCR data aided on determining the biocompatibility of the nano ZnO composite coatings. The protein assay aided in comparing the proliferation of the osteoblast cells grown on the different coatings (Brie *et al.*, 2014). The protein assay was also used to normalise the other biochemical assays providing further confirmation of the proliferation of the cells. For all the assays there were no big differences between the concentrations of the different reactants from the various assays on day 4. This was because, by day 4, the cells exposed to the different surfaces behaved similarly due to the fresh medium with the required nutrients. However by day 10, the assay results were different for the different exposure. Although from SEM images, more cells could be viewed on the surface of TiO₂-ZnO-HA/350 than on TiO₂-ZnO/350 (Figure 6.21), the protein concentration was higher on the coating without HA as shown in Figure 6.16. This observation was associated with the content of the cells and the fact that lower level of zinc in a cell lead to less molecular protein being synthesised (Liu *et al.*, 2015).

After the normalisation of ALP, LDH and GSH with respect to the protein concentration on each samples, it was observed that as compared to the cells on TiO₂ and control, the cells on TiO₂-ZnO/350 and TiO₂-ZnO-HA/350 were found to attach and proliferate more. . To start with, the ALP activity was higher on both TiO₂-ZnO/350 and TiO₂-ZnO-HA/350 on day 10 as compared to the controls. And the latter activity was higher for TiO₂-ZnO-HA/350 than TiO₂-ZnO/350. The absence of LDH leak into the external media and the absence of GSH depletion indicated healthy cells on both types of coatings. However, since GSH was induced, it could be because the cells were preparing for stress, responding to the presence of zinc. This meant that the osteoblast cells on TiO₂-ZnO-HA/350 were more ready to mineralise than the cells on the other samples. This was confirmed by the significantly high level of phosphorus in the cell homogenate on day 10, measured by ICP-OES as shown in Table 6.1. As compared to the others, the cells on TiO₂-ZnO-HA/350 were ready to mineralise from as early as day 10. The high level of GSH also showed that the cells were initially challenged by oxidative stress which was successfully combatted by the GSH. Once more, the cells on TiO₂-ZnO-HA/350 were able to survive better by day 10 than the cells on TiO₂-ZnO/350 and TiO₂. The cells exposed to TiO₂-ZnO-HA/350 obtained zinc ions for bone formation (Liu *et al.*, 2015) from the coating while being exposed to nano HA which enhanced bone osteoblast cells attachment and proliferation (Lugovskoy *et al.*, 2016). Further confirmation was provided by the PCR data.

The expression of the specific genes provided an indication on the protein that were to be produced after the day 4 or day 10 based on the gene expression. To start with, of expression of the adhesion marker, FAK, led to the deduction that at the beginning the cells could adhere better to TiO₂-ZnO-HA/350 than

TiO₂-ZnO/350 and later the contrary would happen. This was in agreement with the fact that HA on the surface of TiO₂ enhanced cell attachment (Goncalves Coelho, Rui Fernandes & Carrico Rodrigues, 2011; Sista *et al.*, 2013). On day 4 the higher expression of ALP for TiO₂-ZnO-HA/350 as compared to TiO₂-ZnO/350 with respect to TiO₂, suggested that there was the intent for more ALP to be produced but due to some side effect of the coating, it was not measurable using the ALP assay. However, since ALP is a differentiation marker and cannot say much about proliferation, the higher level of ALP for TiO₂-ZnO-HA/350 could only mean that the cells on TiO₂-ZnO-HA/350 were ready to differentiate earlier than those cells on TiO₂-ZnO/350 (Pujari-Palmer *et al.*, 2016). The genetic expressions were suggesting that TiO₂-ZnO/350 was more biocompatible than TiO₂-ZnO-HA/350 with the higher expression of RunX and OC as shown in Figure 6.23. The later genes have been associated with proliferation and determining the lineage of osteoblast cells (Komori, 2010). As such, the information for the proteins associated with proliferation and differentiation were mostly present in cells exposed to TiO₂-ZnO-HA/350. The genes for inflammatory markers were more expressed in cells exposed to TiO₂-ZnO-HA/350 than TiO₂-ZnO/350. This observation correlates with the presence of a high concentration of GSH in the cell homogenate which were present to combat high inflammatory response. The GSH cycle happening around day 10 could be related to the expression of SOD on day 4 whereby the expression of SOD was higher on TiO₂-ZnO-HA/350 (Figure 6.25). As such the SOD enzyme produced from the expression on day 4 would happen around day 10 of the experiment. Also SOD is a zinc-dependent enzyme, so the added zinc might have led to upregulated gene expression of such enzymes (Niska *et al.*, 2015). Two different conclusions can be made from the PCR and biochemical assays

performed on the osteoblast cells grown on the coatings. The first one is that until day 10, TiO₂-ZnO-HA/350 was more biocompatible and were able to provide anti-inflammatory response swiftly when compared to TiO₂-ZnO/350. And after day 10, TiO₂-ZnO/350 provided more biocompatibility with the higher expression of proliferation and differentiation genes on day 10. The second conclusion could be that even though the genes for the specific markers were expressed, due to the damaging effects of the coatings, the related protein could not be formed and hence accounting for lower biocompatibility of TiO₂-ZnO/350.

Zinc oxide nanocomposite coating were more antibacterial and biocompatible than the uncoated TiO₂ both in the presence and absence of HA. Following this study, TiO₂-ZnO-HA/350 was concluded to be the best coating as it was able to be more than 50 % bactericidal while promoting osteoblast cell growth on the surface of the latter successfully with visual confirmation from SEM. The presence of zinc ions do promote proliferation of bone cells. However, too much of it can be toxic. The coating from this study will have HA to prevent excess leakage of zinc ions in the human body.

6.5 Conclusion

A uniformly distributed nano zinc oxide composite coating was successfully synthesised in this chapter. A full surface coverage as well as stability of the coating was demonstrated by high resolution electron microscopy and dialysis. The addition of HA maintained the roughness and nanostructure of the coating but instead hindered the release of zinc ions. Both coatings produced in this chapter were shown to be more than 50 % antibacterial while being biocompatible. The PCR data further provided an insight on the molecular changes in the osteoblast cells upon exposure to the nano ZnO composite coatings. Both coatings can be used for implants but there was a 100 % coverage of osteoblast cells on the surface of the coating and would help once an implant is placed in the human body. Also the release of zinc was steady with a minimal toxicity to the osteoblast cells. As such at the end of this chapter, TiO₂-ZnO-HA/350 can be considered better than TiO₂-ZnO/350 as an antibacterial and biocompatible coating for dental/bone implants.

Chapter 7

General Discussion

Throughout the years, infection of bone/dental implants has been the main cause for secondary surgeries with increased risks of further infection (Raphel *et al.*, 2016). With respect to this issue, targeted antibacterial drug delivery has been researched and applied on implants with a slow progress in the research field. The use of nanotechnology in combatting the infection of implants in the body is considered as an incremental step towards improving implants and might offer a significant alternative to antibiotics given major worries about antibiotic resistance and degradation. Nanocomposite coating is one use of nanotechnology which helps provide targeted drug delivery from the surface of bone/dental implants.

This study confirmed that both pH of electrolytes and initial voltage sweep rate affect the resulting morphology of the nanotubes as seen in Chapter 2. Both parameters affect the initial etching sites which are considered to be the factor determining the final morphology of the nanotubes (Peremarch *et al.*, 2010).

This observation agreed with hypothesis 1 of this study (Section 1.8).

Furthermore, changing the crystalline phase of the TiO₂ nanotubes affect the way nanoparticles attach to it. The distribution of the attached nanoparticles on the surface was affected by the post-anodisation treatment of the nanotubes and this was confirmed by Figures 3.1/3.2 and Figure 5.1-5.3. Figure 5.1-5.3 showed the treated nanotubes with the attached nanoparticles as individual particles as compared to those on the untreated nanotubes which were clustered (Figure 3.1 and 3.2). However the morphology of the nanoparticles were not changed and hence part of hypothesis 2 of this study was not proved to be right whereby post anodisation treatment was expected to change the morphology of the nanoparticles. It was concluded that even when the concentration of silver ammonia or the duration of exposure to silver ammonia

was varied, the shape of the nanoparticles remained spherical as shown in Figure 3.1. It was the surface coverage of the nanoparticles on the nanotubes that varied which agreed with the other part of hypothesis 2. The concentration of zinc nitrate used for nano-ZnO synthesis as seen in the Appendix B and annealing of nano-ZnO had an effect on the morphology and distribution of the resulting nano-ZnO coating and nano-HA formed on the coating. This was confirmed by Figure 6.2-6.5 and hence agreed with hypothesis 3 of this study. Nano-ZnO coated TiO₂ nanotubes can exhibit a good level of antibacterial properties against *S. aureus* but this was lower than that of nano-Ag coated TiO₂ nanotubes. Hence this part of the study did not agree with part hypothesis 4. Nano-HA coated on the surface of the nano-Ag did not enhance the biocompatibility of the composite coating as evidenced by Figure 5.18 disagreeing with the last hypothesis of this study. However, the presence of nano-HA on the nano ZnO coating did enhance proliferation of the osteoblast cells even though they were under stress as detailed in section 6.3.4. The latter agreed with the other half of the last hypothesis.

7.1 Nanocomposite coating for implants

Nanocomposite coatings are coatings that consist of two or more materials combined to work together with at least one of them having at least one dimension below 100 nm (Ajayan, Schadler & Braun, 2006). This study successfully fabricated 4 types of nanocomposite coatings, two of which contained silver nanoparticles and the other two containing nano zinc oxide. All of the coatings were allowed to grow on polished, cleaned and anodised Ti-6Al-4V discs.

The anodisation step allowed the self-assembly of the TiO₂ nanotubes which had a uniform distribution over the discs with a full coverage of the disc surface. The initial sweep rate of voltage which was not highlighted enough, in the past, were shown to have an important effect on the anodising current density and the resulting morphology and distribution of the nanotubes grown on the surface. One example was that if the initial increase in the voltage to the anodisation voltage was too quick or too slow, the material could be made insensitive to the remaining anodisation process. Hence nanotubes would not be able to self-assemble. If the right voltage, initial voltage sweep rate, pH, temperature and content of anodising electrolytes are not employed, nanotubes may not form or they may form without uniformity or with micro-particles grown on them. This was observed in Chapter 2 when pH 6 and sweep rate 1.5 was used. This observation agrees with the study by Taveira *et al* (2005) whereby the importance of initial sweep rate in relations to initial etching sites of nanotubes was highlighted briefly (Taveira *et al.*, 2005). However, the latter authors observed and analysed just 2 different sweep rates and did not go into the detailed change in morphology of the resulting nanotubes. When using

phosphate and fluoride containing electrolytes, a pH 4 and initial sweep rate of 0.5 V/s to 20 V, were concluded to be the best conditions to use. This in turn provided a uniformly distributed nanotubes with a good adhesion to the surface of the titanium disc as confirmed by Sections 2.3.1 and 2.3.2.

The as formed TiO₂ nanotubes in the amorphous crystalline phase, reduced individual attachments of metal nanoparticles to them as observed in Chapter 3, in the case of silver nanoparticles. However, the individual nanoparticles were not able to attach the individual nanotubes walls. The nanoparticles formed clusters instead. The anatase phase of the nanotubes was known to be more reactive due to the specific crystalline facets present in the latter phase (Liu, Yu & Jaroniec, 2010). As such, the anatase phase of the TiO₂ nanotubes was able to attach to more individual particles in Chapter 5 as compared to Chapter 3. It was observed in Chapter 5 that individual silver nanoparticles were attached to the walls of the anatase nanotubes as compared to Chapter 3 where the nanoparticles formed clusters on the amorphous nanotubes. It could be concluded that the crystalline structure of the anatase phase helped prevent clustering of silver nanoparticles which were chemically reduced in the presence of δ -gluconolactone. The difference between the nanotubes in Chapter 3 and 5 was that the nanotubes were annealed and exposed to NaOH in Chapter 5. As such, the new crystalline facet and –OH was considered to provide more nucleation sites for the nanoparticles to attach. This corroborate what was concluded by the study done by Kokubo (1997) (Kokubo, 1997).

From Chapter 3 and 5, δ -gluconolactone was concluded to be a novel, good and non-toxic reducing agent for silver ions to silver nanoparticles. Hence, instead of using toxic reducing agents such as sodium citrate (Gorup *et al.*,

2011), sodium borohydride (Dong *et al.*, 2010), hydrazine (Tatarchuk *et al.*, 2013) and hydroquinone (Pérez *et al.*, 2008), alkaline δ -gluconolactone could be used moving forwards. In this study, silver ammonia was used as the source for silver. Such action facilitated the reduction reaction whereby the silver was easily dissociated from the silver ammonia complex, in order to form silver nanoparticles.

The growth of zinc oxide nanocrystals were concluded to be dependent on the morphology and content of the substrate it is growing on (Zhong Lin, 2004). As such, the presence of the anatase phase of the nanotubes and -OH allowed the formation of the uniform nanostructure of the zinc oxide to form on the nanotubes. The nano rod shape of the ZnO was expected from the hydrothermal process (Liu *et al.*, 2014; Sirelkhatim *et al.*, 2015). The heating of the resulting coating causes the zinc oxide to crystallise as observed in Figure 6.2-6.5 and at the same time, the heating resulted in the purification of the zinc oxide from the contaminants involved during the hydrothermal process (Pourrahimi *et al.*, 2015). The annealing process also improved the crystallinity of the coating which in turn improved stability (Elkady *et al.*, 2015). Nonetheless the heating process caused the crystals to expand as seen in Figure 6.2-6.5. This agreed with the theory of ZnO outer shell increasing in size when exposed to high temperatures (Gunawan & Johari, 2008). This behaviour is similar to silver nanoparticles which expand when exposed to high temperature as well (Huang *et al.*, 2015a).

The growth of HA on TiO₂ nanotubes have been shown in the past to improve the bioactivity of the latter surface (Ma *et al.*, 2008). Similar conclusions were made in Chapter 6 as well, whereby the latter improved the bioactivity of the

ZnO nanostructures. Nano-hydroxyapatite as part of a composite coating has been shown to improve the mechanical properties of the ZnO crystals in the past and as such, the nano-HA did not only improve the bioactivity of the coating but also added to the mechanical properties (Kenny, Buggy & Hill, 2001). Further studies can be performed to provide physical evidence for the latter observations. However, the nano HA on the surface of the silver nanoparticles did not improve the biocompatibility of the latter coatings.

7.1.2 Comparison of nano-ZnO to Ag-Np composite coatings

Both zinc oxide and silver nanocomposite coatings were uniformly distributed on the surface of the TiO₂ nanotubes. Both nanoparticles were attached to the walls of the nanotubes as observed in Chapter 5 and Chapter 6. The highly visible difference between both nanoparticles was that the silver nanoparticle had a spherical shape as shown in the SEM images in Chapter 5 as compared to the zinc oxide which had a spike shape as shown in Chapter 6. In the case of zinc oxide coating, when HA was added, the coating was found to still be porous as viewed under the microscope in Figure 6.2C-6.5 C. For the silver nanocomposite coating, the nano HA grouped together forming a layer of HA on the surface of the silver nanoparticles with micro-cracks on the surface as exhibited by Leon and Jansen (2009) (León & Jansen, 2009). There was a heat treatment to the nano coating before HA was added to the zinc oxide coating which changed the crystalline phase of the zinc oxide and as such enhanced the growth of the nano HA. However, the heat treatment was done after HA was added in the case of AgNP coating which resulted in the silver nanocomposite coating to get delaminated when exposed to osteoblast cells. The HA was as such more stable on the zinc oxide as compared to the AgNp. The ZnO

crystalline structure behaved similarly to that of hydroxyapatite which resulted in better integration of the coating and as such improved the function of the coating (Kenny, Buggy & Hill, 2001). Nonetheless, the silver nanoparticles and hydroxyapatite composite were not well adhered to the nanotubes, the reason for the delamination as seen in Section 5.3.4.

Both coatings with and without HA were proved to be antibacterial against *S. aureus* as concluded by Chapter 5 and 6. However there were various differences between the antibacterial reactions of the coatings. To start with, morphologically, they had different nanostructures and different ways of interacting with the nano HA. As such, the differences in antibacterial properties could be associated with the physical structures of the nanocoatings as mentioned in previous studies (Sirelkhatim *et al.*, 2015). Firstly the distribution of the coatings was different. There was more coverage with zinc oxide and more release of zinc as compared to the coverage of less surface coverage of silver nanoparticles with less release of silver. Nonetheless the bactericidal effect of silver nanocomposite coating was highest as compared to that of zinc oxide nanocomposite coatings. As such, this study corroborated what was mentioned in the literature in Chapter 1 whereby silver nanoparticle was concluded to be the strongest bactericidal metallic agent. Zinc oxide has been shown to have some level of antibacterial activity in the past (Sirelkhatim *et al.*, 2015). However, such bactericidal effect from zinc oxide nanocomposite coating with more than 50 % antibacterial activity had first been observed and described in Chapter 6. Furthermore, the combination of nano zinc oxide and nano hydroxyapatite on titanium alloy were successfully synthesised in Chapter 6. The latter nanocomposite coating exhibited good antibacterial properties. The release of zinc was better controlled in the presence of the nano-hydroxyapatite

as confirmed by the dialysis experiment in Figure 6.8 A. The release of zinc was lower from the coating containing nano HA as compared to TiO₂-ZnO/350. . In comparison to the osteoblast cells on silver nanocomposite coating, the cells, on the nano ZnO composite coatings were more metabolically active with more cells adhesion as confirmed by Figure 6.21. The genetic markers for the cells under stress, IL6 and COX2 were expressed in higher quantity in cells exposed to AgNp composite coatings as compared to nano ZnO composite coating as confirmed by Figures 5.22 and 6.24. This allowed zinc oxide nanocomposite coating to be a better coating for implants to be placed in the human body. Even though the presence of nano HA, on the coating, increased the cell growth on the coating's surface, the higher antibacterial activity of the zinc oxide nanocomposite coating without the nano HA suggested that TiO₂-ZnO/350 was the best coating in this study. The cells grown on the latter did express an increased amount of genetic markers for differentiation (Figure 6.23) and the antioxidant defence system, SOD (Figure 6.25) . On top of this, biofilm formation was reduced in the presence of *S.aureus* by more than 75 % as expressed in Figure 6.10 B. Biofilm, being a major reason for bacterial resistance, have been targeted by researchers throughout the years (Besinis *et al.*, 2017). Hence the ability to reduce biofilm formation by this coating brought the antibacterial properties of nano ZnO forwards.

7.2 Clinical perspective

Existing titanium alloy implants have been shown to be mechanically strong and possess good biocompatibility. Nonetheless, the addition of antibacterial properties to the latter has been a struggle due to various reasons such as resistance to antibiotics or increased toxicity to nanoparticles. This study was

able to provide nanocomposite coatings that could successfully combat infection such as peri-implantitis, or at least the first line of infection caused by *S. aureus* when implants are inserted in the human body. The coatings synthesised in this study also successfully reduced the formation of biofilm as described in Section 6.4.1 and hence the formation of plaque in the case of dental implants could be reduced when using this coating. The coatings were more biocompatible as compared to the silver composite coatings or TiO₂ nanotubes on their own. Thus TiO₂-ZnO/350 would be able to provide antibacterial effect while enhancing osseointegration of titanium alloy implants. Also, the dialysis study confirmed the stability of the composite coating in simulated body fluid. As such, the coating would not disintegrate in the presence of bodily fluid. The presence of the proteins in BHI broth and DMEM media increased the release of zinc from the coating but the maximum release did not exceed the maximum amount of zinc in the coating as described in Chapter 6. As such, the latter coating would provide a positive impact in the clinical environment. As mentioned in Chapter 1, nanoparticles cause toxicity in the human body. Nonetheless in this study, the release was found to be minimal and hence would be expected to be less toxic. Also the release of zinc over 10 days was maintained at a low concentration and as such would not be toxic at any point.

7.3 Limitations

There were a few limitations to this study which would require attention when moving forwards with the presented work which are as follows. At the beginning, the adhesion test done was limited by the glue being used and the surface area being considered. The bonding strength between the glue and the rod being pulled off come in the way of the experiment at most times. The diameter of the rod being pulled off was small and the surface from which it was pulled off as well was small. There was two types of HA being used on the different coatings, hence the resulting coating cannot be compared in details. The sintering effect of the HA in the case of TiO₂-Ag7-HA, could have had adverse effect on the silver nanoparticles and could have caused the delamination. The delamination of the HA itself is a limitation which needs further investigation. The antibacterial work was limited to *S.aureus* which is the main cause of infection in bone implants whereas, for dental implants other bacteria such as *Streptococcus mutans* are one of the main cause of infection and has not been investigated in this study. The antibacterial test was run for less than 24 hours. Although fabricating a long term antibacterial coating was the aim of this study, we can only assume that it is going to be long term unless the test is done for a longer period of time.

All the tests in this study were based on flat titanium discs. During the study, basic scratch tests (without data collection) were performed using scalpels in the lab and it was observed that the TiO₂ nanotubes were not affected with and without the Ag-Np and nano ZnO. However when HA was added there would be some changes to the coating. In real life, the implants would be in different shapes and would face mechanical forces in different situations. For example, screws would have to be able to endure the mechanical forces applied while

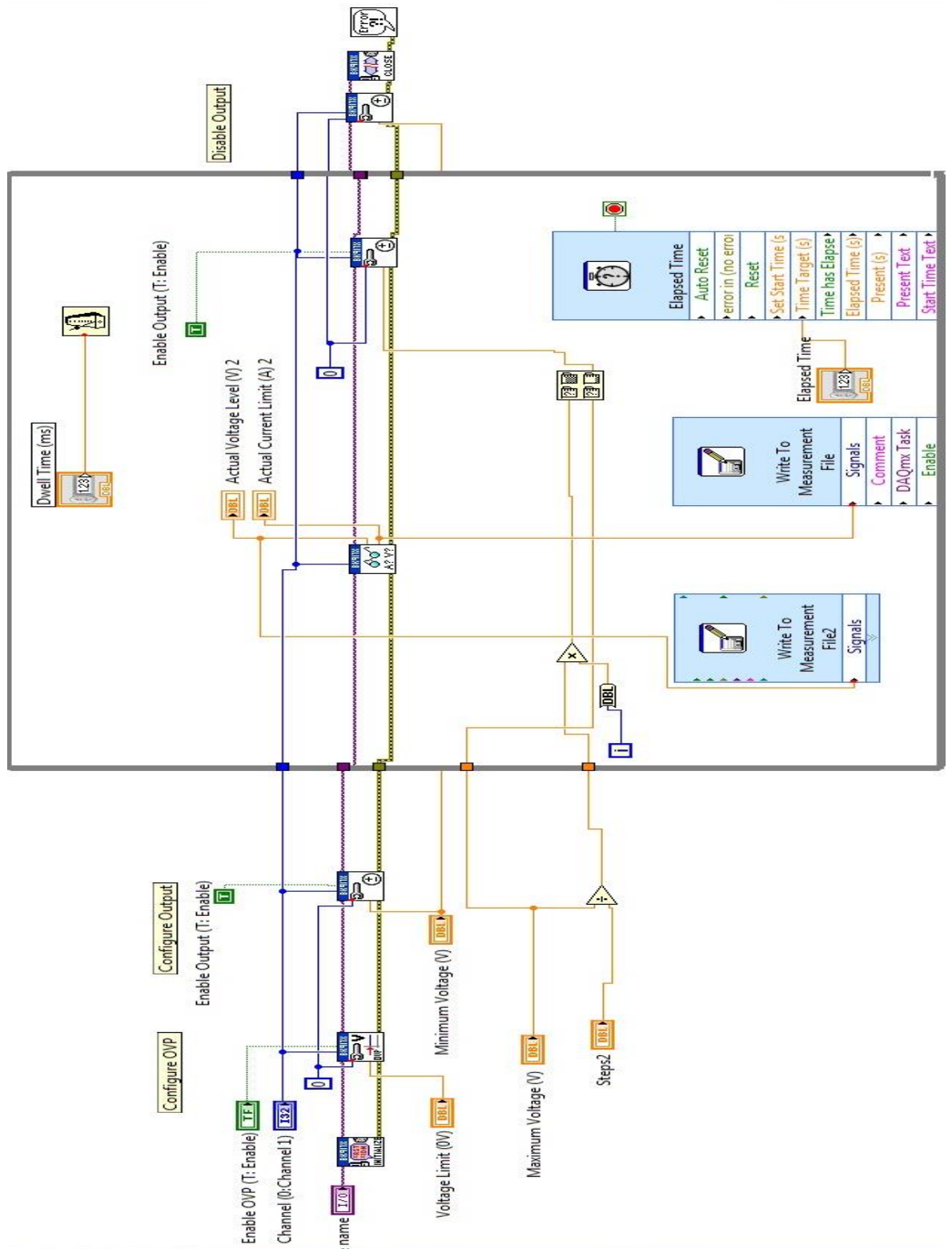
maintaining the coating. In this context, TiO₂ nanotubes coated Ti alloy have been tested in the past whereby the integrity of the coating was maintained (Friedrich *et al.*, 2014). However, in the presence of antibacterial nanoparticles, similar studies would be useful in determining the use of these coatings on bone implants.

7.4 Future works

The limitations and results of this work provides the space for various future works which once brought to life, will allow the coating to be actually used on implants, in-vivo. The future works are as follows. There is a need for optimisation of the adhesion test for the TiO₂ coating and performing the same test for the composite coatings as well. An improvement of the TiO₂-Ag7-HA coating with biomimetic growth of HA on the latter with 10 times the concentration of SBF could be beneficial, with the aim of reducing loss of silver nanoparticle. An additional improvement of TiO₂-ZnO/350 and TiO₂-ZnO-HA/350 coating with the aim of increasing the antibacterial effect could be beneficial in terms of targeted antibacterial drug delivery. This could involve the modification of the ZnO morphology at the fabrication stage. The dialysis experiment could be run for a longer period of time in SBF and the media that the cells grow in and the broth that the bacteria grew in. This is just to be able to confirm that the various release of silver or zinc is not related to the external media rather than the cells or bacteria they are exposed to. Performing antibacterial test over longer period of time with various micro-organisms such as *S. mutans*, *Porphyromonas gingivalis*, *Prevotella intermedia*, *Veillonella species* and a few more could be beneficial in confirming the antimicrobial effect against the common cause of infections in implants. After confirming the expression of differentiation markers in the osteoblast cells, a differentiation experiment can be performed just to confirm whether the cells actually were able to differentiate. Last but the most important future work would be to test the nanocomposite coating in-vivo in rodents followed by human beings in clinical trials. This would have to comply with the regulations for medical devices / implants with transparency involved in the product testing.

APPENDIX

Appendix A



Appendix B

At the beginning, the nano zinc oxide coating were grown using similar conditions as mentioned in section 6.3.1 with the exception of the concentration of the source of zinc being used (0.05, 0.075 and 0.1 M of zinc nitrate). This pilot study was done with the aim of optimising the concentration of the zinc nitrate to be used for the nanocomposite coating. Following the observations in the figure below, 0.075 M was considered to be the best due to the uniformity and coverage of the resulting coating.

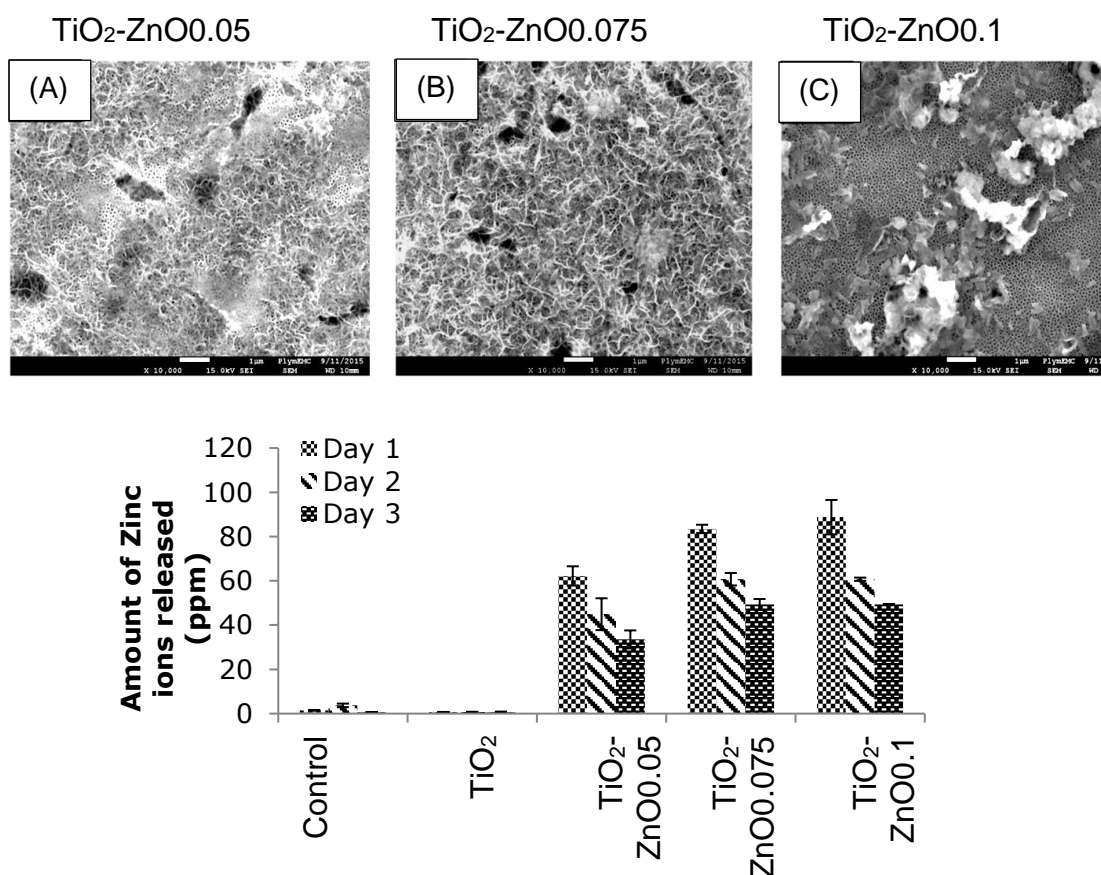


Figure : SEM images of TiO₂ coated with nano ZnO grown using the same hydrothermal method maintaining the same conditions as described in section 6.3.1 with the exception of the concentration of zinc nitrate being (A) 0.05, (B) 0.075 and (C) 0.1 M respectively at $\times 10\,000$ magnification. (D) The concentration of zinc ions present in the acidified SBF after the coated samples have been exposed to SBF for 3 days.

References

Abou El-Nour, K. M. M., Eftaiha, A. a., Al-Warthan, A. & Ammar, R. A. A. (2010) 'Synthesis and applications of silver nanoparticles'. *Arabian Journal of Chemistry*, 3 (3), pp. 135-140.

Ajayan, P. M., Schadler, L. S. & Braun, P. V. (2006) *Nanocomposite Science and Technology*. Wiley.

Akhavan, O. & Ghaderi, E. (2010) 'Cu and CuO nanoparticles immobilized by silica thin films as antibacterial materials and photocatalysts'. *Surface and Coatings Technology*, 205 (1), pp. 219-223.

Al-Mobarak N. A., Al-Swayih A. A. & A., A.-R. F. (2011) 'Corrosion Behavior of Ti-6Al-7Nb Alloy in Biological Solution for Dentistry Applications'. *International Journal of ELECTROCHEMICAL Science and Technology of Advanced Materials*, 6 pp. 11.

Ali, G., Chen, C., Yoo, S. H., Kum, J. M. & Cho, S. O. (2011) 'Fabrication of complete titania nanoporous structures via electrochemical anodization of Ti'. *Nanoscale Res Lett*, 6 (1), pp. 332.

Arafat, M. T., Lam, C. X., Ekaputra, A. K., Wong, S. Y., Li, X. & Gibson, I. (2011) 'Biomimetic composite coating on rapid prototyped scaffolds for bone tissue engineering'. *Acta Biomater*, 7 (2), pp. 809-820.

Arifin, A., Sulong, A. B., Muhamad, N., Syarif, J. & Ramli, M. I. (2014) 'Material processing of hydroxyapatite and titanium alloy (HA/Ti) composite as implant materials using powder metallurgy: A review'. *Materials & Design*, 55 pp. 165-175.

Bai, L., Hang, R., Gao, A., Zhang, X., Huang, X., Wang, Y., Tang, B., Zhao, L. & Chu, P. K. (2015) 'Nanostructured titanium–silver coatings with good antibacterial activity and cytocompatibility fabricated by one-step magnetron sputtering'. *Applied Surface Science*, 355 pp. 32-44.

Balakrishnan, M. & Narayanan, R. (2013) 'Synthesis of anodic titania nanotubes in Na₂SO₄/NaF electrolyte: A comparison between anodization time and specimens with biomaterial based approaches'. *Thin Solid Films*, 540 pp. 23-30.

Balint, R., Cassidy, N. J. & Cartmell, S. H. (2014) 'Conductive polymers: towards a smart biomaterial for tissue engineering'. *Acta Biomater*, 10 (6), pp. 2341-2353.

Bandyopadhyay, A., Dittrick, S., Gualtieri, T., Wu, J. & Bose, S. (2016) 'Calcium phosphate-titanium composites for articulating surfaces of load-bearing implants'. *J Mech Behav Biomed Mater*, 57 pp. 280-288.

Baskar, K., Anusuya, T. & Devanand Venkatasubbu, G. (2017) 'Mechanistic investigation on microbial toxicity of nano hydroxyapatite on implant associated pathogens'. *Materials Science and Engineering: C*, 73 pp. 8-14.

Bauer, S., Kleber, S. & Schmuki, P. (2006) 'TiO₂ nanotubes: Tailoring the geometry in H₃PO₄/HF electrolytes'. *Electrochemistry Communications*, 8 (8), pp. 1321-1325.

Bauer, S., Schmuki, P., von der Mark, K. & Park, J. (2013) 'Engineering biocompatible implant surfaces'. *Progress in Materials Science*, 58 (3), pp. 261-326.

Bekbölet, M. & Araz, C. V. (1996) 'Inactivation of Escherichia coli by photocatalytic oxidation'. *Chemosphere*, 32 (5), pp. 959-965.

Benea, L., Mardare-Danaila, E., Mardare, M. & Celis, J.-P. (2014) 'Preparation of titanium oxide and hydroxyapatite on Ti-6Al-4V alloy surface and electrochemical behaviour in bio-simulated fluid solution'. *Corrosion Science*, 80 pp. 331-338.

Besinis, A., De Peralta, T. & Handy, R. D. (2014) 'The antibacterial effects of silver, titanium dioxide and silica dioxide nanoparticles compared to the dental disinfectant chlorhexidine on Streptococcus mutans using a suite of bioassays'. *Nanotoxicology*, 8 (1), pp. 1-16.

Besinis, A., Hadi, S. D., Le, H. R., Tredwin, C. & Handy, R. D. (2017) 'Antibacterial activity and biofilm inhibition by surface modified titanium alloy medical implants following application of silver, titanium dioxide and hydroxyapatite nanocoatings'. *Nanotoxicology*, 11 (3), pp. 327-338.

Beyth, N., Hourri-Haddad, Y., Domb, A., Khan, W. & Hazan, R. (2015) 'Alternative antimicrobial approach: nano-antimicrobial materials'. *Evid Based Complement Alternat Med*, 2015 pp. 246012.

Bingqiang Cao and Weiping Cai and Yue Li and Fengqiang Sun and Lide, Z. (2005) 'Ultraviolet-light-emitting ZnO nanosheets prepared by a chemical bath deposition method'. *Nanotechnology*, 16 (9), pp. 1734.

Bjurstén, L. M., Rasmusson, L., Oh, S., Smith, G. C., Brammer, K. S. & Jin, S. (2010) 'Titanium dioxide nanotubes enhance bone bonding in vivo'. *J Biomed Mater Res A*, 92 (3), pp. 1218-1224.

Bondarenko, O., Juganson, K., Ivask, A., Kasemets, K., Mortimer, M. & Kahru, A. (2013) 'Toxicity of Ag, CuO and ZnO nanoparticles to selected environmentally relevant test organisms and mammalian cells in vitro: a critical review'. *Archives of Toxicology*, 87 (7), pp. 1181-1200.

Bortolan, C. C., Campanelli, L. C., Bolfarini, C. & Oliveira, N. T. C. (2016) 'Fatigue strength of Ti-6Al-4V alloy with surface modified by TiO₂ nanotubes formation'. *Materials Letters*, 177 pp. 46-49.

Bose, S., Roy, M. & Bandyopadhyay, A. (2012) 'Recent advances in bone tissue engineering scaffolds'. *Trends Biotechnol*, 30 (10), pp. 546-554.

Brammer, K. S., Choi, C., Frandsen, C. J., Oh, S., Johnston, G. & Jin, S. (2011) 'Comparative cell behavior on carbon-coated TiO₂ nanotube surfaces for osteoblasts vs. osteo-progenitor cells'. *Acta Biomater*, 7 (6), pp. 2697-2703.

Brammer, K. S., Oh, S., Cobb, C. J., Bjursten, L. M., van der Heyde, H. & Jin, S. (2009) 'Improved bone-forming functionality on diameter-controlled TiO₂ nanotube surface'. *Acta Biomater*, 5 (8), pp. 3215-3223.

Brie, I.-C., Soritau, O., Dirzu, N., Berce, C., Vulpoi, A., Popa, C., Todea, M., Simon, S., Perde-Schrepler, M., Virag, P., Barbos, O., Chereches, G., Berce, P. & Cernea, V. (2014) 'Comparative in vitro study regarding the biocompatibility of titanium-base composites infiltrated with hydroxyapatite or silicatitanate'. *Journal of Biological Engineering*, 8 pp. 14-14.

Burrows, A., Holman, J., Parsons, A., Pilling, G. & Price, G. (2013) *Chemistry³: Introducing Inorganic, Organic and Physical Chemistry*. OUP Oxford.

Cai, Q., Paulose, M., Varghese, O. K. & Grimes, C. A. (2005) 'The effect of electrolyte composition on the fabrication of self-organised titanium oxide nanotubes arrays by anodic oxidation'. *Journal of material research*, 20 (1), pp. 6.

Chang, X., Zheng, Y., Yang, Q., Wang, L., Pan, J., Xia, Y., Yan, X. & Han, J. (2012) 'Carbonic anhydrase I (CA1) is involved in the process of bone formation and is susceptible to ankylosing spondylitis'. *Arthritis Research & Therapy*, 14 (4), pp. R176.

Chaves, J. M., Escada, A. L. A., Rodrigues, A. D. & Alves Claro, A. P. R. (2016) 'Characterization of the structure, thermal stability and wettability of the TiO₂ nanotubes growth on the Ti-7.5Mo alloy surface'. *Applied Surface Science*, 370 pp. 76-82.

Chekin, F. & Ghasemi, S. (2014) 'Silver nanoparticles prepared in presence of ascorbic acid and gelatin, and their electrocatalytic application'. *Bulletin of Materials Science*, 37 (6), pp. 1433-1437.

Chen, P. C., Hsieh, S. J., Chen, C. C. & Zou, J. (2013a) 'The Microstructure and Capacitance Characterizations of Anodic Titanium Based Alloy Oxide Nanotube'. *Journal of Nanomaterials*, 2013 pp. 1-9.

Chen, Q. & Thouas, G. A. (2015) 'Metallic implant biomaterials'. *Materials Science and Engineering: R: Reports*, 87 pp. 1-57.

Chen, S. (2007) '2 - Practical Electrochemical Cells A2 - Zoski, Cynthia G', *Handbook of Electrochemistry*. Amsterdam: Elsevier, pp. 33-56.

Chen, X., Cai, K., Fang, J., Lai, M., Li, J., Hou, Y., Luo, Z., Hu, Y. & Tang, L. (2013b) 'Dual action antibacterial TiO₂ nanotubes incorporated with silver nanoparticles and coated with a quaternary ammonium salt (QAS)'. *Surface and Coatings Technology*, 216 pp. 158-165.

Cheng, M., Qiao, Y., Wang, Q., Jin, G., Qin, H., Zhao, Y., Peng, X., Zhang, X. & Liu, X. (2015) 'Calcium Plasma Implanted Titanium Surface with Hierarchical Microstructure for Improving the Bone Formation'. *ACS Appl Mater Interfaces*, 7 (23), pp. 13053-13061.

Cheng, T. C., Chang, C. Y., Chang, C. I., Hwang, C. J., Hsu, H. C., Wang, D. Y. & Yao, K. S. (2008) 'Photocatalytic bactericidal effect of TiO₂ film on fish pathogens'. *Surface and Coatings Technology*, 203 (5), pp. 925-927.

Cheng, Z. A., Zouani, O. F., Glinel, K., Jonas, A. M. & Durrieu, M. C. (2013) 'Bioactive chemical nanopatterns impact human mesenchymal stem cell fate'. *Nano Lett*, 13 (8), pp. 3923-3929.

Chennell, P., Feschet-Chassot, E., Devers, T., Awitor, K. O., Descamps, S. & Sautou, V. (2013) 'In vitro evaluation of TiO₂ nanotubes as cefuroxime carriers on orthopaedic implants for the prevention of periprosthetic joint infections'. *Int J Pharm*, 455 (1-2), pp. 298-305.

Chernousova, S. & Epple, M. (2013) 'Silver as antibacterial agent: ion, nanoparticle, and metal'. *Angew Chem Int Ed Engl*, 52 (6), pp. 1636-1653.

Chistyakov, D. A., Savost'anov, K. V., Zotova, E. V. & Nosikov, V. V. (2001) 'Polymorphisms in the Mn-SOD and EC-SOD genes and their relationship to diabetic neuropathy in type 1 diabetes mellitus'. *MBMC Medical Genetics*, 2 (4), pp. 7.

Connaughton, A., Childs, A., Dylewski, S. & Sabesan, V. J. (2014) 'Biofilm Disrupting Technology for Orthopedic Implants: What's on the Horizon?'. *Front Med (Lausanne)*, 1 pp. 22.

Crofford, L. J. (1997) 'COX-1 and COX-2 tissue expression: implications and predictions'. *J Rheumatol Suppl*, 49 pp. 15-19.

D'Alonzo, R. C., Kowalski, A. J., Denhardt, D. T., Nickols, G. A. & Partridge, N. C. (2002) 'Regulation of collagenase-3 and osteocalcin gene expression by collagen and osteopontin in differentiating MC3T3-E1 cells'. *J Biol Chem*, 277 (27), pp. 24788-24798.

Dalal, A., Pawar, V., McAllister, K., Weaver, C. & Hallab, N. J. (2012) 'Orthopedic implant cobalt-alloy particles produce greater toxicity and inflammatory cytokines than titanium alloy and zirconium alloy-based particles in vitro, in human osteoblasts, fibroblasts, and macrophages'. *J Biomed Mater Res A*, 100 (8), pp. 2147-2158.

Dapunt, U., Maurer, S., Giese, T., Gaida, M. M., & nsch, G. M. (2014) 'The Macrophage Inflammatory Proteins MIP1 (CCL3) and MIP2 (CXCL2) in Implant-Associated Osteomyelitis: Linking Inflammation to Bone Degradation'. *Mediators of Inflammation*, 2014 pp. 10.

Dasari, V. R., Kaur, K., Velpula, K. K., Dinh, D. H., J., T. A., Mohanam, S. & Rao, J. S. (2010) 'Downregulation of Focal Adhesion Kinase (FAK) by cord blood stem cells inhibits angiogenesis in glioblastoma'. *Aging*, 2 (11), pp. 11.

Dikova, T. D., Hahm, M. G., Hashim, D. P., Narayanan, N. T., Vajtai, R. & Ajayan, P. M. (2014) 'Mechanism of TiO₂ Nanotubes Formation on the Surface of Pure Ti and Ti-6Al-4V Alloy'. *Advanced Materials Research*, 939 pp. 655-662.

Dong, X., Ji, X., Jing, J., Li, M., Li, J. & Yang, W. (2010) 'Synthesis of Triangular Silver Nanoprisms by Stepwise Reduction of Sodium Borohydride and Trisodium Citrate'. *The Journal of Physical Chemistry C*, 114 (5), pp. 2070-2074.

dos Santos, C. A., Seckler, M. M., Ingle, A. P., Gupta, I., Galdiero, S., Galdiero, M., Gade, A. & Rai, M. (2014) 'Silver nanoparticles: therapeutical uses, toxicity, and safety issues'. *J Pharm Sci*, 103 (7), pp. 1931-1944.

Durual, S., Rieder, P., Garavaglia, G., Filieri, A., Cattani-Lorente, M., Scherrer, S. S. & Wiskott, H. W. (2013) 'TiNOx coatings on roughened titanium and CoCr alloy accelerate early osseointegration of dental implants in minipigs'. *Bone*, 52 (1), pp. 230-237.

Elkady, M. F., Shokry Hassan, H., Hafez, E. E. & Fouad, A. (2015) 'Construction of Zinc Oxide into Different Morphological Structures to Be Utilized as Antimicrobial Agent against Multidrug Resistant Bacteria'. *Bioinorganic Chemistry and Applications*, 2015 pp. 536854.

Escada, A. L. A., Machado, J. P. B., Nakazato, R. Z. & Alves Claro, A. P. R. (2012) 'Obtaining of Nanoapatite in Ti-7.5Mo Surface after Nanotube Growth'. *Materials Science Forum*, 727-728 pp. 1199-1204.

Feng, B., Weng, J., Yang, B. C., Qu, S. X. & Zhang, X. D. (2003) 'Characterization of surface oxide films on titanium and adhesion of osteoblast'. *Biomaterials*, 24 (25), pp. 4663-4670.

Fernandes, E. M., Pires, R. A., Mano, J. F. & Reis, R. L. (2013) 'Bionanocomposites from lignocellulosic resources: Properties, applications and future trends for their use in the biomedical field'. *Progress in Polymer Science*, 38 (10-11), pp. 1415-1441.

Francis, M. J. O., Lees, R. L., Trujillo, E., Martín-Vasallo, P., Heersche, J. N. M. & Mobasher, A. (2002) 'ATPase pumps in osteoclasts and osteoblasts'. *The International Journal of Biochemistry & Cell Biology*, 34 (5), pp. 459-476.

Friedrich, C. R., Kolati, M., Moser, T., Sukotjo, C. & Shokuhfar, T. (2014) 'Survivability of TiO₂nanotubes on the surface of bone screws'. *Surface Innovations*, 2 (1), pp. 60-68.

Gallo, J., Holinka, M. & Moucha, C. S. (2014) 'Antibacterial surface treatment for orthopaedic implants'. *Int J Mol Sci*, 15 (8), pp. 13849-13880.

Galstyan, V., Comini, E., Faglia, G. & Sberveglieri, G. (2013) 'TiO₂ nanotubes: recent advances in synthesis and gas sensing properties'. *Sensors (Basel)*, 13 (11), pp. 14813-14838.

Gao, A., Hang, R., Huang, X., Zhao, L., Zhang, X., Wang, L., Tang, B., Ma, S. & Chu, P. K. (2014) 'The effects of titania nanotubes with embedded silver oxide nanoparticles on bacteria and osteoblasts'. *Biomaterials*, 35 (13), pp. 4223-4235.

Geetha, M., Singh, A. K., Asokamani, R. & Gogia, A. K. (2009) 'Ti based biomaterials, the ultimate choice for orthopaedic implants – A review'. *Progress in Materials Science*, 54 (3), pp. 397-425.

Getzlaf, M. A., Lewallen, E. A., Kremers, H. M., Jones, D. L., Bonin, C. A., Dudakovic, A., Thaler, R., Cohen, R. C., Lewallen, D. G. & van Wijnen, A. J. (2016) 'Multi-disciplinary antimicrobial strategies for improving orthopaedic implants to prevent prosthetic joint infections in hip and knee'. *J Orthop Res*, 34 (2), pp. 177-186.

Ghicov, A., Tsuchiya, H., Macak, J. M. & Schmuki, P. (2005) 'Titanium oxide nanotubes prepared in phosphate electrolytes'. *Electrochemistry Communications*, 7 (5), pp. 505-509.

Gilbert, L., He, X., Farmer, P., Rubin, J., Drissi, H., van Wijnen, A. J., Lian, J. B., Stein, G. S. & Nanes, M. S. (2002) 'Expression of the osteoblast differentiation factor RUNX2 (Cbfa1/AML3/PeBP2alpha A) is inhibited by tumor necrosis factor-alpha'. *J Biol Chem*, 277 (4), pp. 2695-2701.

Gitrowski, C., Al-Jubory, A. R. & Handy, R. D. (2014) 'Uptake of different crystal structures of TiO₂ nanoparticles by Caco-2 intestinal cells'. *Toxicology Letters*, 226 (3), pp. 264-276.

Goncalves Coelho, P., Rui Fernandes, P. & Carrico Rodrigues, H. (2011) 'Multiscale modeling of bone tissue with surface and permeability control'. *J Biomech*, 44 (2), pp. 321-329.

Gopi, D., Collins Arun Prakash, V., Kavitha, L., Kannan, S., Bhalaji, P. R., Shinyjoy, E. & Ferreira, J. M. F. (2011) 'A facile electrodeposition of hydroxyapatite onto borate passivated surgical grade stainless steel'. *Corrosion Science*, 53 (6), pp. 2328-2334.

Gorup, L. F., Longo, E., Leite, E. R. & Camargo, E. R. (2011) 'Moderating effect of ammonia on particle growth and stability of quasi-monodisperse silver nanoparticles synthesized by the Turkevich method'. *Journal of Colloid and Interface Science*, 360 (2), pp. 355-358.

Gulati, K., Aw, M. S., Findlay, D. & Losic, D. (2012a) 'Local drug delivery to the bone by drug-releasing implants: perspectives of nano-engineered titania nanotube arrays'. *Therapeutic Delivery*, 3 (7), pp. 857-873.

Gulati, K., Aw, M. S. & Losic, D. (2011) 'Drug-eluting Ti wires with titania nanotube arrays for bone fixation and reduced bone infection'. *Nanoscale Res Lett*, 6 pp. 571.

Gulati, K., Ramakrishnan, S., Aw, M. S., Atkins, G. J., Findlay, D. M. & Losic, D. (2012b) 'Biocompatible polymer coating of titania nanotube arrays for improved drug elution and osteoblast adhesion'. *Acta Biomater*, 8 (1), pp. 449-456.

Gultepe, E., Nagesha, D., Sridhar, S. & Amiji, M. (2010) 'Nanoporous inorganic membranes or coatings for sustained drug delivery in implantable devices'. *Advanced Drug Delivery Reviews*, 62 (3), pp. 305-315.

Gunawan, L. & Johari, G. P. (2008) 'Specific Heat, Melting, Crystallization, and Oxidation of Zinc Nanoparticles and Their Transmission Electron Microscopy Studies'. *The Journal of Physical Chemistry C*, 112 (51), pp. 20159-20166.

Hadi, S. D. (2014) *The Antibacterial Properties and Biocompatibility of Silver-Hydroxyapatite nanoparticles Coating on Dental implants*. Masters. Plymouth University.

Handy, R. D., Owen, R. & Valsami-Jones, E. (2008) 'The ecotoxicology of nanoparticles and nanomaterials: current status, knowledge gaps, challenges, and future needs'. *Ecotoxicology*, 17 (5), pp. 315-325.

Hao, Y. Q., Li, S. J., Hao, Y. L., Zhao, Y. K. & Ai, H. J. (2013) 'Effect of nanotube diameters on bioactivity of a multifunctional titanium alloy'. *Applied Surface Science*, 268 pp. 44-51.

Hasan, A., Memic, A., Annabi, N., Hossain, M., Paul, A., Dokmeci, M. R., Dehghani, F. & Khademhosseini, A. (2014) 'Electrospun scaffolds for tissue engineering of vascular grafts'. *Acta Biomater*, 10 (1), pp. 11-25.

Hostynek, J. J. & Maibach, H. I. (2004) 'Skin Irritation Potential of Copper Compounds'. *Toxicology Mechanisms and Methods*, 14 (4), pp. 205-213.

Huang, H., Sivayoganathan, M., Duley, W. W. & Zhou, Y. (2015a) 'Efficient localized heating of silver nanoparticles by low-fluence femtosecond laser pulses'. *Applied Surface Science*, 331 pp. 392-398.

Huang, J., Wan, S., Liu, B. & Xue, Q. (2014) 'Improved adaptability of PEEK by Nb doped graphite-like carbon composite coatings for bio-tribological applications'. *Surface and Coatings Technology*, 247 pp. 20-29.

Huang, Y., Han, S., Pang, X., Ding, Q. & Yan, Y. (2013) 'Electrodeposition of porous hydroxyapatite/calcium silicate composite coating on titanium for biomedical applications'. *Applied Surface Science*, 271 pp. 299-302.

Huang, Y., Zhang, X., Mao, H., Li, T., Zhao, R., Yan, Y. & Pang, X. (2015b) 'Osteoblastic cell responses and antibacterial efficacy of Cu/Zn co-substituted hydroxyapatite coatings on pure titanium using electrodeposition method'. *RSC Adv.*, 5 (22), pp. 17076-17086.

Hussain, J. I., Talib, A., Kumar, S., Al-Thabaiti, S. A., Hashmi, A. A. & Khan, Z. (2011) 'Time dependence of nucleation and growth of silver nanoparticles'. *Colloids and Surfaces A: Physicochemical and Engineering Aspects*, 381 (1-3), pp. 23-30.

Hutchinson, J. W. & Suo, Z. (1992) 'Mixed mode cracking in layered materials'. *Advances in applied mechanics*, 29 pp. 188.

Iavicoli, I., Leso, V. & Bergamaschi, A. (2012) 'Toxicological Effects of Titanium Dioxide Nanoparticles: A Review of In Vivo Studies'. *Journal of Nanomaterials*, 2012 pp. 36.

Indira, K., Mudali, U. K. & Rajendran, N. (2014) 'In-vitro biocompatibility and corrosion resistance of strontium incorporated TiO₂ nanotube arrays for orthopaedic applications'. *J Biomater Appl*, 29 (1), pp. 113-129.

Jia, H. & Kerr, L. L. (2013) 'Sustained ibuprofen release using composite poly(lactic-co-glycolic acid)/titanium dioxide nanotubes from Ti implant surface'. *J Pharm Sci*, 102 (7), pp. 2341-2348.

Kaneshiro, S., Ebina, K., Shi, K., Higuchi, C., Hirao, M., Okamoto, M., Koizumi, K., Morimoto, T., Yoshikawa, H. & Hashimoto, J. (2014) 'IL-6 negatively regulates osteoblast differentiation through the SHP2/MEK2 and SHP2/Akt2 pathways in vitro'. *Journal of Bone and Mineral Metabolism*, 32 (4), pp. 378-392.

Kenny, S., Buggy, M. & Hill, R. G. (2001) 'The influence of hydroxyapatite: Zinc oxide ratio on the setting behavior and mechanical properties of polyalkenoate cements'. *Journal of Materials Science: Materials in Medicine*, 12 (10), pp. 901-904.

Khaydarov, R. A., Khaydarov, R. R., Gapurova, O., Estrin, Y. & Scheper, T. (2009) 'Electrochemical method for the synthesis of silver nanoparticles'. *Journal of Nanoparticle Research*, 11 (5), pp. 1193-1200.

Khudhair, D., Bhatti, A., Li, Y., Hamedani, H. A., Garmestani, H., Hodgson, P. & Nahavandi, S. (2016) 'Anodization parameters influencing the morphology and electrical properties of TiO₂ nanotubes for living cell interfacing and investigations'. *Materials Science and Engineering: C*, 59 pp. 1125-1142.

Kim, D., Schmidt-Stein, F., Hahn, R. & Schmuki, P. (2008a) 'Gravity assisted growth of self-organized anodic oxide nanotubes on titanium'. *Electrochemistry Communications*, 10 (7), pp. 1082-1086.

Kim, K., Alam, T. M., Lichtenhan, J. D. & Otaigbe, J. U. (2017) 'Synthesis and characterization of novel phosphate glass matrix nanocomposites containing polyhedral oligomeric silsesquioxane with improved properties'. *Journal of Non-Crystalline Solids*, 463 pp. 189-202.

Kim, S. E., Lim, J. H., Lee, S. C., Nam, S.-C., Kang, H.-G. & Choi, J. (2008b) 'Anodically nanostructured titanium oxides for implant applications'. *Electrochimica Acta*, 53 (14), pp. 4846-4851.

Kokubo, T. (1997) 'Apatite formation on surfaces of ceramics, metals and polymers in body environment'. *Acta Materialia*, 46 (7), pp. 8.

Komori, T. (2010) 'Regulation of Osteoblast Differentiation by Runx2', in Choi, Y. (ed.) *Osteoimmunology: Interactions of the Immune and skeletal systems II*. Boston, MA: Springer US, pp. 43-49.

Kowalski, D., Kim, D. & Schmuki, P. (2013) 'TiO₂ nanotubes, nanochannels and mesosponge: Self-organized formation and applications'. *Nano Today*, 8 (3), pp. 235-264.

Krasicka-Cydzik, E., Kowalski, K., Kaczmarek, A., Glazowska, I. & Heltowski, K. B. (2010) 'Competition between phosphates and fluorides at anodic formation of titania nanotubes on titanium'. *Surface and Interface Analysis*, 42 (6-7), pp. 471-474.

Kwon, S., Singh, R. K., Perez, R. A., Abou Neel, E. A., Kim, H.-W. & Chrzanowski, W. (2013) 'Silica-based mesoporous nanoparticles for controlled drug delivery'. *Journal of Tissue Engineering*, 4 pp. 2041731413503357.

Lai, M., Jin, Z. & Su, Z. (2017) 'Surface modification of TiO₂ nanotubes with osteogenic growth peptide to enhance osteoblast differentiation'. *Materials Science and Engineering: C*, 73 pp. 490-497.

Lan, M. Y., Liu, C. P., Huang, H. H. & Lee, S. W. (2013) 'Both enhanced biocompatibility and antibacterial activity in Ag-decorated TiO₂ nanotubes'. *PLoS One*, 8 (10), pp. e75364.

Lee, B.-G., Choi, J.-W., Lee, S.-E., Jeong, Y.-S., Oh, H.-J. & Chi, C.-S. (2009) 'Formation behavior of anodic TiO₂ nanotubes in fluoride containing electrolytes'. *Transactions of Nonferrous Metals Society of China*, 19 (4), pp. 842-845.

Lee, P. C. & Meisel, D. (1982) 'Adsorption and surface-enhanced Raman of dyes on silver and gold sols'. *The Journal of Physical Chemistry*, 86 (17), pp. 3391-3395.

Lewandowski, A. & Świdarska-Mocek, A. (2009) 'Ionic liquids as electrolytes for Li-ion batteries—An overview of electrochemical studies'. *Journal of Power Sources*, 194 (2), pp. 601-609.

León, B. & Jansen, J. (2009) *Thin Calcium Phosphate Coatings for Medical Implants*. Springer New York.

Li, H., Cui, Q., Feng, B., Wang, J., Lu, X. & Weng, J. (2013) 'Antibacterial activity of TiO₂ nanotubes: Influence of crystal phase, morphology and Ag deposition'. *Applied Surface Science*, 284 pp. 179-183.

Li, Y., Yu, X. & Yang, Q. (2009) 'Fabrication of TiO₂ Nanotube Thin Films and Their Gas Sensing Properties'. *Journal of Sensors*, 2009 pp. 1-19.

Liu, C., Dong, J. Y., Yue, L. L., Liu, S. H., Wan, Y., Liu, H., Tan, W. Y., Guo, Q. Q. & Zhang, D. (2017) 'Rapamycin/sodium hyaluronate binding on nano-hydroxyapatite coated titanium surface improves MC3T3-E1 osteogenesis'. *PLoS One*, 12 (2), pp. e0171693.

Liu, D. & Yu, J. (2009) 'Otsu Method and K-means'. pp. 344-349.

Liu, K., Tian, Y. & Jiang, L. (2013) 'Bio-inspired superoleophobic and smart materials: Design, fabrication, and application'. *Progress in Materials Science*, 58 (4), pp. 503-564.

Liu, S., Yu, J. & Jaroniec, M. (2010) 'Tunable Photocatalytic Selectivity of Hollow TiO₂ Microspheres Composed of Anatase Polyhedra with Exposed {001} Facets'. *Journal of the American Chemical Society*, 132 (34), pp. 11914-11916.

Liu, W., Su, P., Chen, S., Wang, N., Ma, Y., Liu, Y., Wang, J., Zhang, Z., Li, H. & Webster, T. J. (2014) 'Synthesis of TiO₂ nanotubes with ZnO nanoparticles to achieve antibacterial properties and stem cell compatibility'. *Nanoscale*, 6 (15), pp. 9050-9062.

Liu, W., Su, P., Gonzales, A., 3rd, Chen, S., Wang, N., Wang, J., Li, H., Zhang, Z. & Webster, T. J. (2015) 'Optimizing stem cell functions and antibacterial properties of TiO₂ nanotubes incorporated with ZnO nanoparticles: experiments and modeling'. *Int J Nanomedicine*, 10 pp. 1997-2019.

Liu, X., Chu, P. & Ding, C. (2004) 'Surface modification of titanium, titanium alloys, and related materials for biomedical applications'. *Materials Science and Engineering: R: Reports*, 47 (3-4), pp. 49-121.

Lockman, Z., Sreekantan, S., Ismail, S., Schmidt-Mende, L. & MacManus-Driscoll, J. L. (2010) 'Influence of anodisation voltage on the dimension of titania nanotubes'. *Journal of Alloys and Compounds*, 503 (2), pp. 359-364.

Losic, D., Aw, M. S., Santos, A., Gulati, K. & Bariana, M. (2015) 'Titania nanotube arrays for local drug delivery: recent advances and perspectives'. *Expert Opin Drug Deliv*, 12 (1), pp. 103-127.

Lotz, E. M., Olivares-Navarrete, R., Hyzy, S. L., Berner, S., Schwartz, Z. & Boyan, B. D. (2016) 'Comparable responses of osteoblast lineage cells to microstructured hydrophilic titanium-zirconium and microstructured hydrophilic titanium'. *Clin Oral Implants Res*,

Lu, H., Liu, Y., Guo, J., Wu, H., Wang, J. & Wu, G. (2016) 'Biomaterials with Antibacterial and Osteoinductive Properties to Repair Infected Bone Defects'. *International Journal of Molecular Sciences*, 17 (3), pp. 334.

Lugovskoy, A. & Lugovskoy, S. (2014) 'Production of hydroxyapatite layers on the plasma electrolytically oxidized surface of titanium alloys'. *Mater Sci Eng C Mater Biol Appl*, 43 pp. 527-532.

Lugovskoy, S., Weiss, D., Tsadok, U. & Lugovskoy, A. (2016) 'Morphology and antimicrobial properties of hydroxyapatite-titanium oxide layers on the surface of Ti-6Al-4V alloy'. *Surface and Coatings Technology*, 301 pp. 80-84.

Luo, B., Yang, H., Liu, S., Fu, W., Sun, P., Yuan, M., Zhang, Y. & Liu, Z. (2008) 'Fabrication and characterization of self-organized mixed oxide nanotube arrays by electrochemical anodization of Ti-6Al-4V alloy'. *Materials Letters*, 62 (30), pp. 4512-4515.

Ma, Q., Li, M., Hu, Z., Chen, Q. & Hu, W. (2008) 'Enhancement of the bioactivity of titanium oxide nanotubes by precalcification'. *Materials Letters*, 62 (17), pp. 3035-3038.

Macak, J. M., Tsuchiya, H., Ghicov, A., Yasuda, K., Hahn, R., Bauer, S. & Schmuki, P. (2007) 'TiO₂ nanotubes: Self-organized electrochemical formation, properties and applications'. *Current Opinion in Solid State and Materials Science*, 11 (1-2), pp. 3-18.

Mali, S. S., Betty, C. A., Bhosale, P. N., Devan, R. S., Ma, Y.-R., Kolekar, S. S. & Patil, P. S. (2012) 'Hydrothermal synthesis of rutile TiO₂ nanoflowers using Brønsted Acidic Ionic Liquid [BAIL]: Synthesis, characterization and growth mechanism'. *CrystEngComm*, 14 (6), pp. 1920.

Manke, A., Wang, L. & Rojanasakul, Y. (2013) 'Mechanisms of nanoparticle-induced oxidative stress and toxicity'. *Biomed Res Int*, 2013 pp. 942916.

Matykina, E., Conde, A., de Damborenea, J., Marero, D. M. y. & Arenas, M. A. (2011) 'Growth of TiO₂-based nanotubes on Ti-6Al-4V alloy'. *Electrochimica Acta*, 56 (25), pp. 9209-9218.

Mazaheri, M., Eslahi, N., Ordikhani, F., Tamjid, E. & Simchi, A. (2015) 'Nanomedicine applications in orthopedic medicine: state of the art'. *Int J Nanomedicine*, 10 pp. 6039-6053.

Miller, F. P., Vandome, A. F. & McBrewster, J. (2009) *Fick's Law of Diffusion*. VDM Publishing.

Min, J., Choi, K. Y., Dreaden, E. C., Padera, R. F., Braatz, R. D., Spector, M. & Hammond, P. T. (2016) 'Designer Dual Therapy Nanolayered Implant Coatings Eradicate Biofilms and Accelerate Bone Tissue Repair'. *ACS Nano*, 10 (4), pp. 4441-4450.

Mishra, S. K., Ferreira, J. M. & Kannan, S. (2015) 'Mechanically stable antimicrobial chitosan-PVA-silver nanocomposite coatings deposited on titanium implants'. *Carbohydr Polym*, 121 pp. 37-48.

Mizukoshi, Y., Ohtsu, N. & Masahashi, N. (2013) 'Structural and characteristic variation of anodic oxide on pure Ti with anodization duration'. *Applied Surface Science*, 283 pp. 1018-1023.

Mohamed, M. S., Torabi, A., Paulose, M., Kumar, D. S. & Varghese, O. K. (2017) 'Anodically Grown Titania Nanotube Induced Cytotoxicity has Genotoxic Origins'. *Scientific Reports*, 7 pp. 41844.

Mor, G. K., Varghese, O. K., Paulose, M., Shankar, K. & Grimes, C. A. (2006) 'A review on highly ordered, vertically oriented TiO₂ nanotube arrays: Fabrication, material properties, and solar energy applications'. *Solar Energy Materials and Solar Cells*, 90 (14), pp. 2011-2075.

Navaladian, S., Viswanathan, B., Viswanath, R. P. & Varadarajan, T. K. (2006) 'Thermal decomposition as route for silver nanoparticles'. *Nanoscale Research Letters*, 2 (1), pp. 44.

Navale, G. R., Thripuranthaka, M., Late, D. J. & Shinde, S. S. (2015) 'Antimicrobial activity of ZnO nanoparticles against pathogenic bacteria and fungi'. *JSM nanotechnology and nanomedicine*, 3 (1), pp. 9.

Neacsu, P., Mazare, A., Cimpean, A., Park, J., Costache, M., Schmuki, P. & Demetrescu, I. (2014) 'Reduced inflammatory activity of RAW 264.7 macrophages on titania nanotube modified Ti surface'. *Int J Biochem Cell Biol*, 55 pp. 187-195.

Nemmar, A., Holme, J. A., Rosas, I., Schwarze, P. E. & Alfaro-Moreno, E. (2013) 'Recent advances in particulate matter and nanoparticle toxicology: a review of the in vivo and in vitro studies'. *Biomed Res Int*, 2013 pp. 279371.

Niska, K., Pyszka, K., Tukaj, C., Wozniak, M., Radomski, M. W. & Inkielewicz-Stepniak, I. (2015) 'Titanium dioxide nanoparticles enhance production of superoxide anion and alter the antioxidant system in human osteoblast cells'. *Int J Nanomedicine*, 10 pp. 1095-1107.

Oberdorster, G., Ferin, J. & Lehnert, B. E. (1994) 'Correlation between particle size, in vivo particle persistence, and lung injury'. *Environ Health Perspect*, 102

Ortiz, I. Y., Raybolt dos Santos, A., Costa, A. M., Mavropoulos, E., Tanaka, M. N., Prado da Silva, M. H. & de Souza Camargo, S. (2016) 'In vitro assessment of zinc apatite coatings on titanium surfaces'. *Ceramics International*, 42 (14), pp. 15502-15510.

Oshida, Y., Tuna, E. B., Aktoren, O. & Gencay, K. (2010) 'Dental implant systems'. *Int J Mol Sci*, 11 (4), pp. 1580-1678.

Parcharoen, Y., Kajitvichyanukul, P., Sirivisoot, S. & Termsuksawad, P. (2014) 'Hydroxyapatite electrodeposition on anodized titanium nanotubes for orthopedic applications'. *Applied Surface Science*, 311 pp. 54-61.

Park, Y. J., Song, Y. H., An, J. H., Song, H. J. & Anusavice, K. J. (2013) 'Cytocompatibility of pure metals and experimental binary titanium alloys for implant materials'. *J Dent*, 41 (12), pp. 1251-1258.

Patete, J. M., Peng, X., Koenigsmann, C., Xu, Y., Karn, B. & Wong, S. S. (2011) 'Viable methodologies for the synthesis of high-quality nanostructures'. *Green Chemistry*, 13 (3), pp. 482.

Paul, J. W., Hua, S., Ilicic, M., Tolosa, J. M., Butler, T., Robertson, S. & Smith, R. (2017) 'Drug delivery to the human and mouse uterus using immunoliposomes targeted to the oxytocin receptor'. *American Journal of Obstetrics and Gynecology*, 216 (3), pp. 283.e281-283.e214.

Paulose, M., Varghese, O. K., Mor, G. K., Grimes, C. A. & Ong, K. G. (2006) 'Unprecedented ultra-high hydrogen gas sensitivity in undoped titania nanotubes'. *Nanotechnology*, 17 (2), pp. 398-402.

Paulose, M., E., P. H., K., V. O., L., P., C., P. K., K., M. G., A., D. T. & A., G. C. (2007) 'TiO₂ Nanotube Arrays of 1000 μ m Length by Anodization of Titanium Foil: Phenol Red Diffusion'. *J. Phys. Chem C*, 111 pp. 5.

Peng, Z., Ni, J., Zheng, K., Shen, Y., Wang, X., He, G., Jin, S. & Tang, T. (2013) 'Dual effects and mechanism of TiO₂ nanotube arrays in reducing bacterial colonization and enhancing C3H10T1/2 cell adhesion'. *Int J Nanomedicine*, 8 pp. 3093-3105.

Peremarch, C. P.-J., Tanoira, R. P., Arenas, M. A., Matykina, E., Conde, A., De Damborenea, J. J., Barrena, E. G. & Esteban, J. (2010) 'Bacterial adherence to anodized titanium alloy'. *Journal of Physics: Conference Series*, 252 pp. 012011.

Perez-Jorge, C., Conde, A., Arenas, M. A., Perez-Tanoira, R., Matykina, E., de Damborenea, J. J., Gomez-Barrena, E. & Esteban, J. (2012) 'In vitro assessment of Staphylococcus epidermidis and Staphylococcus aureus adhesion on TiO₂ nanotubes on Ti-6Al-4V alloy'. *J Biomed Mater Res A*, 100 (7), pp. 1696-1705.

Persson, G. R. & Renvert, S. (2014) 'Cluster of Bacteria Associated with Peri-Implantitis'. *Clinical Implant Dentistry and Related Research*, 16 (6), pp. 783-793.

Pinto, V. V., Ferreira, M. J., Silva, R., Santos, H. A., Silva, F. & Pereira, C. M. (2010) 'Long time effect on the stability of silver nanoparticles in aqueous medium: Effect of the synthesis and storage conditions'. *Colloids and Surfaces A: Physicochemical and Engineering Aspects*, 364 (1-3), pp. 19-25.

Portan, D. V., Papanicolaou, G. C., Jiga, G. & Caposi, M. (2012) 'A novel experimental method for obtaining multi-layered TiO₂ nanotubes through electrochemical anodizing'. *Journal of Applied Electrochemistry*, 42 (12), pp. 1013-1024.

Pourrahimi, A. M., Liu, D., Strom, V., Hedenqvist, M. S., Olsson, R. T. & Gedde, U. W. (2015) 'Heat treatment of ZnO nanoparticles: new methods to achieve high-purity nanoparticles for high-voltage applications'. *Journal of Materials Chemistry A*, 3 (33), pp. 17190-17200.

Pozio, A., Carewska, M., Mura, F., D'Amato, R., Falconieri, M., De Francesco, M. & Appetecchi, G. B. (2014) 'Composite anodes based on nanotube titanium oxide from electro-oxidation of Ti metal substrate'. *Journal of Power Sources*, 247 pp. 883-889.

Poznyak, S. K., Lisenkov, A. D., Ferreira, M. G. S., Kulak, A. I. & Zheludkevich, M. L. (2012) 'Impedance behaviour of anodic TiO₂ films prepared by galvanostatic anodisation and powerful pulsed discharge in electrolyte'. *Electrochimica Acta*, 76 pp. 453-461.

Prabhu., S. & Poulouse, E. K. (2012) 'Silver nanoparticles: mechanism of antimicrobial action, synthesis, medical applications, and toxicity effects'. *International Nano Letters*, 2 (32), pp. 10.

Prosini, P. P., Cento, C. & Pozio, A. (2013) 'Electrochemical characterization of titanium oxide nanotubes'. *Electrochimica Acta*, 111 pp. 120-125.

Pujari-Palmer, M., Pujari-Palmer, S., Lu, X., Lind, T., Melhus, H., Engstrand, T., Karlsson-Ott, M. & Engqvist, H. (2016) 'Pyrophosphate Stimulates Differentiation, Matrix Gene Expression and Alkaline Phosphatase Activity in Osteoblasts'. *PLoS One*, 11 (10), pp. e0163530.

Pérez, M. A., Moiraghi, R., Coronado, E. A. & Macagno, V. A. (2008) 'Hydroquinone Synthesis of Silver Nanoparticles: A Simple Model Reaction To Understand the Factors That Determine Their Nucleation and Growth'. *Crystal Growth & Design*, 8 (4), pp. 1377-1383.

Raghupathi, K. R., Koodali, R. T. & Manna, A. C. (2011) 'Size-Dependent Bacterial Growth Inhibition and Mechanism of Antibacterial Activity of Zinc Oxide Nanoparticles'. *Langmuir*, 27 (7), pp. 4020-4028.

Raphel, J., Holodniy, M., Goodman, S. B. & Heilshorn, S. C. (2016) 'Multifunctional coatings to simultaneously promote osseointegration and prevent infection of orthopaedic implants'. *Biomaterials*, 84 pp. 301-314.

Razavi, M., Fathi, M., Savabi, O., Beni, B. H., Razavi, S. M., Vashae, D. & Tayebi, L. (2014) 'Coating of biodegradable magnesium alloy bone implants using nanostructured diopside (CaMgSi₂O₆)'. *Applied Surface Science*, 288 pp. 130-137.

Reidy, B., Haase, A., Luch, A., Dawson, K. & Lynch, I. (2013) 'Mechanisms of Silver Nanoparticle Release, Transformation and Toxicity: A Critical Review of Current Knowledge and Recommendations for Future Studies and Applications'. *Materials*, 6 (6), pp. 2295.

Rekha, K., Nirmala, M., Nair, M. G. & Anukaliani, A. (2010) 'Structural, optical, photocatalytic and antibacterial activity of zinc oxide and manganese doped zinc oxide nanoparticles'. *Physica B: Condensed Matter*, 405 (15), pp. 3180-3185.

Remya, N. S., Syama, S., Sabareeswaran, A. & Mohanan, P. V. (2017) 'Investigation of chronic toxicity of hydroxyapatite nanoparticles administered orally for one year in wistar rats'. *Materials Science and Engineering: C*, 76 pp. 518-527.

Rodríguez-Cano, A., Pacha-Olivenza, M.-Á., Babiano, R., Cintas, P. & González-Martín, M.-L. (2014) 'Non-covalent derivatization of aminosilanized titanium alloy implants'. *Surface and Coatings Technology*, 245 pp. 66-73.

Rogers, J. V., Parkinson, C. V., Choi, Y. W., Speshock, J. L. & Hussain, S. M. (2008) 'A Preliminary Assessment of Silver Nanoparticle Inhibition of Monkeypox Virus Plaque Formation'. *Nanoscale Research Letters*, 3 (4), pp. 129-133.

Roguska, A., Belcarz, A., Pisarek, M., Ginalska, G. & Lewandowska, M. (2015) 'TiO₂ nanotube composite layers as delivery system for ZnO and Ag nanoparticles - an unexpected overdose effect decreasing their antibacterial efficacy'. *Mater Sci Eng C Mater Biol Appl*, 51 pp. 158-166.

Roguska, A., Belcarz, A., Suchecki, P., Andrzejczuk, M. & Lewandowska, M. (2016) 'Antibacterial Composite Layers on Ti: Role of ZnO Nanoparticles'. *Archives of Metallurgy and Materials*, 61 (1),

Roguska, A., Pisarek, M., Andrzejczuk, M. & Lewandowska, M. (2014) 'Synthesis and characterization of ZnO and Ag nanoparticle-loaded TiO₂ nanotube composite layers intended for antibacterial coatings'. *Thin Solid Films*, 553 pp. 173-178.

Roos-Jansåker, A.-M., Almhöjd, U. S. & Jansson, H. (2017) 'Treatment of peri-implantitis: clinical outcome of chloramine as an adjunctive to non-surgical therapy, a randomized clinical trial'. *Clinical Oral Implants Research*, 28 (1), pp. 43-48.

Roy, P., Berger, S. & Schmuki, P. (2011) 'TiO₂ nanotubes: synthesis and applications'. *Angew Chem Int Ed Engl*, 50 (13), pp. 2904-2939.

Sabokbar, A., Millett, P. J., Myer, B. & Rushton, N. (1994) 'A rapid, quantitative assay for measuring alkaline phosphatase activity in osteoblastic cells in vitro'. *Bone and Mineral*, 27 (1), pp. 57-67.

Schmittgen, T. D. & Livak, K. J. (2008) 'Analyzing real-time PCR data by the comparative CT method'. *Nature Protocols*, 3 (6), pp. 1101-1108.

Sheikhpour, M., Barani, L. & Kasaeian, A. (2017) 'Biomimetics in drug delivery systems: A critical review'. *Journal of Controlled Release*, 253 pp. 97-109.

Sieniawski, J., Ziąja, W., Kubiak, K. & Motyk, M. (2013) 'Microstructure and Mechanical Properties of High Strength Two-Phase Titanium Alloys'.

Sirelkhatim, A., Mahmud, S., Seeni, A., Kaus, N. H. M., Ann, L. C., Bakhori, S. K. M., Hasan, H. & Mohamad, D. (2015) 'Review on Zinc Oxide Nanoparticles: Antibacterial Activity and Toxicity Mechanism'. *Nano-Micro Letters*, 7 (3), pp. 219-242.

Sista, S., Wen, C., Hodgson, P. D. & Pande, G. (2013) 'Expression of cell adhesion and differentiation related genes in MC3T3 osteoblasts plated on titanium alloys: role of surface properties'. *Mater Sci Eng C Mater Biol Appl*, 33 (3), pp. 1573-1582.

Sivasakthi, P., Ramesh Babu, G. N. K., Murugavel, K. & Mohan, S. (2017) 'Facile method of pulse electrodeposited NiO-CeO₂Sm doped nanocomposite electrode on copper foam for supercapacitor application'. *Journal of Alloys and Compounds*, 709 pp. 240-247.

So, S., Lee, K. & Schmuki, P. (2012) 'Ultrafast Growth of Highly Ordered Anodic TiO₂ Nanotubes in Lactic Acid Electrolytes'. *Journal of the American Chemical Society*, 134 (28), pp. 11316-11318.

Song, J., Chen, Q., Zhang, Y., Diba, M., Kolwijck, E., Shao, J., Jansen, J. A., Yang, F., Boccaccini, A. R. & Leeuwenburgh, S. C. (2016) 'Electrophoretic Deposition of Chitosan Coatings Modified with Gelatin Nanospheres To Tune the Release of Antibiotics'. *ACS Appl Mater Interfaces*, 8 (22), pp. 13785-13792.

Sreekantan, S., Saharudin, K. A. & Wei, L. C. (2011) 'Formation of TiO₂nanotubes via anodization and potential applications for photocatalysts, biomedical materials, and photoelectrochemical cell'. *IOP Conference Series: Materials Science and Engineering*, 21 pp. 012002.

Stankovic, A., Dimitrijevic, S. & Uskokovic, D. (2013) 'Influence of size scale and morphology on antibacterial properties of ZnO powders hydrothermally synthesized using different surface stabilizing agents'. *Colloids Surf B Biointerfaces*, 102 pp. 21-28.

Sul, Y. (2003) 'The significance of the surface properties of oxidized titanium to the bone response: special emphasis on potential biochemical bonding of oxidized titanium implant'. *Biomaterials*, 24 (22), pp. 3893-3907.

Sun, T., Xue, N., Liu, C., Wang, C. & He, J. (2015) 'Bioactive (Si, O, N)/(Ti, O, N)/Ti composite coating on NiTi shape memory alloy for enhanced wear and corrosion performance'. *Applied Surface Science*, 356 pp. 599-609.

Swank, K. & Drago, J. L. (2013) 'Postarthroscopic Infection in the Knee following Medical or Dental Procedures'. *Case Rep Orthop*, 2013 pp. 974017.

Talebian, N., Amininezhad, S. M. & Doudi, M. (2013) 'Controllable synthesis of ZnO nanoparticles and their morphology-dependent antibacterial and optical properties'. *Journal of Photochemistry and Photobiology B: Biology*, 120 pp. 66-73.

Tarun, A. S. (2003) 'Gene Expression for Carbonic Anhydrase Isoenzymes in Human Nasal Mucosa'. *Chemical Senses*, 28 (7), pp. 621-629.

Tatarchuk, V. V., Sergievskaya, A. P., Korda, T. M., Druzhinina, I. A. & Zaikovskiy, V. I. (2013) 'Kinetic Factors in the Synthesis of Silver Nanoparticles by Reduction of Ag⁺ with Hydrazine in Reverse Micelles of Triton N-42'. *Chemistry of Materials*, 25 (18), pp. 3570-3579.

Taveira, L. V., Macák, J. M., Tsuchiya, H., Dick, L. F. P. & Schmuki, P. (2005) 'Initiation and Growth of Self-Organized TiO₂ Nanotubes Anodically Formed in NH₄F / (NH₄)₂SO₄ Electrolytes'. *Journal of The Electrochemical Society*, 152 (10), pp. B405.

Tay, C. Y., Fang, W., Setyawati, M. I., Chia, S. L., Tan, K. S., Hong, C. H. L. & Leong, D. T. (2014) 'Nano-hydroxyapatite and Nano-titanium Dioxide Exhibit Different Subcellular Distribution and Apoptotic Profile in Human Oral Epithelium'. *ACS Applied Materials & Interfaces*, 6 (9), pp. 6248-6256.

Tonelli, F. M. P., Santos, A. K., Gomes, K. N., Lorençon, E., Guatimosim, S., Ladeira, L. O. & Resende, R. R. (2012) 'Carbon nanotube interaction with extracellular matrix proteins producing scaffolds for tissue engineering'. *International Journal of Nanomedicine*, 7 pp. 4511-4529.

Tran, Q. H., Nguyen, V. Q. & Le, A.-T. (2013) 'Silver nanoparticles: synthesis, properties, toxicology, applications and perspectives'. *Advances in Natural Sciences: Nanoscience and Nanotechnology*, 4 (3), pp. 033001.

Tsaryk, R., Peters, K., Unger, R. E., Feldmann, M., Hoffmann, B., Heidenau, F. & Kirkpatrick, C. J. (2013) 'Improving cytocompatibility of Co₂₈Cr₆Mo by TiO₂ coating:

gene expression study in human endothelial cells'. *J R Soc Interface*, 10 (86), pp. 20130428.

Tsikandylakis, G., Berlin, O. & Branemark, R. (2014) 'Implant survival, adverse events, and bone remodeling of osseointegrated percutaneous implants for transhumeral amputees'. *Clin Orthop Relat Res*, 472 (10), pp. 2947-2956.

Uhm, S.-H., Song, D.-H., Kwon, J.-S., Lee, S.-B., Han, J.-G., Kim, K.-M. & Kim, K.-N. (2013) 'E-beam fabrication of antibacterial silver nanoparticles on diameter-controlled TiO₂ nanotubes for bio-implants'. *Surface and Coatings Technology*, 228 pp. S360-S366.

Vaca-Cornejo, F., Reyes, H., Jiménez, S., Velázquez, R. & Jiménez, J. (2017) 'Pilot Study Using a Chitosan-Hydroxyapatite Implant for Guided Alveolar Bone Growth in Patients with Chronic Periodontitis'. *Journal of Functional Biomaterials*, 8 (3), pp. 29.

Valverde-Alva, M. A., García-Fernández, T., Villagrán-Muniz, M., Sánchez-Aké, C., Castañeda-Guzmán, R., Esparza-Alegría, E., Sánchez-Valdés, C. F., Llamazares, J. L. S. & Herrera, C. E. M. (2015) 'Synthesis of silver nanoparticles by laser ablation in ethanol: A pulsed photoacoustic study'. *Applied Surface Science*, 355 pp. 341-349.

Vandebriel, R. J. & De Jong, W. H. (2012) 'A review of mammalian toxicity of ZnO nanoparticles'. *Nanotechnol Sci Appl*, 5 pp. 61-71.

Venkatesan, J., Qian, Z.-J., Ryu, B., Ashok Kumar, N. & Kim, S.-K. (2011) 'Preparation and characterization of carbon nanotube-grafted-chitosan – Natural hydroxyapatite composite for bone tissue engineering'. *Carbohydrate Polymers*, 83 (2), pp. 569-577.

Venugopal, J., Prabhakaran, M. P., Zhang, Y., Low, S., Choon, A. T. & Ramakrishna, S. (2010) 'Biomimetic hydroxyapatite-containing composite nanofibrous substrates for bone tissue engineering'. *Philosophical Transactions of the Royal Society A: Mathematical, 	 	 	 	 Physical and Engineering Sciences*, 368 (1917), pp. 2065-2081.

Wagoner Johnson, A. J. & Herschler, B. A. (2011) 'A review of the mechanical behavior of CaP and CaP/polymer composites for applications in bone replacement and repair'. *Acta Biomaterialia*, 7 (1), pp. 16-30.

Wang, J. & Lin, Z. (2008) 'Freestanding TiO₂ nanotube arrays with ultrahigh aspect ratio via electrochemical anodisation'. *Chemistry of Materials*, 20 (4), pp. 5.

Wang, N., Li, H., Lu, W., Li, J., Wang, J., Zhang, Z. & Liu, Y. (2011) 'Effects of TiO₂ nanotubes with different diameters on gene expression and osseointegration of implants in minipigs'. *Biomaterials*, 32 (29), pp. 6900-6911.

Wang, W. & Poh, K., Chye (2013) 'Titanium Alloys in Orthopaedics'. [in Sieniawski, J. *Titanium alloys-Advances in properties control*. InTech. Available at: <https://www.intechopen.com/books/titanium-alloys-advances-in-properties-control/titanium-alloys-in-orthopaedics> (Accessed: Wang, W. & Poh, K., Chye

Wei, L., Lu, J., Xu, H., Patel, A., Chen, Z. S. & Chen, G. (2015) 'Silver nanoparticles: synthesis, properties, and therapeutic applications'. *Drug Discov Today*, 20 (5), pp. 595-601.

Widmer, A. F. (2001) 'New Developments in Diagnosis and Treatment of Infection in Orthopedic Implants'. *Clinical Infectious Diseases*, 33 (Supplement_2), pp. S94-S106.

Wu, S., Liu, X., Yeung, K. W. K., Liu, C. & Yang, X. (2014) 'Biomimetic porous scaffolds for bone tissue engineering'. *Materials Science and Engineering: R: Reports*, 80 pp. 1-36.

X L Liu, C. C. Z. a. S. J. X. a. J. Q. N. a. W. B. a. J. F. W. a. J. G. a. J. M. L. a. J. H. Z. a. (2012) 'Residual strains and optical properties of ZnO thin epilayers grown on r -sapphire planes'. *Semiconductor Science and Technology*, 27 (3), pp. 035008.

Xiao, F. X. (2012) 'Construction of highly ordered ZnO-TiO₂ nanotube arrays (ZnO/TNTs) heterostructure for photocatalytic application'. *ACS Appl Mater Interfaces*, 4 (12), pp. 7055-7063.

Xie, Y., He, Y., Irwin, P. L., Jin, T. & Shi, X. (2011) 'Antibacterial activity and mechanism of action of zinc oxide nanoparticles against *Campylobacter jejuni*'. *Appl Environ Microbiol*, 77 (7), pp. 2325-2331.

Xin, W., Meng, C., Jie, W., Junchao, T., Yan, S. & Ning, D. (2010) 'Morphology dependence of TiO₂ nanotube arrays on anodization variables and buffer medium'. *Journal of Semiconductors*, 31 (6), pp. 063003.

Yang, S., Wang, H., Yu, H., Zhang, S., Fang, Y., Zhang, S. & Peng, F. (2016) 'A facile fabrication of hierarchical Ag nanoparticles-decorated N-TiO₂ with enhanced photocatalytic hydrogen production under solar light'. *International Journal of Hydrogen Energy*, 41 (5), pp. 3446-3455.

Yanovska, A., Kuznetsov, V., Stanislavov, A., Danilchenko, S. & Sukhodub, L. (2011) 'Synthesis and characterization of hydroxyapatite-based coatings for medical implants obtained on chemically modified Ti6Al4V substrates'. *Surface and Coatings Technology*, 205 (23-24), pp. 5324-5329.

Yao, K. S., Wang, D. Y., Chang, C. Y., Weng, K. W., Yang, L. Y., Lee, S. J., Cheng, T. C. & Hwang, C. C. (2007) 'Photocatalytic disinfection of phytopathogenic bacteria by

dye-sensitized TiO₂ thin film activated by visible light'. *Surface and Coatings Technology*, 202 (4), pp. 1329-1332.

Yeniyol, S., He, Z., Yuksel, B., Boylan, R. J., Urgen, M., Ozdemir, T. & Ricci, J. L. (2014) 'Antibacterial Activity of As-Annealed TiO₂ Nanotubes Doped with Ag Nanoparticles against Periodontal Pathogens'. *Bioinorg Chem Appl*, 2014 pp. 829496.

Zeng, L. & Bieler, T. R. (2005) 'Effects of working, heat treatment, and aging on microstructural evolution and crystallographic texture of α , α' , α'' and β phases in Ti - 6Al - 4V wire'. *Materials Science and Engineering: A*, 392 (1-2), pp. 403-414.

Zhang, H., Sun, Y., Tian, A., Xue, X. X., Wang, L., Alquhali, A. & Bai, X. (2013) 'Improved antibacterial activity and biocompatibility on vancomycin-loaded TiO₂ nanotubes: in vivo and in vitro studies'. *Int J Nanomedicine*, 8 pp. 4379-4389.

Zhao, L., Wang, H., Huo, K., Cui, L., Zhang, W., Ni, H., Zhang, Y., Wu, Z. & Chu, P. K. (2011) 'Antibacterial nano-structured titania coating incorporated with silver nanoparticles'. *Biomaterials*, 32 (24), pp. 5706-5716.

Zhao, X., Wang, G., Zheng, H., Lu, Z., Zhong, X., Cheng, X. & Zreiqat, H. (2013) 'Delicate refinement of surface nanotopography by adjusting TiO₂ coating chemical composition for enhanced interfacial biocompatibility'. *ACS Appl Mater Interfaces*, 5 (16), pp. 8203-8209.

Zhong Lin, W. (2004) 'Zinc oxide nanostructures: growth, properties and applications'. *Journal of Physics: Condensed Matter*, 16 (25), pp. R829.

Zhu, B., Zhang, X., Wang, S., Zhang, S., Wu, S. & Huang, W. (2007) 'Synthesis and catalytic performance of TiO₂ nanotubes-supported copper oxide for low-temperature CO oxidation'. *Microporous and Mesoporous Materials*, 102 (1), pp. 333-336.

Zhu, R., Yadama, V., Liu, H., Lin, R. J. T. & Harper, D. P. (2017) 'Fabrication and characterization of Nylon 6/cellulose nanofibrils melt-spun nanocomposite filaments'. *Composites Part A: Applied Science and Manufacturing*, 97 pp. 111-119.

Čapek, J., Hauschke, M., Brůčková, L. & Roušar, T. (2017) 'Comparison of glutathione levels measured using optimized monochlorobimane assay with those from ortho-phthalaldehyde assay in intact cells'. *Journal of Pharmacological and Toxicological Methods*, 88, Part 1 pp. 40-45.

Publication



The Effect of Initial Etching Sites on the Morphology of TiO₂ Nanotubes on Ti-6Al-4V Alloy

U. Danookdharree,^{a,*} H. R. Le,^{a,*} and C. Tredwin^b

^aSchool of Marine Science and Engineering, Plymouth University, Plymouth PL4 8AA, United Kingdom

^bPeninsula Schools of Medicine and Dentistry, Plymouth University, Plymouth PL6 8BU, United Kingdom

Anodisation was performed in phosphate and fluoride containing electrolytes at different pH and sweep rates with the aim of analysing the variation in current density during the process continuously. The effect of pH and sweep rate on the morphology of titanium dioxide (TiO₂) nanotubes, grown on Ti-6Al-4V alloy, has been explicitly examined in this study. At the same time a microscopic analysis of the different stages of the formation of the nanotubes was performed. A new perspective to the growth mechanisms of the nanotubes was brought about in this study. The morphology of the nanotubes was closely related to the density of initial etching sites.

© 2015 The Electrochemical Society. [DOI: 10.1149/2.0011511jes] All rights reserved.

Manuscript submitted March 2, 2015; revised manuscript received June 23, 2015. Published 00 0, 2015.

Surface modification of bone and dental implants at micro and nano-level has attracted significant interest in the last decade. The application of such modification to titanium and its alloys has a positive effect on the bioactivity property of the latter.¹⁻³ This effect has been partly ascribed to the biomimicking of bone nanostructure.⁴⁻⁷ Meanwhile, the nano-modification acts as a coating preventing the leaching of ions, such as vanadium and aluminum in the case of Ti-6Al-4V, from the implant's surface, as such, preventing the loosening of the latter and avoiding further complications.⁸⁻¹⁰ Converting the nanostructured coating to a porous tubular structure, can make the latter act as a drug carrier.^{11,12} Antibacterial agent is one example of the drugs that can be inserted to add antibacterial properties to the surface.

Several methods have been employed for the self-assembly of nanotubes on titanium surface, out of which anodisation is a successful electrochemical process having the ability of producing well defined nanotubes. The procedure involves different types of electrolytes, among which aqueous electrolytes have been shown to allow the manipulation of the morphology of the nanotubes while generating rough exterior walls as compared to non-aqueous ones. Such property has been associated with stronger adhesion forces between the nanotubes.¹³⁻¹⁵ Since one of the objectives of this work was to produce good adhesion for the nanotubes coating, aqueous electrolytes were used.

Apart from the presence of water, the ions in the electrolytes also have a role to play in the fabrication of the nanotubes. They are involved in both the oxidation and etching processes during the electrochemical process. In this study phosphate ions were used because of their pH buffering capacity in association of fluoride ions which are responsible for the etching process to a large extent.¹⁶⁻¹⁸

There are additional parameters affecting the self-assembly of the nanotubes on titanium or its alloy such as the pH of the electrolyte, voltage, temperature and duration of anodisation. The pH of electrolyte and the duration of the anodisation have been shown to affect the thickness of the coating. In 2005, Cai and colleagues, published their work whereby they observed the increase in height of nanotubes, formed in the presence of sulfate ions. For the growth duration of 20 hours, at 10 V, the thickness of the nanotubes increased from 0.32 μm to 1.40 μm when the pH was changed from 1.3 to 5.0.¹⁹ Paulose and associates worked with sulfate ions similarly for just 30 minutes and observed the same pattern with nanotubes length being 0.35 μm at pH 1.1 and 2 μm at pH 5.0.²⁰ Even when phosphate ions were used, the same pattern was observed with a height of 0.32 μm at pH 4.2 and 1.75 μm at pH 4.6.²¹ Moreover, increasing the duration of the anodisation process increases the thickness too.^{8,22,23} At the same time, the anodisation voltage has been shown to affect both the diameter and length of the nanotubes. The group of Schmuki demonstrated the change of diameter from 15 to 120 nm and length from 20 nm to 1 μm with respect to voltage variation from 1 to 25 V.²⁴ However

several studies focusing on the effects of the applied voltage showed that there is a limit in the increase in diameter.^{24,25} Those papers emphasized the effects of voltage applied in the anodisation process. Nonetheless little attention was given to the effect of the initial voltage ramp in phosphate containing electrolytes on the nanotubes morphology. Taveira and colleagues did examine the effect of the initial ramp and their results indicated that the initial formation of the barrier layer, which was considered to have a major role in the final morphology obtained was dependent on the sweep rate.^{23,25} Consecutively, it could be presumed that the initial change in voltage affects the interfacial adhesion between the nanotubes and the substrate. These authors however concentrated their work on the morphology of the nanotubes grown in sulfate containing electrolytes and did not consider the adhesive strength of the coating.

Following the initiation stage, the nanotubes are self-assembled by the competition between the oxidation and chemical dissolution. The process as to why the nanotubes are uniformly arranged had been described by different groups.^{26,27} The group of Dikova performed a step by step analysis of the nanotube formation in hydrofluoric acid at 25 V and provided microscopic images of the different structures at different intervals. Meanwhile, the group of Macak used ammonium sulfate in the presence of fluoride ions at 20 V in order to obtain nanotubes with an average diameter of 100 nm. They concentrated on the changes in morphology during the formation of the nanotubes especially with the change in pH but they did not analyse the details at different stages of formation.

This is what motivated this study to aim at analysing the effect of pH and sweep rate on the final morphology of the nanotubes formed on medical grade titanium alloys in phosphate and fluoride containing electrolytes. This research work also looked into the different stages of nanotube formation in order to understand how the respective morphology was developed.

Experimental

Materials.— Medical grade 5, e.g. Ti-6Al-4 V titanium alloy, having 6% aluminum and 4% vanadium was laser-cut into discs of 15 mm in diameter and 1 mm in thickness. The polishing with sand paper (#600-1200) was done using a rotary instrument (Grinder-Polisher, Buehler, UK Ltd, Coventry, UK). The cleaning (Sodium carbonate, Na₂CO₃; Sodium Hydroxide, NaOH and Sodium Citrate, NaH₂C₆H₅O₇) and anodisation (Ammonium Sulphate, (NH₄)₂SO₄; Ammonium dihydrogen Phosphate, NH₄H₂PO₄; Ammonium Fluoride, NH₄F) stages were performed using solutions prepared from reagent grade chemicals from Sigma Aldrich (UK). The power for the anodisation process was supplied from a programmable power supply and the pH and temperature were measured using a Seven Compact™ pH/Ion Meter S220, both purchased from Metrix Electronics Limited. Roughness measurements were done using a LEXT OLS 3000 confocal laser microscope. Microscopic images were obtained using a field

*E-mail: huirong.le@plymouth.ac.uk; urvashi.danookdharree@plymouth.ac.uk

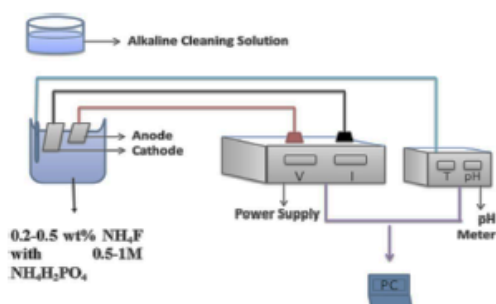


Figure 1. Anodisation process followed by adhesion test.

112 emission scanning electron microscope (FE-SEM JEOL 7001F) which
 113 was combined with an Oxford Instrument AzTEC energy-dispersive
 114 X-ray spectroscopy (EDS) in the Electron Microscopy Centre at the
 115 University of Plymouth.

116 *Self-assembly of nanotubes.*— The discs were polished using grade
 117 #500-1200 silicon carbide paper followed by a diamond paste finishing to
 118 R_a roughness of less than 100 nm from R_a roughness above 300 nm.
 119 Anodisation was then performed using 0.2–0.5 wt% (weight percent)
 120 ammonium fluoride and 0.5–1 M (mole/litre) ammonium dihydrogen
 121 phosphate after an alkaline cleaning in an ultrasonic bath. The sweep
 122 rate was varied from 0.2–1.5 Volts per second (V/s) from zero to 20 V
 123 using a personalised Labview program. The latter would communicate
 124 with the power supply which in turn ramped the voltage supplied to
 125 the anode and cathode in the electrolytes. The set-up was as shown
 126 in Figure 1. The pH was adjusted using aqueous sodium hydroxide
 127 (3 M), for more alkalinity and aqueous phosphoric acid (3M) for more
 128 acidity. The pH range used was from 3 to 6. The current value was
 129 recorded at every 0.2 s for 3600 s.

130 *Analysis of nanotubes.*— The nanotubes formed were initially,
 131 qualitatively, analyzed using SEM associated with the EDS analysis.
 132 From the results, the average diameter, wall thickness and composition
 133 of elements present in the coating were then acquired at different for-

134 mation stages. Furthermore, the porosity of the coating was calculated
 135 using Matlab image analysis. The steps taken were as follows:

- 1) Initial cropping of the image, in order to remove the labels. 136
- 2) Contrast enhancement aiming at adjusting the pixel intensity. 137
- 3) Application of median and average filter in order to smoothen the 138
 image. 139
- 4) Otsu's Method of thresholding was performed to distinguish in 140
 between intensities. 141
- 5) The image was then converted to black and white 142
- 6) The porosity was then calculated using the following formula: 143

$$144 \text{ Porosity} = \frac{\text{Number of Black pixels}}{\text{Total Number of pixels}}$$

145 Results and Discussion

146 The current value recorded during the whole anodisation process
 147 was analyzed and correlated with the SEM images of the sample.
 148 The results were used to interpret the different stages of nanotube
 149 formation. 149

150 *Anodising current variation.*— The anodising current densities
 151 varied with respect to time, as shown in Figure 2, during the
 152 process of nanotube fabrication. The time and current density values are
 153 taken from an initial sweep rate of 0.5 V/s. The values were used for
 154 comparison at various stages of the experiment.

155 It could be observed that in the first second, there was a steep
 156 increase in current density to a very high value, in the range of 10
 157 mA mm^{-2} (Peak A), as compared to the whole process. It decreased
 158 within the first second itself. The rise to peak A happened in order
 159 to develop an electrode potential at the anode as soon as a circuit
 160 was made. There was a fast rate of electron transfer between the
 161 electrolyte and the electrode during that second. This current was
 162 determined by the initial resistance of the electrolyte. Subsequently
 163 the current density increased to a maximum of 0.5 mAmm^{-2} (B) when
 164 the voltage was about 10 V (that is about half way during the change
 165 in the anodising voltage). It then decreased to a minimum point after
 166 which it increased slightly during part C until 20 V was reached. The
 167 current density stayed momentarily at that value to follow a minor
 168 decrease after which it stayed almost constant for one hour. This was
 169 associated with the fact that the equilibrium of the electrochemical
 170 cell was reached.

171 Between the decrease from peak A to the increase to peak B, there
 172 was no detectable current for about 500 ms, (From 1 to 1.5 s) as shown

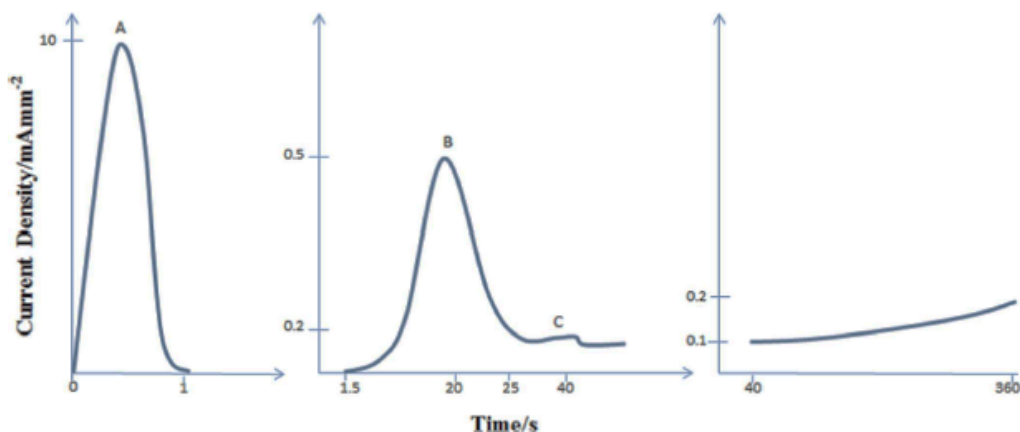


Figure 2. Current Density variation during anodisation.

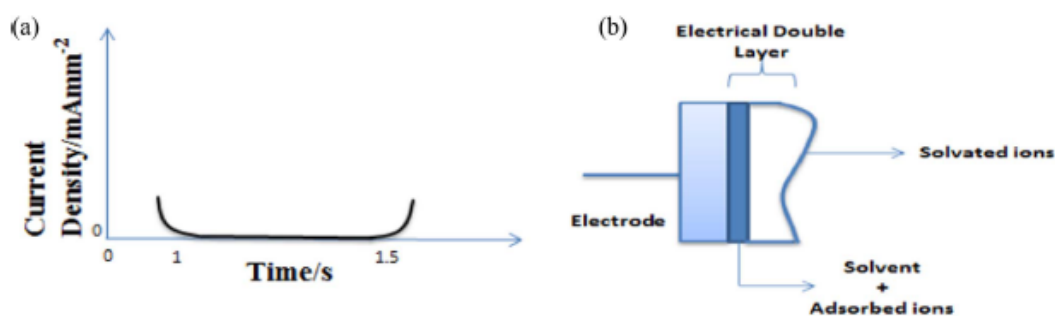


Figure 3. (a) Current density variation during the anodisation whereby the IPE effect was seen and (b) the presence of the electrical double layer.

173 in Figure 3a. This was associated with the ideal polarisable electrode
 174 (IPE) as even though there was a change in voltage, no charge was
 175 flowing between the electrolyte and electrode. Therefore the electrical
 176 double layer at the solution/electrode interface acted as a capacitor.
 177 When the electrode potential was applied, some of the ions from the
 178 electrolyte got adsorbed on the surface of the electrode giving rise
 179 to desolvated ions.²⁸ Hence the double layer was formed by firstly,
 180 the solvent molecules along with the adsorbed ions and secondly the
 181 solvated ions in the electrolyte as shown in Figure 3b. In this situation
 182 the capacitance was dependent on the electric potential applied and
 183 the effect was independent of the content of the electrolyte.

184 The increase to peak B occurred due to the resistance of the electro-
 185 lyte and was considered to be non-faradaic and was related to
 186 Ohm's law. Therefore according to Ohm's equation, $V = IR_s$ (R_s is
 187 the resistance of the solution), the current density increased, as the
 188 voltage increased, to peak B. It stopped increasing at that point as the
 189 potential for barrier formation was reached.

190 The following decrease was due to the formation of the barrier
 191 layer on the titanium alloy sample:



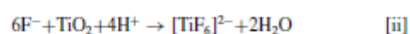
192 This decrease in current can be explained using the following
 193 equations:

$$i = \alpha \exp(\beta E) \quad [1]$$

$$i = \alpha \exp(\beta U/d) \quad [2]$$

196 where i is the current density, E is the electric field across the
 197 oxide layer and U is the voltage across the oxide with thickness, d .
 198 According to equations 1 and 2, as the thickness of the oxide layer d
 199 is increased, the current density would decrease exponentially.

200 The current density increased slightly until peak C where the voltage
 201 reaches the level of 20 V. This increase is owing to the increase in
 202 voltage and the polarization of the anode. The current density drops
 203 after the voltage reaches the maximum 20 V and the polarization
 204 stops. The gradual increase in the current density after peak C was
 205 due to the etching of the oxide layer in the presence of the F^- ions
 206 which react with the TiO_2 layer forming soluble $[\text{TiF}_6]^{2-}$ ions



207 This reaction becomes almost constant when equilibrium between
 208 oxide layer formation and etching was reached. Therefore there was
 209 a further equilibrium (ii). As such the rate of oxide formation equated
 210 the rate of chemical dissolution. Following the theory proposed by
 211 Macak and colleagues, the dissolution allowed the nanotubes to grow
 212 deeper in the oxide layer while the continuous oxidation helped the
 213 nanotubes to grow longer 2. In the meantime small nanotubes will
 214 disappear leaving the larger nanotubes leading to a small increase in
 215 nanotube diameter and porosity with time. Therefore a small increase
 216 in current density is observed.

The different parts of the anodisation curve (peak A and B and part C) would be used as a reference in the following subsections in order to be able to analyse the different parameters with respect to those part of the anodisation curve.

Effect of pH.— While the pH value was varied, the initial sweep rate was maintained at 0.5 V/s. The change was found to affect the anodising current with respect to time and voltage, especially in the initial stage which is crucial in the formation of the nanotubes.

In Figure 4, no pattern was visible in the increase in current density to peak B. This was because this part was independent of the reactions.

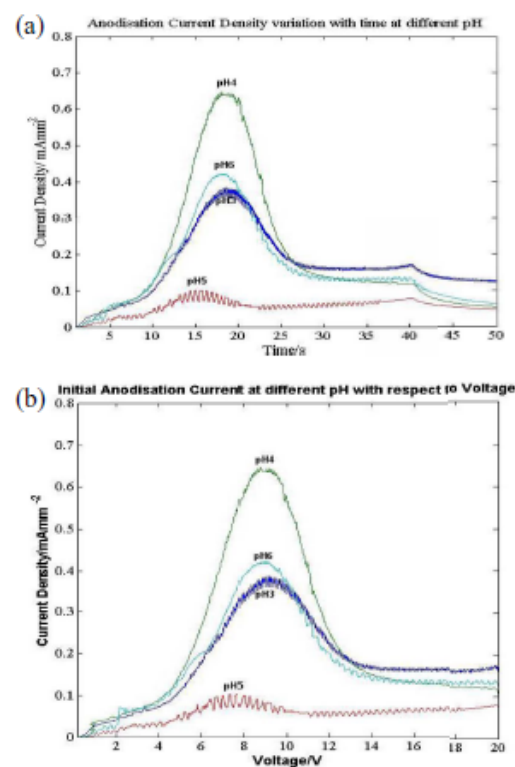


Figure 4. Anodisation Current Density variation at different pH with (a) time and (b) voltage at SR 0.5 V/s.

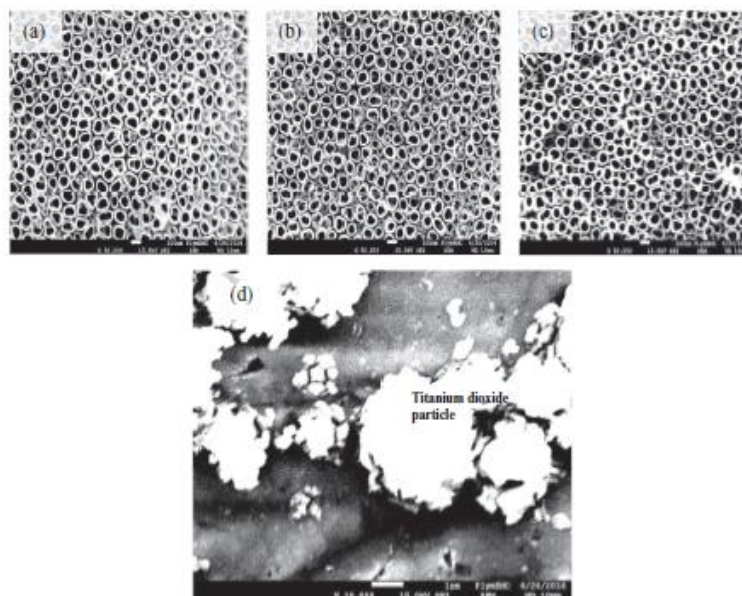


Figure 5. Surface microscopic view of nanotubes coating grown at 0.5 V/s and (a) pH 3, (b) pH 4, (c) pH 5 at 50 000 magnification and (d) pH 6 at 10 000 magnification.

It was mainly dependent on the resistance of the electrolytes which was reliant on the rate of electron transfer.

No visible pattern again was observed in the formation of the barrier oxide layer both in the peak value and the rate of change in current density. However the etching was dependent on the pH. The final value reached just before equilibrium was higher at a lower pH even though faster etching was expected in the presence of more hydrogen ions. This can be explained by the etching and oxidation process on the oxide-metal interface. The etching reaction (ii) is the slowest process among them, as such could be chosen as the rate determining step. The etching process was a temperature dependent reaction (Arrhenius type relationship) and followed Fick's Law of diffusion. Therefore it was characterised by the following equation:

$$i = \alpha \exp\left(\frac{-\Delta G}{RT}\right) \quad [3]$$

whereby α is a constant, R is the gas constant, T is the temperature and ΔG is the Gibbs energy change.

At chemical equilibrium,

$$\Delta G = \Delta G^\circ + RT \ln Q \quad [4]$$

Whereby G° is the maximum amount of energy change happening and Q is the reaction quotient dependent on the reactants in the reaction and can be expressed as follows:

$$Q = \frac{[\text{TiF}_6^{2-}]}{[\text{H}^+]^4 [\text{F}^-]^6} \quad [5]$$

Thus at equilibrium,

$$i = \frac{\alpha}{Q} \exp\left(\frac{-\Delta G^\circ}{RT}\right) \quad [6]$$

$$i = \alpha \frac{[\text{H}^+]^4 [\text{F}^-]^6}{[\text{TiF}_6^{2-}]} \exp\left(\frac{-\Delta G^\circ}{RT}\right) \quad [7]$$

Since the energy change to the electric field by the following:

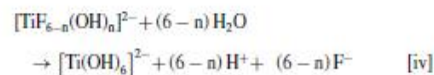
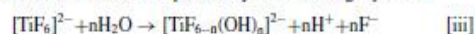
$$G^\circ = -nFE^\circ \quad [8]$$

the current density can be related to the concentrations of different ions as follows:

$$i = \alpha \frac{[\text{H}^+]^4 [\text{F}^-]^6}{[\text{TiF}_6^{2-}]} \exp\left(\frac{nFE^\circ}{RT}\right) \quad [9]$$

These equations were correlated with the etching process whereby the current density was dependent on the reactants, the number of electrons involved and the field potential. The concentration of fluoride ions was determined by the concentration of NH_4F while the concentration of H^+ was determined by pH. The lower the pH, the higher the H^+ concentration, as such leading to higher current density.

However, pH 6 was an exception. This could be associated with the fact that when doing anodisation at pH 6, hydroxide particles were formed along with the formation of nanotubes. This could be further explained by the associated high resolution microscopic images. Figure 5 showed the different microscopic image of the coating formed after anodisation for 3600 s. It could be observed that from pH 3 to pH 5, nanotubes were formed with a uniform distribution with the number of nanotubes being higher at pH 5 than at pH 3 with thicker walls. This observation would be further discussed below. The observation at pH 6 could be explained by the fact that the concentration of H^+ ions was lower and could be better explained by the following equations:



Normally following the above reactions, titanium dioxide nanotubes were expected to form. However at pH 6, the presence of lower concentration of H^+ ions causes a reduction in reaction (v), allowing the accumulation of titanium hydroxide which later decomposed to oxide particles.

Figure 6b showed how the final current density value decreased from pH 3 to pH 4 and slightly higher at pH 5 than that at pH 4. The

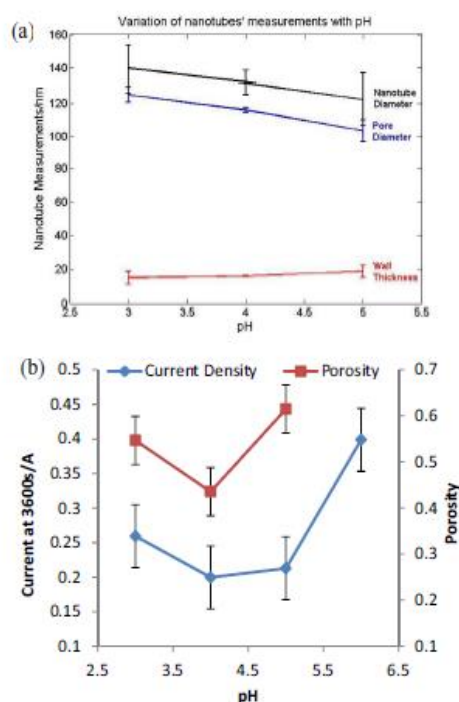


Figure 6. (a) Nanotube morphology and (b) Final Current value variation with pH.

diameter of the nanotubes was found to be affected by about 10 nm for every increment in pH. The final current value at pH 5 and pH 6 was found to be higher due to the additional particles being formed on the surface of the alloy. It was noted that even though the wall thickness increased with increasing pH, the general diameter of the nanotubes was found to be decreasing. Figure 6b also showed that there was an increase in porosity with increasing pH while Figure 7 highlighted the higher current density change during the last 30 minutes of anodisation at pH 6. The current density values at pH 3, 4 and 5 were lower than that at pH 6 further highlighting the effect of increase in hydroxide concentration. Nanotubes formed on titanium or its alloy can have a U-shape or a V-shape.^{11,29,30} Chen and colleagues further demonstrated the effect of temperature on the resulting shape. Gradual increase in temperature led to the formation of a U-shape and steady temperature led to the growth of V-shaped nanotubes. Since the anodisation in this work was done at steady room temperature, V-shaped nanotubes were expected. Figure 8 emphasized on the change in pore diameter in with height of nanotube as per previous researches. This effect has been seen in nanotubes formed in the presence of phosphate ions as well.³¹ During the review of the literature, there was an emphasis on the effect of pH on the thickness of titania nanotubes whereby longer nanotubes were obtained in electrolytes having a higher pH. Combining both theories related to the growth of titania nanotubes, the longer nanotubes formed at a higher pH would be expected to have a larger pore diameter as compared to the short nanotubes formed at lower pH. However in this study it was found that the pore diameter becomes smaller with increasing pH. This was associated with the fact that at a higher pH, the hydrogen ions mediated reaction (equation (ii))

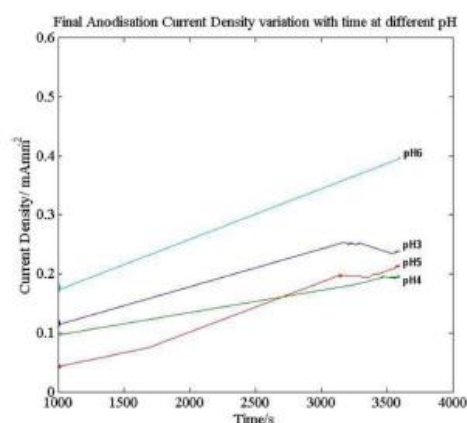


Figure 7. Variation of current density with time for the last 30 minutes at different pH.

was reduced. Therefore the wall thickness did not decrease with increase in the length of the nanotubes.

Meanwhile more nanotubes were grown at pH 5 (144 nanotubes per square micrometer) as compared to pH 3 (72 per square micrometer). The number of nanotubes was doubled in quantity when pH increased from 3 to 5. This could be explained by the fact that the etching started earlier at a lower pH. This resulted in larger etching sites at a lower pH and hence accounting for fewer sites on a specific area as shown in Figure 5. At a higher pH, the rate of oxidation was quicker as such more nanotubes were formed per unit area and hence smaller in diameter, as illustrated by Figure 5.

Effects of sweep rate.— The value and the rate of change in current density increased with increasing sweep rate prior to the peak B in Figure 9. The general increase was because for the same time period a larger voltage was applied to the system. As such following Ohm's Law, the current value would be higher at a specific time at a higher sweep rate. Although the final potentials reached by all the systems were the same, it could be observed that the maximum current density value reached was higher with increasing sweep rate, as shown in Figure 9. The general increase could be correlated with a larger power density being applied at SR1.5 in order to form the oxide barrier layer as compared to SR0.2. As such a greater stress would be generated at the electrode/oxide interface at a higher sweep rate. It was also

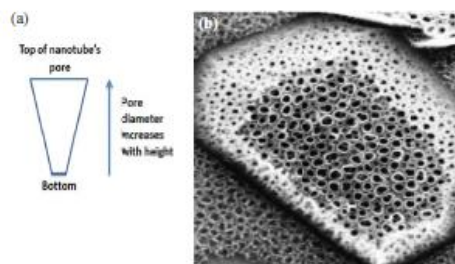


Figure 8. (a) V-shape nanotube depicting change in pore diameter (b) Cross section of nanotubes at different heights showing smaller pores at the bottom and larger pore at the top.

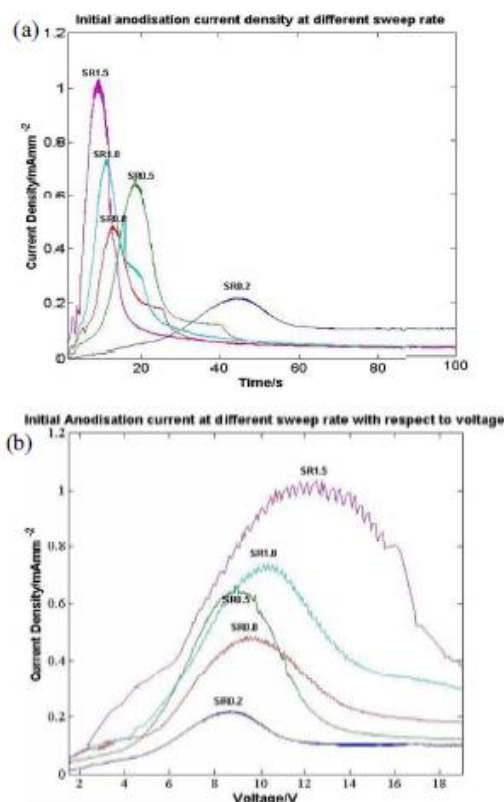


Figure 9. Current density variation with respect to (a) time and (b) voltage at different sweep rate.

observed that the reaction at sweep rate 0.8 V/s does not follow the pattern. In fact the maximum current density reached did not change massively at sweep rate between 0.5 V/s and 1.0 V/s. It could be presumed that the barrier layer was formed with the appropriate stress needed when the anodisation was done between those two sweep rates. A faster sweep rate (e.g. 1.5 V/s) would cause higher stress and more defects in the barrier layer and hence higher maximum current density. On the other hand a very slow sweep rate (e.g. 0.2 V/s) would generate less stress for the barrier formation.

Figure 9b highlighted the start of etching at a lower voltage at SR0.2 as compared to SR1.5. Basically because of a longer time taken to reach 20 V at SR 0.2, part C of the anodisation curve was supposed to occur later as compared to SR 1.5. This was visible in Figure 9a. However peak C was reached at a higher voltage at SR1.5 than at SR 0.2. And at the highest sweep rate peak C was not even reached prior to 10 V. This would mean that at a lower sweep rate a smaller potential was required before etching could occur. A justification for this behavior would be that at SR0.2, lower impedance was encountered so that the total voltage is lower when etching occurs. This could be confirmed by the area under the graph in Figure 9b whereby at SR 1.5, larger impedance was encountered during etching.

Figure 11 showed a general decrease in the pore diameter of the nanotubes with increase in sweep rate. The value decreased from about 120 nm at sweep rate 0.2 V/s to about half that value at sweep rate 1.5 V/s. It was also observed that the wall thickness of the nanotubes slightly increased as visible on the microscopic images in Figure 10. The final current density value followed the same pattern as pore diameter shown in Figure 11b. The porosity however remained unchanged. This was because as the sweep rate increased the number of etching sites increased as well. However since there was a decrease in the diameter of the nanotubes, these two parameters counteracted each other causing the porosity to stay almost the same at the different SR.

This would lead to the conclusion that there were more etching sites at a higher sweep rate so that more nanotubes were formed per unit area as shown in Figure 10. Figure 12 zoomed in on the change in current density for the last 30 minutes of the process and it was seen that the current values were lower at higher sweep rates in general even though the maximum current reached at the beginning was higher. This could be correlated with the pore diameter shown in Figure 11. The lower the pore diameter, the lower the current density due to increased resistance to ion diffusion.

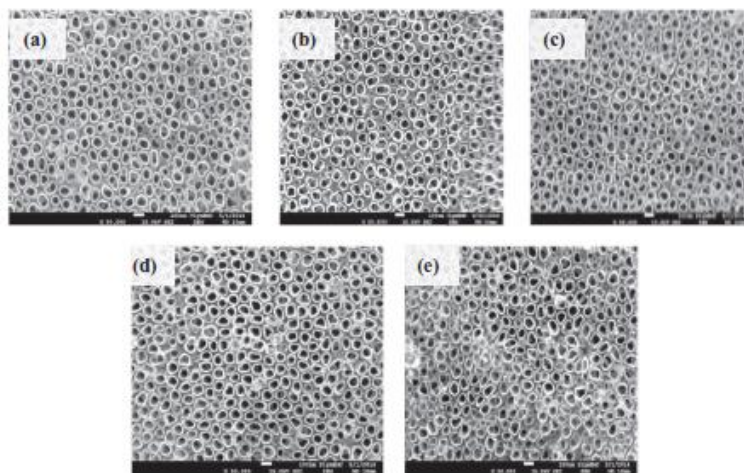


Figure 10. Microscopic images of the TiO₂ nanotubes coating at pH 4 and sweep rate (a) 0.2, (b) 0.5, (c) 0.8 (d) 1.0 and (e) 1.5 V/s.

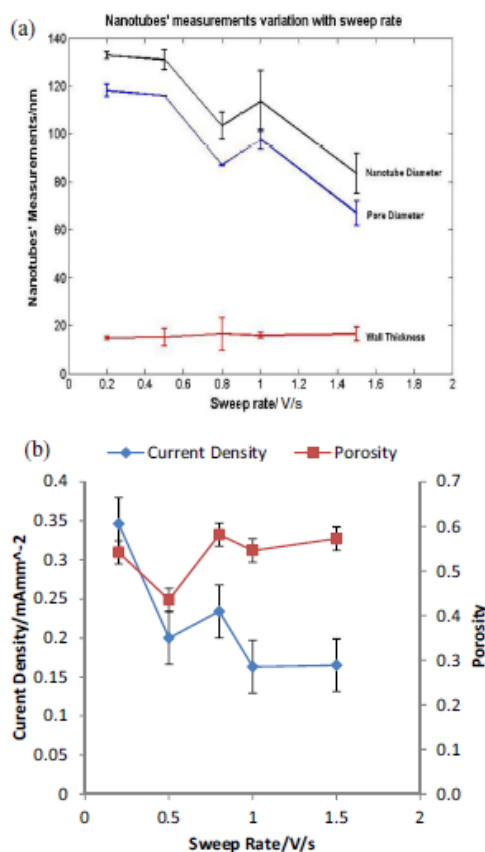


Figure 11. (a) Nanotube morphology and (b) final Current value variation with pH.

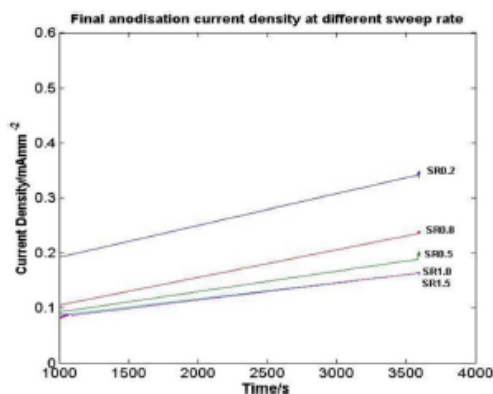


Figure 12. Variation of current density with time during the last 30 minutes of anodisation at different sweep rates.

Stages of nanotube formation.— The different stages of the fabrication of nanotubes were analyzed by stopping the anodisation at different time and then analysing the resulting substrate using the SEM. The detailed images were presented in Figure 13. After the formation of the barrier layer, etching was seen to take place before 20 V was reached, due to the presence of nanoparticles of average diameter 25 nm, not well-defined. Five minutes after 20 V was reached, it was observed that the beta phase was more etched than the alpha phase. At the same time, small doughnut-shaped pores were formed with diameter ranging from 50 nm to 100 nm.

Following Figure 13, it was observed that with time, more etching was taking place with increased size of the nanoparticles to about 100 nm. At 10 minutes (Figure 13b) the beta phase was further etched with the presence of nanograins (100 nm). Five minutes after this, the nanoparticles were further etched giving rise to nanoporous structures with pores (50 nm–100 nm) in the beta phase as shown in Figure 13c. The dissolved nanoparticles were believed to be vanadium oxide. This was because vanadium oxide is highly soluble. Vanadium is the β -stabiliser in a Ti-6Al-4V alloy and as such the vanadium to aluminum content is normally present in a higher quantity in the beta-phase than the alpha-phase.^{32–34} The difference in the vanadium content in the alpha and beta phase accounted for more etching in the beta phase. The EDS analysis further showed the difference in Figure 14 (3.1% in alpha phase and 3.8% in beta phase).

At 20 minutes (Figure 13d), the porous structures in the beta phase, became nanograins while the alpha phase maintained the porous structures with thicker walls of the pores. The nanograins could be assumed to be the underlying alpha phase grains which developed into a thin layer of nanoporous layer five minutes later. Then these grains developed into nanoporous structures (~100 nm) while the randomly arranged nanopores (<50 nm) in the alpha phase became uniformly arranged nanotubes after 40 minutes. After one hour, the nanotubes had an average diameter of 100 nm in the alpha phase as could be seen in Figure 13g. The beta phase contained similar sized nanopores alongside a smaller amount of smaller sized pores as well.

The above observations allowed a new perspective into the growth of nanotubes. Chen and colleagues did obtain a pattern in the growth of nanotubes on the surface of Ti-10Ta similar to what was obtained in this study.¹¹ The anodisation started with randomly arranged porous structures and ended with uniformly arranged nanotubes. Meanwhile, Dikova and colleagues defined the mechanism behind the growth of nanotube on the surface of Ti-6Al-4V with the surface of their samples being coated up to 80% with nanotubes in 7 hours.²⁶ During the process, where they used just hydrofluoric acid (HF), the synthesis of the nanotubes started with the presence of nano-seeds. The latter looked different from the ones obtained in this study whereby nanograins with a rough surface structure were the first result of etching. It was only in the beta phase that the 'bowl-like' structures were grown on the titanium alloy used in this study (Figure 13d). The buffering effect of the electrolyte being used in this study was responsible for this effect.

This analysis led to the mechanism behind nanotube assembly in the alpha-phase being as follows:

- 1) Formation of nanoparticles,
- 2) Development of 'doughnut-shaped' structures due to arrangement of the nanoparticles leading to the formation of pores slightly bigger than 200 nm pore diameter.
- 3) Evolution of the nanoparticles and above mentioned structures into nanoporous structures, with varying diameters, all over the surface.
- 4) Growth of the nanoporous surface into nanotubes with solid wall and a distance in between each nanotube.

The nanoparticles formed, at the beginning, was due to the etching process in the presence of fluoride ions. Since fluoride ions have small diameter, they were able to force nano-cracks on the surface of the barrier-oxide layer. The latter led to the presence of the uniformly spread nanoparticles all over the surface of the sample. Since

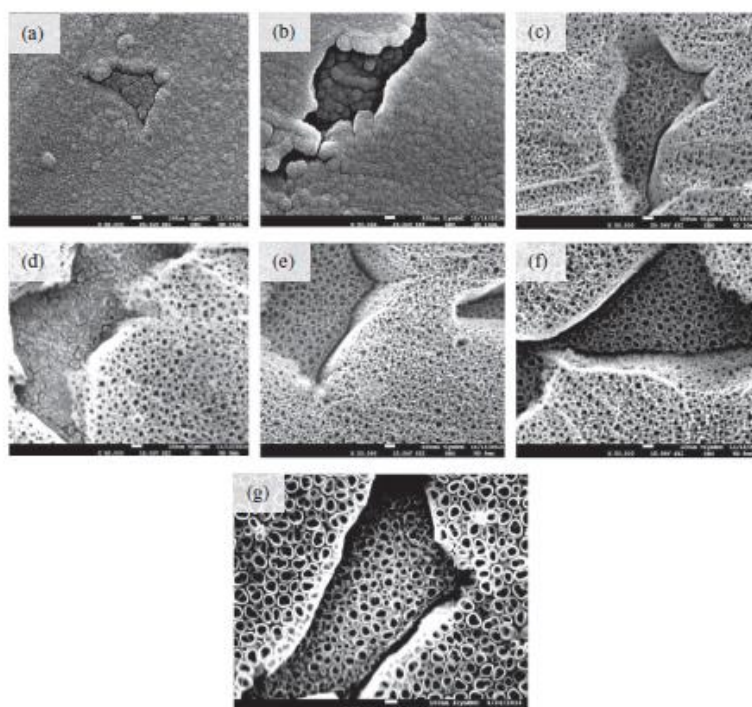


Figure 13. Coating grown at pH 4 and sweep rate 0.5 V/s viewed at 50 000 magnification at (a) 5 minutes, (b) 10 minutes, (c) 15 minutes (d) 20 minutes, (e) 25 minutes, (f) 30 minutes and (g) 60 minutes of anodisation.

436 nanoparticles have the tendency to stick to each other, they arranged
 437 themselves in such a way that the doughnut-shaped structures were
 438 formed as shown in Figure 15. The presence of the pore inside the
 439 structure was due to the fluoride ions. Growth of similar structures all
 440 over the place led to the formation of the nanoporous layer. Since there
 441 was oxidation and chemical dissolution at the same time, neighbour-
 442 ing, 'doughnut-shaped' structures was assumed to be stacked together
 443 so that the competition reactions and lateral forces resulted in the
 444 formation of the nanoporous surface. The pores in the nanoporous
 445 structures do have smaller pore diameters than the previous structures
 446 because oxidation was taking place at the same time as dissolution.

447 This process continued for 30 min whereby the pores were arranged
 448 uniformly with solid walls differentiating the pores from each other.
 449 It was observed that there was a distance in between the walls of
 450 nanotubes. This followed the theory derived by the group of Schmuki
 451 whereby it was explained that as the nanotubes grew longer, the pore
 452 diameter decreased, accounting for larger base and smaller opening.²⁹

453 *Theory of initial etching sites.*— In this study, Ti-6Al-4V alloy
 454 was used and as such, during the anodisation process, the oxides of
 455 aluminum and vanadium was formed along with titanium dioxide.
 456 Nonetheless, the discussion in this work was limited to the oxide of

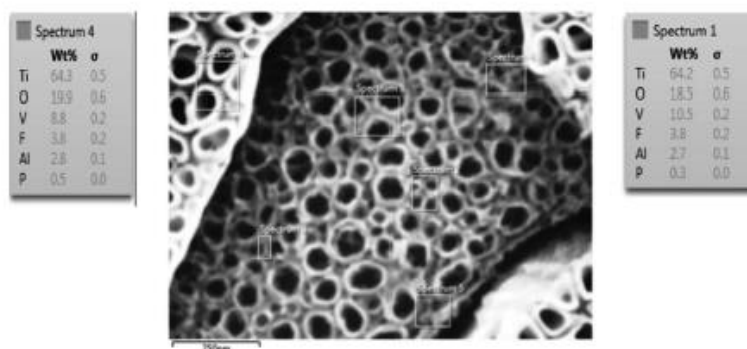


Figure 14. The EDS analysis results comparing the vanadium content in the alpha and beta phase.

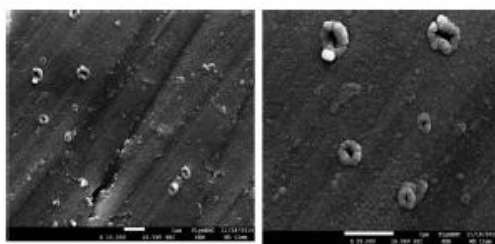


Figure 15. Presence of 'doughnut-shaped' structures at 5 minutes of anodization at low magnification.

457 titanium only, due to the predominance of titanium over aluminum
458 and vanadium on the coating (EDS analysis in Figure 14).

459 Following the observations at different pH and sweep rate, a new
460 theory was deduced which related the growth of nanotubes to the
461 etching sites at very early stage. The effect of pH and sweep rate
462 could be illustrated using Figures 16 and 17 respectively. Due to the
463 large volumetric expansion in the oxidation process, the oxide layer
464 is under large in-plane compressive stress. This could cause buckling
465 or wrinkling according to Hutchinson and Suo.³⁵ The valley of the
466 wrinkles is under additional surface energy and becomes preferred
467 sites for etching. At lower pH, etching started earlier so that the
468 barrier layer was thinner and less stressed. Fewer etching sites per
469 unit area were expected so that smaller number of nanotubes per unit
470 area compared to a higher pH. Figure 16a illustrated that there are
471 fewer nanotubes at lower pH. The wall is thinner while pores are
472 larger due to the ongoing etching of the walls at higher concentration
473 of hydrogen ions. Part (b) showed the growth of the nanotubes at
474 higher pH. Due to lower concentration of hydrogen ions and hence
475 higher $[\text{OH}^-]$, more oxide was deposited on the inner walls of the
476 tubes. This caused the wall thickness to increase with time. Therefore
477 nanotubes with thicker walls and smaller pores were obtained at a
478 higher pH. This is in agreement with the images in Figure 6.

479 Figure 17 illustrated the effect of sweep rate on the growth. At
480 a higher sweep rate, the reaction was quicker, resulting in a higher
481 stress being generated accounting for more bulging and as such the
482 presence of more etching sites with smaller size. It is expected that
483 the in-plane stress due to the oxidation expansion is proportional
484 to the reaction rate. This was imaged by Figure 17 whereby more

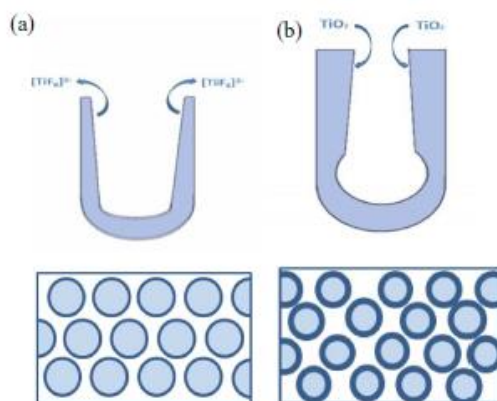


Figure 16. The nanotube morphology at (a) low pH and (b) high pH highlighting the dominating reaction taking place.

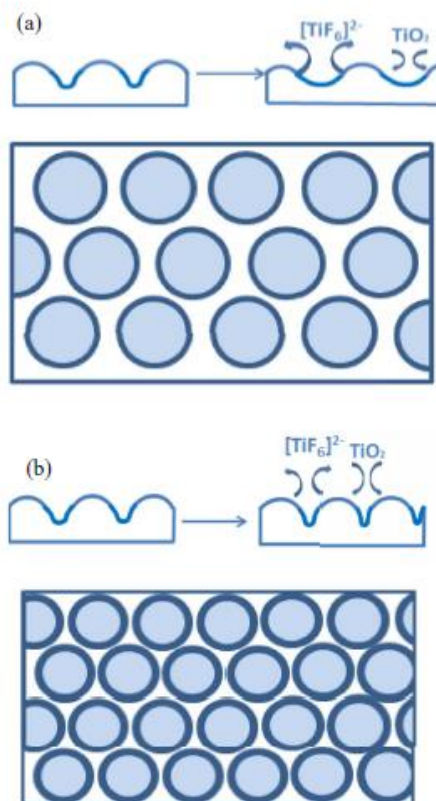


Figure 17. The nanotube morphology at (a) low sweep rate and (b) high sweep rate highlighting the main reaction taking place.

485 nanotubes with much smaller pores were formed at higher sweep rate
486 than at lower sweep rate. The final current density is determined by
487 the etching rate which is determined by the impedance of the smaller
488 pores. Therefore the final density decreases with increasing sweep rate
489 due to higher impedance of the pores. Nevertheless the wall thickness
490 is not significantly affected as shown in Figure 9b.

491 In summary the rate of formation of barrier layer plays an important
492 role. Higher reaction rate leads to higher stress and hence higher
493 density of nanotubes. In turn this will increase the impedance of the
494 pores and reduces the growth rate.

Conclusions

495 This study proved that sweep rate did have a significant role to
496 play in the self-assembly of titanium dioxide nanotubes as well as the
497 pH of the electrolyte. The morphology was dependent on the rate at
498 which the voltage was increased to the target value along with the
499 concentration of hydrogen ions in the electrolytes. Furthermore, this
500 research work provided a deeper insight to the different stages of the
501 nano self-assembly which allowed a new theory related to the initial
502 etching sites to be derived involving the formation of titanium dioxide
503 nanotubes on the surface of Ti-6Al-4V, in the presence of phosphate
504 ions. This would be beneficial in carrying antibacterial agents in the
505 nanotubes providing a good surface coverage.
506

Acknowledgments

The authors acknowledge the funding through a joint PhD studentship for UD by the Faculty of Science and Engineering and Peninsular Schools of Medicine and Dentistry is acknowledged. The assistance by the technical team in the School of Marine Science and Engineering and the Electron Microscopy Centre (EMC) of Plymouth University is gratefully acknowledged.

References

- N. H. Ahmad Barudin, S. Sreekantan, O. M. Thong, and L. K. Lay, "Studies of Cell Growth on TiO₂ Nanotubes," *Adv. Mater. Res.*, **620**, 325 (2012).
- K. S. Brammer, C. J. Frandsen, and S. Jin, "TiO₂ nanotubes for bone regeneration," *Trends Biotechnol.*, **30**(6), 315 (2012).
- B. Feng, J. Weng, B. C. Yang, S. X. Qu, and X. D. Zhang, "Characterization of surface oxide films on titanium and adhesion of osteoblast," *Biomaterials*, **24**, 4663 (2003).
- L. M. Bjrsten, L. Rasmussen, S. Oh, G. C. Smith, K. S. Brammer, and S. Jin, "Titanium dioxide nanotubes enhance bone bonding in vivo," *J Biomed Mater Res A*, **92**(3), 1218 (2010).
- K. S. Brammer, S. Oh, C. J. Cobb, L. M. Bjrsten, H. van der Heyde, and S. Jin, "Improved bone-forming functionality on diameter-controlled TiO₂ nanotube surface," *Acta Biomater.*, **5**(8), 3215 (2009).
- J. Park, S. Bauer, P. Schmuki, and K. von der Mark, "Narrow window in nanoscale dependent activation of endothelial cell growth and differentiation on TiO₂ nanotube surfaces," *Nano Lett.*, **9**(9), 3157 (2009).
- N. Wang, H. Li, W. Lu, J. Li, J. Wang, Z. Zhang, and Y. Liu, "Effects of TiO₂ nanotubes with different diameters on gene expression and osseointegration of implants in minipigs," *Biomaterials*, **32**(29), 6900 (2011).
- M. Balakrishnan and R. Narayanan, "Synthesis of anodic titania nanotubes in Na₂SO₄/NaF electrolyte: A comparison between anodization time and specimens with biomaterial based approaches," *Thin Solid Films*, **540**, 23 (2013).
- V. S. A. Challa, S. Mali, and R. D. K. Misra, "Reduced toxicity and superior cellular response of preosteoblasts to Ti-6Al-7Nb alloy and comparison with Ti-6Al-4V," *J Biomed Mater Res A*, **101A**(7), 2083 (2013).
- J. Fojt, "Ti-6Al-4V alloy surface modification for medical applications," *Appl. Surf. Sci.*, **262**, 163 (2012).
- X. Chen, K. Cai, J. Fang, M. Lai, J. Li, Y. Hou, Z. Luo, Y. Hu, and L. Tang, "Dual action antibacterial TiO₂ nanotubes incorporated with silver nanoparticles and coated with a quaternary ammonium salt (QAS)," *Surf. Coatings Technol.*, **216**, 158 (2013).
- L. Zhao, H. Wang, K. Huo, L. Cui, W. Zhang, H. Ni, Y. Zhang, Z. Wu, and P. K. Chu, "Antibacterial nano-structured titania coating incorporated with silver nanoparticles," *Biomaterials*, **32**(24), 5706 (2011).
- W. Xin, C. Meng, W. Jie, T. Junchao, S. Yan, and D. Ning, "Nanotube Arrays on Anodization Variables and Buffer Medium," *J. Semicond.*, **31**(6), 063003 (2010).
- J. M. Macak, H. Tsuchiya, and P. Schmuki, "High-aspect-ratio TiO₂ nanotubes by anodization of titanium," *Angew Chem Int Ed Engl.*, **44**(14), 2100 (2005).
- D. Kowalski, D. Kim, and P. Schmuki, "TiO₂ nanotubes, nanochannels and mesopore: Self-organized formation and applications," *Nano Today*, **8**(3), 235 (2013).
- D. Kim, F. Schmidt-Stein, R. Hahn, and P. Schmuki, "Gravity assisted growth of self-organized anodic oxide nanotubes on titanium," *Electrochem. commun.*, **10**, 1082 (2008).
- B.-G. Lee, J.-W. Choi, S.-E. Lee, Y.-S. Jeong, H.-J. Oh, and C.-S. Chi, "Formation behavior of anodic TiO₂ nanotubes in fluoride containing electrolytes," *Trans. Nonferrous Met. Soc. China*, **19**(4), 842 (2009).
- H. Tsuchiya, J. M. Macak, L. Taveira, E. Balaur, A. Ghicov, K. Sirotka, and P. Schmuki, "Self-organized TiO₂ nanotubes prepared in ammonium fluoride containing acetic acid electrolytes," *Electrochem. commun.*, **7**(6), 576 (2005).
- Q. Cai, M. Paulose, O. Varghese, and C. A. Grimes, "The effect of electrolyte composition on the fabrication of self-organized titanium oxide nanotube arrays by anodic oxidation," *Mater. Res. Soc.*, **20**(1), 230 (2005).
- M. Paulose, O. K. Varghese, G. K. Mor, C. A. Grimes, and K. G. Ong, "Unprecedented ultra-high hydrogen gas sensitivity in undoped titania nanotubes," *Nanotechnology*, **17**, 398 (2006).
- E. Matykina, J. M. Hernandez-López, A. Conde, C. Domingo, J. J. De Damborenea, and M. A. Arenas, "Morphologies of nanostructured TiO₂ doped with F on Ti-6Al-4V alloy," *Electrochim. Acta*, **56**, 2221 (2011).
- Y. Q. Hao, S. J. Li, Y. L. Hao, Y. K. Zhao, and H. J. Ai, "Effect of nanotube diameters on bioactivity of a multifunctional titanium alloy," *Appl. Surf. Sci.*, **268**, 44 (2013).
- C. P.-J. Peremarch, R. P. Tanaira, M. A. Arenas, E. Matykina, A. Conde, J. J. De Damborenea, E. G. Barrena, and J. Esteban, "Bacterial adherence to anodized titanium alloy," *J. Phys. Conf. Ser.*, **252**, 12011 (2010).
- S. Bauer, S. Kleber, and P. Schmuki, "TiO₂ nanotubes: Tailoring the geometry in H₃PO₄/HF electrolytes," *Electrochem. commun.*, **8**(8), 1321 (2006).
- L. V. Taveira, J. M. Macak, H. Tsuchiya, L. F. P. Dick, and P. Schmuki, "Initiation and Growth of Self-Organized TiO₂ Nanotubes Anodically Formed in NH₄F/(NH₄)₂SO₄ Electrolytes," *J. Electrochem. Soc.*, **152**, B405 (2005).
- T. D. Dikova, M. G. Hahn, D. P. Hashim, N. T. Narayanan, R. Vajtai, and P. M. Ajayan, "Mechanism of TiO₂ Nanotubes Formation on the Surface of Pure Ti and Ti-6Al-4V Alloy," *Proc. AMPT2013*, **939**, CD-ROM (2013).
- J. M. Macak, H. Tsuchiya, L. Taveira, A. Ghicov, and P. Schmuki, "Self-organized nanotubular oxide layers on Ti-6Al-7Nb and Ti-6Al-4V formed by anodization in NH₄F solutions," *J Biomed Mater Res A*, **75**(4), 928 (2005).
- C. Zoski, *Handbook for Electrochemistry*, First Edit. Netherland: Elsevier B. V. (2007).
- J. M. Macak, H. Tsuchiya, A. Ghicov, K. Yasuda, R. Hahn, S. Bauer, and P. Schmuki, "TiO₂ nanotubes: Self-organized electrochemical formation, properties and applications," *Curr Opin. Solid State Mater. Sci.*, **11**(1-2), 3 (2007).
- X. Chen, J. Chen, and J. Lin, "Self-assembled TiO₂ nanotube arrays with U-shaped profile by controlling anodization temperature," *J. Nanomater.*, **2010**, 1 (2010).
- A. Ghicov, H. Tsuchiya, J. M. Macak, and P. Schmuki, "Titanium oxide nanotubes prepared in phosphate electrolytes," *Electrochem. commun.*, **7**(5), 505 (2005).
- J. Sieniawski, W. Ziąza, K. Kubiak, and M. Motyka, "Titanium Alloys - Advances in Properties Control," *InTech Open Publisher*, pp. 70 (2013).
- L. Zeng and T. R. Bieler, "Effects of working, heat-treatment, and aging on microstructural evolution and crystallographic texture of α , α' , and β phases in Ti-6Al-4V wire," *Mater. Sci. Eng. A*, **392**, 403 (2005).
- B. Luo, H. Yang, S. Liu, W. Fu, P. Sun, M. Yuan, Y. Zhang, and Z. Liu, "Fabrication and characterization of self-organized mixed oxide nanotube arrays by electrochemical anodization of Ti-6Al-4V alloy," *Mater. Lett.*, **62**, 4512 (2008).
- J. W. Hutchinson and Z. Suo, "Mixed Mode Cracking in Layered Materials," *Advances in Applied Mechanics*, **29**, 63 (1991).

Publication 2

Composite coatings for implants and tissue engineering scaffolds

Huirong Le and Urvashi F. Gunpath

Abstract

Medical implants and scaffolds for tissue engineering involve the use of composite coatings with various aims and objectives depending on the location and the reason behind their use. One example of their use is in the field of orthopaedics whereby composite coatings are used on bone implants with the aim of replicating the bone chemical and physical properties and they act as scaffolds for osteoblast cells to adhere and proliferate successfully hence promoting osseointegration. Once placed in the body, the composite coatings are expected to have specific properties depending on the location and the function required from the implant. In this context, three types of composite coatings have been defined as anti-wear, biocompatible and anti-bacterial coatings. The composites can be synthesised on the required material using various methods which have their own advantages and disadvantages. Moving with the smart and nano- technology, smart nanocomposite coatings have been introduced on implants and scaffolds for tissue engineering with the aim of providing more than one properties when required.

Keywords: *Implants, tissue engineering, scaffolds, orthopaedics, composite, nanotechnology, smart technology, anti-wear, biocompatible, anti-bacterial*

TABLE OF CONTENTS

6.1 INTRODUCTION	282
6.2 TYPES OF COMPOSITE COATINGS	283
6.2.1 ANTI-WEAR COATINGS	284
6.2.2 BIOCOMPATIBLE COATINGS	286
6.2.3 ANTI-BACTERIAL COATINGS	288
6.3 SYNTHESIS OF COMPOSITE COATINGS.....	290
6.3.1 CHEMICAL DEPOSITION	291
6.3.2 ELECTROPHORETIC DEPOSITION	294
6.3.3 ELECTROCHEMICAL DEPOSITION (ANODISING, ELECTROPLATING)	295

6.3.4 BIOMIMETIC DEPOSITION.....	296
6.3.5 OTHER DEPOSITION METHODS.....	298
6.4 SMART COMPOSITE COATINGS	300
6.5 SUMMARY	301
ACKNOWLEDGMENTS.....	301
REFERENCES	301

6.1 Introduction

Composite coatings have successfully been used with the aim of enhancing the function and lifespan of implants and acting as tissue engineering scaffolds. An implant is a manmade material inserted in the human body with the aim of repairing or replacing previous damaged tissue and tissue engineering is the use of cell biology and material engineering to induce tissue growth in specific chemical and physical environment [1-3]. Scaffolds in this context are biocompatible templates which act as a platform promoting the attachment and growth of cells [4]. Composite coatings are used on different types of materials whereby they add to the already present properties of the biomaterial.

Metallic materials are considered to be the best biomaterial for dental and orthopaedic implants owing to their exceptional mechanical properties [5-8]. Cobalt based alloys, stainless steel and titanium and its alloys are known metallic materials which have been used as implants. However, due to the lowest Young's modulus and corrosion resistance of titanium and its alloys, they are considered to be the best option for metallic implants even though the modulus is still higher than natural bone [9]. The factor that contributes to the corrosion resistance of titanium is the presence of the inert surface of a naturally formed oxide layer on the latter [10]. Nonetheless, since titanium alloy is preferred over pure titanium in the medical field due to the higher mechanical strength, the naturally formed oxide layer on the alloy is not always stable and alloy metal species are released from the surface which can be toxic [11, 12]. Modifying the oxide layer under certain conditions can prevent such leaching and even add enhancing properties to the implant [11, 13]. Further emphasis has been placed on the modification of surface topography and/or surface chemistry of biomaterials with the aim of functionalising the surface and making the implant last longer [14]. Roughening the oxide layer on titanium or its alloy is one functionalisation process which makes the surface more bioactive. This can be achieved through plasma spraying, sand blasting, acid etching and anodisation [15, 16]. And since the surface of bone is nano-structured, more interest has been granted to nano-modification of surface topography with the aim of simulating the latter surface [14, 17]. Growing titanium dioxide (TiO₂) nanotubes on the surface of Ti and Ti alloy is a mean of providing the required

roughness with a high surface to volume ratio and high reactivity [18]. Anodisation is an electrochemical process whereby TiO₂ nanotubes can be self-assembled on the surface of titanium/titanium alloy. This fabrication process is chosen over all the synthetic methods available as it allows the formation of uniform nanotubes arrays and a controllable pore size [19]. TiO₂ nanotubes on titanium are known to improve the ability of apatite formation and to increase the cell activity in the surrounding [20]. Due to their tubular structure and the increased surface area to volume ratio the nanotubes can be used as scaffolds for other materials with the aim of providing additional properties to the metal depending on where it is going to be used and what is expected.

In the case of orthopaedic implants, the implants need to mechanically attach to the bone and integrate in the body environment as well [21]. In this context, implants have been made in such a way that they provide the mechanical properties required while being able to act as a scaffold for tissue engineering and provide local drug delivery as well. This chapter sheds light on the different types of composite coatings available (section 6.2) depending on where they are needed and the methods used to fabricate them (section 6.3). Last but not least section 6.4 concentrates on the science behind smart composite coatings in the field of implants and tissue engineering.

6.2 Types of Composite Coatings

Composite coatings are used on different biomaterials. In this chapter, Ti-6Al-4V was chosen as the biomaterial in question as a base for the composite coatings owing to the vast usage in the orthopaedic world. They are used as implants and their surface can be modified to act as a scaffold for tissue engineering. In this context, ceramics and biomolecules are the two main types of composite coatings that are commonly used on Ti-6Al-4V based implants depending on the purpose of the latter [22].

In the world of orthopaedics, however complex properties a composite may have, the coating has to be able to work under load bearing conditions. As mentioned before, Ti-6Al-4V has good mechanical strength and can perform as bone implants. Nonetheless, due to difference in modulus and high friction, loosening of implants after a few years, results in the demand of a secondary

surgery [23, 24]. Preventing such situation is thus of great importance. Making composite coatings with anti-wear properties is one of the main solutions to such issues. They help lower the friction between implants and bone resulting in longer lasting implants [25]. Further details on anti-wear composite coatings are discussed in section 6.2.1. More importantly, any implant or scaffold has to be biocompatible before even being considered to be placed in a human body. And in the case of bone implants, the coatings have to be biocompatible even under stress [26]. Furthermore, the concept behind tissue engineering itself depends on the ability of materials to promote cell adhesion and proliferation [27, 28]. With regards to biocompatibility of implants and tissue engineering scaffolds, section 6.2.2 is dedicated to biocompatible composite coatings and concentrates on ceramic grown on titanium based material. However much biocompatible a material can be, there is always the risk of infection due to the involvement of a foreign material inside a human body. In the case of implants, infection is a common case of malfunction and failure [29-31]. Depending on the location where a biomaterial is needed, it can be made anti-infective with the aim of combatting infections when needed or as a prophylaxis [30, 32]. Anti-infective agents can as such be coated on or added to biomaterials to provide the necessary properties to the latter [30, 32]. Section 6.2.3 concentrates on the third type of composite coating, namely anti-bacterial coating. Silver nanoparticles acting as antibacterial agents embedded in TiO₂ nanotubes on Ti-6Al-4V were studied as composite coatings.

6.2.1 Anti-wear coatings

Composite coating used on articulating surfaces of implants is the type of coating that is mostly concerned in this section. Articulating surface as per its name, has to be able to move smoothly so that the implant could work successfully without any issues. It is hard to fabricate the perfect coating or implant but tackling most of the issues lead the way to effective implants. One of the most common material used in articulating implants is titanium in the field of orthopaedic implants. In this context, titanium alloy do have a high strength and a lower modulus (60 – 110 GPa) than other metals (including titanium metal) which is closer to the modulus of bone (10 – 30 GPa) [9, 33, 34]. Nevertheless, the gap between the modulus have still to be filled with the aim of

preventing stress shielding [33, 34]. Along with stress shielding, corrosion is one factor which leads to wearing of the surface of an implant which in turn increases friction between articulating surfaces resulting in mal-functioning of the latter implant [23, 35]. And in orthopaedics, malfunctioning leads to secondary surgery which can be life threatening. Thus there is a need to reduce or prevent corrosion on implant surfaces with the aim of reducing wear, hence the need for anti-wear coating on those implants.

In this context, several researches have been done in the past and are still being done with the aim of reducing friction between articulation surfaces. And composite coating is a good solution to this issue. Examples of such coatings being used are diamond-like carbon (DLC), graphite-like carbon (GLC), tantalum (Ta), titanium nitride (TiN), Al₂O₃ - Fluorapatite (Fap) and HAp/TiO₂-based composite [23, 36-38]. The common interest in working with the mentioned composite coatings is that they need to provide anti-wear properties while being biocompatible and able to work under load bearing environment in some cases. Sahasrabudhe *et al.* (2016) confirmed wear resistance and an increase in hardness when pure titanium was coated with Ti/N [39]. Graphene nanoplatelets reinforced Bioglass has also been shown to have lubricating effect and increased toughness while being biocompatible [40]. With respect to anti-wear composite coatings, carbon nanocomposite coatings on Co/Cr alloy has proved to have high wear resistance while allowing cells to grow successfully on the latter [41]. Co/Cr alloy is a good choice for medical implants, however it still has a lower modulus than bone as mentioned before and as such, titanium alloy being the best choice for bone implants. MoS₂-containing TiO₂ composite coating on Ti6Al4V was investigated by Mu *et al.* (2013) and it was found that the uniformly coated nanoparticle coating had low friction and could act as a lubricant between the articulating surfaces [42].

Several anti-wear composite coatings have been tested and used successfully. However, the need to combine biocompatibility and additional properties to the coatings keeps the research going on. With the aim of being able to blend in the human body, biocompatible composite coatings on implants have been extensively researched about and the next section shed more light on the topic.

6.2.2 Biocompatible coatings

Different locations in the body require different types of implant materials. The whole aim is to allow the implant to integrate successfully in the human body while being able to deliver the necessary function. In the case of orthopaedic implants, metals are mostly chosen especially in load bearing applications due to their high strength. However, osseointegration is still an issue when used on its own in the human body, hence the need for surface modification which fill in the gap [43, 44]. Increasing the roughness of the surface of titanium alloy is one option which has gained enormous interests over the last few years. Grit blasting and chemical etching are examples of such methods but the roughness and morphology of the resulting surface cannot be controlled [43, 44]. Self-assembly of TiO₂ nanotubes on the surface of Ti alloy is one way of providing a controllable nano-roughness to the latter surface whereby the nanotubes provide the necessary platform for bone cells to grow on the latter and provide good biocompatibility [45-47]. Stress shielding still remains an issue with surface modification. In this context, composite coatings with lower modulus can help reduce and/or prevent the effect of stress shielding.

Hydroxyapatite is a bioceramic material which has similar structure to bone but it does not have the mechanical strength required to work in load bearing application [34, 48, 49]. Nonetheless when used in conjunction with titanium alloy, HA add to the properties of the alloy, hence increasing the osseointegration of the alloy in the body [49, 50]. Several techniques have been used to grow or add HA on the surface of metals and alloys such as sol-gel technique, plasma-spraying, biomimetic deposition, electrodeposition, laser ablation and so on [48, 51].

With the aim of improving the adhesion and stability of HA coating on Ti, Liu *et al.* (2017) investigated the behaviour of osteoblast cells grown on HA coated Ti [52]. After having polished the titanium (PT), it was acid etched with the aim of roughening the surface forming ET. With the aim of increasing bioactivity of the surface, the etched surface was exposed to 10 M NaOH in a high pressure kettle at 100 °C for 24 hours hence labelled NT. Subsequently HA was deposited biomimetically on the alkali treated surface by dipping NT in simulated body fluid (SBF) hence forming HAp/NT. The surfaces of PT, ET, NT

and HAp/NT were then viewed under high resolution scanning electron microscopy (SEM, Hitachi S-4800) and the elements present were analysed using energy dispersive X-ray spectrum (EDX). Afterwards they were exposed to mouse osteoblastic MC3T3-E1 subclone 14 cell line in a-MEM (Minimum essential media) media. 3-(4,5-dimethyl-2-thiazolyl)-2,5-diphenyl-2-H-tetrazolium bromide (MTT) and alkaline phosphatase (ALP) assays were then performed on the cells grown on the coated and uncoated titanium after 2, 4, 6 and 8 days of exposure [53].

Insert Figure 6.1

The SEM images of the PT, ET, NT and HAp/NT are shown in figure A, B, C and D. Figure C shows a flowery nano-structure from the sodium titanate formed from the alkali treatment and figure C illustrates nano-needles structures formed on the surface of the alkali treated titanium whereby a full coverage and uniformity was present. Figure E confirms the presence of HA after exposure to SBF with the ratio of calcium to phosphorus being 1.67. Further details on the chemistry involved in the growth of HA would be discussed further in section 6.3.4. The calculations from MTT assay by Liu *et al.* (2017) was expressed in figure A whereby it could be observed that the cell growth during day 2 and 4 was not significantly different on PT, NT and HAp/NT [52]. But as from day 6, both NT and HAp/NT showed higher number of cells. The ALP assay showed similar observations (figure B). The change in morphology and the presence of HA did increase the biocompatibility of the titanium successfully. As mentioned before, the nanostructure did mimic the nano-morphology of bone which allows the coating to blend in. Also, since HA have similar natural phase to bone, osteoblast cells finds it easier to attach to the latter surface thereby preventing rejection [54]. The study by Liu *et al.* (2017) is one example where HA was used as a composite coating which enhanced the biocompatibility of the implant material [52].

Insert figure 6.2

Several more types of composite coatings containing organic molecules, nanoparticles and many more are used on metals with the aim of providing biocompatibility to the material so that they can integrate successfully in the body hence reducing the risk of malfunction and/or rejection [33]. Nonetheless

biocompatibility in different parts of the body would require different composite coatings. In the study by Liu *et al.* (2017) the coating was aimed at bone implants and bone tissue engineering and as such, hydroxyapatite was the best option [52]. However, implants aiming at being in the heart or eye or any other part of the body, would require composite coatings made of biomaterials promoting their integration in the respective organs.

6.2.3 Anti-bacterial coatings

Targeting infections in implants is of great significance and composite coatings could be the solution. Local anti-bacterial agent delivery is one such example which has been researched extensively for use as composite coatings on implants. This method has been shown to be more efficient with low toxicity [55]. TiO₂ nanotubes have nanotubular structures which can act as a carrier and/or act as a scaffold for antibacterial nanoparticles aiming at local delivery [56]. Antibiotics have been used as a bactericidal agent on nanotubes. However implant related infections are often caused by more than one bacterium and they occasionally develop resistance to antibiotics [57]. This is where metallic antibacterial feature becomes the alternative solution. Silver, copper and zinc nanoparticles have been used positively on TiO₂ nanotubes due to their antibacterial property and nanostructures [58-63]. Nonetheless, silver nanoparticle is considered the best owing to the better antibacterial properties and the better resistance to bacteria [64-66]. Thus integrating silver nanoparticles to TiO₂ nanotubes grown on titanium alloy is an excellent example of an anti-bacterial composite coating for implants. The nanostructured morphology of the embedded silver nanoparticles on the nanotubes attracts human cells to grow on the surface hence acting as a scaffold for tissue engineering [67, 68]. However, silver nanoparticles are toxic if released in high amounts at one time. Most studies analysing the behaviour of silver nanoparticles in the presence of human cells, showed different levels of toxicity depending on the release rate and size of the nanoparticles [63, 69]. For this reason, the size and attachment of the nanoparticles to the nanotubes wall and the control of silver release from the coatings are the main factors to be considered when growing the latter as composite coatings.

Different methods have been employed to fabricate silver nanoparticles on the surface of TiO₂ nanotubes grown on titanium or its alloy. One method of assembling uniformly distributed silver nanoparticles on the nanotubes is electron beam evaporation [68, 70]. The latter method successfully produced uniformly distributed silver nanoparticles on the surface of nanotubes coating on titanium. In the study by Lan *et al*, 2013, the distribution of the nanoparticles were uniform with different sites of attachments depending on the diameter of the nanotubes on which they are attached [68]. Figure 6.3 shows the SEM images of the attached Ag nanoparticles on titania nanotubes of diameter 25, 50 and 100 nm. The size of the nanoparticles remained the same even though the diameter increased. The nanoparticles were attached to the inside of the nanotubes wall when the diameter was 100 nm as seen in Figure F and Figure D showed that when the diameter of the nanotube was 25 nm the Ag particles were on the surface of the nanotubes layer affecting the nano-topology of the coating on titanium [68]. However Figure G showed that the release of silver from the composite coating over 2 weeks was the same in both cases. The silver release was a steady release over the 14 days in both cases.

Insert Figure 6.3

The antibacterial property of the composite coatings containing silver nanoparticles on TiO₂ nanotubes were tested in the presence of *Staphylococcus aureus* grown in tryptic soy broth [68]. Figure 6.4 shows the composite coatings after 4 hours of exposure to *S.aureus*. The coatings with Ag nanoparticles on 100 nm diameter nanotubes had the least bacteria present on the surface after the exposure (Figure F) as compared to the coatings involving 25 nm diameter nanotubes (Figure D).

Insert Figure 6.4

After confirming the antibacterial property of the composite coatings on titanium, there was a need to make sure that the surface was not toxic to human cells. As such the coated surfaces with silver nanoparticles on TiO₂ nanotubes with diameters ranging from 25 nm to 100 nm were exposed to human fibroblast cells grown in Eagle's minimum essential medium. It was observed that the cells grew better on the 25 nm diameter nanotubes both in the presence and absence of silver nanoparticles as shown on Figure A and D.

Insert Figure 6.5

In the study by Lan *et al* (2013) a composite coating on titanium was successfully synthesised. The coating provided the necessary antibacterial property against one of the main cause of infection in implants, *S.aureus* (REF). It was also shown to allow human fibroblast cells grow on the silver containing surface as they would grow on just TiO₂ nanotubes. As such, it could be concluded that the silver nanoparticles added to titania nanotubes by e-beam are antibacterial while enhancing biocompatibility of the titanium [68]. The low level of toxicity could be due to the steady release of silver form the composite coatings as seen in Figure G over 14 days as release of large amount of silver in the first 24 hours have been shown to be toxic to cells. Several more similar coatings have been synthesised throughout the last few years. These types of antibacterial composite coatings combat infection as soon as they come in contact with bodily fluid. More research are still being done with respect to growing silver nanoparticles on TiO₂ nanotubes with the aim of providing antibacterial effect for as long as possible [69]. This implies a slower release of silver from the composite coating and/or a release of the antibacterial agent only when infection is present. This is where smart coatings could enhance the characteristics of composite coatings [71]. Section 6.4 concentrates on the development of smart composite coatings which can have antibacterial properties as well.

6.3 Synthesis of composite coatings

There are different methods through which composite coatings can be synthesised, some of which have been discussed in the previous section. Depending on the methods which are being used mostly and which are more cost effective, section 6.3 gives more details on the different methods employed. This segment divides the different techniques that have been used to synthesise composite coatings successfully in the past into 4 categories namely chemical deposition (6.3.1), electrophoretic deposition (6.3.2), electrochemical deposition (anodising, electroplating) (6.3.3), biomimetic deposition (6.3.4) and the remaining less used techniques such as plasma spraying, Ion beam, laser

deposition were condensed into a fifth category named other deposition methods (section 6.3.5).

6.3.1 Chemical deposition

Composite coatings on implants consist of different chemical components and manipulating the chemistry involved is the main concept behind the synthesis of the coatings on different materials. Chemical deposition is one fabrication technique whereby the material to be coated are allowed to react to different chemicals allowing specific reactions to take place in a way that the coating forms successfully. Chemical deposition can vary in different ways and examples of chemical deposition include the chemical reduction, chemical vapour deposition, sol-gel technique and dip coating. Examples of complex version of chemical deposition are electrochemical deposition, spray deposition, and biomimetic deposition [72]. The sol gel technique is a method whereby a chemical solution is used to produce a network of particles after the solvent from the solution has been evaporated and this method is used very often in the fabrication of composite coatings because of its ability to produce multicomponent coatings of various size, shape and format [73-75]. The latter synthesis technique is effective while being cost-effective and simple [75-77]. Issues with the sol-gel method are that it is most time consuming and the adhesive strength between the composite coating and the material is not that strong [78, 79]. Chemical vapour deposition (CVD) is a widely used chemical deposition method whereby the substrate to be coated is exposed to the precursor of the material to be coated which reacts on the substrate forming the required coating. It has many advantages as being a low cost and low maintenance procedure which can produce pure uniform coating with structural control at nanometer level [80-83]. CVD has been selected as it is a low-cost, low maintenance and effective process for depositing uniform films exhibiting good adhesion to the growing substrate; moreover, the easiness in controlling the growth rate allows a high reproducibility of the samples. However, CVD requires very high temperature and specific precursor material which can be evaporated [23, 84, 85]. Chemical reduction is a process whereby the required coating is reduced from a source on the substrate with the help of a reducing agent. It is a method widely used for the synthesis of graphene oxide and silver

nanoparticles [86-88]. In the world of implants, AgNp/TiO₂ composite coating on titanium has been used successfully as mentioned in section 6.2.3. There are issues with toxicity which have been overcome by ongoing research by the authors but the antibacterial properties of the latter coating provide that triumph over the toxicity issue (section 6.2.3). There are several methods of synthesis among which chemical reduction is one of the simplest and most commonly used [86, 89]. The commonly used reducing agents for this reaction are sodium borohydride, sodium dodecyl sulphate, citrate, ascorbate and elemental hydrogen [86, 89, 90]. The reason behind its vast use is the fact that nanoparticles of different morphology and dimensions can be fabricated using this method [86, 91]. In a previous work, silver nanoparticles have been successfully synthesised on the surface of TiO₂ nanotubes. In this section, chemical reduction of silver nanoparticles on the nanotubes would be discussed while section 6.3.3 would analyse the electrochemical method of synthesising the underlying nanotubes.

In the study by Gunpath and Le (submitted to Material science and Engineering C journal in March 2017) delta-gluconolactone was used as a reducing agent for silver ammonia with the aim of forming silver nanoparticles (S) of diameter less than 100 nm were formed in clusters of varied dimensions. In the latter study, the concentration of the δ -gluconolactone used was maintained at 0.002 M throughout. Initially, in method 1, the TiO₂ coated Ti-6Al-4V alloy was exposed to the mixture of the silver source, silver ammonia and gluconolactone for 10 minutes. The concentration of the silver ammonia was varied from 0.005 M to 0.015 M and the resulting clusters formed on the surface of the nanotubes (TNT) were illustrated in Figure 6.6. Panels A-C shows a low magnification of the TNT-S coating and D-F shows a higher magnification of TNT-S0.005, TNT-S0.01 and TNT-S0.015 whereby micro-clustering was observed with an increase in the size of the clusters with increase in the concentration of silver source. The low magnification showed the coverage of the coating while the higher magnification zoomed in to have a closer look at the morphology of the clusters.

Insert 6.6

Using the same chemical reduction method, in method 2, TNT was exposed to 0.015 M silver ammonia for 1-10 min followed by an exposure to 0.002 M gluconolactone for 5 minutes. Figure panel A-C shows the low magnification image of the coated surfaces of S1G5, S5G5 and S10 G5 respectively with the number being the duration for which the samples was left in the latter solution. Panels D-F shows the same coatings at a higher magnification whereby the size of the nano-clusters was seen reducing with increasing duration of exposure to silver ammonia. In both figure and figure, G represents the EDS analysis which confirms the nanoparticles to be silver.

Insert Figure 6.7

The clustering was assumed to happen because of the large size of the gluconolactone molecule reducing silver ammonia. The latter molecule has several –OH and as such for each molecule of reducing agent, 4 silver components were reduced and they would attach to each other. After each coating was synthesised, the coated material was ultrasonicated in deionised water for 10 minutes to remove the excessive silver attached to the surface. Then they were exposed to simulated body fluid in triplicates (n=3) with the aim of measuring the amount of silver released from the coating after 24 hours. The micro-clustering was seen to release significantly larger amount of silver as measured by ICP-MS as compared to the nano-clustering (Figure). After analysing the distribution and release of silver from the coating, coating from method 2, TNT-S10G5 was found to be the best to be used as a coating on implants as it had a uniform distribution of nanoclusters of silver nanoparticles fully covering TNT while releasing the least amount of silver from the coating after 24 hours exposure to SBF. In the human body, too much silver can be toxic as mentioned in section 6.2.3, as such an ideal implant need to release enough silver to be bactericidal while being biocompatible.

Insert Figure 6.8

To summarise, in general chemical deposition is a cheap and simple method of synthesising composite coating whereby huge effort is not needed and the resulting nano-structure and distribution of the coating can be manipulated by modifying the involved parameters such as concentration of chemicals or duration of exposure to substrate.

6.3.2 Electrophoretic deposition

Electrophoretic deposition is an electrodeposition method whereby an electric field is applied between two electrodes in a suspension, whereby the particles move towards the oppositely charged electrode which is the substrate to be coated [78, 92, 93]. It has been successfully used to fabricate composite coatings for biomedical devices [94, 95]. Examples of such coatings are HA, reinforced HA, polymers, bioglass, graphene containing material and many more [96-98]. Electrophoretic method also allows the co-deposition of polymers and ceramics which make this method favourable when it comes to composite coating [92]. However, sometimes pre-treatment and/or post-treatment is required in order to stabilise or strengthen the coating [78, 98]. Even though sometimes the electrophoretic deposition is used as a 2-step procedure, it is still widely used in the synthesis of composite coatings because of its efficiency, homogeneity, high deposition rate, ability to produce controllable thickness, inexpensiveness and versatility [94, 95, 99]. It has been successfully used to coat surfaces of bulk objects and to infiltrate porous substrates.

Several authors have positively coated biomaterials with composite coatings which in turn provide the required biological properties as hypothesised. Seuss *et al.* (2014) were able to use alternating current-electrophoretic deposition (AC-EPD) to produce composite coatings made of chitosan and Bioglass on Ti-6Al-4V. The latter coatings were shown to be bioactive and antibacterial while being robust [93]. Chen *et al.* (2014) fabricated a PVA reinforced alginate-Bioglass composite coating on 316L stainless steel with excellent adhesive strength [100]. Xiong *et al.* (2014) synthesised a HA composite coating on Mg alloy using micro-arc oxidation followed by EPD [101]. The latter composite coating was shown to have good anti-corrosion properties [101]. Similar observations were made when a ceramic/organic composite coated Mg alloy was shown to be corrosion resistant [102].

Electrophoretic deposition on its own or used in collaboration with another technique has been shown to give rise to robust, corrosion resistant, biocompatible and even antibacterial composite coating. Several researches have been done on the latter and more is being done with the aim of combining all the required properties in one composite coating. The whole aim is to be able

to coat implants successfully while acting as a platform for successful tissue engineering.

6.3.3 Electrochemical deposition (anodising, electroplating)

Electrochemical deposition, as per its name is a deposition method whereby chemical deposition is assisted by a current. During this process, an electric field is applied in a liquid containing dispersed charged particles, between the substrate to be coated and another electrode so that a thin layer of the coating is formed [103-105]. Similar to chemical deposition, an electrochemical deposition, involves no high temperature or pressure and no high cost and the technique is easily portable [43, 103, 104]. Electrochemical deposition allows the synthesis of homogeneous coating of micro to nanoparticles [78, 105]. The most important reason for its use in composite coatings is the fact that this method allows deposition of more than one material on a substrate [48, 104]. Several composite coatings have been successfully synthesised on the surface of metal with respect to using it on implants and for tissue engineering. Examples of such coatings are the different chemical phase of calcium phosphates including hydroxyapatite and hydroxyapatite reinforced with carbon nanotubes (CNTs), TiO₂, ZrO₂ and chitosan [106-108]. The hydroxyapatite formed using this method was shown to have higher wear and corrosion resistance and a higher adhesive strength when reinforced with other materials. There are several factors which influence the characterisation of the coatings such as the structure, coverage, morphology and associated properties. The influencing parameters of the electrochemical reaction are the type of current or voltage applied and composition and pH of electrolytic bath [81, 104].

An example of an electrochemical method is the anodisation method whereby the substrate to be coated is made the anode [78]. Anodisation is one of the main methods of synthesising TiO₂ nanotubes which can be embedded with other nanoparticles for the use as drug carrying composite coating on titanium alloy as mentioned in section 6.3.1. Among the various electrolytes that have been used in the latter synthesis, aqueous electrolytes are considered to produce strongly adhered nanotubes due to the rougher exterior nanotube walls

[109, 110]. A previous study by Danookdharree (Gunpath) et al (2015) shed light on the influencing factors of the process such as pH and initial voltage ramp. 0.2-0.5 wt% NH_4F and 0.5-1 M $\text{NH}_4\text{H}_2\text{PO}_4$ was used as electrolytes which provided the necessary ions for the redox reaction as shown in Figure A [111]. The reaction led to the formation of uniformly distributed TiO_2 nanotubes with 116.2 ± 6.4 nm (mean \pm S.E.M., $n = 6$) diameter on the majority of the surface of Ti-6Al-4V disc as shown in Figure B and C whereby Figure C zoomed on the β -phase of the alloy which had smaller nanotubes than the α -phase (104.4 ± 4.7 nm).

Insert Figure 6.9 here

The pH did not have any effect on the diameter of the nanotubes as seen in Figure A but the increase in the initial sweep rate from 0.2 to 1.5 V/s led to a decrease in the diameter of the nanotubes as shown in Figure B. Nonetheless when there is an increase in the actual voltage used for anodisation, the nanotubes diameter are known to increase (Bauer et al, 2006).

Insert Figure 6.10 here

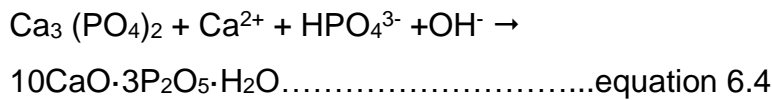
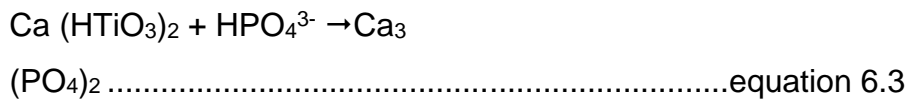
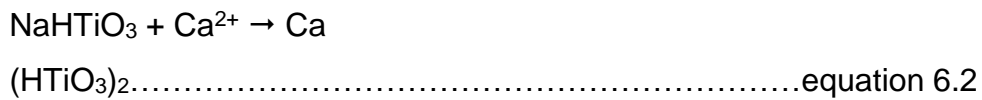
The electrochemical technique can be simple but every single aspects of the experiment does affect the resulting coating and has to be carefully considered [112-114]. This is what makes the latter method one of the best deposition techniques for composite coating especially at a nano-level.

6.3.4 Biomimetic deposition

Biomimetic deposition, as per its name, is a deposition method whereby a synthetic deposition is made by mimicking a biochemical reaction. Among the different methods of synthesis of composite coatings, the biomimetic deposition method which takes place on its own and does not require any reducing agent or external voltage for the process [115, 116]. It is also considered to be environmental friendly and inexpensive [117]. Different types of materials such as metals and metal oxides like Au, Ag, SiO_2 , TiO_2 , ZrO_2 can be synthesised using the biomimetic method [118, 119]. In the world of orthopaedics, there is a bigger interest in the biomimetic synthesis of hydroxyapatite on metals with the aim of increasing biocompatibility and promoting osseointegration as mentioned

in section 6.2.2. The biomimetic growth of HA on metals started with the work of Kokubo (1997) when the author grew TiO₂ nanotubes on the surface of titanium followed by the exposure of the latter coated surface to simulated body fluid with pH (7.4) and ion concentrations (Na⁺ 142.0, K⁺ 5.0, Mg²⁺ 1.5, Ca²⁺ 2.5, HCO₃⁻ 4.2, Cl⁻ 147.8, HPO₄³⁻ 1.0, SO₄²⁻ 0.5 mM) which are nearly equal to those of human blood plasma at 36.5 °C for 10 days [120]. Hydroxyapatite having 10CaO·3P₂O₅·H₂O as a chemical formula has a calcium to phosphorus ratio (Ca/P) of 1.67 [121, 122]. As such, when growing the latter on metal, several parameters have to be considered to make sure that the resulting coating does have the specific Ca/P ratio.

An example of HA coating formed using this method is shown in Figure C. The latter figure illustrates the uniformly distributed nanostructure of HA on the surface of titanium foil. The EDS analysis also confirmed the calcium to phosphorus ratio of 1.67 (Figure D). The original method used by Kokubo (1997) took 10 days for HA to successfully grow on the surface of metal [120]. A quicker method of fabricating the coating using biomimetic deposition would be to use a concentrated version of the SBF while making sure that the pH and temperature is maintained with continuous replenishment of the concentrated SBF so that the appropriate ratio of Ca/P is obtained [115, 123]. The concept around the synthesis of hydroxyapatite revolves around the initial nucleation stage whereby calcium attached on the surface of the material before crystallising to HA crystals [120, 124-126]. With the aim of growing hydroxyapatite at a nano-level, in order for nucleation to happen, a rough base is required. In the case of the study of the growth on titanium, the metal was initially etched in concentrated acids hence creating a rough TiO₂ surface [52]. The following alkali treatment with NaOH then created a layer of sodium titanate (NaHTiO₃) as per equation (1) [120, 124]. Then, the titanate act as a base for the nucleation to start once exposed to SBF. As a result, calcium titanate is formed according to equation (2) after which, calcium phosphate (equation (3)) is formed which allows the apatite crystals to successfully form as per equation (4) [124, 126]. The concept behind the growth of the HA on the titanium foil was summarised in figure whereby the effect of the different steps on the surface morphology was demonstrated.



Insert Figure 6.11 here.

The biomimetic method is already time consuming and difficult to get it perfectly right. And sometimes, the method does not last long on surfaces like magnesium metal (Gao *et al*, 2015). In such situation, adding other material to the base material allow a better bond between the HA and the base. Example of such materials are graphene oxide, collagen, gelatin, carbon nanotubes and many more [115, 117, 123].

6.3.5 Other deposition methods

There are many more deposition methods which are used and which are being continuously researched about. Examples of such methods are the layer by layer coating, plasma spraying, physical vapour deposition, ion beam deposition, laser deposition and many more.

The layer-by-layer deposition method involves the deposition of oppositely charged particles layer by layer and is mainly used when it comes to producing a coating involving more than one component hence the research in relation to composite coating [127, 128]. It is an easy, versatile and efficient deposition method which has attracted attention in biomaterials synthesis [22, 129]. In the world of composite coatings, the latter deposition method has been used with the aim of functionalising the surface of inert material, synthesising drug carrying coating for fast and slow release and fabricating thin coatings with high strength [127, 129, 130]. The materials involved in the synthesis of composite

coatings by this method include polymers, peptides, nanoparticles, ceramic and metals.

Plasma spraying is a method that has been used to coat medical implants in the past and is still being used. The process involved is the use of high temperature from ionised inert gas to melt ceramic or metal powders which are sprayed on the substrate to be coated [72, 131]. It is very common to coat medical implants with HA using this method with the aim of increasing biocompatibility and preventing corrosion [34, 131]. However due to the brittleness and low adhesion force of the HA formed from this method, plasma spraying could be combined with other techniques such as isostatic pressing or the HA being fabricated could be reinforced with other materials such as carbon nanotubes [34, 131, 132]. As a whole, plasma spraying is considered to be cost-effective and the method has the ability to control the microstructure of coatings and make them have good properties [34, 133]. Nonetheless, it has drawbacks such as low adhesive strength, non-uniform coating and the induction of changes in the microstructure of the coating.

Physical vapor deposition is an environmental friendly coating technique which is used to deposit inorganic material of variable thickness and good adhesion strength on the required substrate with the aim of providing good corrosion resistance [23, 131, 134]. The technique involves the deposition of plasma metals ions on the substrate to be coated with the help of an electric field [23, 135]. With respect to the resulting coating, PVD has been used in the synthesis of composite coating for orthopaedics implants. Examples of such coatings are HA, diamond like coating, TiO₂ and nano-silicon [23, 134]. The weak link in this context is the low crystallinity of the resulting coating and the high cost of the procedure [136].

The above mentioned deposition techniques are continuously being researched and many more are being investigated with the aim of having the appropriate composite coating for the respective implant or the required tissue engineering. This is a long process as so many aspects have to be taken into consideration ranging from mechanical properties to biological properties. Other aspects to be considered are the feasibility, accessibility and economic aspects.

6.4 Smart composite coatings

Various composite coatings have been magnificently put together by so many researchers in the past. Trying to combat all possible problems from implants and in relation to tissue engineering has been the centre of attraction. However getting the recipe for the perfect biomaterial or composite coating right, is not simple and would require more extensive work. One of the solutions to addressing this issue is the use of smart coating. It is a functional coating that has at least one property which can be modified when induced by stimuli generated by intrinsic or extrinsic factors such as pH, stress, temperature, electric and magnetic fields [119, 137, 138]. Smart composite coatings are being constantly studied about in the medical world with different aims. Examples are anti-corrosion coating, drug carrying coating and self-healing coating [138, 139].

In this context, Ananth *et al.* (2016) synthesised a smart anticorrosion composite coating consisting of Sr, Zn and Mg substituted hydroxyapatite and silica nanotube composite coatings on polypyrrole coated surgical grade 316L stainless steel [140]. The coating was concluded to provide the necessary anticorrosion properties when required while being biocompatible [140]. In the field of drug delivery, TiO₂ nanotubes have been considered to carry drugs for implants and tissue engineering in different medical needs and deliver them when required by different types of external stimuli but some drawbacks need to be taken into consideration as well just in case, the external stimuli does not reach the coating adequately or the coating is not biocompatible [62, 139, 141]. Nanoparticle involved composite coatings have been reviewed with the aim of acting as scaffold for smart tissue regeneration/repair and with respect to this review, composite materials like chondroitin sulfate reinforced collagen scaffolds, fibrin gel incorporating transforming growth factor beta-1 and porous HA scaffolds combined with biodegradable PLGA microspheres loading dexamethasone have been investigated [142].

The above mentioned properties and materials are examples of where smart composite coatings are heading. With the world heading towards smart technology, smart coating could be considered as the solution to the issues faced by implants in the human body. The aim is to provide the necessary

properties as soon as contact is made while being able to combat expected problems as time goes by.

6.5 Summary

Composite coatings have a significant importance in the world of orthopedics both on the surface of implants and scaffolds for tissue engineering. The components of the latter composite coatings are selected depending on the location where needed and the function they are expected to perform. The fabrication methods are selected depending on the characteristic of the coatings required. Since the biological reactions occur at a nano-level in the human body, nano-composite coatings have gained more attention recently and smart coatings have also been considered to be important in this field.

Acknowledgments

The funding through a joint PhD studentship for UD by the Faculty of Science and Environment and Peninsular Schools of Medicine and Dentistry of Plymouth University is acknowledged. Prof R Handy and Prof C Tredwin are acknowledged for constructive discussions and advices. The assistance by the technical team in the School of Marine Science and Engineering, the School of Biological and Biomedical Science and the Electron Microscopy Centre (EMC) of Plymouth University is gratefully acknowledged.

References

1. Valente, M.L.d.C., et al., *Comparative analysis of stress in a new proposal of dental implants*. Materials Science and Engineering: C, 2017. **77**: p. 360-365.
2. Balint, R., N.J. Cassidy, and S.H. Cartmell, *Conductive polymers: towards a smart biomaterial for tissue engineering*. Acta Biomater, 2014. **10**(6): p. 2341-53.
3. Hasan, A., et al., *Electrospun scaffolds for tissue engineering of vascular grafts*. Acta Biomater, 2014. **10**(1): p. 11-25.
4. Bose, S., M. Roy, and A. Bandyopadhyay, *Recent advances in bone tissue engineering scaffolds*. Trends Biotechnol, 2012. **30**(10): p. 546-54.
5. Niinomi, M., *Recent research and development in titanium alloys for biomedical applications and healthcare goods*. Science and Technology of Advanced Materials, 2003. **4**(5): p. 445-454.

6. Yoshimitsu Okazaki, et al., *Corrosion resistance and corrosion fatigue strength of new titanium alloys for medical implants without V and Al*. Materials Science and Engineering 1996. **A213**: p. 13.
7. Elias, C.N., et al., *Relationship between surface properties (roughness, wettability and morphology) of titanium and dental implant removal torque*. J Mech Behav Biomed Mater, 2008. **1**(3): p. 234-42.
8. M. E. Engelbrecht, et al., *Functional performance and machinability of titanium alloys for medical implants: A review* 2013, SAIIE25 Proceedings: Stellenbosch, South Africa. p. 14.
9. Geetha, M., et al., *Ti based biomaterials, the ultimate choice for orthopaedic implants – A review*. Progress in Materials Science, 2009. **54**(3): p. 397-425.
10. Al-Mobarak N. A., Al-Swayih A. A. , and A.-R.F. A., *Corrosion Behavior of Ti-6Al-7Nb Alloy in Biological Solution for Dentistry Applications*. International Journal of ELECTROCHEMICAL Science and Technology of Advanced Materials, 2011. **6**: p. 11.
11. Oshida, Y., et al., *Dental implant systems*. Int J Mol Sci, 2010. **11**(4): p. 1580-678.
12. Liu, X., P. Chu, and C. Ding, *Surface modification of titanium, titanium alloys, and related materials for biomedical applications*. Materials Science and Engineering: R: Reports, 2004. **47**(3-4): p. 49-121.
13. Sul, Y., *The significance of the surface properties of oxidized titanium to the bone response: special emphasis on potential biochemical bonding of oxidized titanium implant*. Biomaterials, 2003. **24**(22): p. 3893-3907.
14. Bjursten, L.M., et al., *Titanium dioxide nanotubes enhance bone bonding in vivo*. J Biomed Mater Res A, 2010. **92**(3): p. 1218-24.
15. Oh, S.H., et al., *Growth of nano-scale hydroxyapatite using chemically treated titanium oxide nanotubes*. Biomaterials, 2005. **26**(24): p. 4938-43.
16. Durual, S., et al., *TiNOx coatings on roughened titanium and CoCr alloy accelerate early osseointegration of dental implants in minipigs*. Bone, 2013. **52**(1): p. 230-7.
17. Brammer, K.S., et al., *Improved bone-forming functionality on diameter-controlled TiO(2) nanotube surface*. Acta Biomater, 2009. **5**(8): p. 3215-23.
18. Mor, G.K., et al., *A review on highly ordered, vertically oriented TiO2 nanotube arrays: Fabrication, material properties, and solar energy applications*. Solar Energy Materials and Solar Cells, 2006. **90**(14): p. 2011-2075.
19. Sreekantan, S., K.A. Saharudin, and L.C. Wei, *Formation of TiO2nanotubes via anodization and potential applications for photocatalysts, biomedical materials, and photoelectrochemical cell*. IOP Conference Series: Materials Science and Engineering, 2011. **21**: p. 012002.
20. Jeong, Y.-H., H.-C. Choe, and W.A. Brantley, *Silicon-substituted hydroxyapatite coating with Si content on the nanotube-formed Ti–Nb–Zr alloy using electron beam-physical vapor deposition*. Thin Solid Films, 2013. **546**: p. 189-195.
21. Lavenus, S., G. Louarn, and P. Layrolle, *Nanotechnology and dental implants*. Int J Biomater, 2010. **2010**: p. 915327.
22. Goodman, S.B., et al., *The future of biologic coatings for orthopaedic implants*. Biomaterials, 2013. **34**(13): p. 3174-83.
23. Ching, H.A., et al., *Effects of surface coating on reducing friction and wear of orthopaedic implants*. Sci Technol Adv Mater, 2014. **15**(1): p. 014402.
24. Wang, W. and K. Poh, Chye, *Titanium Alloys in Orthopaedics*, in *Titanium alloys-Advances in properties control*, J. Sieniawski, Editor. 2013, InTech.

25. Bandyopadhyay, A., et al., *Calcium phosphate-titanium composites for articulating surfaces of load-bearing implants*. J Mech Behav Biomed Mater, 2016. **57**: p. 280-8.
26. Huang, J., et al., *Improved adaptability of PEEK by Nb doped graphite-like carbon composite coatings for bio-tribological applications*. Surface and Coatings Technology, 2014. **247**: p. 20-29.
27. Puppi, D., et al., *Polymeric materials for bone and cartilage repair*. Progress in Polymer Science, 2010. **35**(4): p. 403-440.
28. Kolk, A., et al., *Current trends and future perspectives of bone substitute materials - from space holders to innovative biomaterials*. J Craniomaxillofac Surg, 2012. **40**(8): p. 706-18.
29. Lima, A.L., et al., *Periprosthetic joint infections*. Interdiscip Perspect Infect Dis, 2013. **2013**: p. 542796.
30. Gallo, J., M. Holinka, and C.S. Moucha, *Antibacterial surface treatment for orthopaedic implants*. Int J Mol Sci, 2014. **15**(8): p. 13849-80.
31. Connaughton, A., et al., *Biofilm Disrupting Technology for Orthopedic Implants: What's on the Horizon?* Front Med (Lausanne), 2014. **1**: p. 22.
32. Campoccia, D., L. Montanaro, and C.R. Arciola, *A review of the biomaterials technologies for infection-resistant surfaces*. Biomaterials, 2013. **34**(34): p. 8533-54.
33. Bauer, S., et al., *Engineering biocompatible implant surfaces*. Progress in Materials Science, 2013. **58**(3): p. 261-326.
34. Arifin, A., et al., *Material processing of hydroxyapatite and titanium alloy (HA/Ti) composite as implant materials using powder metallurgy: A review*. Materials & Design, 2014. **55**: p. 165-175.
35. Gnedenkov, S.V., et al., *Composite polymer-containing protective coatings on magnesium alloy MA8*. Corrosion Science, 2014. **85**: p. 52-59.
36. Cui, W., et al., *A graded nano-TiN coating on biomedical Ti alloy: Low friction coefficient, good bonding and biocompatibility*. Mater Sci Eng C Mater Biol Appl, 2017. **71**: p. 520-528.
37. Ghorbel, H.F., et al., *Alumina-fluorapatite composite coating deposited by atmospheric plasma spraying: An agent of cohesion between bone and prostheses*. Mater Sci Eng C Mater Biol Appl, 2017. **71**: p. 1090-1098.
38. Durdu, S., M. Usta, and A.S. Berkem, *Bioactive coatings on Ti6Al4V alloy formed by plasma electrolytic oxidation*. Surface and Coatings Technology, 2016. **301**: p. 85-93.
39. Sahasrabudhe, H., J. Soderlind, and A. Bandyopadhyay, *Laser processing of in situ TiN/Ti composite coating on titanium*. J Mech Behav Biomed Mater, 2016. **53**: p. 239-49.
40. Li, Z., et al., *Mechanical, tribological and biological properties of novel 45S5 Bioglass(R) composites reinforced with in situ reduced graphene oxide*. J Mech Behav Biomed Mater, 2017. **65**: p. 77-89.
41. Penkov, O.V., et al., *Highly wear-resistant and biocompatible carbon nanocomposite coatings for dental implants*. Biomaterials, 2016. **102**: p. 130-6.
42. Mu, M., et al., *One-step preparation of TiO₂/MoS₂ composite coating on Ti6Al4V alloy by plasma electrolytic oxidation and its tribological properties*. Surface and Coatings Technology, 2013. **214**: p. 124-130.
43. Lee, J.K., et al., *Improved osseointegration of dental titanium implants by TiO₂ nanotube arrays with recombinant human bone morphogenetic protein-2: a pilot in vivo study*. Int J Nanomedicine, 2015. **10**: p. 1145-54.

44. Salou, L., et al., *Enhanced osseointegration of titanium implants with nanostructured surfaces: an experimental study in rabbits*. Acta Biomater, 2015. **11**: p. 494-502.
45. Ding, X., et al., *The effects of hierarchical micro/nanosurfaces decorated with TiO₂ nanotubes on the bioactivity of titanium implants in vitro and in vivo*. Int J Nanomedicine, 2015. **10**: p. 6955-73.
46. Lee, T., et al., *A facile approach to prepare biomimetic composite separators toward safety-enhanced lithium secondary batteries*. RSC Adv., 2015. **5**(49): p. 39392-39398.
47. Hazan, R., et al., *Study of TiO₂ nanotubes as an implant application*. AIP Conference Proceedings, 2016. **1704**(1): p. 6.
48. Huang, Y., et al., *Electrodeposition of porous hydroxyapatite/calcium silicate composite coating on titanium for biomedical applications*. Applied Surface Science, 2013. **271**: p. 299-302.
49. Lugovskoy, A. and S. Lugovskoy, *Production of hydroxyapatite layers on the plasma electrolytically oxidized surface of titanium alloys*. Mater Sci Eng C Mater Biol Appl, 2014. **43**: p. 527-32.
50. Fernandes, E.M., et al., *Bionanocomposites from lignocellulosic resources: Properties, applications and future trends for their use in the biomedical field*. Progress in Polymer Science, 2013. **38**(10-11): p. 1415-1441.
51. Gopi, D., et al., *A facile electrodeposition of hydroxyapatite onto borate passivated surgical grade stainless steel*. Corrosion Science, 2011. **53**(6): p. 2328-2334.
52. Liu, C., et al., *Rapamycin/sodium hyaluronate binding on nano-hydroxyapatite coated titanium surface improves MC3T3-E1 osteogenesis*. PLoS One, 2017. **12**(2): p. e0171693.
53. Liu, C., et al., *Biomimetic synthesis of TiO₂-SiO₂-Ag nanocomposites with enhanced visible-light photocatalytic activity*. ACS Appl Mater Interfaces, 2013. **5**(9): p. 3824-32.
54. Türk, S., et al., *Microwave-assisted biomimetic synthesis of hydroxyapatite using different sources of calcium*. Materials Science and Engineering: C, 2017. **76**: p. 528-535.
55. Mihok P., Murray J. , and W. R., *Novel Antibiotic delivery and Novel Antimicrobials in Prosthetic Joint infection*. JTO Peer-reviewed articles, 2016. **4**(1): p. 5.
56. Losic, D., et al., *Titania nanotube arrays for local drug delivery: recent advances and perspectives*. Expert Opin Drug Deliv, 2015. **12**(1): p. 103-27.
57. Getzlaf, M.A., et al., *Multi-disciplinary antimicrobial strategies for improving orthopaedic implants to prevent prosthetic joint infections in hip and knee*. J Orthop Res, 2016. **34**(2): p. 177-86.
58. Ferraris, S. and S. Spriano, *Antibacterial titanium surfaces for medical implants*. Mater Sci Eng C Mater Biol Appl, 2016. **61**: p. 965-78.
59. Sirelkhatim, A., et al., *Review on Zinc Oxide Nanoparticles: Antibacterial Activity and Toxicity Mechanism*. Nano-Micro Letters, 2015. **7**(3): p. 219-242.
60. Hang, R., et al., *Antibacterial activity and cytocompatibility of Cu-Ti-O nanotubes*. J Biomed Mater Res A, 2014. **102**(6): p. 1850-8.
61. Beyth, N., et al., *Alternative antimicrobial approach: nano-antimicrobial materials*. Evid Based Complement Alternat Med, 2015. **2015**: p. 246012.
62. Wang, Q., et al., *TiO₂ nanotube platforms for smart drug delivery: a review*. Int J Nanomedicine, 2016. **11**: p. 4819-4834.
63. Zhao, L., et al., *Antibacterial nano-structured titania coating incorporated with silver nanoparticles*. Biomaterials, 2011. **32**(24): p. 5706-16.

64. Liu, X., et al., *Antibacterial abilities and biocompatibilities of Ti-Ag alloys with nanotubular coatings*. Int J Nanomedicine, 2016. **11**: p. 5743-5755.
65. Mahltig, B., U. Soltmann, and H. Haase, *Modification of algae with zinc, copper and silver ions for usage as natural composite for antibacterial applications*. Mater Sci Eng C Mater Biol Appl, 2013. **33**(2): p. 979-83.
66. Top, A. and S. Ülkü, *Silver, zinc, and copper exchange in a Na-clinoptilolite and resulting effect on antibacterial activity*. Applied Clay Science, 2004. **27**(1-2): p. 13-19.
67. Das, K., et al., *Surface coatings for improvement of bone cell materials and antimicrobial activities of Ti implants*. J Biomed Mater Res B Appl Biomater, 2008. **87**(2): p. 455-60.
68. Lan, M.Y., et al., *Both enhanced biocompatibility and antibacterial activity in Ag-decorated TiO₂ nanotubes*. PLoS One, 2013. **8**(10): p. e75364.
69. Chen, P.C., et al., *The Microstructure and Capacitance Characterizations of Anodic Titanium Based Alloy Oxide Nanotube*. Journal of Nanomaterials, 2013. **2013**: p. 1-9.
70. Uhm, S.-H., et al., *E-beam fabrication of antibacterial silver nanoparticles on diameter-controlled TiO₂ nanotubes for bio-implants*. Surface and Coatings Technology, 2013. **228**: p. S360-S366.
71. Wang, Y., F. Papadimitrakopoulos, and D.J. Burgess, *Polymeric "smart" coatings to prevent foreign body response to implantable biosensors*. J Control Release, 2013. **169**(3): p. 341-7.
72. Surmenev, R.A., M.A. Surmeneva, and A.A. Ivanova, *Significance of calcium phosphate coatings for the enhancement of new bone osteogenesis--a review*. Acta Biomater, 2014. **10**(2): p. 557-79.
73. Sarafraz-Yazdi, A. and H. Vatani, *A solid phase microextraction coating based on ionic liquid sol-gel technique for determination of benzene, toluene, ethylbenzene and o-xylene in water samples using gas chromatography flame ionization detector*. J Chromatogr A, 2013. **1300**: p. 104-11.
74. Catauro, M., F. Bollino, and F. Papale, *Preparation, characterization, and biological properties of organic-inorganic nanocomposite coatings on titanium substrates prepared by sol-gel*. J Biomed Mater Res A, 2014. **102**(2): p. 392-9.
75. Owens, G.J., et al., *Sol-gel based materials for biomedical applications*. Progress in Materials Science, 2016. **77**: p. 1-79.
76. Catauro, M., et al., *Influence of PCL on mechanical properties and bioactivity of ZrO₂-based hybrid coatings synthesized by sol-gel dip coating technique*. Mater Sci Eng C Mater Biol Appl, 2014. **39**: p. 344-51.
77. Mahadik, D.B., R.V. Lakshmi, and H.C. Barshilia, *High performance single layer nano-porous antireflection coatings on glass by sol-gel process for solar energy applications*. Solar Energy Materials and Solar Cells, 2015. **140**: p. 61-68.
78. Asri, R.I., et al., *A review of hydroxyapatite-based coating techniques: Sol-gel and electrochemical depositions on biocompatible metals*. J Mech Behav Biomed Mater, 2016. **57**: p. 95-108.
79. Lim, C.S., *Upconversion photoluminescence properties of SrY₂(MoO₄)₄:Er³⁺/Yb³⁺ phosphors synthesized by a cyclic microwave-modified sol-gel method*. Infrared Physics & Technology, 2014. **67**: p. 371-376.
80. Laurenti, M., et al., *Zinc oxide nanostructures by chemical vapour deposition as anodes for Li-ion batteries*. Journal of Alloys and Compounds, 2015. **640**: p. 321-326.
81. Yang, Y. and Y.F. Cheng, *Fabrication of Ni-Co-SiC composite coatings by pulse electrodeposition — Effects of duty cycle and pulse frequency*. Surface and Coatings Technology, 2013. **216**: p. 282-288.

82. Cheah, Y.L., et al., *High-rate and elevated temperature performance of electrospun V₂O₅ nanofibers carbon-coated by plasma enhanced chemical vapour deposition*. *Nano Energy*, 2013. **2**(1): p. 57-64.
83. Long, Y., et al., *Phase composition, microstructure and mechanical properties of ZrC coatings produced by chemical vapor deposition*. *Ceramics International*, 2014. **40**(1): p. 707-713.
84. Wilkinson, M., et al., *Combinatorial atmospheric pressure chemical vapor deposition of graded TiO₂(2)-VO₂(2) mixed-phase composites and their dual functional property as self-cleaning and photochromic window coatings*. *ACS Comb Sci*, 2013. **15**(6): p. 309-19.
85. Wang, J., et al., *Chemical vapor deposition prepared bi-morphological carbon-coated Fe₃O₄ composites as anode materials for lithium-ion batteries*. *Journal of Power Sources*, 2015. **282**: p. 257-264.
86. Pinto, V.V., et al., *Long time effect on the stability of silver nanoparticles in aqueous medium: Effect of the synthesis and storage conditions*. *Colloids and Surfaces A: Physicochemical and Engineering Aspects*, 2010. **364**(1-3): p. 19-25.
87. Zhuo, Q., et al., *Facile synthesis of graphene/metal nanoparticle composites via self-catalysis reduction at room temperature*. *Inorg Chem*, 2013. **52**(6): p. 3141-7.
88. Park, J., et al., *Narrow window in nanoscale dependent activation of endothelial cell growth and differentiation on TiO₂ nanotube surfaces*. *Nano Lett*, 2009. **9**(9): p. 3157-64.
89. Prabhu., S. and E.K. Poulouse, *Silver nanoparticles: mechanism of antimicrobial action, synthesis, medical applications, and toxicity effects*. *International Nano Letters*, 2012. **2**(32): p. 10.
90. Abou El-Nour, K.M.M., et al., *Synthesis and applications of silver nanoparticles*. *Arabian Journal of Chemistry*, 2010. **3**(3): p. 135-140.
91. Devi, L.B. and A.B. Mandal, *Self-assembly of Ag nanoparticles using hydroxypropyl cyclodextrin: synthesis, characterisation and application for the catalytic reduction of p-nitrophenol*. *RSC Advances*, 2013. **3**(15): p. 5238.
92. Pishbin, F., et al., *Single-step electrochemical deposition of antimicrobial orthopaedic coatings based on a bioactive glass/chitosan/nano-silver composite system*. *Acta Biomater*, 2013. **9**(7): p. 7469-79.
93. Seuss, S., M. Lehmann, and A.R. Boccaccini, *Alternating current electrophoretic deposition of antibacterial bioactive glass-chitosan composite coatings*. *Int J Mol Sci*, 2014. **15**(7): p. 12231-42.
94. Farnoush, H., J. Aghazadeh Mohandesi, and H. Cimenoglu, *Micro-scratch and corrosion behavior of functionally graded HA-TiO₂ nanostructured composite coatings fabricated by electrophoretic deposition*. *J Mech Behav Biomed Mater*, 2015. **46**: p. 31-40.
95. Li, S., et al., *Nanosized Ge@CNF, Ge@C@CNF and Ge@CNF@C composites via chemical vapour deposition method for use in advanced lithium-ion batteries*. *Journal of Power Sources*, 2014. **253**: p. 366-372.
96. Pishbin, F., et al., *Electrophoretic deposition of gentamicin-loaded bioactive glass/chitosan composite coatings for orthopaedic implants*. *ACS Appl Mater Interfaces*, 2014. **6**(11): p. 8796-806.
97. Boccaccini, A.R., et al., *Electrophoretic deposition of carbon nanotubes*. *Carbon*, 2006. **44**(15): p. 3149-3160.
98. Singh, B.P., et al., *The production of a corrosion resistant graphene reinforced composite coating on copper by electrophoretic deposition*. *Carbon*, 2013. **61**: p. 47-56.

99. Chen, Q., et al., *Electrophoretic deposition of antibiotic loaded PHBV microsphere-alginate composite coating with controlled delivery potential*. Colloids Surf B Biointerfaces, 2015. **130**: p. 199-206.
100. Chen, Q., et al., *Electrophoretic co-deposition of polyvinyl alcohol (PVA) reinforced alginate-Bioglass(R) composite coating on stainless steel: mechanical properties and in-vitro bioactivity assessment*. Mater Sci Eng C Mater Biol Appl, 2014. **40**: p. 55-64.
101. Xiong, Y., et al., *The n-MAO/EPD bio-ceramic composite coating fabricated on ZK60 magnesium alloy using combined micro-arc oxidation with electrophoretic deposition*. Applied Surface Science, 2014. **322**: p. 230-235.
102. Cordero-Arias, L., A.R. Boccaccini, and S. Virtanen, *Electrochemical behavior of nanostructured TiO₂/alginate composite coating on magnesium alloy AZ91D via electrophoretic deposition*. Surface and Coatings Technology, 2015. **265**: p. 212-217.
103. Lajevardi, S.A., T. Shahrabi, and J.A. Szpunar, *Synthesis of functionally graded nano Al₂O₃-Ni composite coating by pulse electrodeposition*. Applied Surface Science, 2013. **279**: p. 180-188.
104. Kılıç, F., et al., *Effect of CTAB concentration in the electrolyte on the tribological properties of nanoparticle SiC reinforced Ni metal matrix composite (MMC) coatings produced by electrodeposition*. Colloids and Surfaces A: Physicochemical and Engineering Aspects, 2013. **419**: p. 53-60.
105. Wang, Z., et al., *Electrodeposition of alginate/chitosan layer-by-layer composite coatings on titanium substrates*. Carbohydr Polym, 2014. **103**: p. 38-45.
106. Huang, Y., et al., *Bioactivity and corrosion properties of gelatin-containing and strontium-doped calcium phosphate composite coating*. Applied Surface Science, 2013. **282**: p. 583-589.
107. Pei, X., et al., *Single-walled carbon nanotubes/hydroxyapatite coatings on titanium obtained by electrochemical deposition*. Applied Surface Science, 2014. **295**: p. 71-80.
108. Dorozhkin, S.V., *Calcium orthophosphate coatings on magnesium and its biodegradable alloys*. Acta Biomater, 2014. **10**(7): p. 2919-34.
109. Xin, W., et al., *Morphology dependence of TiO₂nanotube arrays on anodization variables and buffer medium*. Journal of Semiconductors, 2010. **31**(6): p. 063003.
110. Kowalski, D., D. Kim, and P. Schmuki, *TiO₂ nanotubes, nanochannels and mesosponge: Self-organized formation and applications*. Nano Today, 2013. **8**(3): p. 235-264.
111. Danookdharree, U.L., H. R. Tredwin, C, *The Effect of Initial Etching Sites on the Morphology of TiO₂ Nanotubes on Ti-6Al-4V Alloy*. Journal of Electrochemical Society, 2015. **162**(10): p. 213-222.
112. Xia, F., et al., *Microstructures of Ni-AlN composite coatings prepared by pulse electrodeposition technology*. Applied Surface Science, 2013. **271**: p. 7-11.
113. Calderón, J.A., J.E. Henao, and M.A. Gómez, *Erosion-corrosion resistance of Ni composite coatings with embedded SiC nanoparticles*. Electrochimica Acta, 2014. **124**: p. 190-198.
114. Zeng, Y., et al., *Graphene oxide/hydroxyapatite composite coatings fabricated by electrochemical deposition*. Surface and Coatings Technology, 2016. **286**: p. 72-79.
115. Arafat, M.T., et al., *Biomimetic composite coating on rapid prototyped scaffolds for bone tissue engineering*. Acta Biomater, 2011. **7**(2): p. 809-20.

116. Sharifi, E., et al., *Preparation of a biomimetic composite scaffold from gelatin/collagen and bioactive glass fibers for bone tissue engineering*. Mater Sci Eng C Mater Biol Appl, 2016. **59**: p. 533-41.
117. Gao, F., et al., *Biomimetic synthesis and characterization of hydroxyapatite/graphene oxide hybrid coating on Mg alloy with enhanced corrosion resistance*. Materials Letters, 2015. **138**: p. 25-28.
118. Xing, R., et al., *Colloidal Gold--Collagen Protein Core--Shell Nanoconjugate: One-Step Biomimetic Synthesis, Layer-by-Layer Assembled Film, and Controlled Cell Growth*. ACS Appl Mater Interfaces, 2015. **7**(44): p. 24733-40.
119. Liu, K., Y. Tian, and L. Jiang, *Bio-inspired superoleophobic and smart materials: Design, fabrication, and application*. Progress in Materials Science, 2013. **58**(4): p. 503-564.
120. Kokubo, T., *Apatite formation on surfaces of ceramics, metals and polymers in body environment*. Acta Materialia, 1997. **46**(7): p. 8.
121. Lugovskoy, S., et al., *Morphology and antimicrobial properties of hydroxyapatite-titanium oxide layers on the surface of Ti-6Al-4V alloy*. Surface and Coatings Technology, 2016. **301**: p. 80-84.
122. Tan, C.Y., et al., *The Effects of Calcium-to-Phosphorus Ratio on the Densification and Mechanical Properties of Hydroxyapatite Ceramic*. International Journal of Applied Ceramic Technology, 2015. **12**(1): p. 223-227.
123. Wu, S., et al., *Biomimetic porous scaffolds for bone tissue engineering*. Materials Science and Engineering: R: Reports, 2014. **80**: p. 1-36.
124. Benea, L., et al., *Preparation of titanium oxide and hydroxyapatite on Ti-6Al-4V alloy surface and electrochemical behaviour in bio-simulated fluid solution*. Corrosion Science, 2014. **80**: p. 331-338.
125. Ciobanu, G. and O. Ciobanu, *Investigation on the effect of collagen and vitamins on biomimetic hydroxyapatite coating formation on titanium surfaces*. Mater Sci Eng C Mater Biol Appl, 2013. **33**(3): p. 1683-8.
126. Wu, M., et al., *Biomimetic synthesis and characterization of carbon nanofiber/hydroxyapatite composite scaffolds*. Carbon, 2013. **51**: p. 335-345.
127. S. S. Qureshi, et al., *Nanoprotective Layer-by-Layer Coatings with Epoxy Components for Enhancing Abrasion Resistance: Toward Robust Multimaterial Nanoscale Films*. ACS Nano, 2013. **7**(10): p. 10.
128. Min, J., R.D. Braatz, and P.T. Hammond, *Tunable staged release of therapeutics from layer-by-layer coatings with clay interlayer barrier*. Biomaterials, 2014. **35**(8): p. 2507-17.
129. Qin, L., et al., *Preparation and bioactive properties of chitosan and casein phosphopeptides composite coatings for orthopedic implants*. Carbohydr Polym, 2015. **133**: p. 236-44.
130. Raphel, J., et al., *Multifunctional coatings to simultaneously promote osseointegration and prevent infection of orthopaedic implants*. Biomaterials, 2016. **84**: p. 301-14.
131. Mohseni, E., E. Zalnezhad, and A.R. Bushroa, *Comparative investigation on the adhesion of hydroxyapatite coating on Ti-6Al-4V implant: A review paper*. International Journal of Adhesion and Adhesives, 2014. **48**: p. 238-257.
132. Xie, Y., et al., *Graphene-reinforced calcium silicate coatings for load-bearing implants*. Biomed Mater, 2014. **9**(2): p. 025009.
133. Liu, W., et al., *Synthesis of TiO₂ nanotubes with ZnO nanoparticles to achieve antibacterial properties and stem cell compatibility*. Nanoscale, 2014. **6**(15): p. 9050-62.

134. Bakhsheshi-Rad, H.R., et al., *Bi-layer nano-TiO₂/FHA composite coatings on Mg–Zn–Ce alloy prepared by combined physical vapour deposition and electrochemical deposition methods*. Vacuum, 2014. **110**: p. 127-135.
135. Trivedi, P., et al., *Characterization and in vitro biocompatibility study of Ti–Si–N nanocomposite coatings developed by using physical vapor deposition*. Applied Surface Science, 2014. **293**: p. 143-150.
136. Boke, F., et al., *Plasma-Enhanced Chemical Vapor Deposition (PE-CVD) yields better Hydrolytical Stability of Biocompatible SiO_x Thin Films on Implant Alumina Ceramics compared to Rapid Thermal Evaporation Physical Vapor Deposition (PVD)*. ACS Appl Mater Interfaces, 2016. **8**(28): p. 17805-16.
137. Badami, V. and B. Ahuja, *Biosmart materials: breaking new ground in dentistry*. ScientificWorldJournal, 2014. **2014**: p. 986912.
138. Montemor, M.F., *Functional and smart coatings for corrosion protection: A review of recent advances*. Surface and Coatings Technology, 2014. **258**: p. 17-37.
139. Bagherifard, S., *Mediating bone regeneration by means of drug eluting implants: From passive to smart strategies*. Mater Sci Eng C Mater Biol Appl, 2017. **71**: p. 1241-1252.
140. Prem Ananth, K., et al., *A novel silica nanotube reinforced ionic incorporated hydroxyapatite composite coating on polypyrrole coated 316L SS for implant application*. Mater Sci Eng C Mater Biol Appl, 2016. **59**: p. 1110-24.
141. Wang, Q., et al., *Recent advances on smart TiO₂ nanotube platforms for sustainable drug delivery applications*. Int J Nanomedicine, 2017. **12**: p. 151-165.
142. Perez, R.A., et al., *Naturally and synthetic smart composite biomaterials for tissue regeneration*. Adv Drug Deliv Rev, 2013. **65**(4): p. 471-96.